METAL- AND LIGAND-CENTERED CHIRALITY IN SQUARE-PLANAR COORDINATION COMPOUNDS

This dissertation is submitted for the degree of “Doctor rerum naturalium”

within the PhD program of the Georg – August – University School of

Science (GAUSS)

Thorben Rüdiger Schulte

from Minden

October 2018

The left-hand fits only in the right glove,

so does the right-hand.

BETREUUNGSAUSSCHUSS

Prof. Dr. Guido H. Clever

Institut für Chemie und Chemische Biologie, Technische Universität Dortmund, Otto-Hahn-Str. 6, 44227 Dortmund

Prof. Dr. Dietmar Stalke

Institut für Anorganische Chemie, Georg – August – Universität Göttingen, Tammannstraße 4, 37077 Göttingen

MITGLIEDER DER PRÜFUNGSKOMMISSION

Referent:	Prof. Dr. Guido H. Clever
Koreferent:	Prof. Dr. Dietmar Stalke

WEITERE MITGLIEDER DER PRÜFUNGSKOMMISSION

Prof. Dr. Dirk Schwarzer

Max-Planck-Institut für biophysikalische Chemie, am Fassberg 11, 37077 Göttingen

Dr. Matthias Otte

Institut für Anorganische Chemie, Georg – August – Universität Göttingen, Tammannstraße 4, 37077 Göttingen

Dr. Michael John

Institut für Organische Chemie, Georg – August – Universität Göttingen, Tammannstraße 2, 37077 Göttingen

Dr. Holm Frauendorf

Institut für Anorganische Chemie, Georg – August – Universität Göttingen, Tammannstraße 2, 37077 Göttingen

Tag der mündlichen Prüfung: 26.10.2018

DECLARATION

I hereby declare that I wrote this dissertation on my own and without the use of any other than the cited sources and tools, and all explanations that I copied directly or in their sense are marked as such, as well as that this thesis has not yet been handed in neither in this nor in equal form at any other official examination commission.

Eidesstattliche Erklärung:

Ich versichere hiermit, dass ich die Doktorarbeit selbstständig und ohne Benutzung anderer als der angegebenen Quellen und Hilfsmittel angefertigt habe und alle Ausführungen, die wörtlich oder sinngemäß übernommen wurden, als solche gekennzeichnet sind, sowie dass die Doktorarbeit in gleicher oder ähnlicher Form noch keiner anderen Prüfungsbehörde vorgelegt wurde.

Thorben Schulte

Dortmund, October 15, 2018

SUMMARY

Chirality is an ubiquitous phenomenon in nature and fundamental for the principle of life we know.

One part of this thesis explores the self-assembly and the host-guest chemistry of novel chiral coordination compounds based on chiral organic bispyridyl ligands and Pd(II) metal centers. The structure and the properties of the assemblies are the result of a combination of variables like the temperature, the counter ions, the solvent, the shape and the flexibility of the ligand. The cavity provided by these structures is of high interest, as it can provide a chiral environment for guests to mimic chiral biological systems. The chiral environment can be used as enantioselective sensor or for enantioselective catalysis. Therefore, the preparation of chiral ligands and assemblies is described. The structures are characterized by NMR, ESI-MS, UV-Vis, CD and X-ray techniques. The variety of the formed three-dimensional structures includes monomeric cages, interpenetrated double cages, rings and catenanes. The conditions for the selective formation have been studied and even the enantiomeric excess of the used ligand was shown to have a tremendous effect on the structure and the properties of the assembly. Host guest experiments showed the potential of the provided chiral cavity as sensor, as a chiral helicene-based cage showed different binding affinities towards enantiomeric guests that could be monitored via NMR.

Another part of this thesis explores chiral cyclometalated Pt(II) complexes. Cyclometalated Pt(II) complexes are heavily studied for their interesting photophysical properties and their use in OLEDs. In contrast to luminescent octahedral complexes, the number of reported chiral Pt(II) complexes is comparable low. In octahedral complexes, where chirality is often the result of the assembly, the square planar coordination sphere needs a special design of achiral ligands for the formation of a chiral complex. A new kind of ligand motif for luminescent Pt(II) complexes is reported in this thesis. The synthesis of the achiral *trans*-chelating ligand and the formation of several chiral Pt(II) complexes is shown. The complexes are characterized by NMR, ESI-MS, UV-Vis, CD and X-ray techniques and the photoluminescent properties are reported, which showed circularly polarized luminescence for this new kind of binding motif.

LIST OF PUBLICATIONS AND CONFERENCE CONTRIBUTIONS

Publications

- "Subtle backbone modifications control the interpenetration of dibenzosuberone-based coordination cages" T. R. Schulte, M. Krick, C. I. Asche, S. Freye, G. H. Clever, *RSC Adv.* **2014**, *4,* 29724
- "Chiral-at-Metal Phosphorescent Square-Planar Pt(II)-Complexes from an Achiral Organometallic Ligand" T. R. Schulte, J. J. Holstein, L. Krause, R. Michel, D. Stalke, E. Sakuda, K. Umakoshi, G. Longhi, S. Abbate, G. H. Clever, *J. Am. Chem. Soc.* **2017**, *139*, 6863.
- *"Chiral Self-discrimination and Guest Recognition in Helicene-based Coordination Cages"* T. R. Schulte, J. J. Holstein, G. H. Clever, **2018**, submitted.

Award

- Poster Price at the "Tag der Chemie", **2017**, *Dortmund*, Germany.

Conference Contribution

- *Poster*, Tag der Chemie, **2017**, *Dortmund*, Germany
- *Poster*, SupraChem, **2017**, *Aachen*, Germany
- *Talk*, Jung Chemiker Symposium, **2016**, *Dortmund*, Germany
- *Poster*, The 11th International Symposium on Macrocyclic and Supramolecular Chemistry (ISMSC), **2016**, *Seoul*, South Korea
- *Poster*, Tag der Chemie, **2016**, *Dortmund*, Germany
- *Poster*, The 10th International Symposium on Macrocyclic and Supramolecular Chemistry (ISMSC), **2015**, *Strasbourg*, France
- *Poster*, Norddeutsches Doktorandenkolloquium, **2015**, Goslar, Germany
- *Talk*, Norddeutsches Doktorandenkolloquium, **2014**, Kiel, Germany
- *Poster,* IRTG Münster-Nagoya Abschlusssymposium, **2014**, Münster, Germany
- *Poster,* Niedersächsiches Katalyse Symposium, **2014**, *Göttingen*, Germany
- *Talk*, *Koordinationschemie-Tagung*, **2014**, *Kaiserlautern*, Germany

ACKNOWLEDGEMENTS

Special thanks go to my supervisor Prof. Guido Clever, for giving me the chance to do work with an international group in a challenging, but supportive atmosphere, numerous opportunities and constructive feedback with a sufficient amount of sarcasm.

I would like to thank Prof. Dietmar Stalke for being my secondary supervisor and cooperation partner and I thank Prof. Dirk Schwarzer, Dr. Matthias Otte, Dr. Michael John and Dr. Holm Frauendorf for being part of the examination committee.

I would like to thank Prof. L. Tietze, Prof. U. Diederichsen, Prof. L. Ackermann, Prof. C. Strohmann and Prof. S. Schneider for sharing their HPLC, CD, X-ray and irradiation equipment, which allowed the first and important break throughs before we had our own equipment.

I would like to thank my cooperation partners Prof. Keisuke Umakoshi, Prof. Eri Sakuda, Prof. Giovanna Longhi, Prof. Sergio Abbate, Prof. Gebhard Haberhauer, Prof. Herbert Waldmann and Dr. Andrey Antonchick for their contributions, that either led already or will hopefully lead to successful publications.

I would like to thank Dr. Michael John, Ralf Schöne and Prof. Dr. Wolf Hiller for help with NMR spectroscopy, especially Dr. Michael John for his help in interpretation.

I would also like to thank Mrs. Christiane Heitbrink and especially Dr. Holm Frauendorf and his team for measuring mass spectra.

I would like to thank Dr. Julian Holstein, Dr. Reent Michel, Dr. Lennard Krause and Prof. Dietmar Stalke for the X-ray structure determination, even after I challenged them with up to 12 disordered ligands in the asymmetric unit.

I would like to thank my research, bachelor and master students for their contributions to this work, namely Christian Schürmann, Philipp Schodder, Rahel Ziemer, Nazdar Reshu, Magiliny Manisegaran, Tobias Heitkemper, Mirco Weber, Fridolin Sommer, Atida Nasufovska, Anna Koelpin, Leif Antonschmidt and Sabine Malzkuhn.

I am thankful for the great cooperative atmosphere in the Clever lab from Version 1.0 till 3.0. I won’t look back on colleagues, but on friends I worked with, 我愛你.

I would like to thank Arne Glüer, Susanne Löffler, Rujin Li, Bin Chen, Samantha Darling and Marina Versäumer for correcting my thesis and much more.

Finally, I would like to thank my family and friends for their unconditional support.

TABLE OF CONTENT

1 Introduction -- 1

1.1 Historic Development--- 2

1.1.1 Development of the Concept of Chirality -- 2

1.1.2 Development of supramolecular chemistry --- 4

1.2 Chiral supramolecular assemblies -- 7

1.2.1 Chiral assemblies with achiral components -- 9

1.2.2 Chiral assemblies with chiral auxiliaries -- 11

1.2.3 Chiral assemblies with chiral organic bridging units ---------------------------- 13

2 Chiral-at-Metal Phosphorescent Square-Planar Pt(II)-Complexes from an Achiral Organometallic Ligand -- 17

2.1 Introduction --- 18

2.1.1 CPL--- 18

2.1.2 OLEDs-- 20

2.1.3 Chiral Phosphorescent Platinum(II) complexes---------------------------------- 22

2.2 Project target -- 25

2.3 Ligand Synthesis -- 26

2.4 Complex Synthesis -- 28

2.4.1 $PtL^{CN}(SEt_2)Cl$-- 28

2.4.2 Synthesis of *trans* PtL^{CN}_2--- 32

2.4.3 Yield Optimization-- 35

2.4.4 *cis* PtL^{CN}_2-- 37

2.5 Photophysical properties of *trans*-2 --- 40

2.6 Conclusion --- 42

3 Chiral Cages based on a Helicene Backbone -------------------------------------- 43

3.1 Introduction --- 43

3.1.1 Synthesis of helicenes-- 44

3.1.2 The helical pitch of helicenes and its consequences---------------------------- 46

3.1.3 Helicene based assemblies -- 48

3.2 Ligand synthesis ---------- 51
3.3 Cage formation ---------- 53
3.3.1 Short helicene cage C1 ---------- 53
3.3.2 Host-Guest Chemistry of C1 ---------- 58
3.3.3 Long helicene Cage C2 ---------- 59
3.3.4 Host Guest Chemistry of $C2^{P/M}$ ---------- 61
3.3.5 Formation of the chiral interpenetrated double cage DCM2 ---------- 65
3.4 Conclusion ---------- 67
4 Chiral Structures based on natural product inspired ligands ---------- 68
4.1 Introduction ---------- 68
4.2 Assemblies with L^{H1} and L^{H2} ---------- 69
4.3 5,5,5-Tricyclic backbone for assemblies ---------- 72
4.3.1 L^{W1} ---------- 72
4.3.2 L^{W2} ---------- 74
4.4 Conclusion ---------- 75
5 Experimental Section ---------- 77
5.1 Chiral-at-Metal Phosphorescent Square-Planar Pt(II)- Complexes from an Achiral Organometallic Ligand ---------- 78
5.1.1 Synthesis and characterization ---------- 78
5.1.2 Single-crystal X-ray Crystallography ---------- 87
5.2 Helicene based Cages ---------- 94
5.2.1 Synthesis of the compounds L^1 and L^2 ---------- 94
5.2.2 Cage synthesis ---------- 103
5.2.3 DOSY of $C1^{meso}$, $C1^{P/M}$ and $C2^{P/M}$ ---------- 110
5.2.4 Titration Experiments ---------- 110
5.2.5 Pascal's triangle for the cage formation with a racemic ligand mixture ---------- 111
5.2.6 Single-crystal X-ray Crystallography ---------- 112
5.2.7 Conformational flexibility of the helicene backbone ---------- 116
5.3 Nature inspired backbones for supramolecular assemblies ---------- 117
5.3.1 L^{H2} in DMSO ---------- 117
6 List of Figures ---------- 119

7 References --- 129

1 INTRODUCTION

Chirality is an ubiquitous phenomenon. The fact that chiral objects and their mirror images are not congruent is a fundamental principle and affects our daily live in every moment.[1] Even so a chiral object has in principle the same properties as its mirror image, this changes dramatically in the moment of interaction with other chiral objects.

The left hand fits only in the glove for the left hand, the left foot fits only in the left shoe and screws fit only in their corresponding screw thread with the same handedness. The examples might seem trivial, but this fundamental principle is the same for interaction of chiral chemical compounds on the molecular level and crucial for the biochemistry of live.[1] Enantiomers often have a different odor, as they fit in different receptors that are chiral as well.[2] Because of fitting into different receptors, the enantiomers of the drug thalidomide became tragically famous. The (*S*) enantiomer of thalidomide leads to a malformation of limbs if woman take it during their pregnancy, where the (*R*) enantiomer does not lead to a malformation and works only as desired as sedative.[3] Until today, several theories exist to explain why the biological systems on earth often use only one of two possible enantiomers of every chiral compound that exists exclusively. Nevertheless, the origin of homochirality in nature is still unknown.[4]

Whatever the origin is, the need of chiral compounds is definite. Therefore tools that work for example as chiral sensors to distinguish between enantiomers or catalysts for enantioselective reactions are of high interest and are therefore heavily studied.[1] The control over the chirality of compounds made big improvements and led to a Nobel Prize in the field of asymmetric catalysis awarded to Noyori, Knowles and Sharpless.[3] Nevertheless, the way that chemists control the stereochemistry of compounds differs significantly from biological systems and the efficiency of artificial systems is still far behind the efficiency of biological systems. Supramolecular chemistry has a great potential to improve catalytic reactions by giving a specially designed microenvironment, for example via the selective recognition of a particular catalytic intermediate.[5]

One part of this work concentrated on the development of new chiral supramolecular hosts and their interaction with chiral compounds to mimic the biological principle in enantioselective guest recognition. The other part of this work was to develop a new binding motif for cyclometalated chiral square planar complexes.

1.1 Historic Development

"If I have seen further it is by standing on the shoulders of Giants."[6] These words in a letter to Robert Hooke in the year 1675 are from Isaac Newton and some of the biggest “shoulders” in the field of chirality and supramolecular chemistry are depicted in the next chapters.

1.1.1 Development of the Concept of Chirality

In 1904 Lord Kelvin defined chirality based on the Greek word “*cheir*” for “hand” and that “any geometrical figure, or group of points,” is chiral “if its image in a plane mirror, ideally realized, cannot be brought to coincide with itself”.[7] But it was a long way to this definition and it started with a fight:[8] In the 1820s Wöhler and Liebig reported silver salts with the same elemental composition, but very different characteristics. Liebig accused Wöhler of false results, but after receiving a sample of Wöhler, he was able to verify Wöhler’s results. Both results were correct, but the compounds were not the same, even when the elemental composition was the same. On the one hand Wöhler discovered the silver fulminate, on the other hand Liebig discovered the silver cyanate which are composed of the elements in the same ratio, but with a different constitution (**Figure 1.1 a**), but the concept of constitution did not exist until that date.[9] A few years later their results led, together with a series of similar findings of compounds with same elemental compositions, but different characteristics, to the concept of isomerism developed by Berzelius in 1831.[8] It marks a fundamental change in the scientific society, that the way of the connectivity, the constitution, effects the properties of compounds.

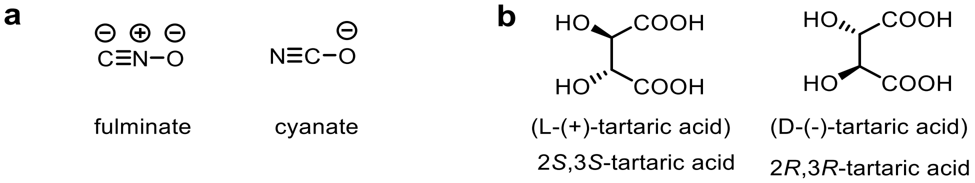

Figure 1.1 a: Silver fulminate discovered by Wöhler and silver cyanate discovered by Liebig led to the concept of constituion; b: the first stereoisomers discovered by Pasteur.[9]

In 1848 Pasteur extended the understanding of isomers by a very important one, the stereoisomers.[7] Pasteur studied tartaric acid. Solutions of tartaric acid, when isolated out of living things, rotated the plane of polarization of polarized light. In contrast, solutions of tartaric acid synthesized by chemical synthesis did not show rotation of the plane of polarized light. Pasteur crystallized chemically synthesized tartaric acid and found crystals with two different shapes, which showed opposite rotation of polarized light in solution. The stereoisomers of tartaric acid are like mirror images of each other and cannot be turned into each other by rotation (**Figure 1.1 b**). Without knowing, Pasteur was the first one to observe the seldom phenomena of spontaneous resolution that allowed him his findings. The term spontaneous resolution describes the phenomenon, that a solution with a mixture of both enantiomers present in same proportions can crystalize in a way, where each crystal contains only one of the two enantiomers.[10]

It took 51 years to extend the concept of stereoisomers to metal complexes, which can be chiral even without the use of chiral organic ligands. Pioneer on this subject was Alfred Werner, who received a Nobel Prize for his works in 1913.[11] Werner predicted in 1899 the existence of chirality for octahedral complexes with chelating ligands like ethylenediamine (en) *cis*-$[M(en)_2XY]$ which he reported 12 years later in the form of $[Co(en)_2(NH_3)X]X_2$ (X = Cl, Br)] (**Figure 1.2 a**).[12] A related chiral octahedral complex, which is heavily studied in literature is the tris(bipyridine)ruthenium(II)cation $[Ru(bpy)_3]^{2+}$ and its numerous derivatives that are studied for their interesting photochemistry (**Figure 1.2 b**).[13]

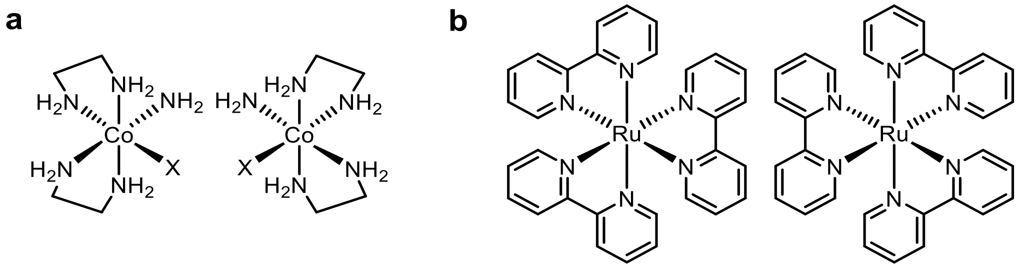

Figure 1.2 a: The enantiomers of the first reported chiral octahedral complex by Werner $[Co(en)_2(NH_3)X]X_2$ (X = Cl, Br)]; b: the enantiomers of the metal complex $[Ru(bpy)_3]^{2+}$.

In contrast to the awareness of chirality for octahedral and tetrahedral complexes without the use of a chiral ligands, for complexes with a square planar coordination sphere, the chirality is often overlooked to this date.[14] Ironically the square planar coordination sphere of Pt(II) has been proven in 1935 with an achiral ligand that led to chirality of the complex (**Figure 1.3**).[15] In absence of X-ray structures, the design of the ligands (meso1,2-diphenylethane-1,2-diamine (dpen) and 2-methylpropane-1,2-diamine (mpn)) was chosen in a certain way, that only the square planar coordination sphere would lead to enantiomers. The enantiomers were proven by the optical activity and therefore the square planar coordination sphere was verified.

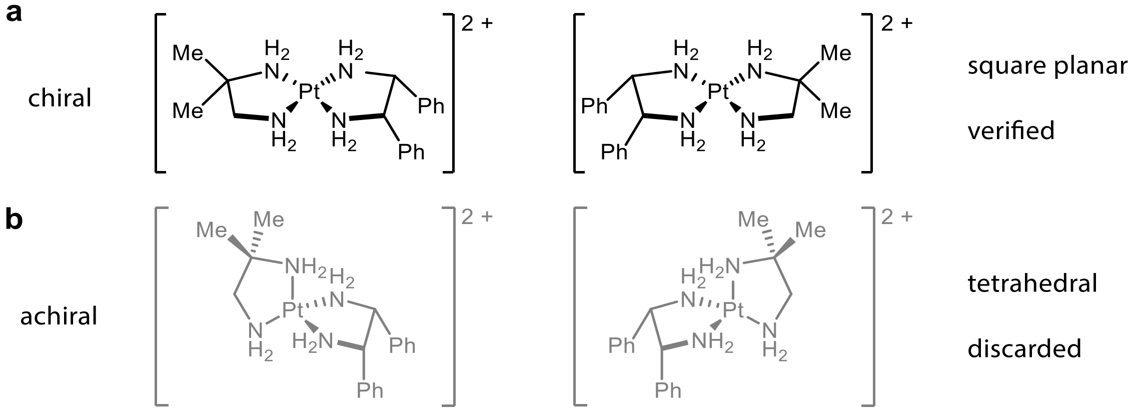

Figure 1.3 The intelligent design of the ligands was used to prove the square planar coordination sphere of Pt(II). Only in case of the square planar coordination sphere the complex is chiral and can show optical activity after separation of the isomers.[15]

1.1.2 Development of supramolecular chemistry

Since the early discoveries supramolecular chemistry is intensively studied with around 20,000 corresponding publications per year covering applications in the field of sensing, separation, catalysis, biomedical technologies and more.[16]

The first artificial host has been produced accidently.[17] Pedersen used 1-butanol bis(2-chloroethyl)ether and the sodium salt of 2-(o-hydroxyphenoxy)tetrahydropyran in the synthesis of bis[2-(o-hydroxyphenoxy)ethyl] where he found a very small amount of a white, fibrous, crystalline byproduct, the first crown ether (**Figure 1.4**).[18] The byproduct was caused by a little contamination with catechol and led to the discovery of the crown ethers and their outstanding binding properties, for which Pedersen shared the Nobel Prize with Jean-Marie Lehn and Donald Cram in 1987.[19]

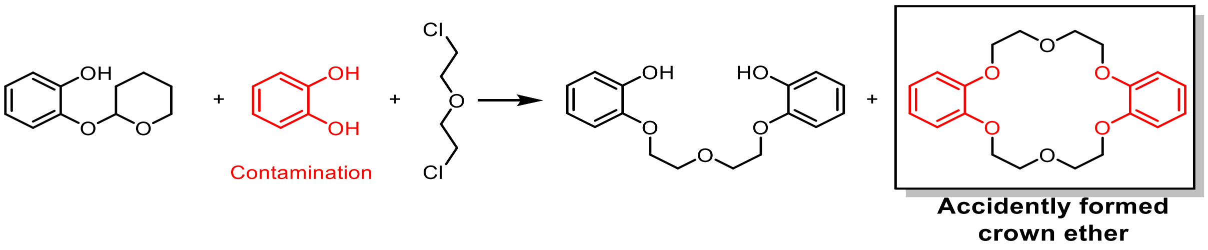

Figure 1.4 The first crown ether, that was accidently synthesized by Pedersen.[17]

The cyclic hexaether increased the solubility of potassium permanganate in organic solvents and the solubility of the crown ether in methanol was increased after addition of a sodium salt.[17] The high binding affinity of crown ethers can be explained with a cavity created by the cyclic host and was thoroughly studied for a series of systems. The structures of 12-crown-4, 15-crown-5, 18-crown-6 and 21-crown-7 and their size depending selectivity towards some cations are depicted in **Figure 1.5**. To name a crown ether, the total number of atoms in the cycle is written before “crown” and the number of oxygen atoms is written after “crown”. Due to their high electronegativity, the oxygen atoms act as binding site for the cations through dipole-ion interactions. Therefore, the number of oxygen atoms effects the binding affinity, but the matching size of the host and the guest are critical for the binding efficiency and the selectivity, which makes 18-crown-6 the host with the highest binding affinity for K^+.

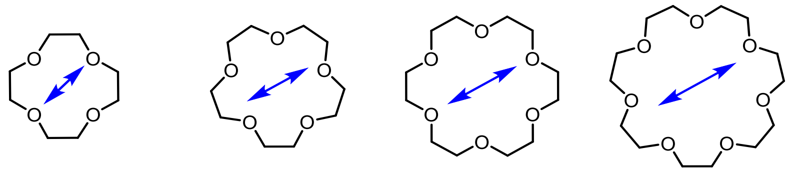

	12-Crown-4	**15-Crown-5**	**18-Crown-6**	**21-Crown-7**
	0.12 - 0.15 nm	0.15 - 0.22 nm	0.26 - 0.32 nm	0.34 - 0.43 nm

Binding Constants in Methanol (Log K_a)

Li^+ (0.136 nm)	-0.57	**1.21**	0.00	-
Na^+ (0.194 nm)	1.67	3.32	**4.28**	2.12
K^+ (0.266 nm)	1.60	3.5	**5.67**	4.3
Cs^+ (0.334 nm)	1.63	2.74	4.5	**5.01**

Figure 1.5 Structures of 12-Crown-4, 15-Crown-5, 18-Crown-6 and 21-Crown-7, their inner diameter and selectivity towards Li^+, Na^+, K^+, Cs^+.

Further advance of the concept of crown ethers led to cryptands, developed by Jean-Marie Lehn, and spherands, developed by Donald Cram.[2,20] The fundamental principles that make this systems to such strong binding hosts can be understood by comparing their binding properties. Four hosts with the same number and equal binding sites but different level of preorganization are compared in **Figure 1.6**. Pentaethylenglycoldimethylether (EG5) is an open chain molecule and represents the class of podands. It has the lowest binding constant for the potassium cation of all four. The cyclic 18-crown-6 represents the class of corands and shows a much higher binding constant, beaten by the three-dimensional bicyclic [2.2.2]cryptand which is only beaten by the spherand-6, which cannot bind K^+ due to the small inner diameter and is compared with Li^+.

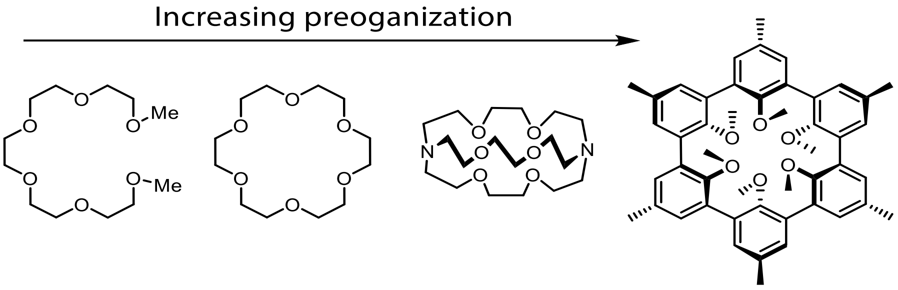

	EG5	**18-Crown-6**	**[2.2.2]cryptand**	**spherand-6**
log $K(K^+)$ MeOH, 25 °C	2.3	6.08	10.0	16 (for Li^+)

Figure 1.6 Four different hosts with the same number of binding sites but different binding constants due to the level of preorganization of the host.

The increased stability of the host guest complexes compared to the open chains is called the macrocyclic effect and has entropic and enthalpic reasons. Macrocyclic hosts are frequently less strongly solvated compared to the open chain molecules. Decreasing the number of solvent-ligand bonds to break is an enthalpic driving force. The lower flexibility of the more organized cyclic structures leads to a decreased loss of freedom upon complexation and is an entropic reason for the higher binding.[2,20]

In 2016 Fraser Stoddart, Bernard Feringa and Jean-Pierre Sauvage received the Nobel Prize for their work on mechanical bounding and nanomachines.[21] Sauvage *et al.* developed catenanes, molecular interlocked rings which marked a new way to bind molecules (**Figure 1.7 a**).[21,22] Transition metals like Cu(I) were used to template the catenanes allowing the synthesis in high yields. Before catenanes were synthesized in a statistical approach in very low yields of less than 1 %.[2,23]

The concept was extended with a big variety of binding motifs to template the supramolecular assemblies allowing the formation of a vast number of topologies like a [3]catenane, a [5]catenane[24] called olympiadane due to its similarity to the Olympic rings, a [2]rotaxane[25], a chiral molecular trefoil knot[26] and many more (**Figure 1.7 b**).[27]

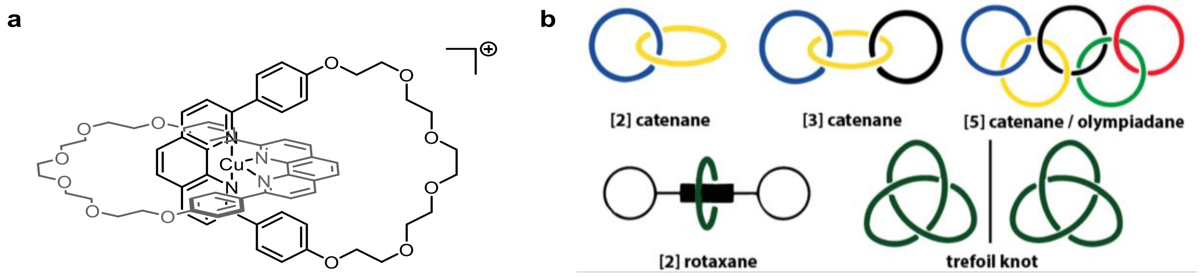

Figure 1.7: a: [2]catenane reported by Sauvage, the Cu(I) is used as template before the ring closure leading to high yields for the formation; b: simplified schematic overview of reported catenanes, a rotaxane and the chiral trefoil knot.[22]

Stoddart *et al.* saw the potential of Sauvage's work for molecular machines and developed molecular shuttles.[28] A rotaxane is a molecular cycle around a linear molecule, the axle (**Figure 1.7**). The molecular cycle can be moved to certain positions on the axle and is hindered from leaving the axle by stoppers. A variety of methods have been developed to control the position on the axle for example via light irradiation, change in pH or temperature. Extending of this concept Stoddart *et al.* made molecular "lifts", which can move itself up above a surface, and molecular muscles, that can bend and stretch.[28,29]

Feringa *et al.* reported more than 50 molecular motors that allow an unidirectional turning.[28] Their first synthetic molecular motor published in 1999, marked a turning point in the field. The motor was made out of a single molecule, that contained two chiral "paddle" units connected through a double bond and the turning could be controlled via thermal isomerization and photoisomerization (**Figure 1.8**).[30] Depending on the wavelength, the paddles can rotate in two directions after breaking of the double bond via light irradiation for the *cis*-*trans* isomerization, but the thermal isomerization occurs only in one direction and therefore the full 360° rotation is only possible in the clockwise sense. The chirality of the paddles is necessary to dictate the direction of thermal isomerization to the energetically favored (*P*,*P*) isomers with the methyl groups in axial position.

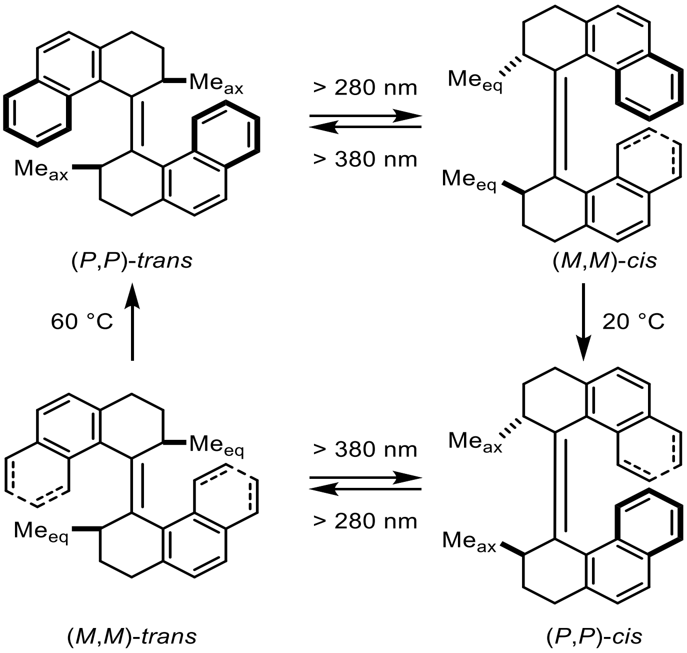

Figure 1.8 The combination of photoisomerization and thermal isomerization leads to a clockwise monodirectional rotation of the first reported molecular motor.[30]

1.2 Chiral supramolecular assemblies

Supramolecular chemistry is often defined as the “chemistry beyond the molecule”, and the definition was initially restricted to noncovalent interactions and host guest chemistry.[2,31] As the scope developed over time and the definitions were extended, noncovalent interactions still play a major role in the host guest chemistry, which is an important aspect in this chapter. As discussed in the introduction, the interaction of two chiral compounds can differ strongly depending on the combination of stereoisomers. Even so enantiomers have mainly the same properties, the combination of two stereoisomers leads to diastereomers which differ in their properties and are only enantiomers to the opposite combination (**Figure 1.9**).[1] Based on this principle chiral hosts can differentiate between enantiomers or catalyze the formation of one stereoisomer preferably making chiral supramolecular assemblies an interesting class to study.[1]

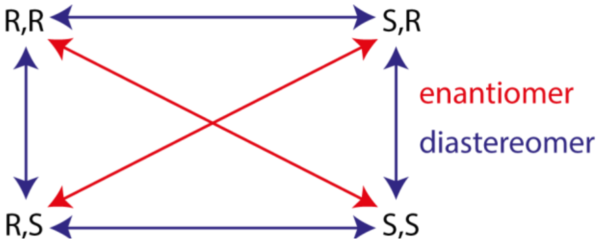

Figure 1.9 The four combinations of stereoisomers in the case of two chiral centers and their relationship to each other as enantiomers and diastereomers.[1]

Self-assembly is a very important concept in supramolecular chemistry and describes the formation of ideally one defined structure from an unorganized system with different compounds.[2,31] The process is spontaneous and leads normally to the thermodynamic product. To reach the thermodynamic product, the formation has to be under reversible conditions to allow corrections in the building process. For an efficient self-assembly, the geometry of the interacting components should match well with all binding sites involved.[2] Metal cations are often used to template the assemblies and have been especially successful in the formation of highly complex supramolecular architectures.[32] Therefore, this chapter will focus according to this thesis on metal templated chiral supramolecular assemblies.

The formation of chiral coordination complexes and assemblies can be categorized into two main approaches “hard” and “soft”.[33] In the “soft” approach none of the building blocks is chiral itself but chirality is a result of the conformation of the assembly. Examples are the spatial arrangement of the structure or an induced twisting of the ligands that can cause the chirality of the assembly (**Figure 1.10**). An advantage of this approach is the easily available access to achiral ligands. A disadvantage is the difficulty to control of the chirality, as the assembly leads to a racemic mixture. The racemic mixture needs further separation steps to isolate the enantiopure assemblies and the enantiopure assemblies may racemize again.

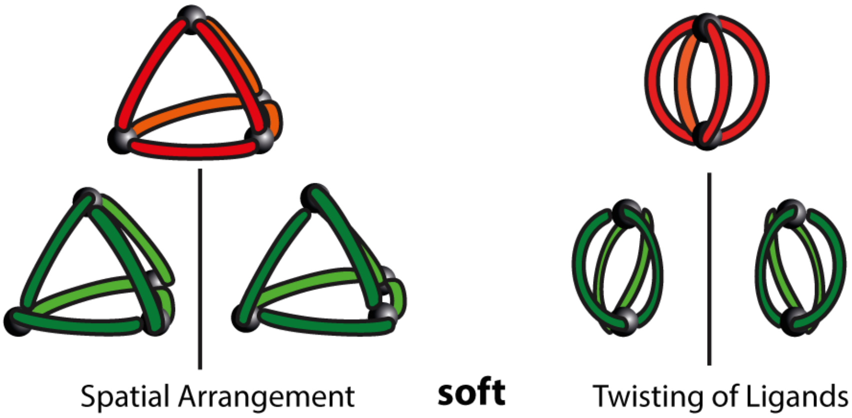

Figure 1.10 The “soft” approach: All parts are achiral but the assembly is chiral as result of the spatial arrangement or a twisting of the ligands.[33]

In the “hard” approach one of the building blocks is chiral, for example a chiral ligand that connects the metal centers with each other or a chiral auxiliary that is attached to the metal center which does not link between metal centers. Advantages of this approach are the predetermined chirality and the lower possibility of racemization. A disadvantage can be the need of enantiopure organic molecules, that may have to be separated.

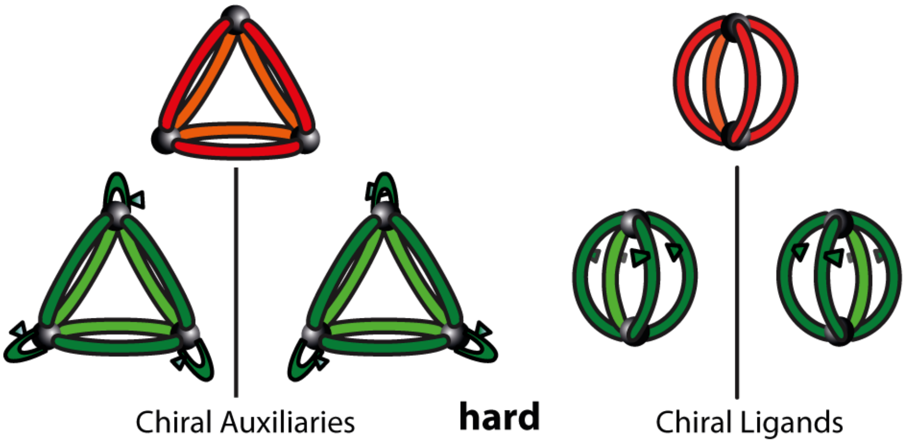

Figure 1.11 The "hard" approach: One component of the assembly is chiral leading to chirality of the whole assembly, that can be a ligand attached to the metal center, that does not link to another metal center or a ligand that connects two (or more) metal centers.[33]

1.2.1 Chiral assemblies with achiral components

Upon coordination, an achiral ligand can be twisted into a chiral conformation. Also, a twisting of the ligand that occurs in solution without dominance for one enantiomer, can be fixated upon assembly.[33] If the chirality is a result from the spatial arrangement, the most prominent assemblies have C_2 symmetric pseudo-tetrahedral structures with *Δ* or *Λ* stereochemistry or have C_3 symmetric pseudo-octahedral structures with *fac* or *mer* stereochemistry.[34]

Tetrahedral clusters with either *ΔΔΔΔ* or *ΛΛΛΛ* stereochemistry have been reported by Raymond *et al.*.[35,36] The four gallium metal ions are positioned in the corners and are linked with naphthalene-based bis-catechol ligands leading to a highly charged anionic complex. Through interaction with chiral guest ions, the racemic mixture of the assembly could be resolved into the enantiomers and the enantiomers were even stable towards racemization, when up to three ligands were replaced by phenyl-derivates.[35,37] A variety of studies for the catalytic activity were shown for this system, either by encapsulation of a catalytic system or the catalytic activity of the host itself. Selective C-H bond activation of aldehydes could be shown after encapsulation of a cationic half-sandwich Ir complex $[Cp^*(PMe_3)Ir(Me)C_2H_4]^+$, where the size and shape of the guest affected the reactivity.[38,39] The 3-aza-Cope rearrangement of enammonium cations to unsaturated aldehydes have been reported for the same host (**Figure 1.12**).[39,40] Addition of $[NEt_4]^+$ as strong binding guest molecule inhibited the catalytic activity and supported the proposed mechanism inside the cavity. The scope of catalyzed reactions for this assembly has been extended including Nazarov cyclisation,[41] hydrolysis,[42] isomeration of allylic alcohols and intramolecular hydroalkoxylation.[43]

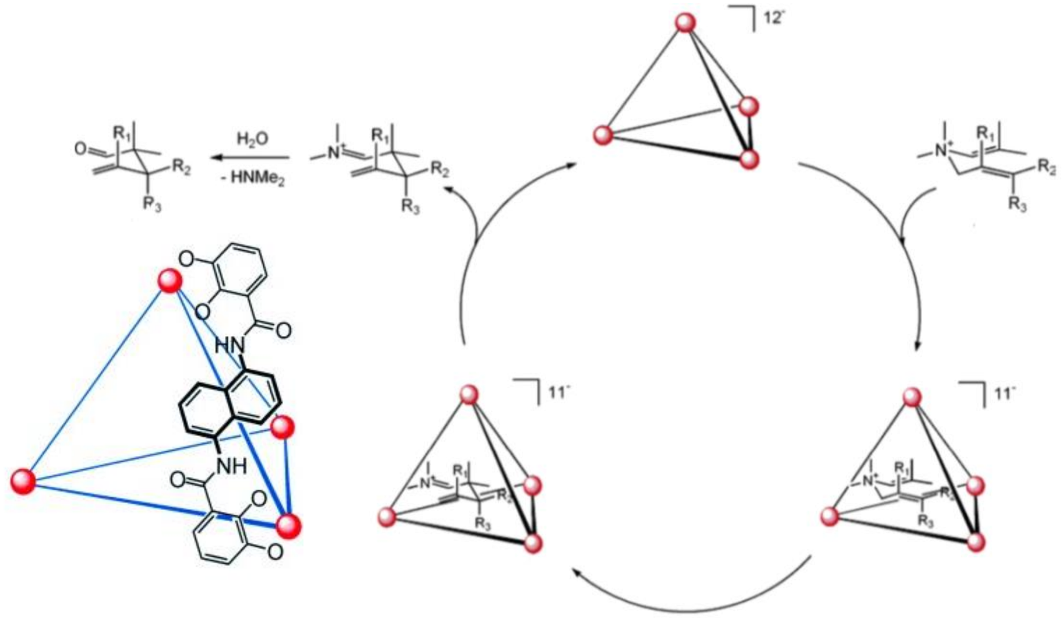

Figure 1.12 left: Tetrahedral cluster with Ga^{III} ions in the corners*;* right: proposed catalytic cycle of 3-aza Cope rearrangement inside the assembly. © American Chemical Society, Wiley-VCH Verlag GmbH & Co[39,40]

A trigonal antiprism based on calixarene ligands has been reported by Shinkai *et al.* (**Figure 1.13**).[44] $[Pd(PPh_3)_2]^{2+}$ was used to link the two bowl shaped homooxacalix[3]-aryl esters linearly. The twist of the triply bridged helical structure causes the chirality, that can be controlled with chiral guests. The normally racemic mixture of (*P*) and (*M*) enantiomers can contain predominantly one enantiomer up to 70 % by uptake of enantiopure chiral $R^{*}NH_3^+$ guests. The chiral induction upon guest uptake resulted in significant CD bands for the assembly.

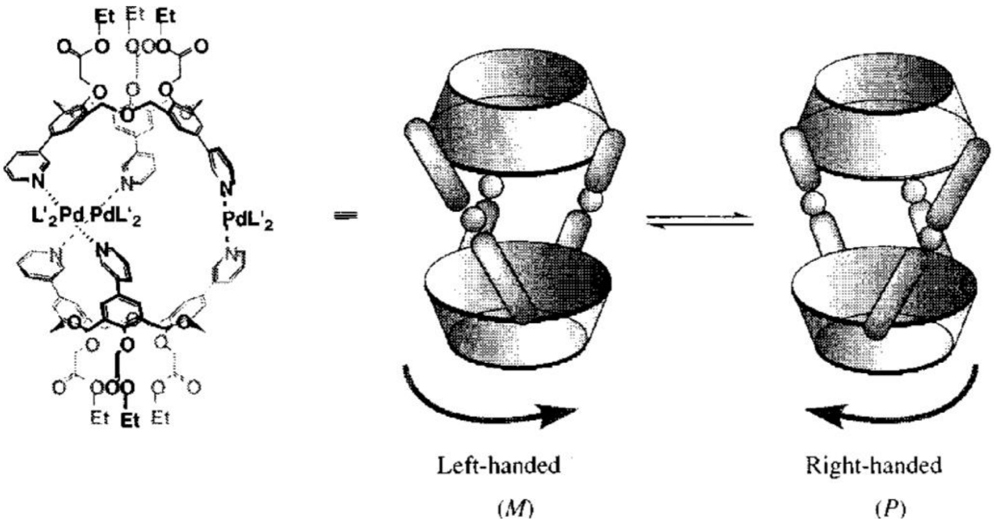

Figure 1.13 The trigonal antiprism based on calixarene ligands is able to switch between the enantiomers (L' = PPh_3). Copyright © American Chemical Society[44]

Tetrahedral nano-cages with the tetrazole based ligands **LT1** and **LT2** have been reported by Mukherjee *et al.* with *cis*-blocked Pd(II) metal corners (**Figure 1.14**).[45] With **LT1** the edge directed tetrahedron **T1** was formed with a ligand to Pd ratio of 1:1. With **LT2** the face directed tetrahedron **T2** was formed with a ligand to Pd ratio of 2:3. The achiral ligands can have either

Δ or *Λ* configuration in the assembly leading to the chirality of the system. A mixture of both ligands with the *cis*-blocked Pd(II) led to the formation of both assemblies showing a clean self-sorting ability of the water-soluble system. Hydrophobic aromatic nitro-olefins have been encapsulated into **T1** and the catalytic activity for Michael reactions of **T1** for the nitro-olefins with 1,3-dimethybarbituric acid could be shown. **T2** showed no catalytic activity due to the absence of large open windows, which did not allow encapsulation of the guests.

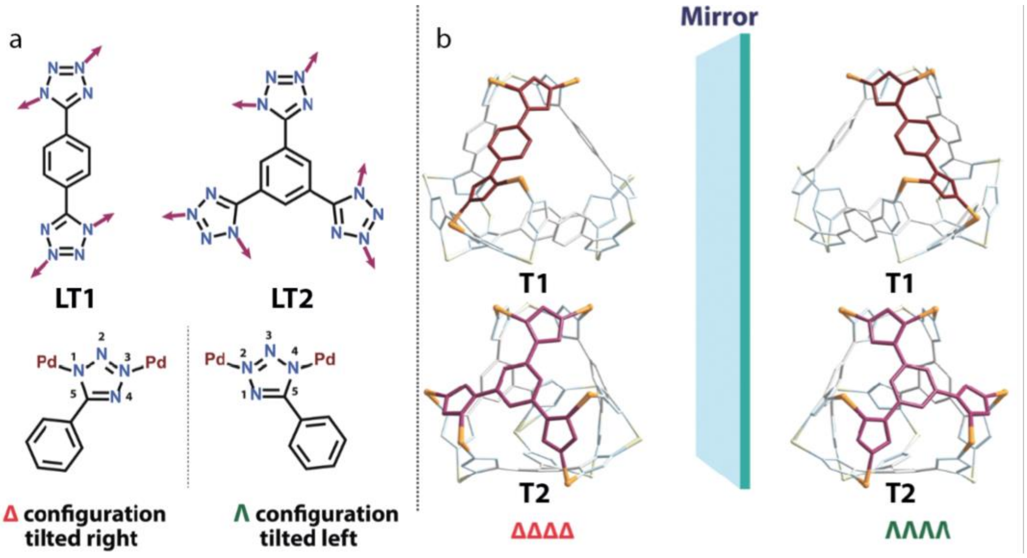

Figure 1.14 a: Coordination modes of LT1 and LT2; b: Enantiomers of the edge directed tetrahedron T1 based on LT1 and enantiomers of the face directed tetrahedron T2 based on LT2. © Royal Society of Chemistry[45]

1.2.2 Chiral assemblies with chiral auxiliaries

The use of achiral *trans*- and *cis*-blocked square planar metals for chiral supramolecular assemblies has been shown in the chapter before but led only to racemic mixtures of the assemblies. To control the stereochemistry of the assembly, an enantiopure auxiliary ligand can be used.

Stang *et al.* reported a variety of tetranuclear assemblies in form of molecular squares (**Figure 1.15**).[46] (*R*)-BINAP as chiral auxiliary was attached as the *cis*-block for a metal with square planar coordination sphere, either Pd(II) or Pt(II), and linear coordinating ligands like 2,6-diazaanthracene were used to link between the metal corners. Experiments with a racemic mixture of the auxiliary led to all six possible isomers.

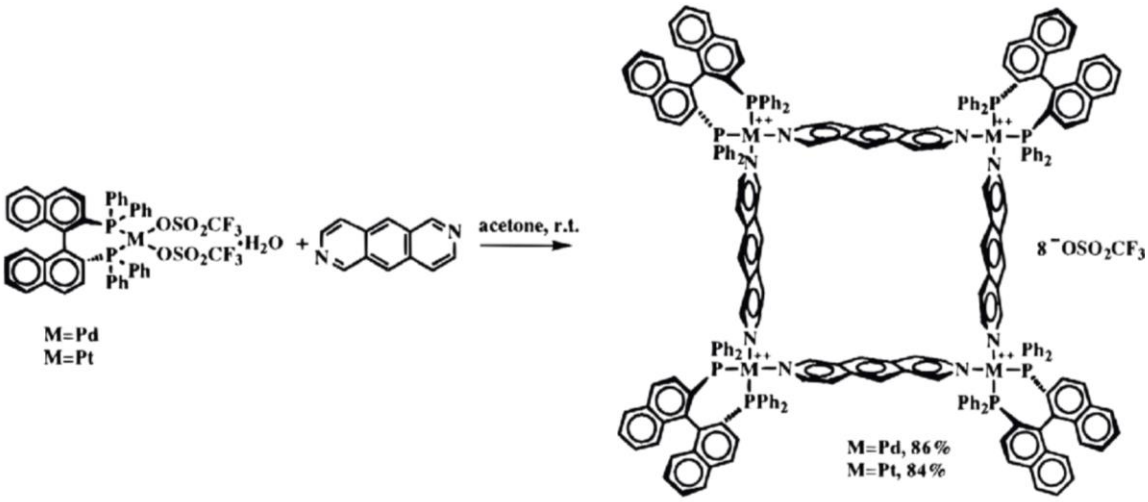

Figure 1.15 A tetranuclear assembly forming a molecular square with the use of a *cis*-blocked metal center. © American Chemical Society[46]

In 2004 Fujita *et al.* reported an achiral octahedral M_6L_4 cage with a triazine based ligand and a strong binding ability due to hydrophobic forces, where two different guests could be selectively recognized by the host in aqueous solution.[47] Further studies showed the ability to catalyze unusual [2+4] and [2+2] cycloaddition of arenes.[48] The system contained *cis*-blocked Pd or *cis*-blocked Pt metal centers, whose blocking ligands could be easily replaced with an chiral auxiliary ligand, leading to a variety of chiral cages which can act as enantioselective catalysts (**Figure 1.16**).[49,50]

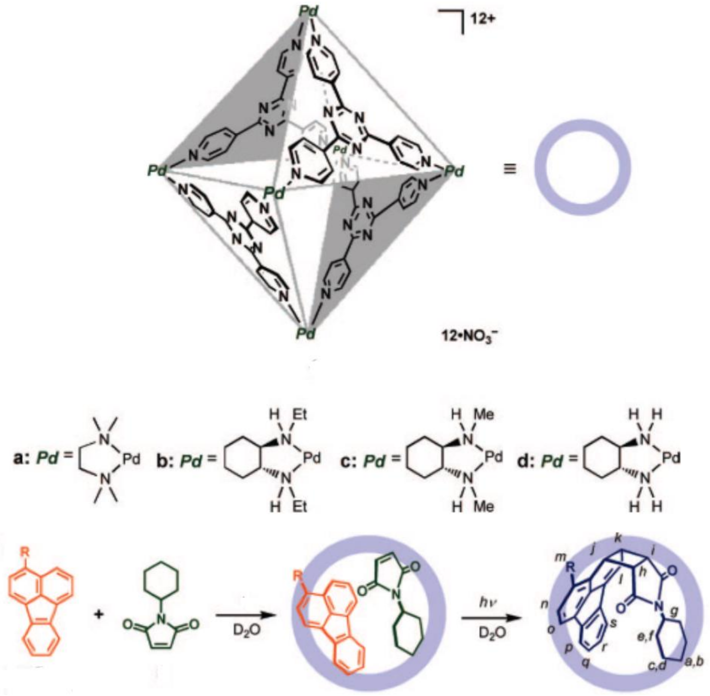

Figure 1.16 top: a: The achiral cage; b-d: the chiral auxiliary ligands leading to the chiral cage ; bottom: [2 + 2] Photoaddition reaction of N- cyclohexylmaleimide with fluoranthene(-derivative, R = H/Me) inside the cage. © American Chemical Society [50]

Fujita *et al.* could show, that the chiral auxiliary influences the central cavity and leads to controlled asymmetric [2+2] olefin cross photoaddition inside the host. The influence of the central cavity is strongly related to the steric bulk of the auxiliary ligand. Therefore the auxiliary ligand with the biggest steric bulk, the *trans*-N,N'-diethyl-cyclohexanediamine led to the strongest CD bands and the highest ee of 50 % for the [2+2] photoadditon at 33 % overall yield.[50]

1.2.3 Chiral assemblies with chiral organic bridging units

Lützen *et al.* reported a variety of BINOL-based bis(pyridine) ligands to form dinuclear coordination compounds. The formed helicates showed a different isomerization depending on the metal cation. Where the addition of Zn(II) ions did not lead to a specific complex formation, Ag(I) and Cu(I) led to D_2-symmetric dinuclear double-stranded helicates (**Figure 1.17**), where Fe(II) led to D_3-symmetric dinuclear triple-stranded helicates.[51] Remarkably the formation with Ag(I) and Cu(I) occurred highly diastereoselective. As product the (*M*)-(*Δ,Λ*) complex could be ruled out, because the ^{1}H NMR spectra should be more complicated. With experimental and calculated CD-spectra the selective formation of the enantiopure (*M*)-(*Δ,Δ*) complex was proven (**Figure 1.17 a**).

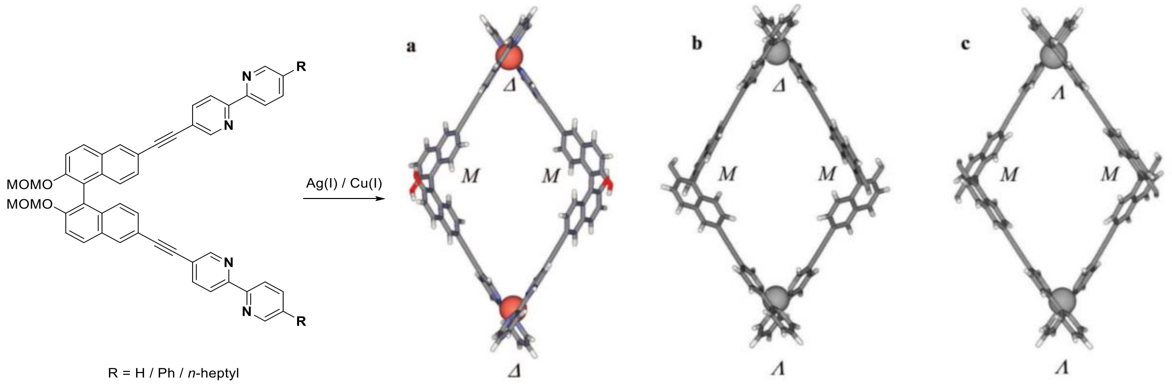

Figure 1.17 RI-BLYP/SVP (TZVP for copper) optimized structures of the three possible diastereomeric doublestranded helicates (a, b, c), but the (*M*)-enantiomers of the ligands selectively induce the (Δ,Δ)-helicate (a). © American Chemical Society[51]

Lützen *et al.* reported also a variety of homochiral supramolecular structures with related bis(pyridine) ligands based on BINOL, that nicely showed a strong dependence on the linker length and angle on the resulting supramolecular assembly as reported for achiral systems before (**Figure 1.18**).[52] The meta substituted pyridine led to assemblies in form of $[Pd_4L_8]$, with two BF_4^- counter ions encapsulated inside the cavity. The BF_4^- counter ions work as templates and were crucial for the formation of the structure.[53] The structure revealed by X-ray structure determination shows the high flexibility of the ligands. The ligands can adopt a suitable angle, leading to four ligands in the short edges with a dihedral angle of the binaphthyl group higher than 90 °, where the other four ligands have dihedral angles significantly smaller than 90 °. The para substituted pyridine led to much bigger $[Pd_6L_{12}]$ assemblies with a much bigger cavity, where the BF_4^- counter anions were not crucial for the structure. Another modification with a para substituted pyridine attached at another position of the BINOL core led to even bigger assemblies in form of $[Pd_{12}L_{24}]$, which could not be characterized via ESI-MS because of the instability under that conditions and could not be characterized via X-ray structure determination due to the very large voids with disordered anions and solvent molecules. Therefore, a combination of different and complimentary analytical techniques such as NMR, dynamic light scattering (DLS), transmission electron microscopy (TEM), electron energy loss spectroscopy (EELS) and CD was needed to prove the structure.

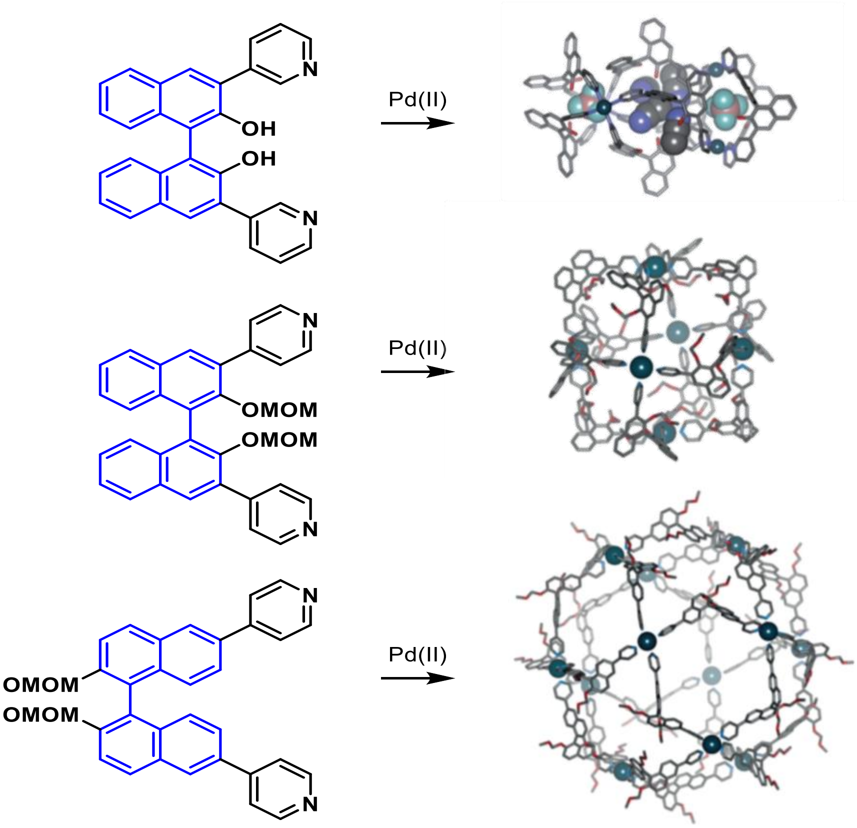

Figure 1.18 The chiral ligands and their resulting supramolecular structures $[2BF_4^-+4CH_3CN@Pd_4L_8]^{6+}$ (X-ray structure)[53], $[Pd_6L_{12}]^{12+}$(DFT-optimized structure) and $[Pd_{12}L_{24}]^{24+}$ (DFT-optimized structure) upon addition of Pd(II). Petrol: Pd, red: O, blue: N, gray C. © Wiley-VCH Verlag GmbH & Co[52,53]

Chiral tetragonal and hexagonal prisms have been reported by Stang *et al.* (**Figure 1.19**).[54] They used an approach with two different ligands and different binding sites. The enantiopure dicarboxylate BINOL based ligand led in combination with flat tetrapyridyl or hexapyridyl ligands and $[Pt(PEt_3)_2(OTf)_2]$ to the self-sorting supramolecular assemblies that have been characterized via $^{31}P\{^1H\}$ NMR, ESI-MS, CD, and optical rotation analyses. The self-assembly of simple chiral squares and chiral rhomboids was shown with the same approach.[54]

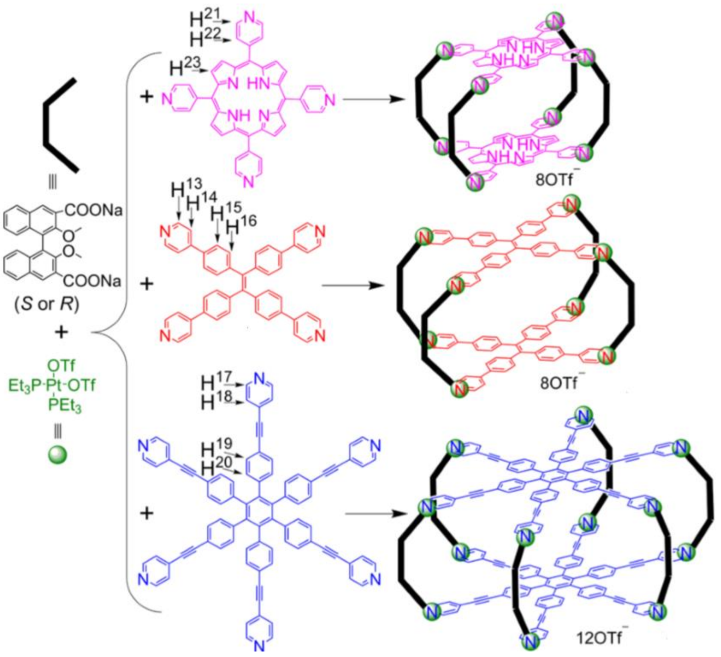

Figure 1.19 Chiral tetragonal and hexagonal prisms. © American Chemical Society[54]

A supramolecular assembly based on enantiopure helicene ligands has been reported by Autschbach, Crassous, Lescop and Réau *et al*..[55] A multitopic 2,6-bis(aza[6]helicenephosphole]-pyridine was synthesized as ligand with enantiopure helicenes, which were resolved by chiral HPLC. The coordination of two ligands with four Cu(I) metal cations could be shown and is depicted for the (*P*)-helicene based ligand (**Figure 1.20**).[55] The C$_2$ symmetric ligands with five binding sites (N,P,N,P,N) coordinate in an unsymmetrical fashion with three binding sites (N,µ-P,N) to one Cu(I)-dimer and with two binding sites to another Cu(I)-dimer. The photophysical properties were studied and showed very strong circular dichroism of up to −514 mol^{-1}cm^{-1} at 266 nm.

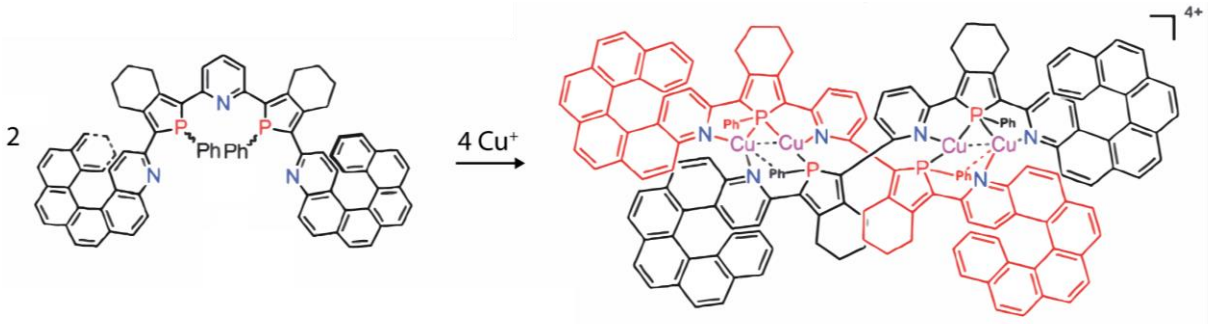

Figure 1.20 Two (*P*)-helicene-capped helicands closely assembled around four Cu(I) metal centers upon addition of the Cu$^+$ cations. ©The Royal Society of Chemistry[56]

2 CHIRAL-AT-METAL PHOSPHORESCENT SQUARE-PLANAR PT(II)-COMPLEXES FROM AN ACHIRAL ORGANOMETALLIC LIGAND

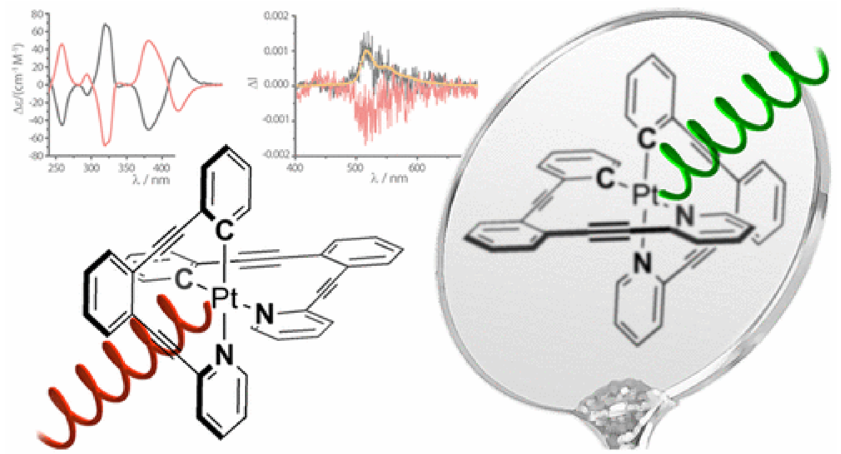
Δε/(cm⁻¹ M⁻¹)
80
60
40
20
0
-20
-40
-60
-80
250
300
350
400
λ / nm
ΔI
0.002
0.001
0.000
-0.001
-0.002
400
500
600
λ / nm
C
C
Pt
N
N
C
C
Pt
N
N

© American Chemical Society.

Results of this chapter are published in: "*Chiral-at-Metal Phosphorescent Square-Planar Pt(II)-Complexes from an Achiral Organometallic Ligand*", T. R. Schulte, J. J. Holstein, L. Krause, R. Michel, D. Stalke, E. Sakuda, K. Umakoshi, G. Longhi, S. Abbate, G. H. Clever, *J. Am. Chem. Soc*. **2017**, *139*, 6863.[57]

2.1 Introduction

2.1.1 CPL

Chiral luminescent compounds show circularly polarized luminescence (CPL), which is studied for a variety of applications like optical probes and sensors,[58] data storage[59] and (3D)-OLED devices[60]. The so called g value provides information about the degree of circularly polarization.[61] With I_L and I_R as the intensities of the circularly polarized emission, the dissymmetric factor g is defined as:

$$g = \frac{2 \times (I_L - I_R)}{(I_L + I_R)}$$

Equation 1 Definition of the dissymmetric factor g with I_L and I_R as the intensities of the circularly polarized emissions.

For completely left-handed emission g is 2, for unpolarized emission g is 0 and for completely right-handed emission g is −2 with values in between for partly circularly polarized light.[61]

Circularly polarized light emitting OLEDs have the potential to increase the efficiency of displays with anti-glare technique.[60,62] To reduce reflections of external light sources on displays, anti-glare filters are used. A often used kind of anti-glare filter makes use of circular polarizers which removes the reflections but leads to a loss of 50 % of the emitted light by the display.[60,62] To remove the reflections, the unpolarized light of the external light source passes the first linearly polarizer, where approximately 50 % of the light is absorbed (**Figure 2.1 a**). The linearly polarized light passes a quarter-wave plate where it is turned into circularly polarized light. The circularly polarized light is reflected and changes to the opposite sign, in this example from left to right circularly polarized light. The right polarized light passes the quarter-wave plate as before, but because of the opposite handedness the linear polarized light is orthogonal to the light passing the linear polarizer in the beginning and is absorbed by it.

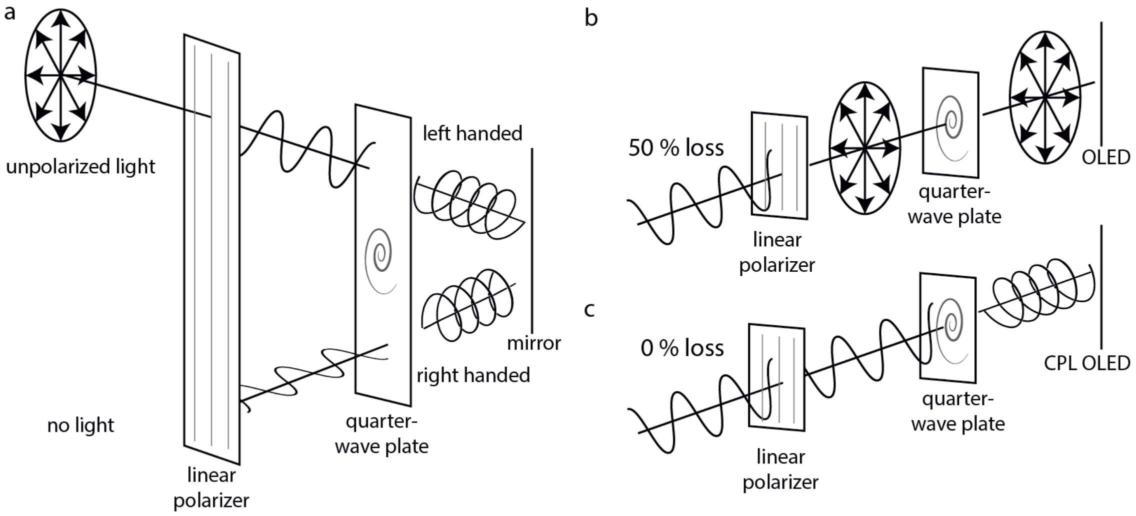

Figure 2.1 a: principle of anti-glare filtes, b: effect of anti-glare filter on "normal" OLED, c: effect of anti-glare filter on CPL OLED.[62]

This is a very efficient way to remove the reflections, but the linear polarizer filters also 50 % of the emitted light, if the light source emits unpolarized light (**Figure 2.1 b**). A circularly polarized light emitting OLED could emit light, that is not filtered out by the linear polarizer after the quarter-wave plate, because the orientation would fit exactly to the linear polarizer, and therefore overcome the 50 % loss and would therefore allow much more efficient non-reflective displays (**Figure 2.1 c**).

One example for the use of CPL as chiral probe has been reported in form of a dynamically racemic europium complex (**Figure 2.2**) with potential use in human serum monitoring.[63] The europium complex can undergo a change of the constitution induced by addition of the acute phase protein α_1-acid glycoprotein (AGP), which occurs during inflammation. The addition of the protein to the europium complex leads to a drastic change of the emission spectra (light blue/red line) and an induced CPL signal (orange line) which are explained with the protein binding to the metal complex under replacement of the coordinated water and one of the azaxanthone moieties showing the potential as chiral probe.

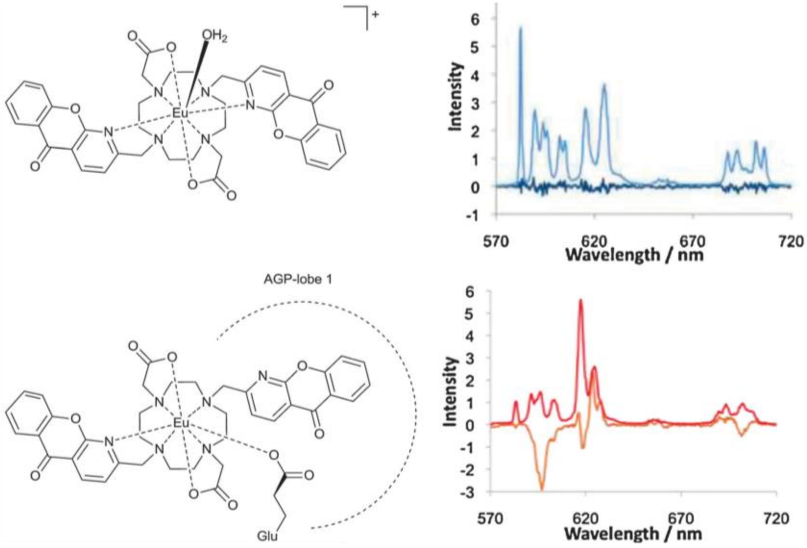

Figure 2.2 CPL used as a chiral probe. The coordination of the protein leads to an induced CPL (dark blue: no CPL before coordination; orange: CPL because of the coordinated protein). © The Royal Society of Chemistry [58]

Y. *Zhao et al.* reported the potential use of CPL as reversible optical storage.[59] The polymer contains an azo unit, that undergoes a *trans-cis* photoisomerization upon irradiation with a laser at 532 nm and a thermal *cis-trans* isomerization. The irradiation with a linear polarized laser causes a *trans-cis-trans* isomerization where the azo molecule is reoriented as long as its component of its electric dipole moment lies in the direction of the polarization of the light. The reorientation ends, when the azo molecules are perpendicular to the polarization of the laser, leading to a photoinduced birefringence of the polymer. In this manner information can be written into the polymer and can be read with a 633 nm laser as the probing light without changing the information. The signal intensity of the probing laser is measured with $I_\perp$ as the intensity of the transmitted light behind two crossed polarizers and with I_0 as the total transmitted laser intensity. The stored information can be erased by irradiation with circularly polarized light to randomize the orientation of the azobenzene groups and the polymer can be rewritten again.

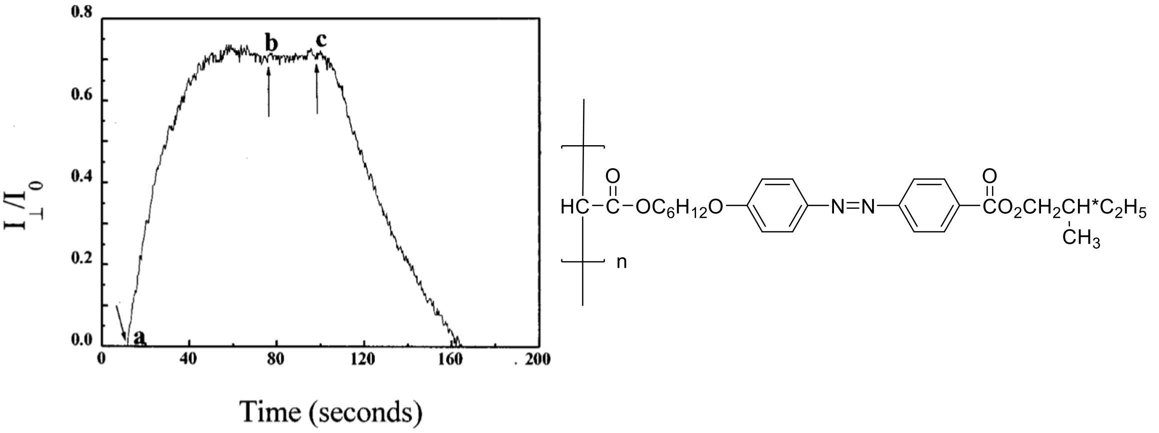

Figure 2.3 a: irradiation with polarized light with the writing laser, b: writing laser is turned off, c: irradiation with circularly polarized light to erase the information saved in the polymer.

2.1.2 OLEDs

Light emitting diodes (LEDs) showed a remarkable improvement in the quality of the color and efficiency over the last decades and mostly replaced all other kinds of light sources in most applications. In a lot of applications organic light emitting diodes (OLED) have the potential to replace LEDs. One advantage is, that white OLEDs (WOLED) have an increased power efficiency compared to other light sources (**Table 2.1**) which makes them interesting as light source for the future.[64] Even so the light efficiency is only about 10 % higher than for LEDs, the possibility to graft OLEDs on flexible materials is outstanding for this technique as the OLEDs can be used as pixels even on flexible displays.[64–66]

Type	η_p (lm / W)	Power consumption (W)	CCT (K)	CRI	Lifetime (h)
Incandescent	15	60	2,854	100	1,500
CFL	60	15	2,940	82	10,000
LED	90	8	3,000	80	60,000
WOLED	102	-	3,900	70	-

Table 2.1 Power efficiency η_p, power consumption at brightness of 800 lm, chromaticity coordinates CCT, color rendering index CRI and lifetime compared for light sources.

The increased efficiency of OLEDs compared to other light sources has the potential to be even bigger, when it comes to displays.[66–68] Displays with CFL or LED backlight use TFT panels with linear polarizers, which absorb around 50 % of the light emitted by the light source, even when a white screen is shown. OLED displays do not need a LCD TFT and the light does not have to pass a polarizer and therefore no emitted light is absorbed.[60,68]

Another example for the advantage of the OLED technology in displays is the individual addressability of the pixels. When a LCD TFT monitor with a CFL or LED backlight shows a black screen, the backlight is still turned on but only the light is absorbed by the orientation of the polarizers in the screen. In contrast OLED screens that shows a black screen, does not emit light at all leading to an increased contrast ratio and power efficiency.[68]

Phosphorescent organic light-emitting compounds for OLEDs are of special interest, because of their potentially higher efficiency compared to fluorescent OLEDs.[65] To understand the quantum physics behind the main photoprocesses of a molecule, the modified Jablonski diagram is discussed (**Figure 2.4**).[65] Starting from the ground S_0 state, excitation of the molecule by light absorption leads to one of the excited singlet S_n states. The thermal relaxation of higher singlet states to the lowest excited state S_1 is fast via non-radiative relaxation pathways and is called internal conversion (IC). Further non-radiative relaxation can be hindered through a large energy gap. Radiative relaxation from S_1 to S_0 leads to emission of a photon with the energy $h\nu_{fl}$. Intersystem crossing (ISC) from the S_1 to T_1 state is a “forbidden” spin transition and therefore rare for organic molecules, but can become high likely due to spin-orbit coupling (SOC) of heavy elements like Ir or Pt. The radiative relaxation from T_1 to S_0 under emission of a photon is called phosphorescence and is as well spin-forbidden, leading to characteristic higher lifetimes of the T_1 state compared to the S_1 state.

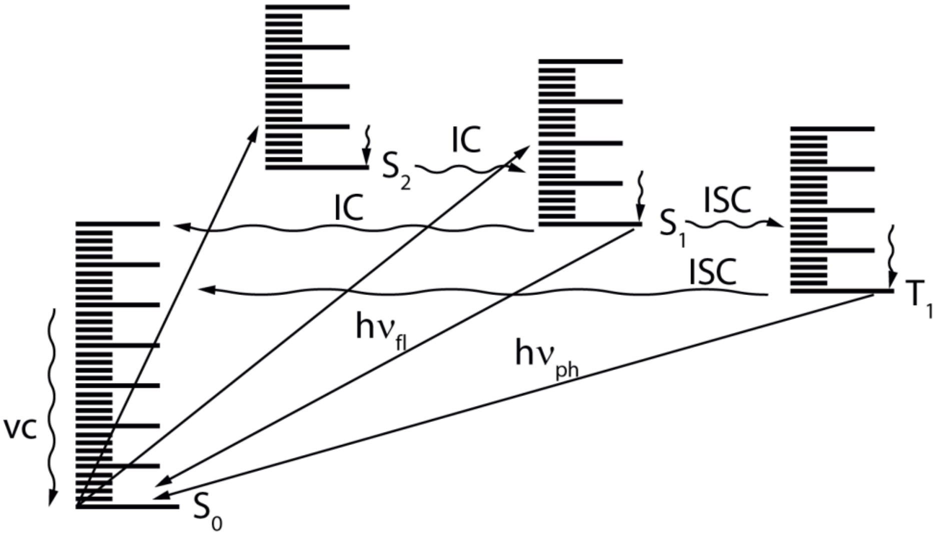

Figure 2.4 The modified Jabłoński diagram.

In an OLED device, bias is applied to inject electrons and holes, which migrate through the polymer.[65] Excitons are a bound state of an electron and a hole and they are formed upon close contact between each other. The spins of the electrons and holes are random on injection and independent from each other. As consequence upon recombination, for the T state three spin-sublevels exist where the S consists of one state. Due to the number of sublevels, the statistical chance is 25 % for a singlet state S and a 75 % for the triplet state T.[65,69] In case of an organic chromophore the emission from the T state has very low rates and cannot compete with non-radiative relaxation pathways end as consequence the efficiency is limited to the 25 % emission from the S state. Chromophores with a strong SOC can emit in high rates from the triplet state and therefore organometallic dyes with heavy metals like Ir or Pt are incorporated into OLED devices to harvest up to 100 % of the injected electrons and holes.[65]

2.1.3 Chiral Phosphorescent Platinum(II) complexes

For a long time the literature reported Pt(II) complexes suffered in the application for OLEDs under the fact that most of them were only emissive at low temperatures in rigid media.[70] Pt(II) complexes overcame this draw back and showed luminescence at room temperature in solution, especially complexes reported by Zelewsky *et al.* in the late 1980s (**Figure 2.5 a+b**).[70,71,72] Since then, the photoluminescence gained extensive attention, especially for their photoluminescent properties with emission from the triplet state.[70] Until today Pt(II) complexes with 2-phenylpyridine-type ligands are extensively studied.[73]

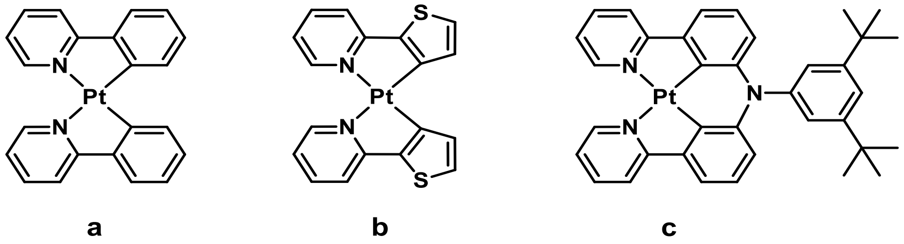

Figure 2.5 Structures of the first cyclometalated Pt(II) complexes reported by Zelewsky (a + b) and a recently further developed complex (c) with very high luminescence quantum efficiency.

From the enormous variety of structurally related compounds, Fukagawa *et al.* reported in 2012 an amine-bridged complex with outstanding high photoluminescence quantum yields Φ_{PL} of 58 % and an emission peak maximum at 621 nm.[74] Such a high Φ_{PL} value is very rare for Pt(II) complexes and can be explained with the rigid structure caused by the bridging amine (**Figure 2.5 c**), which suppresses the vibration and rotation around the metal center causing the effective phosphorescence from the metal-to-ligand charge-transfer (MLCT) state. This allowed the production of OLEDs with an external quantum efficiency η_{ext} of 20 %, 25.5 lm/W and long lifetimes of the device in the range of 10^4 h.

To predetermine the chirality of square-planar complexes Stoeckli-Evans *et al*. used sterically demanding derivatives of thienylpyridine ligands (**Figure 2.6**).[75–78]. The *cis*-arrangement is caused by the strong *trans*-influence of the C-donor and results in combination with the steric interactions in the stereoselective formation of the Δ configuration. The square planar coordination sphere is significantly distorted into a helical arrangement as quantified by the angles N1-Pt-C3′ = 79.0° and N21-Pt-C23’ = 78.9°.

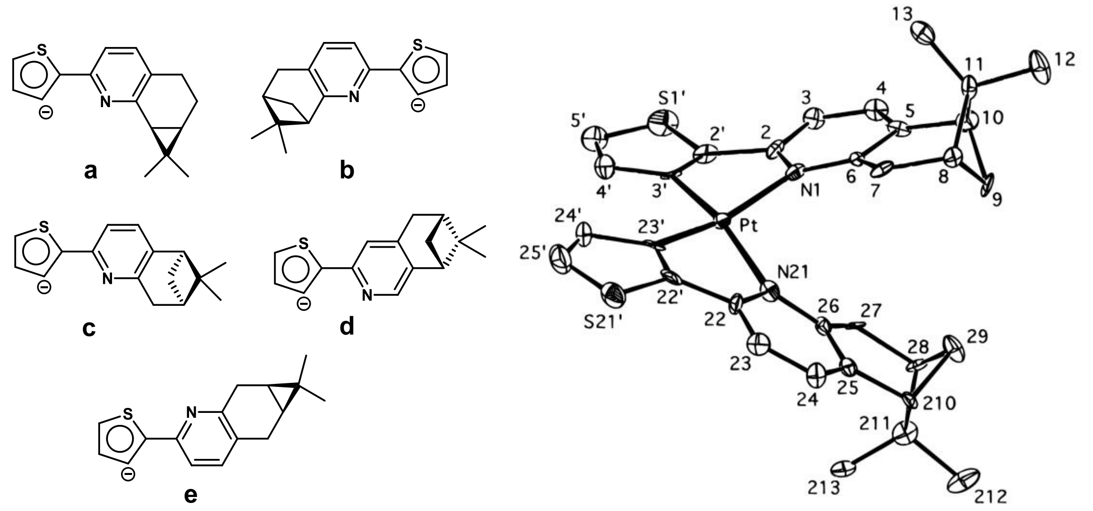

Figure 2.6 Structures of the chiral thienylpyridine based ligands for Pt(II) complexes and the ORTEP plot of the X-ray structure for the Pt(II) complex formed with c. © 1996 American Chemical Society

Chiral Pt(II) complexes have been reported based on achiral ligands by Zelewsky *et al.* (**Figure 2.7**).[76,78,79] The steric demanding ligands cause a distortion upon coordination to the metal leading to a helical chirality of the luminescent complexes. The racemic mixtures were not separated but the enantiomers could be proven to be stable towards racemization on the NMR timescale using Pirkle's reagent. The X-ray structure determination of *cis*-bis(2,6-diphenylpyridinato-N,$C^{2'}$)platinum(II) shows the helical distortion of the ligands upon coordination (**Figure 2.7**).[79,80]

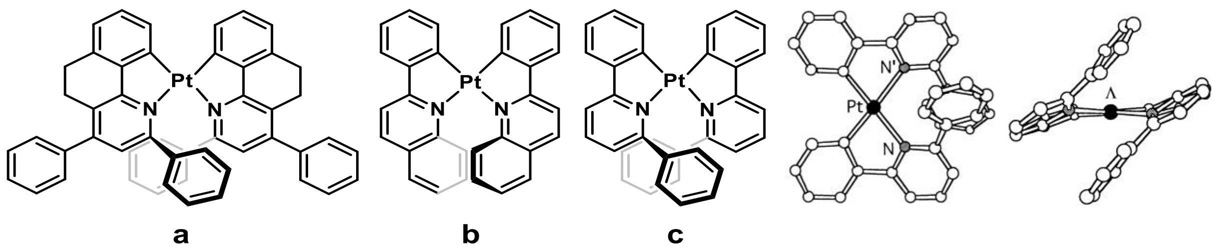

Figure 2.7 Structures of chiral Pt(II)complexes synthesized with achiral ligands and the X-ray structure showing the helical chirality of one formed complex. © 1997 American Chemical Society[76,78,79]

For their very interesting photophysical properties helicenes are studied broadly and are discussed in detail in chapter 3.1 (page 43). Many examples of helicene-based transition metal complexes have been reported in form of helicenic metallocenes, organometallic alkynyl- and vinyl-helicenes and cyclometalated helicenes.[56] A variety of cyclometalated structures has been reported by Autschbach, Crassous, Lescop, Réau *et al*. (**Figure 2.8**),[81–83] which are structurally related to the first complexes synthesized by Zelewesky *et al*. The complexes are chiral due to the inherent chirality of the helicene backbone and show a very strong circular dichroism known for helicenes.

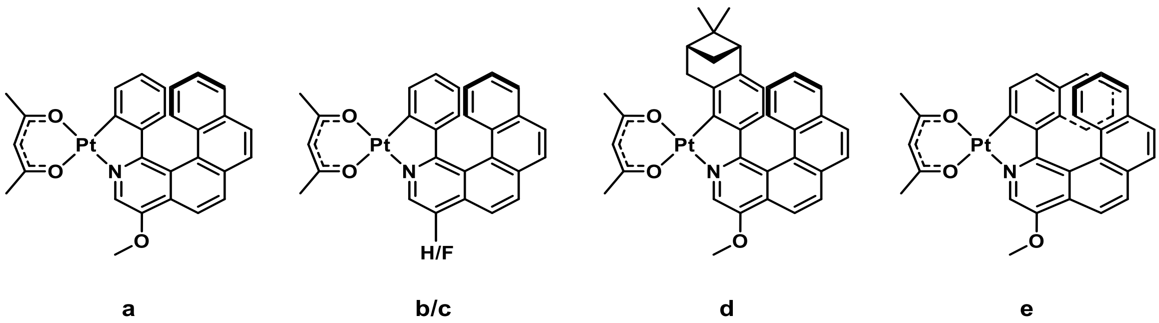

Figure 2.8 Structures of cyclometalated helicene based Pt(II) complexes.

A CPL emitting OLED has been reported by Fuchter *et al*. based on the reported Pt(II) complex containing a cyclometalated heterohelicene (**Figure 2.8 a**) and its properties are compared with other recent approaches (**Table 2.2**).[60] The reported OLED by Fuchter *et al.* shows a great potential, as the luminescence contains the phosphorescent pathway, which allows higher efficiencies in theory. A drawback of chiral polymers, oligomers and helicene dopants is the luminescence limited to fluorescence, even so these approaches allow high g values. The Iridium based complexes have opposite dis-/advantages, they show phosphorescence but the g values are low.[60] Europium complex dopants show a high g value and phosphorescence but their maximal luminescence is very low, a problem that the cyclometalated heterohelicene Pt(II) complex does not have.

Table 2.2 Overview over different approaches for CPL emitting OLEDs.[60]

Material		***Phosphorescence***	***g***	***Luminous Efficacy (lm/w)***
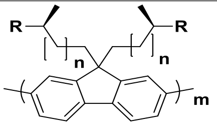	PFO with chiral sidechain	No	0.35	n/a
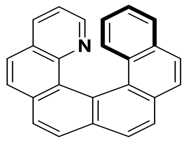	PFO copolymer with 7% helicene	No	0.2	3.67
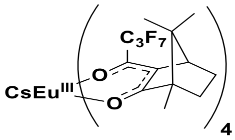	PVK/OXD-7	Yes	0.79	0.0067
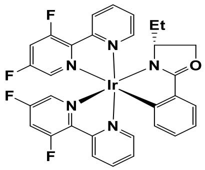	mCP	Yes	0.0026	n/a
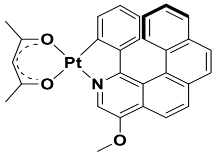	PVK/OXD-7	Yes	0.38	0.25

2.2 Project target

The idea was to create a new binding motif, that has not been reported before for luminescent Pt(II) complexes. The project combines the cyclometalated complexes reported in the chapter before with a *trans* chelating bis(pyridine) ligand, that has been reported by Bosch *et al.* to coordinate a variety of metal ions, leading to achiral complexes.[84] The coordination of the *trans* chelating ligand **L^{NN}** with two different Pd(II) salts and the X-ray structure are shown in **Figure 2.9**.

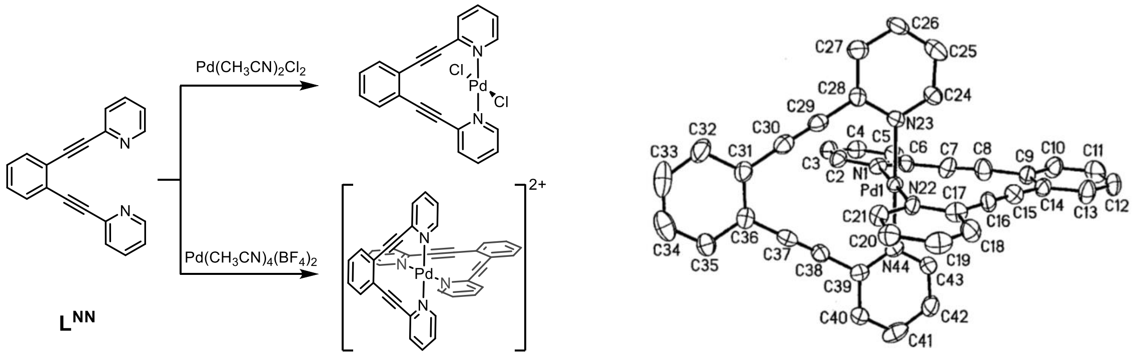

Figure 2.9 left: Structure of the Ligand L^{NN} right: ORTEP drawing of the cation [PdL$^{NN}{}_2$]$^{2+}$. © 2002 American Chemical Society[85]

The first report of a chiral bis(pyridine)ligand *trans* coordinating to a square planar metal center has been published by Lützen *et al*. in 2014 (**Figure 2.10**).[86] Both ligand enantiomers were synthesized with enantiopure starting materials in a Sonogashira cross coupling reaction and ^{1}H NMR spectra showed, that the enantiopure complex was formed with the use of a racemic ligand mixture, showing a chiral-selfsorting with narcissistic self-recognition upon coordination to the metal center.

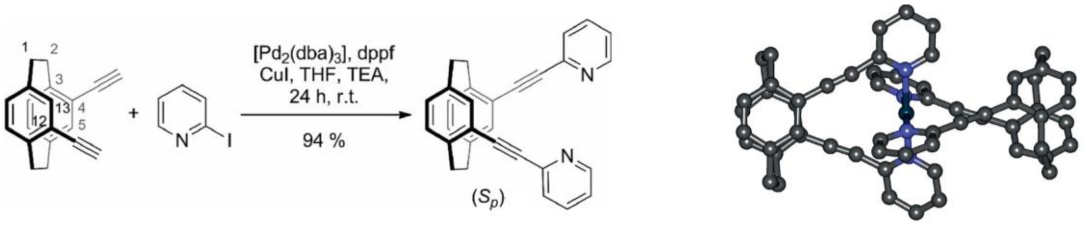

Figure 2.10 Synthesis of the trans chelating ligand enantiomer (*S*) and the X-ray structure of (*R*) enantiomers coordinated to Pd(II). © Wiley-VCH Verlag GmbH & Co[86]

The target of this project was the synthesis and characterization of a chiral square planar metal complex with an achiral ligand to form both enantiomers ***trans*-2(*R*$_a$)** and ***trans*-2(*S*$_a$)** (**Figure 2.11)**. This structure motif was never reported before and would probably own the interesting photophysical properties of the structural related cyclometalated Pt(II) complexes.

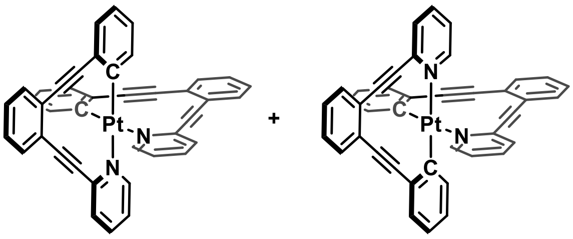

***trans*-2(*R*$_a$)** ***trans*-2(*S*$_a$)**

Figure 2.11 The target structure: the trans cyclometalated Pt(II) complex.

2.3 Ligand Synthesis

Due to the asymmetric nature of the ligand, the synthetic effort is increased, compared to the symmetric ligand (**Figure 2.9**). In the retrosynthetic analysis of the ligand $\mathbf{L}^{\mathbf{CN}}$-Br only one path leads to a synthetic approach, where all synthesis steps are selective using commercially available starting materials (**Figure 2.12**). Sonogashira cross coupling reactions are used for the C-C bond formation of arylhalogenides with alkynes. The reaction rate of aryl halogenides differs strongly in the order Cl << Br < I, and therefore a C-C bond can be formed selectively at the Ar-I position.[87] In the first step of the retrosynthetic approach, four paths are possible. Pathway 1), 2) and 3) contain sooner or later starting materials, that would not allow a selective bond formation or the formed reaction product during a Sonogashira reaction could react with itself leading to unwanted side products. Pathway 4) allows a selective synthesis in all steps and was therefore chosen for the synthesis of the ligand $\mathbf{L}^{\mathbf{CN}}$-Br. The first step (**Figure 2.12 a**) yielded the [(2-bromophenyl)ethynyl]trimethylsilane in 96 % yield and the product was formed selectively at 23 °C. For the formation of 2-((2-((trimethylsilyl)ethynyl)phenyl)ethynyl)pyridine, the more reactive catalytic system[88,89] $Pd(CH_3CN)_2Cl_2$ with [*t-Bu*)]$_3$PH]BF$_4$ had to be used, because of a competing Glaser-coupling reaction of the 2-ethynylpyridine (**Figure 2.12 b**).[90] Deprotection of the alkyne yielded the 2-((2-Ethynylphenyl)ethynyl)pyridine (**Figure 2.12 c**) in 84 % yield, which could be transformed into the target structure with another Sonogashira cross coupling reaction to the 2-((2-((2-Bromophenyl)ethynyl)phenyl)ethynyl)pyridine $\mathbf{L}^{\mathbf{CN}}$-Br in 49 % yield (**Figure 2.12 d**).

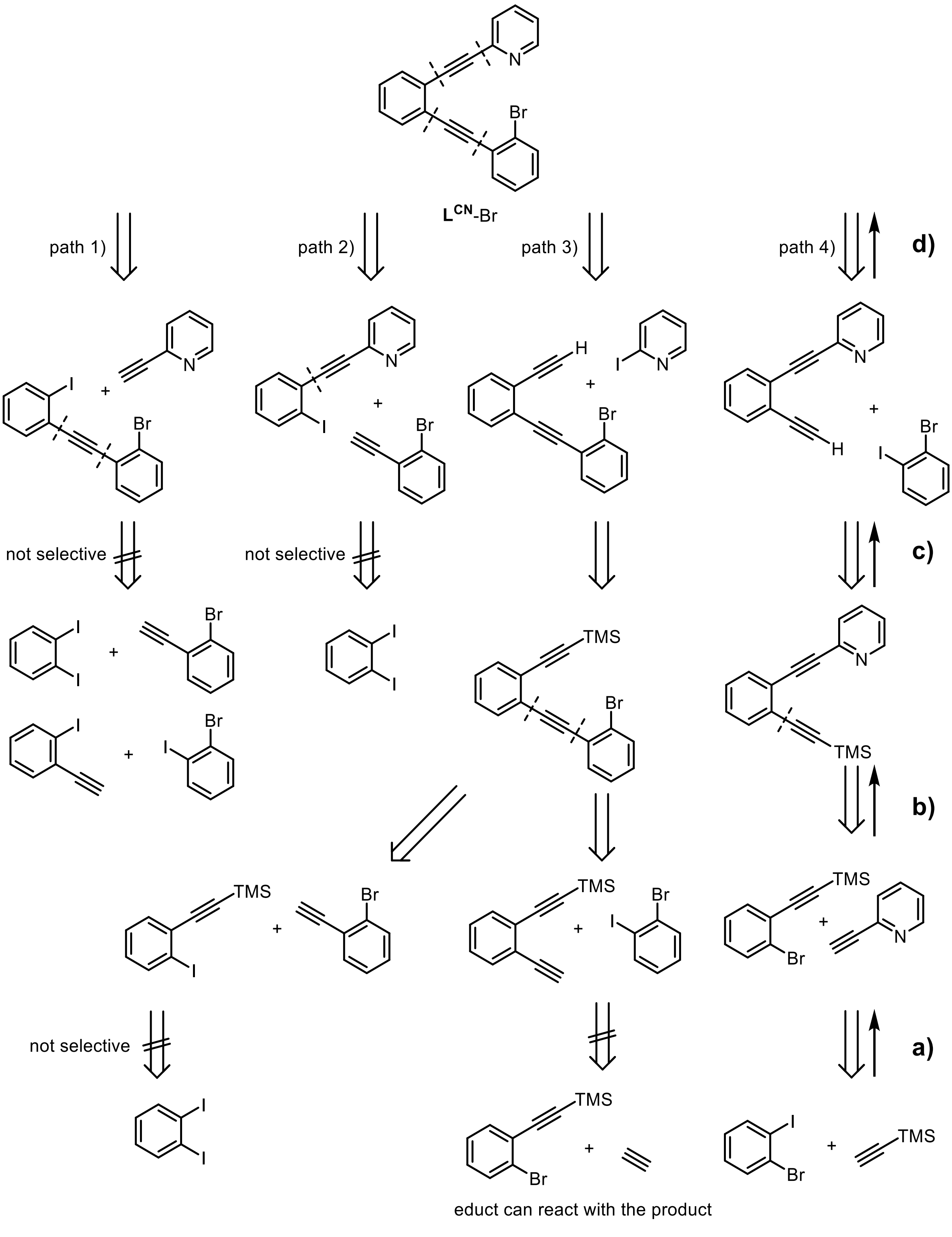
L^{CN}-Br
path 1)
path 2)
path 3)
path 4)
d)
c)
b)
a)
not selective
not selective
not selective
Br
I
N
H
TMS
educt can react with the product

Figure 2.12 Retrosynthetic analysis for ligand L^{CN}-Br.

2.4 Complex Synthesis

2.4.1 PtL^{CN}(SEt$_2$)Cl

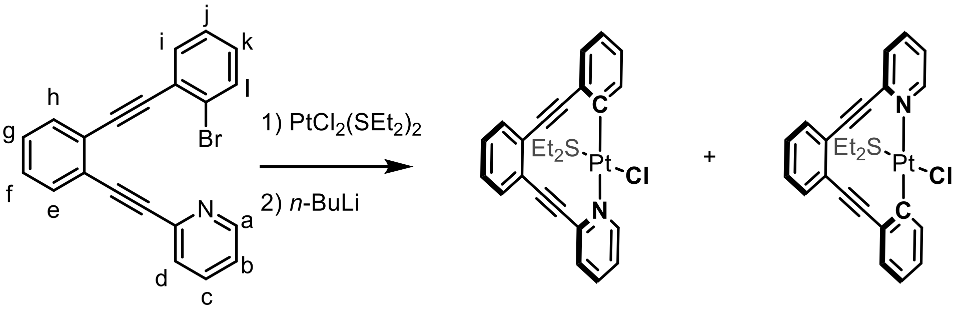

L^{CN}-Br **1**(*R*$_a$) **1**(*S*$_a$)

Figure 2.13 synthesis of 1.

The synthesis of the complex followed the procedures reported for the structural related *cis*-chelating phenylpyridine complexes.[75,78,91] The ligand **L^{CN}**-Br was lithiated at – 78 °C in THF and PtCl$_2$(SEt$_2$)$_2$ was added to the reaction mixture, which then warmed up to room temperature overnight. THF was chosen due to the low solubility of the ligand **L^{CN}**-Br in diethyl ether. The first attempts led only to the formation of product **1**, which could be characterized in the master thesis. In complex **1** only one ligand is attached to the Pt metal center and **1** could be characterized by ^{1}H NMR spectroscopy, mass spectrometry and X-ray diffraction. In the ^{1}H NMR, the signal assigned to the proton H$_a$ next to the nitrogen shows a strong downfield shift compared to the ligand upon coordination to the platinum (**Figure 2.14**). Interestingly, the formation of a complex with only one attached ligand could not be shown for the *cis*-chelated ligands following a similar procedure.[91] Product **1** is chiral and the separated enantiomers can racemize in solution.

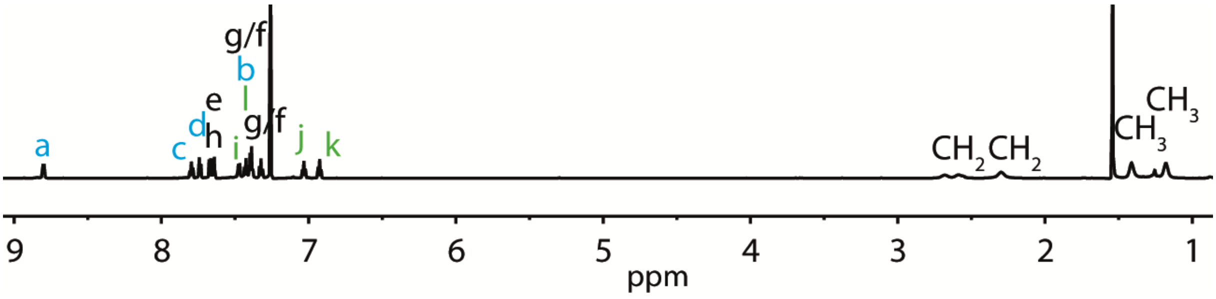

Figure 2.14 ^{1}H NMR of 1 (600 MHz, CDCl$_3$).

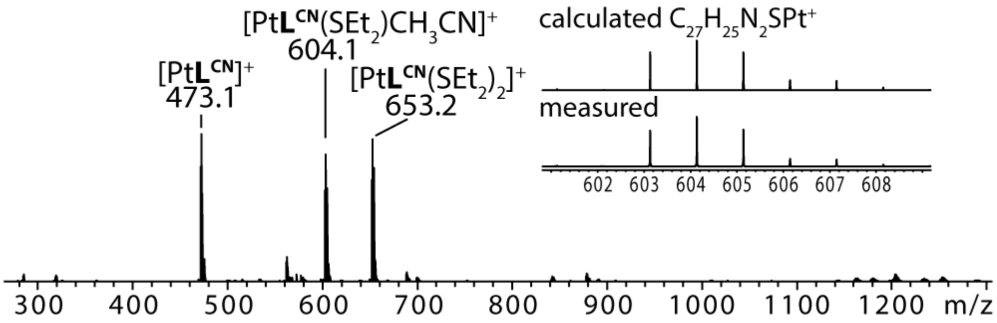

Figure 2.15 ESI-MS of 1.

Signals for the mono-cationic fragments $[\mathrm{Pt}\mathbf{L}^{\mathrm{CN}}]^+$, $[\mathrm{Pt}\mathbf{L}^{\mathrm{CN}}(\mathrm{SEt_2})\mathrm{CH_3CN}]^+$ and $[\mathrm{Pt}\mathbf{L}^{\mathrm{CN}}(\mathrm{SEt_2})_2]^+$ were identified in the ESI mass spectrum. Acetonitrile, as used for the measurement of the spectra, was found to coordinate to the complex after the cleavage of the chloride ion. The found species $[\mathrm{Pt}\mathbf{L}^{\mathrm{CN}}(\mathrm{SEt_2})_2]^+$ is explained with the cleavage of one coordinating chloride anion and in situ reaction with a further molecule of **1**, as otherwise a different integral ratio in the ^{1}H NMR would be expected compared to **1** for the CH_2 and CH_3 groups.

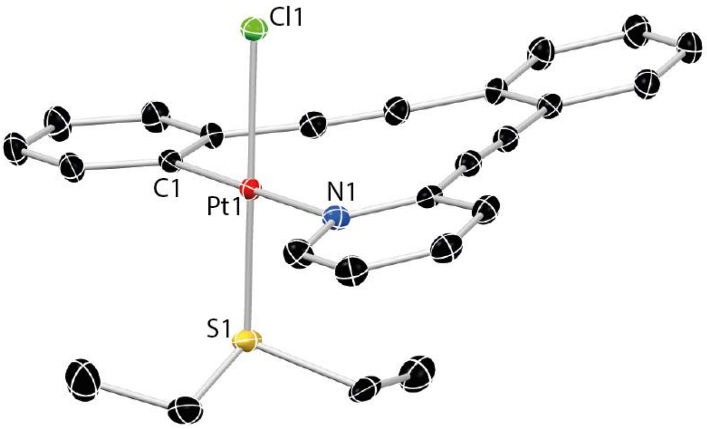

Figure 2.16: X-Ray structure of compound 1, solvent omitted for clarity.

Suitable crystals for X-ray structure determination were obtained of compound **1** under slow evaporation of the solvent in a mixture of hexane and chloroform. $[\mathrm{Pt}\mathbf{L}^{\mathrm{CN}}\mathrm{Cl}(\mathrm{SEt_2})]$ **1** crystallized in the monoclinic space group $P2_1/n$. Compound **1** is chiral and both enantiomers are present in the crystal structure, but only one enantiomer is present in the asymmetric unit, containing one chloroform molecule (**Figure 2.16**). A slight disorder (5 %) of the Pt atom in the equilibrium position between the C and N donor atom and a disorder of the thioether could be found.

The Pt1−N1 (2.1392(15) Å) distance is slightly larger than the Pt1−C1 (1.9909(17) Å) bond, which is reported for literature known phenylpyridine complexes.[92] The C1−Pt1−N1 angle of 179.65(6)° is close to the ideal 180° angle for square planar geometry. A slight distortion from the ideal 90° angle was observed for Cl1−Pt1−N1 (88.19(4)°) and Cl1−Pt1−C1 (91.46(5)°). A bigger distortion, because of the bent away diethyl sulfide ligand; could be observed for S1−Pt1−Cl1 = 85.77(5)° and S1−Pt1−N = 94.58(4)°.

2.4.1.1 Separation of the enantiomers of 1

To separate the enantiomers, chiral high performance liquid chromatography was performed on an Agilent Technologies 1260 infinity HPLC system equipped with Daicel CHIRALPAK IC columns (analytic = 250 x 4.6 mm, 1 mL/min, r.t.) (semiprep = 250 x 10 mm, 5 mL/min, r.t.) with a dichloromethane/methanol (99.5% / 0.5%) mixture as eluent. The chromatograms on the semipreparative column before and on the analytic column after the separation are shown in **Figure 2.17** and show the perfect separation of the enantiomers. The separation of the enantiomers is remarkable, as the enantiomers differ only at the binding positions of nitrogen and carbon at the metal center, where the outer sphere is the same for both enantiomers.

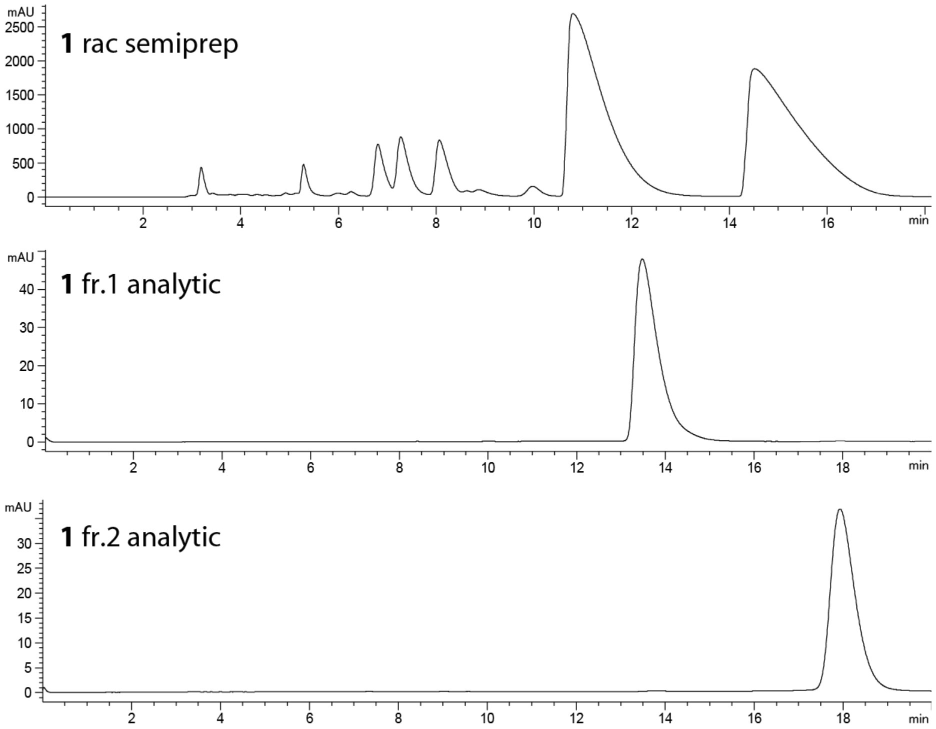

Figure 2.17 Chromatograms of 1 (dichloromethane/methanol (99.5%/0.5%) mixture as eluent, Abs. 300 nm). Both enantiomers could be isolated as base-line separated peaks (c = 5 mg/mL, inject. V = 400µL). They are named "fraction 1" (eluted first) and "fraction 2" (eluted second).

The circular dichroism (CD) spectra were recorded for both enantiomers of **1** (**Figure 2.18 a**). The first fraction shows a strong positive cotton effect with a broad band from 393 to 367 nm and further strong bands at 338, 329, 312, 273, 250 nm. The second fraction of **1** shows the opposite bands, as expected for enantiomers. These results confirm the separation of the enantiomers.

The configurational stability of **1** has been studied toward racemization. Complex **1** could be racemized in acetonitrile at various temperatures. Time resolved CD spectra were recorded at different temperatures (**Figure 2.18 b**). The time resolved CD spectra showed at 40 °C a significant racemization after 60 min. After 60 min at 60 °C the CD band is reduced to one third of the original intensity, indicating that one third of complex **1** racemized resulting in a solution with two third of fraction one and one third of fraction two. After 60 min at 70 °C the CD bands are close to the baseline and complex **1** is nearly completely racemized.

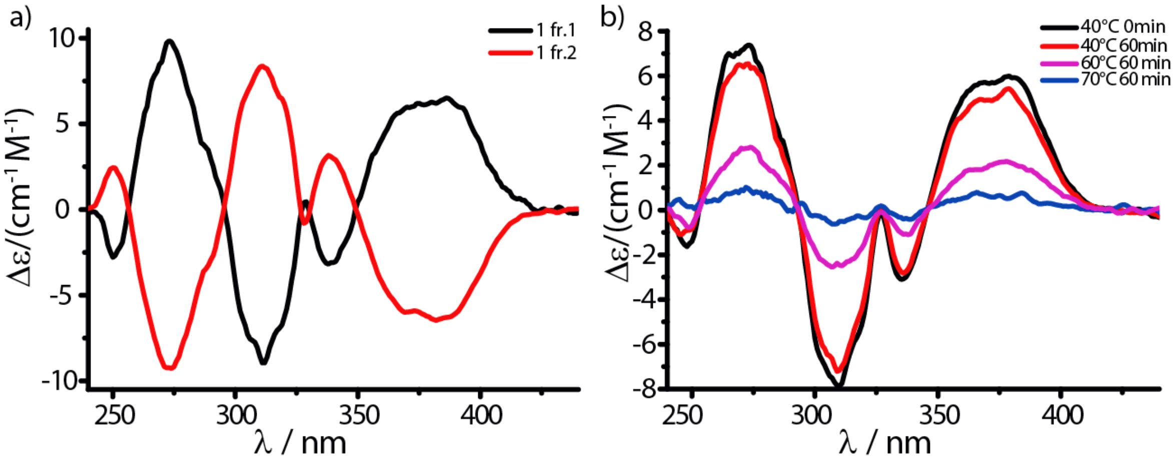

Figure 2.18 a) CD spectra of 1 fraction 1 and 1 fraction 2 in dichloromethane; b) CD spectra after 60 min heating at 40, 60 and 70 °C that show the racemization of 1 fraction 1 in acetonitrile.

For a better understanding of the racemization mechanism, solutions of enantiopure **1** (HPLC fraction 1) in acetonitrile have been heated at 60 °C for different time periods, cooled to 0 °C and as fast as possible injected at 20 °C into the chiral HPLC system (**Figure 2.19**). Based on the CD results, the racemization at r.t. is neglectable for the time period of one injection, which takes about 20 min. The integrals of the peaks allowed the exact determination of the enantiomer ratio and therefore the determination of the enantiomeric excess (ee). The natural logarithm of the ee versus the time was plotted (**Figure 2.19**) and the linear slope indicates a first order kinetic mechanism.[93]

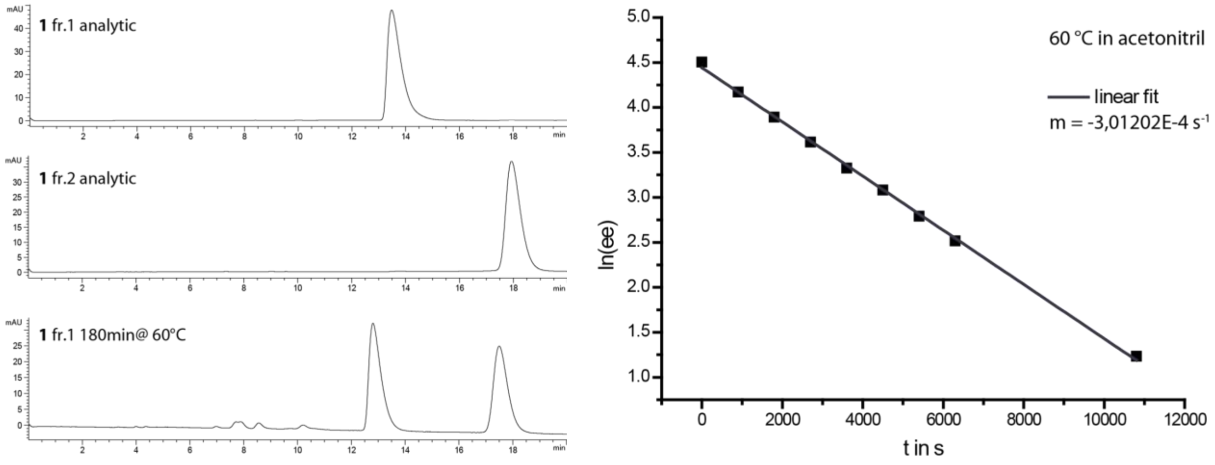

Figure 2.19 Chromatograms of enantiopure 1 (dichloromethane/methanol (99.5%/0.5%) (Abs. 300 nm) and after racemization for 2 h at 60 °C and the linear plot of ln(ee) for a series of injections vs time period at 60 °C indicating the first order kinetics.

2.4.2 Synthesis of *trans* PtL^{CN}_2

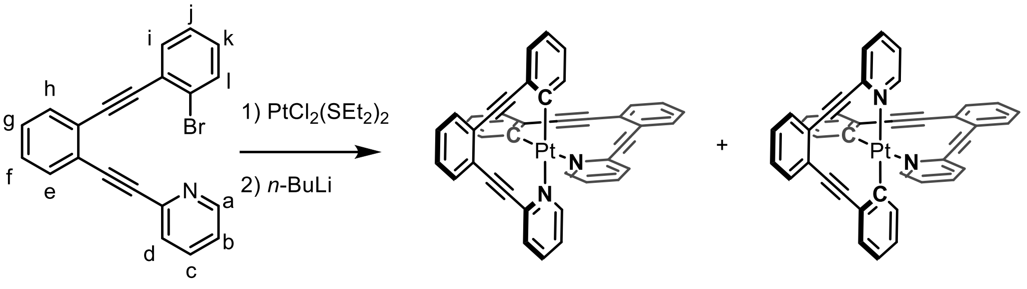

L^{CN}-Br

***trans*-2**(R_a)

***trans*-2**(S_a)

Figure 2.20 Reaction scheme with the two formed stereoisomers of *trans*-2.

The desired complex with two trans chelating ligands was obtained after modification of the reaction conditions. An increase in the yield of product **1** was obtained, by addition of the $PtCl_2(SEt_2)_2$ before the lithiation of the ligand. With the change to this approach, the target structure ***trans*-2** could be isolated in low yields of around 1 % either by column chromatography or by washing of the crude reaction mixture with a small amount of chloroform. The change from THF as the only solvent used for the lithiation to a THF/Et_2O (1/4) mixture increased the yield to 16 %, furthermore the formation of a new side product was observed. The complex ***trans*-2** could be fully characterized via ^1H NMR spectroscopy, mass spectrometry and X-ray diffraction. Compared to the ligand **L^{CN}**-Br and the complex **1**, complex ***trans*-2** shows a stronger downfield shift of the signal assigned to the proton next to the nitrogen H_a, which is very characteristic for the complex formation and allows the identification of **2** in an ^1H NMR measurement of a crude reaction mixture (**Figure 2.21**). The signals assigned to the protons H_k and H_j, show a strong upfield shift upon coordination.

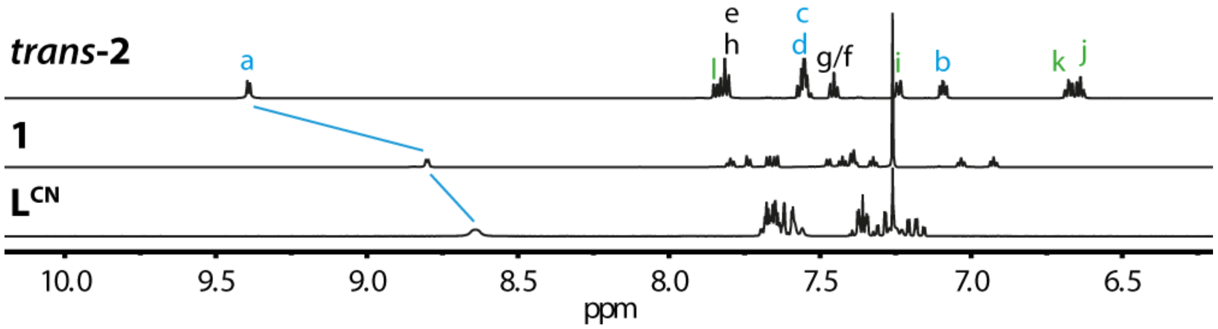

Figure 2.21 ^1H NMR of *trans*-2, 1 and the ligand before the lithiation L^{CN}.

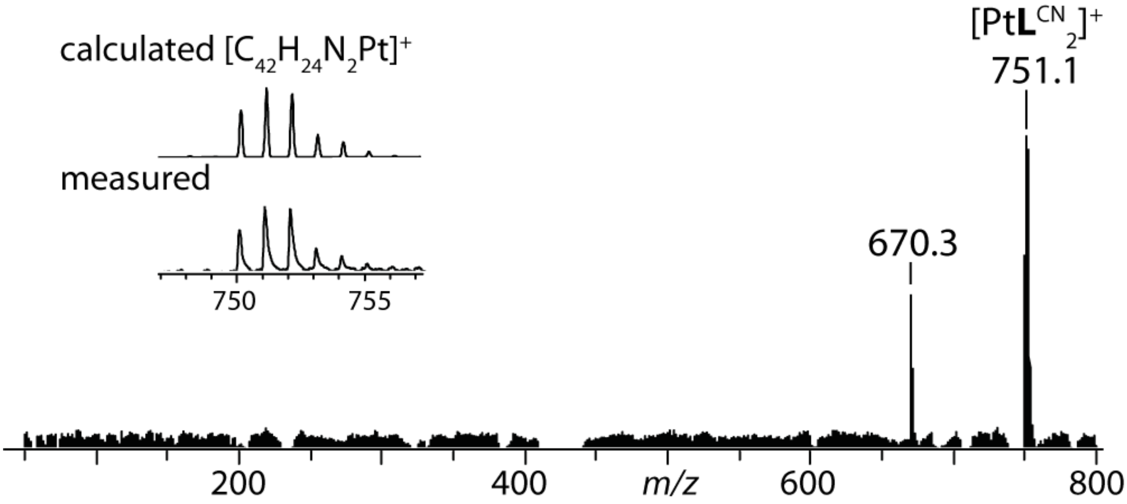

Figure 2.22 FD(+) MS of *trans*-2.

To avoid fragmentation a field desorption (FD) mass spectrum was measured and allowed the detection of the one-electron-oxidized monocationic species $[Pt\mathbf{L}^{CN}{}_2]^+$ (**Figure 2.22**). The simulation of the isotopic pattern is in perfect agreement with the measured spectra confirming the coordination of both ligands to the metal.

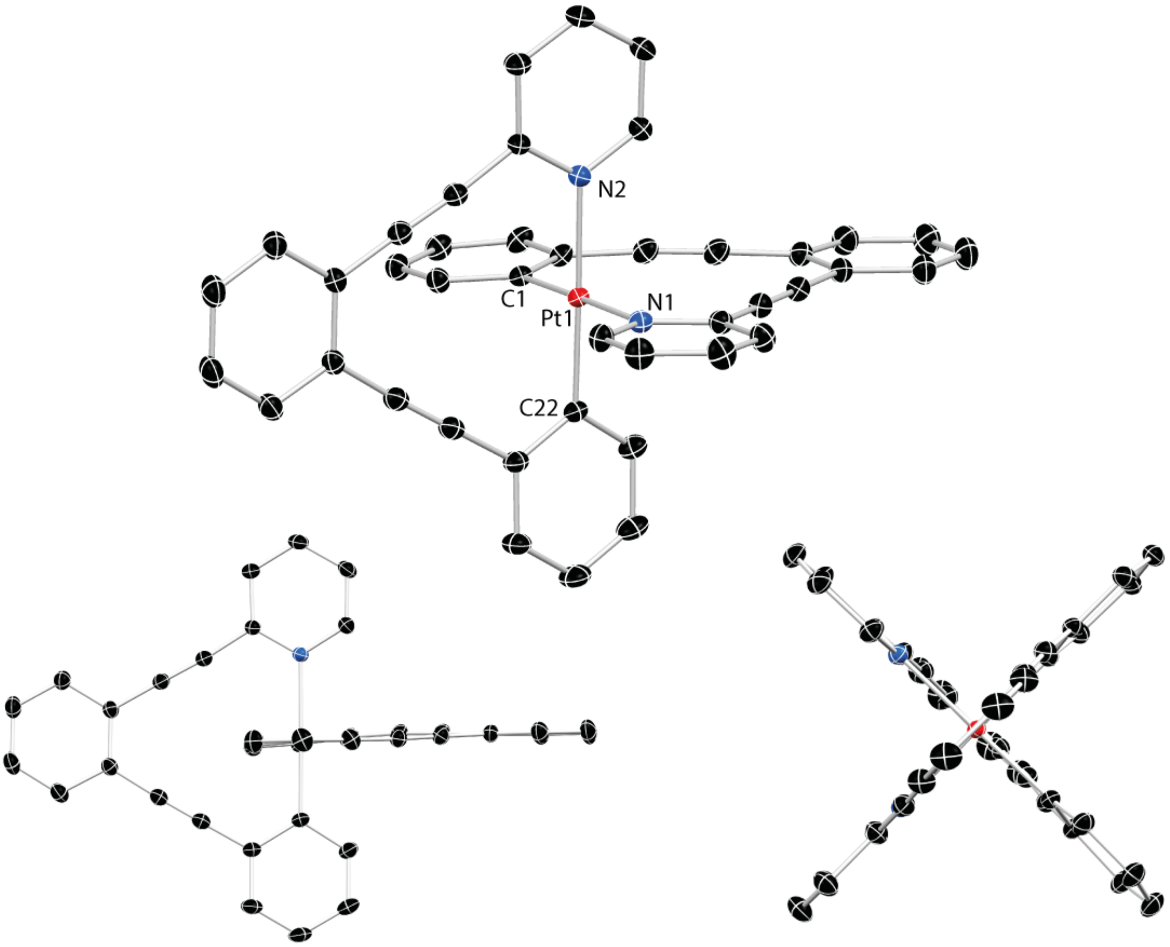

Figure 2.23 ORTEP drawings (50 % probability) of *trans*-2. C black; N blue; Pt red, H omitted for clarity.

To confirm the proposed structure, crystals suitable for X-ray structure determination of a racemic mixture of ***trans*-2** were grown by slow evaporation of a solution of ***trans*-2** in dichloromethane (**Figure 2.23**). ***Trans*-2** crystallized in the monoclinic $P2_1/c$ space group with both enantiomers in ascending order, but with only one enantiomer present in the asymmetric unit. No solvent molecule is present in the structure. The Pt1−N (2.1075(11)−2.1095(11) Å) and Pt1−C (1.9900(13)−1.9895(12) Å) bonds are of similar lengths compared to **1**. The angles N1−Pt1−C1 (178.92(4)°) and C22−Pt1−N2 (179.09(5)°) are close to the ideal square-planar coordination geometry and show the perfect fit of the Pt(II) cation inside the chelating ligand environment. The intermolecular distance for the closest Pt−Pt contact is 8.998(2) Å, much longer than for many other reported solid state structures of related square-planar systems due to the steric hindrance of the ligands that surround the Pt(II) center in ***trans*-2**.[94] Therefore, close metal−metal interactions are not possible for this system, which would require much smaller distances between the Pt centers.[95]

2.4.2.1 Separation of the enantiomers

The separation of the enantiomers of ***trans*-2** was crucial for the project, as only isolated enantiomers of ***trans*-2** could be capable of circularly polarized luminescence. Even so both enantiomers of ***trans*-2** differ only in the inside environment of the molecule, the separation of the enantiomers could be performed successfully (**Figure 2.24**).

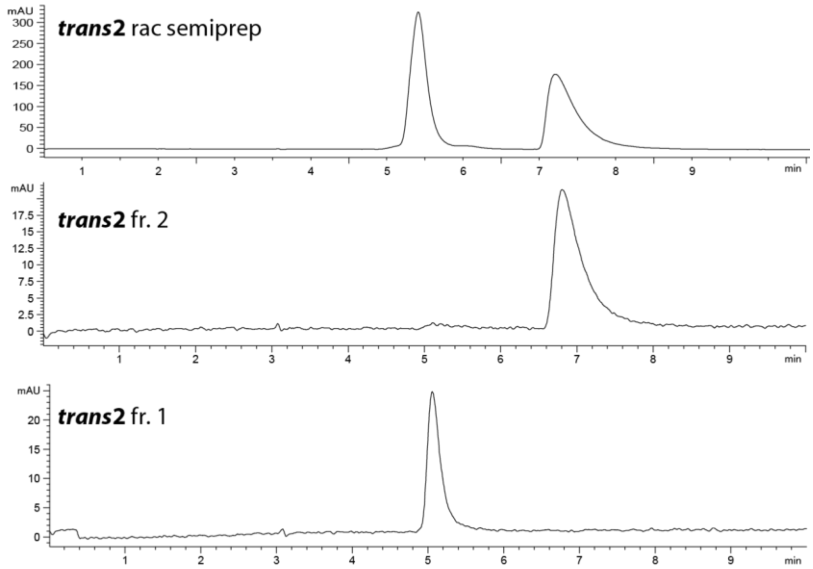

Figure 2.24 Chromatograms of *trans*-2 (Abs. 300 nm, flow rate 5 mL/min); dichloromethane/hexane/propan-2-ol(40.0%/59.5%/0.5%) mixture as eluent for the separation of *trans*-2. Both enantiomers were solved in DCM and could be isolated as base-line separated peaks (c = 1 mg/mL, inject. V = 90µL). They are named "fraction 1" (eluted first) and "fraction 2" (eluted second) in the discussion of the CD and CPL data and the absolute configuration.

To determine the absolute configuration of the chiral compound ***trans*-2(*S*$_a$)**, crystals of the first fraction from the HPLC separation, suitable for X-ray structure determination were grown by slow evaporation of a dichloromethane solution. ***Trans*-2** crystalized in the space group $P2_1$, with only one enantiomer present in the X-ray structure (**Figure 2.25**). Even with the small electronic difference, as the enantiomers differ only in the exchange of one carbon atom with one nitrogen atom, the absolute structure of the first fraction of the HPLC could be determined as the S_a enantiomer. The enantiomer distinguishing parameters have been calculated with the methods of Flack [x = 0.164(8)], Hooft [y = 0.138(7)] and Parsons [z = 0.166(8)].[96–98]

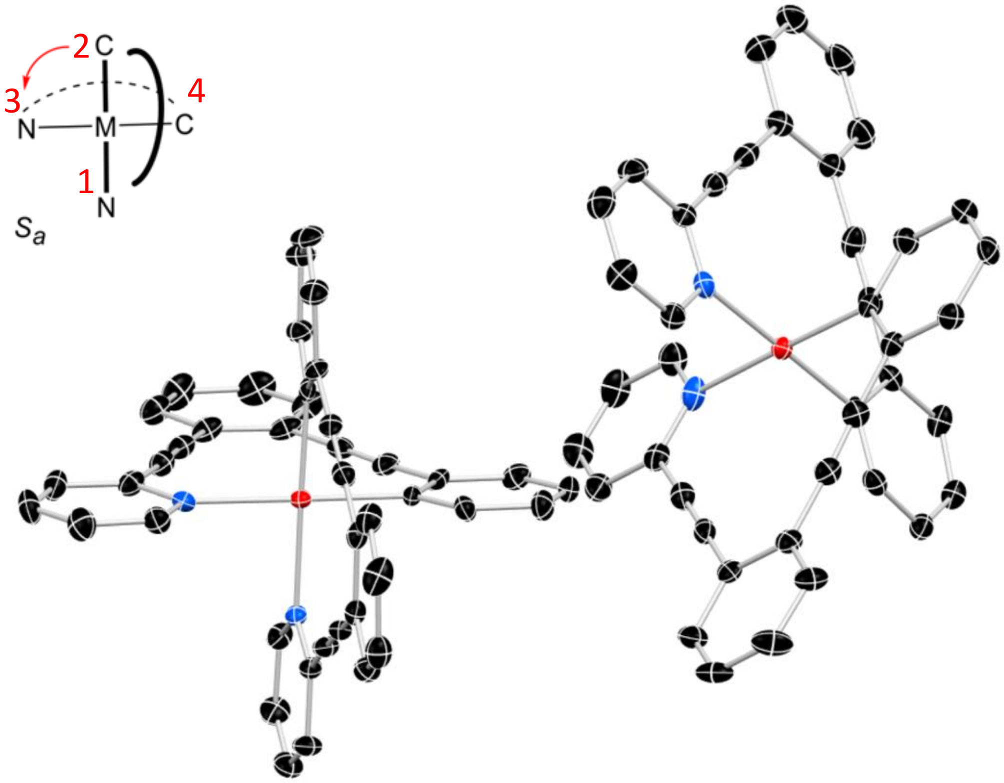

Figure 2.25 left: assignment of the axial chirality; right: ORTEP drawing of the asymmetric unit with two molecules of *trans*-2(S_a); C: black, N: blue; Pt: red; H: grey.

2.4.3 Yield Optimization

To increase the yield of ***trans*-2**, the reaction conditions were varied and crude NMR measurements were performed to monitor the formation of ***trans*-2**. Due to the low solubility of ***trans*-2** and side products, the integral ratios in the ^{1}H NMR of the crude reaction mixture do not represent the yields of the complex formation, but allow the conclusion, if the desired complex ***trans*-2** was formed or not. The variations contain exchange of *n*-BuLi by *t*-BuLi, the use of different solvents and solvent mixtures, time variations, change in the order of the addition and different temperatures for the quenching of the reaction. To verify, that the lithiation of the ligand is not the problem, *t*-BuLi was used for the lithiation instead of *n*-BuLi, as *t*-BuLi is a stronger lithiation reagent. Previous attempts showed a high variety of yields and formed products under the same reaction conditions, all reaction have been carried out several times for a representative result. The ^{1}H NMR spectra of two representative reactions with *t*-BuLi are shown in **Figure 2.26**. With THF as solvent and a lithiation at –78 °C, the use of *t*-BuLi lead to the formation of **1**, but no significant amount of ***trans*-2** was formed. Therefore, the use of *t*-BuLi was not further investigated.

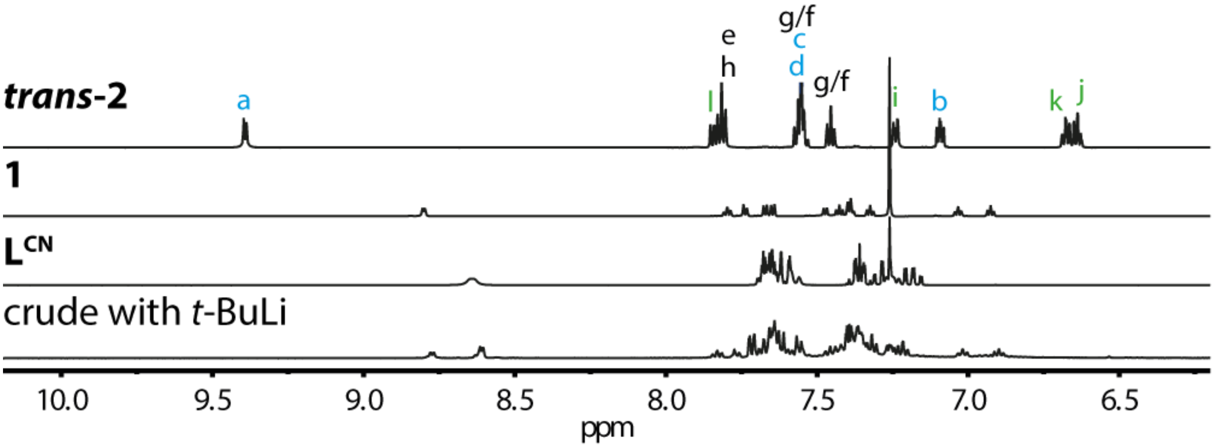

Figure 2.26 ^{1}**H NMR of *trans*-2 (CD_2Cl_2), 1 ($CDCl_3$), L^{CN} ($CDCl_3$), crude reaction mixtures after addition of *t*-BuLi.**

The possibility of a coordination of the pyridines to Pt(II) metal center before the lithiation was studied. Based on the reported mechanism,[92] coordination to the nitrogen could be the first step and the coordination of the carbon after lithiation would be expected to be more successful, due to the chelate effect. The Pt precursor and the ligand were heated in THF, CD_3CN and $CDCl_3$, but showed no signals indicating a significant coordination of the ligand to the Pt(II) metal center (**Figure 2.27**). Prolonging the heating from 1h to 16h did not show any significant increase, therefore a coordination before the lithiation was not further investigated.

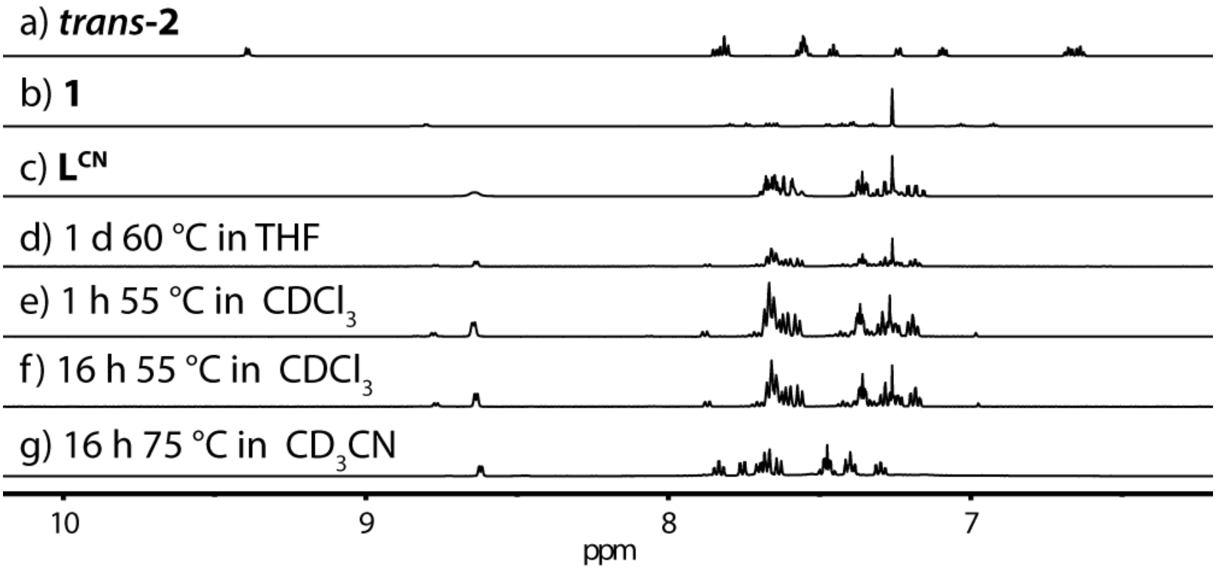

Figure 2.27 ^{1}**H NMR spectra of: a) *trans*-2 (CD_2Cl_2), b) 1 ($CDCl_3$), c) L^{CN} ($CDCl_3$), d-g) crude reaction mixtures after heating, that showed no significant signal indicating a coordination of the ligand L^{CN} without lithiation.**

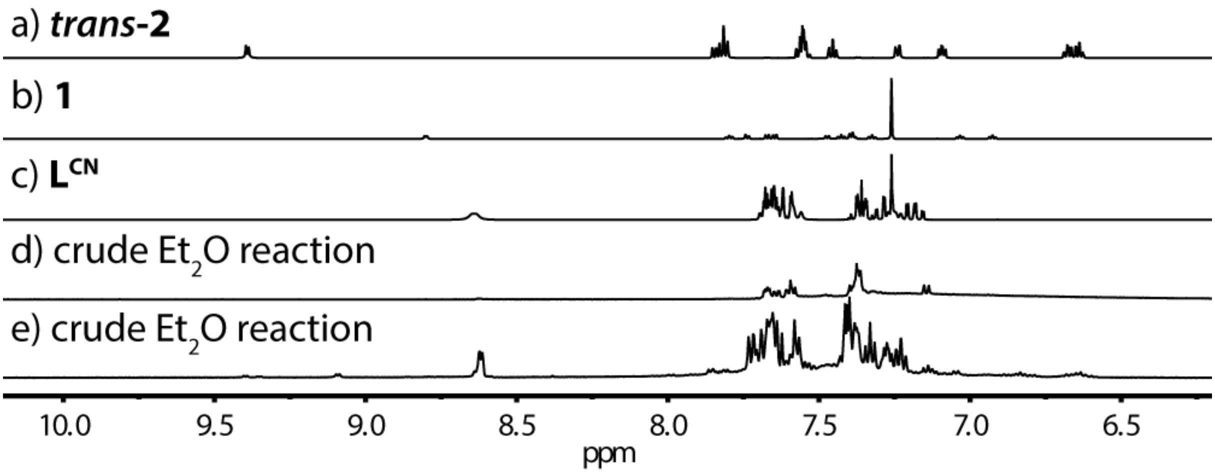

Figure 2.28 ^{1}H NMR spectra of: a) *trans*-2 (CD_2Cl_2), b) 1 ($CDCl_3$), c) L^{CN} ($CDCl_3$), d+e) crude reaction mixtures which show, that the replacement of THF by Et_2O did not result in significant formation of complex 1 or *trans*-2.

The chosen solvent can have a tremendous effect on the lithiation reaction.[99] The use of pure Et_2O was tested, but did not lead to significant formation of ***trans*-2**. In one case (**Figure 2.28 d**) a total disappearing of the signal assigned to the proton next to the nitrogen could be observed, probably due to a replacement with the hexyl group of the *n*-BuLi.[100] The missing of the characteristic upfield shifts of the signals assigned to the protons H_k and H_j indicates no coordination to the metal. A variety of solvent mixture of THF/Et_2O were tested and increased the yield of ***trans*-2**, compared to the use of pure THF, but resulted in the formation of a new species, a *cis* chelating complex, that could not be isolated from ***trans*-2** via column chromatography or HPLC. The characterization of the new species is elaborated in the next chapter and allowed a breakthrough in the yield and work up process of ***trans*-2**.

2.4.4 *cis* PtL^{CN}$_2$

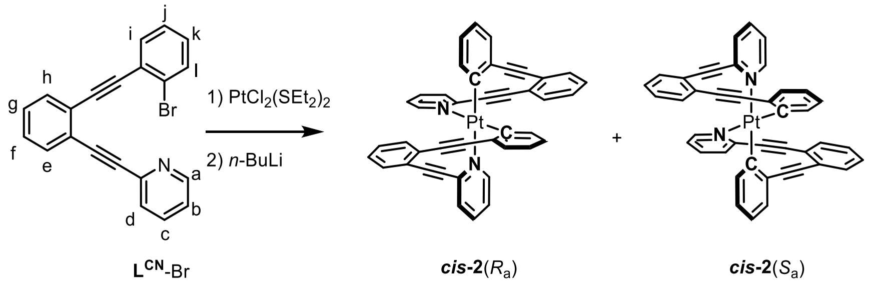

Figure 2.29 The *cis* chelating stereoisomers formed as kinetic product.

During the attempts to optimize the yield of ***trans*-2**, with the change of the solvent from THF to THF/Et_2O solvent mixtures in different ratios up to 1/10, a new product was formed but it could not be isolated from ***trans*-2** via column chromatography or HPLC. A workup procedure of the reaction mixture, by washing with a minimal amount of ether and chloroform allowed the isolation of ***cis*-2**. This finally allowed the full characterization. In contrast to ***trans*-2**, two ligands are attached to the metal center in a *cis* chelating and not in a *trans* chelating motif. The existence of this compound was not expected, especially after the X-ray structure determinations of **1** and ***trans*-2**, which showed the perfect fit of the Pt(II) cation into the trans chelating ligand. In the ESI-MS, only the monocationic species of ***cis*-2** with one attached ligand could be found. In the ^{1}H NMR spectrum, the signal assigned to the proton H_a is between the signals found in **1** and ***trans*-2**. Very characteristic for the formation of the *cis* chelated complex is the contact in the NOESY spectra between the protons H_a and H_l (**Figure 2.31**). In the *trans*-chelating complex ***trans*-2** the protons are too far away and therefore this contact can only be seen for the ***cis*-2** complex.

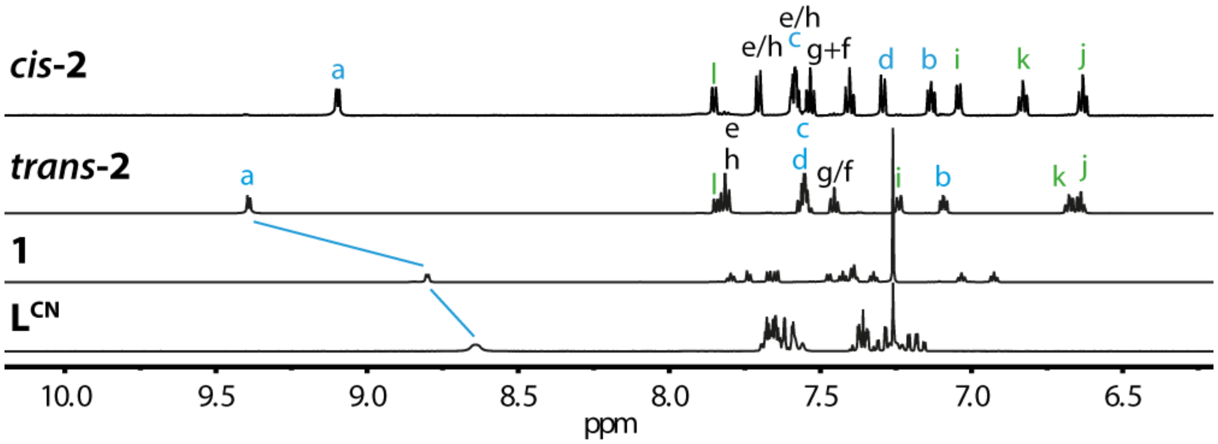

Figure 2.30: ^{1}H NMR of *cis*-2 (CD_2Cl_2), *trans*-2 (CD_2Cl_2), 1 ($CDCl_3$) and L^{CN} ($CDCl_3$).

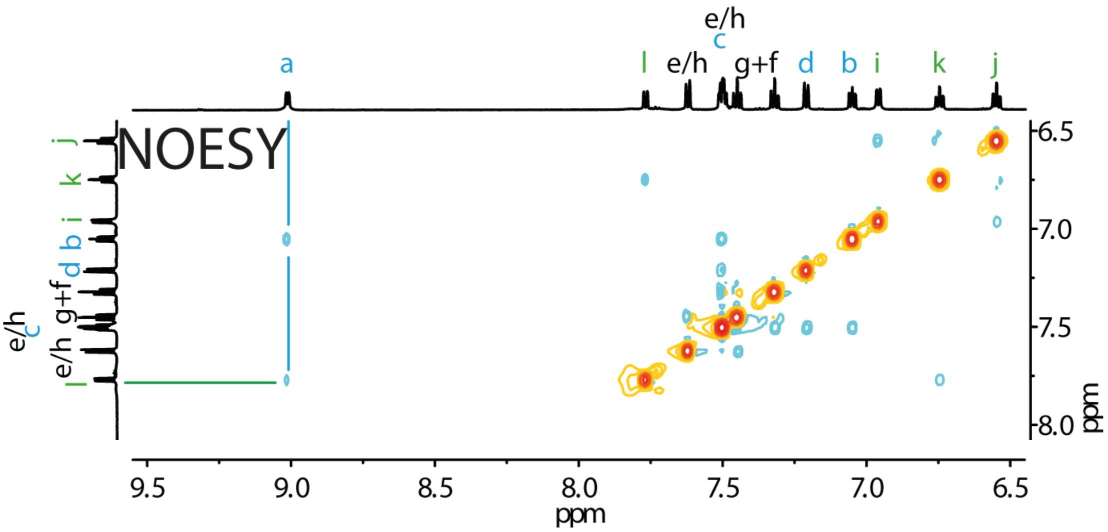

Figure 2.31. NOESY NMR spectrum of *cis*-2 (600 MHz, CD_2Cl_2).

Crystals of ***cis*-2** suitable for X-ray structure determination were grown by slow evaporation of the solvent DCM (**Figure 2.32**). ***Cis*-2** crystallized in the triclinic space group $P\bar{1}$. In contrast to ***trans*-2**, the ligand is distorted upon coordination to the metal. The angles N18_1−Pt1−C2_2 (177.4(1)°) and C2_1−Pt1−N18_2 (175.7(1)°) show a significant difference from the ideal 180° angle of a square planar geometry and the values that were found for ***trans*-2**. The twist of the aromatic groups leads to close H−H (2.553−2.903 Å) distance for the protons H_a and H_l, explaining the contact seen in the NOESY spectrum.

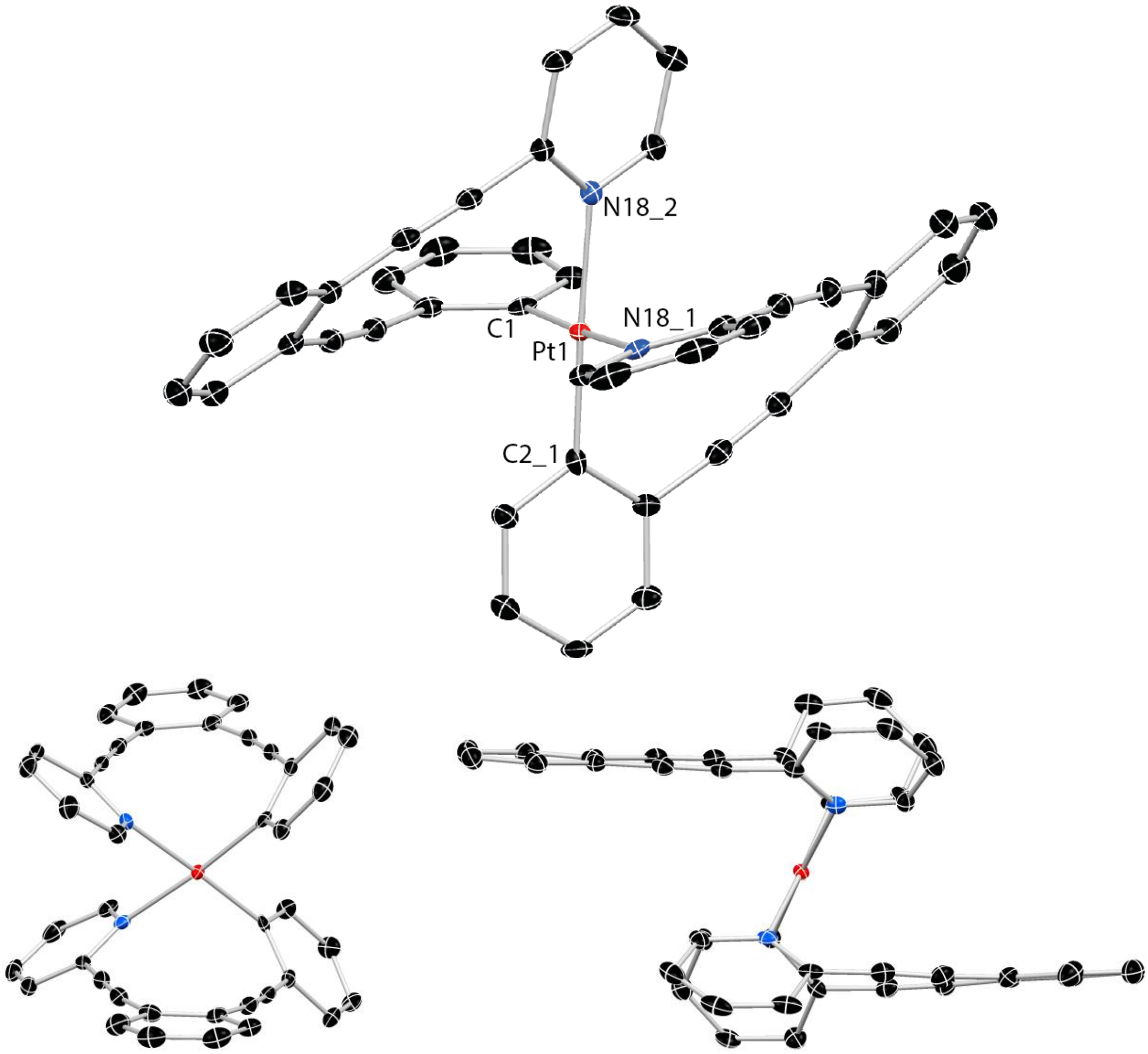

Figure 2.32: X-ray structure of *cis*-2 from three different angles.

The isolated ***cis*-2** complex is stable as solid, but ^{1}H NMR spectra showed a slow transformation to ***trans*-2** in DCM at r.t. (~50 % 7 d), which could be performed quantitatively at 40 °C in $CDCl_3$ within 9 h (**Figure 2.33**) resulting in an increased yield for ***trans*-2** from 16 % to 25 % and solved the problem of the separation of ***trans*-2**. This result allowed insights into the mechanism of the reaction and showed that ***cis*-2** is the kinetic product formed in the reaction, whereas ***trans*-2** is the thermodynamic product.

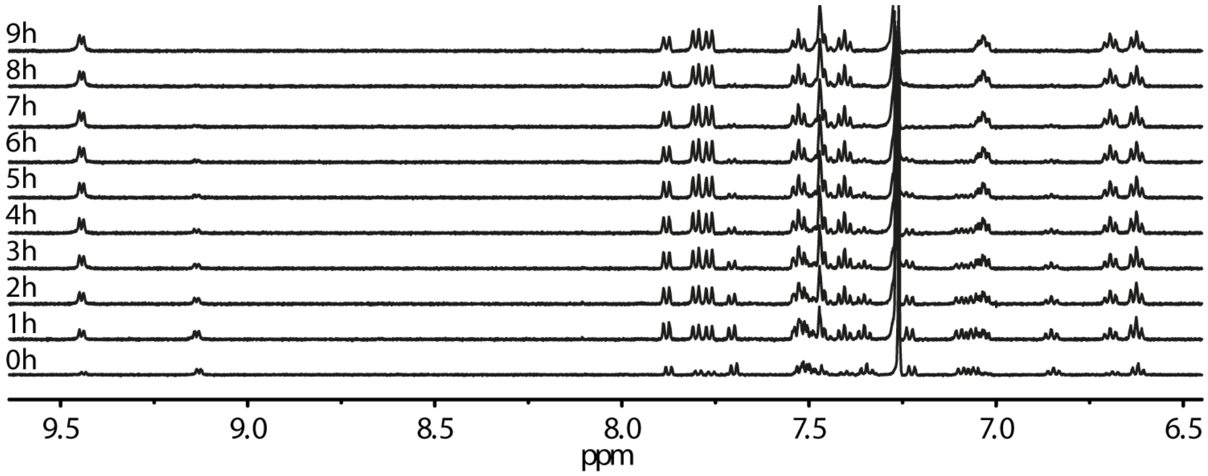

Figure 2.33 ^{1}H NMR spectra of the transformation of *cis*-2 to *trans*-2 within 9 h (500 MHz, $CDCl_3$, 40 °C).

2.5 Photophysical properties of *trans*-2

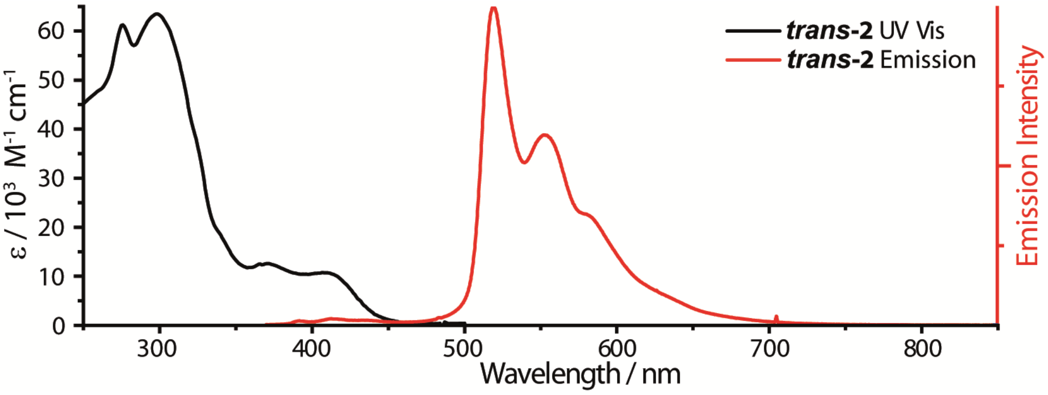

Figure 2.34 Combined UV-vis and emission spectra (excitation wavelength = 350 nm).

The UV-vis spectrum of ***trans*-2** shows two strong absorption maxima at 276 and 298 nm (**Figure 2.34**). To investigate the nature of the transitions, the electronic spectra have been calculated in cooperation with Prof. G. Longhi from university of Brescia, Italy.[57] After a 30 nm shift of the DFT-calculated spectrum to lower wavelenghts, the calculated absorbtion matches well with the measured spectra and allow to give insights into the transition. The absorption band at 412 nm is a combination of metal-to-ligand charge-transfer (MLCT) and ligand-centered (LC) transitions, where a LC transition dominates the absorption band at 370 nm. This result is in agreement with similar shaped bands in literature reported complexes with C^N chelating ligands. The emission spectrum was recorded in dichloromethane with an excitation wavelength of 350 nm at room temperature (**Figure 2.34**). ***Trans*-2** shows emission in the range from 480 to 700 nm, with maxima at 519, 553 and 580 nm.

To differentiate between fluorescence and phosphorescence, the lifetime of the emission was investigated in cooperation with Prof. K. Umakoshi and Prof. E. Sakuda from Nagasaki University, Japan (**Figure 2.35**). The lifetime measurements in dichloromethane solution showed a significant shorter lifetime under air atmosphere compared to the inert gas argon atmosphere. The faster decay under air atmosphere can be explained with the interaction of the excited complex with oxygen in the triplet ground state.[83] According to the selection rules of the transitions of quantum states, transitions with different quantum states are “spin-forbidden” and have a decreased rate. The faster interaction with the triplet state oxygen indicates therefore a triplet state of the excited metal complex, which indicates phosphorescence as the main radiative relaxation pathway. In addition, the linear slope for the emission under argon atmosphere on the logarithmic scale indicates the phosphorescence as the dominating radiative pathway. The found phosphorescence lifetime of ***trans*-2** at 298 K in dichloromethane ($\tau_{298} = 10.9$ µs) and the quantum yield ($\Phi_{PL} = 0.07$) are comparable with literature reported Pt(II) complexes with a C^N ligand.[72]

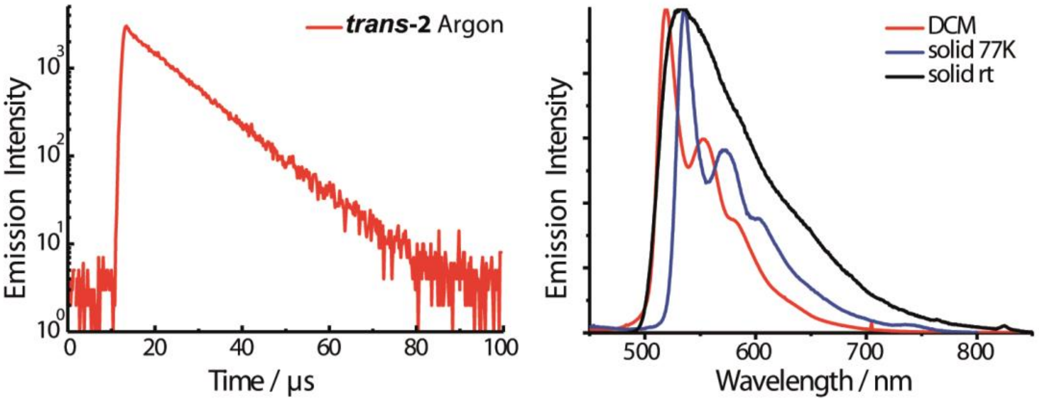

Figure 2.35 Emission lifetime measurement under argon atmosphere of *trans*-2 (left), normalized emission spectra for solution and solid state samples at 77 and 293 K (right).

Additionally, the emission was investigated in the solid state at different temperatures and excitation wavelengths of 350 and 400 nm. In the solid state at 77 K, the emission bands are similar to the solution at room temperature, but with a red shift of ~ 20 nm leading to maxima at 536, 572 and 602 nm. In the solid state at room temperature, the emission bands are indistinguishable broadened to one maxima at 533 nm.

The key experiments were the investigation of the different behavior of the enantiomers. The separated enantiomers were therefore tested for their differential absorption in CD experiments (**Figure 2.36**). The S_a enantiomer is the first fraction of the HPLC separation and shows a positive Cotton effect at 412 nm and further strong bands at 259, 319, and 380 nm with a maximal $\Delta\varepsilon_{319}$ of 71 cm^{-1}M^{-1}. The CD spectrum of the R_a enantiomer, the second fraction of the HPLC separation, is exactly opposite to the S_a enantiomer. The assignment of the enantiomers was based on the X-ray structure determination, but the measured CD spectra allowed a comparison with calculated CD spectra to prove the made assignment. The TD-DFT calculations are in agreement with the proposed assignment. To validate the principle suitability of

***trans*-2** for a chiral OLED device, the emission of circularly polarized light (CPL) in dichloromethane has been investigated in cooperation with Prof. G. Longhi and and Prof. A. Sergio from university of Brescia, Italy. (**Figure 2.36**) with a home-built apparatus.[101,102,103] The gained dissymmetry factor g = 10^{-3} is in the magnitude of g values reported for octahedral Ir complexes (**Table 2.2**).[60]

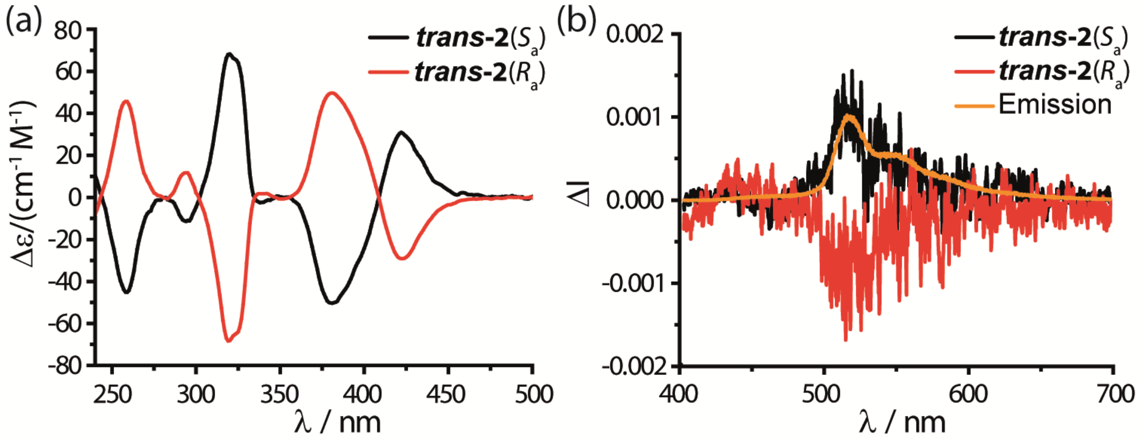

Figure 2.36: CD (left) and CPL spectra (right) of the enantiomers of *trans*-2.

2.6 Conclusion

A new kind of chiral cyclometalated Pt(II) complexes has been developed and characterized via NMR, ESI-MS, CD and X-ray techniques and the photoluminescent properties have been investigated for the *trans*-chelated complex. The complexes are chiral without the use a chiral ligand, but because of the asymmetric out of plane ligand design and the resulting three-dimensional structure. The mono chelated complex racemizes in solution but the *trans*-chelated complex with two attached ligands is conformationally stable. The ligand is flexible to coordinate in *cis* and a *trans* manner to the Pt(II) metal center and the transformation from the kinetic *cis* to the thermodynamic *trans* complex was shown. The enantiomers of the *trans*-complex have been separated and the circularly polarized emission shows the potential for 3D OLED devices, which is currently investigated in cooperation with Prof. M. J. Fuchterat the Imperial College London. Modifications of the ligand should allow tuning of the photophysical properties like reported for the related complexes.

3 CHIRAL CAGES BASED ON A HELICENE BACKBONE

3.1 Introduction

Helicenes are a class of chiral organic molecules with superior chiroptical properties, which have their origin in the distorted π-systems. Helicenes are composed of *ortho*-fused aromatics, which spiral up because of the great steric hindrance causing axial chirality which can be clock or counterclockwise.[61] Helicenes with right-handed helix and a clockwise turn are called the plus (*P*) enantiomer, left-handed with an anticlockwise turn are called the minus (*M*) enantiomer and the number of fused aromatic rings is given in brackets or out-written before the term helicene.[104] The (*P*)-[6]-helicene and the (*M*)-[6]-helicene are depicted in **Figure 3.1**.

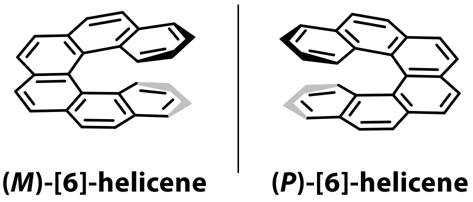

Figure 3.1 (*P*)-[6]-helicene and (*M*)-[6]-helicene.

The helical topology of the distorted delocalized π-systems results in high optical rotation, high circular dichroism and enhanced physical-organic properties which makes helicenes more than 100 years after their discovery still a highly studied compound.[105]

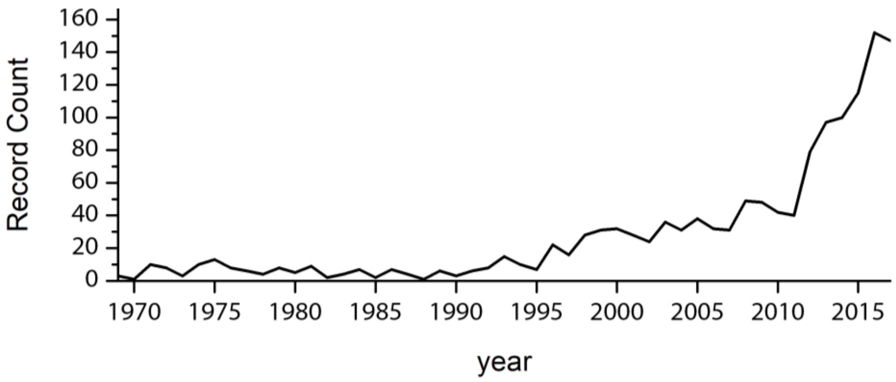

Figure 3.2 Statistics of the literature published from 1969 to 2017, found via Scifinder for the keyword "helicene", retrieved on May 29th, 2018.

3.1.1 Synthesis of helicenes

The first helicenes have been synthesized in 1903 in form of heterohelicenes (**Figure 3.3a**).[106] Heterohelicenes have in contrast to carbohelicenes at least one heteroatom incorporated (e.g. N, S).[105] The first carbohelicene has been reported in form of the [4]-helicene (**Figure 3.3**) in 1912 by Weitzenböck and Lieb synthesized from 2-naphtylacetic acid and 2-nitrobenzaldehyde.[107]

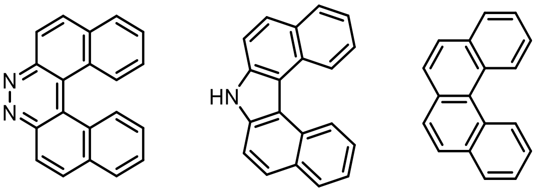

Figure 3.3 the first reported (hetero-)helicenes.

Six years later a [5]-helicene was reported and continuous research until today gave rise to numerous carbohelicenes up to the 3,34-bis(triisopropylsilyloxy)[16]helicene, which was reported in 2015 with a 7 % yield for the last step and is the longest [n]helicene that has been reported to date (**Figure 3.4**).[108]

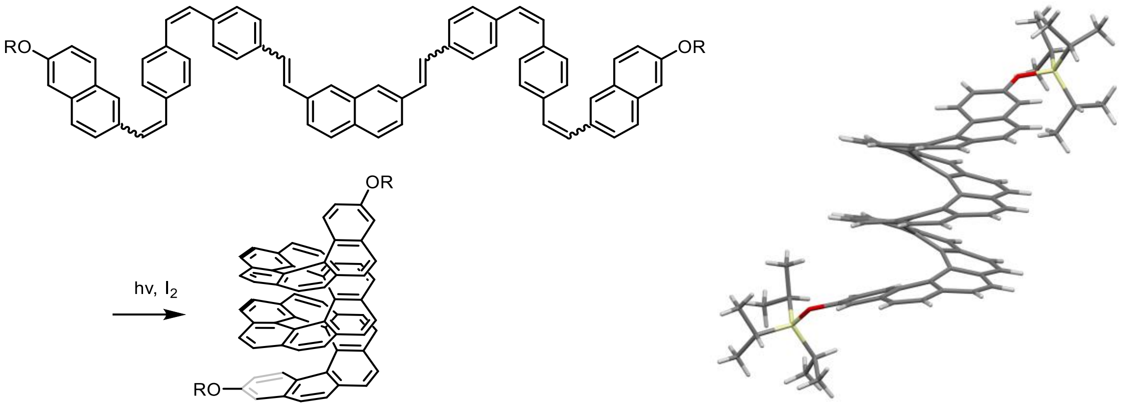

Figure 3.4 Last step of the synthesis (left) and X-ray structure (right) of [16]helicene, R = triisopropylsilyl.

The main synthesis strategies for helicenes are oxidative photocyclizations, Diels-Alder and Friedel-Crafts and metal-mediated reactions,[109] of which the oxidative photocyclization is the most popular strategy for the synthesis of helicenes, since their first reports in 1967.[110][111][112] This approach is based on the photocyclodehydrogenation of stilbene into phenanthrene (**Figure 3.5**). Irradiated with UV light, the stilbene undergoes a rapid interconversion of the *Z*- and *E*-isomers, but only the *Z*-isomer can undergo a conrotatory cyclization into the *trans*-4a,4b-dihydrophenanthrene (DHP). The backreaction of DHP to the starting material will occur either by thermal or photochemical ring opening reaction. Therefore, an oxidizing agent such as iodine is added to the reaction mixture to dehydrogenate the DHP to phenanthrene. The mechanism was carefully studied by Laarhoven *et al.*.[109] Even so oxidative photocyclizations allowed the selective formation of helicenes even with functional groups, a drawback was the low yield of the reactions, which was significantly improved by Katz *et al*. by the addition of propylene oxide.[113]

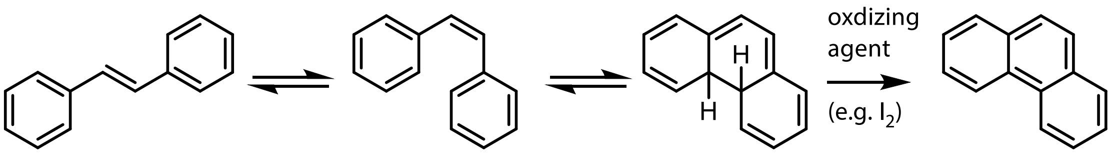

Figure 3.5 photocyclodehydrogenation of stilbene into phenanthrene.

For the synthesis of larger helicenes, the selectivity of the photoreaction is substantial. In the described [16]-helicene six alkyne bonds undergo cyclisation reactions that have to occur selectively to the formation of the helicene. Possible isomers and the selectivity are explained for the simpler case of a [6]-helicene synthesis, in which one half is already cyclized (**Figure 3.6**). The electron distribution in the excited diarylethylene is causing the selectivity, which can be estimated by the sum of the free valence numbers of the atoms r and s involved via $\sum F^*_{r,s}$, with $F_r = \sqrt{3} - \sum P_r$.[109,114] The photocyclization occurs only for $\sum F^*_{r,s} < 1.0$ and in case of several options, the cyclisation is selective if the sum difference is bigger than 0.1 and the options do not differ in planarity, as planar products are preferred over non planar products.

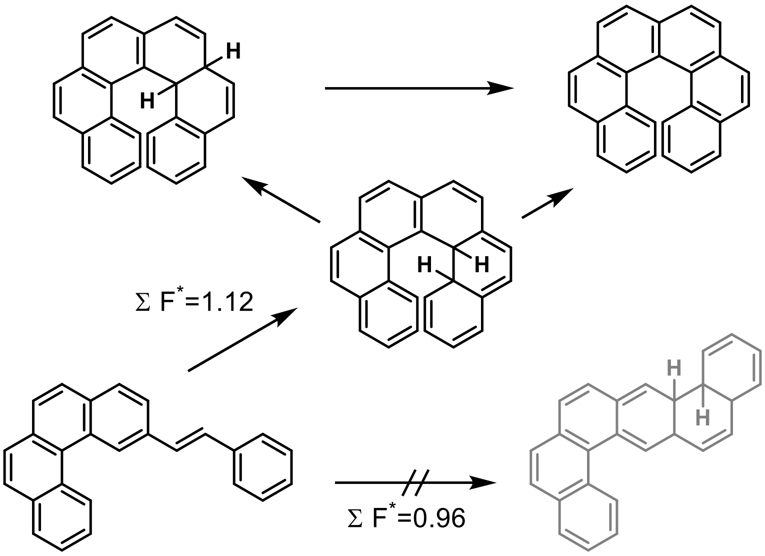

Figure 3.6 The selectivity caused by the electron distribution can lead to the selective synthesis of helicenes, if the starting material is well planned.[109,114]

Since the breakthrough in the optimization of the yield, the oxidative photocyclization is an efficient strategy and has been widely used also for heterohelicenes, but a drawback is the need of highly diluted solutions (ca. 10^{-3} M) to prevent intermolecular cycloadditions. To improve the scale of the oxidative photocyclization the continuous flow strategy has been used.[61,115]

Another way to synthesize helicenes are Friedel-Crafts-type reactions that can be performed in the most cases in less than 5 steps with moderate-to-good yields, but the substrates have to be well designed to controll the regioslectivity.[61] For large-scale preparations Diels-Alder reactions are practial methods for the possibilty of symmetric helicenes and helicene derivatives as helicene qionones. A drawback is the limited amount of dienes and dienophiles that are suitable for the helicene synthesis. In the last years, metal-mediated reactions played an increasing role in the helicene synthesis and became a powerful strategy. The synthesis is performed in moderate to high yields, often under construction of several rings in one step, with high functional group tolerance.[61]

3.1.2 The helical pitch of helicenes and its consequences

As discussed in the introduction of this chapter, helicenes are chiral because of the distortion from the planar geometry due to steric hindrance. An enormous amount of studies investigated the properties of the enantiomers and their stability towards racemization:

Spontaneous resolution has been reported for the [7]helicene, where a crystal of the enantiopure (*P*)-[7]helicene could be separated out of the racemic mixture in benzene.[116] A solution with a racemic mixture with both enantiomers present in same proportions can crystalize under spontaneous resolution, where each crystal contains only one of the two enantiomers.[10] Also [6]-,[8]- and [9]- helicenes could be separated via spontaneous resolution out of chloroform or 1,2-dichloroethane solutions, where CS_2 solutions led to racemic crystals.[117] The optical properties could be determined for the separated enantiomers and all helicenes showed a remarkable similarity between the absorption bands of the same enantiomer. The distortion of the π-system disturbs the conjugation compared to planar polycyclic aromatic hydrocarbons (PAHs) resulting in similar wavelength of the absorption from [4]- to [16]-helicene and a yellow or yellowish color for all of them.[61] This is in contrast to the general trend of conjugated systems, where the wavelength of the absorption increases with the number of double bonds.[118]

If the absolute configuration of a helicene enantiomer cannot be determined from the crystal structure, the optical rotation or the circular dichroism can be used in compare with literature reported systems.[61] The empirical rule for the optical rotation is that levorotatory helicenes with negative specific rotation values are the (*M*)-helicenes, where dextrorotatory helicenes with positive specific rotation values are the (*P)*-helicenes.[61] The enantiomers of helicenes have very high specific rotation values of −3640 ° for the (*M*)-[6]-helicene to −9620 ° for the [13]-helicene.[109,119] The experimental CD spectra for several (*P*)-helicenes are depicted to show the above-mentioned behavior and show the strong circular dichroism of around 250 M^{-1} cm^{-1} for the positive Cotton effect (**Figure 3.7**).[120]

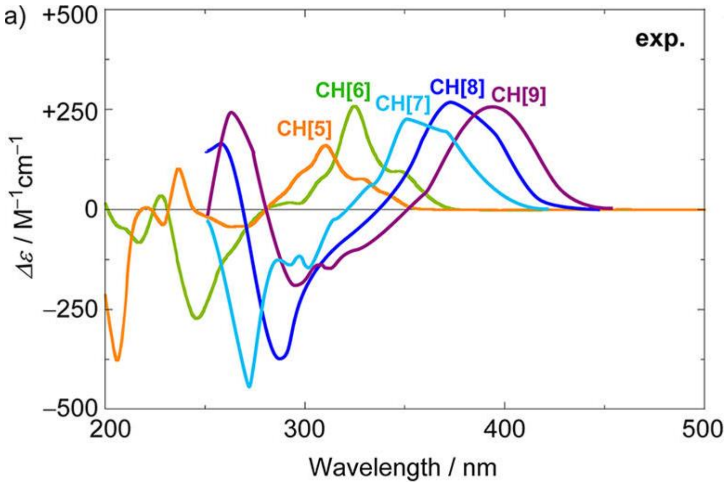

Figure 3.7 Experimental CD spectra for the (*P*) enantiomers of [5]-,[6]-,[7]-,[8]- and [9]-helicenes. © American Chemical Society [120]

The racemization of helicenes has been studied and the results for a series of carbohelicenes in naphtalene are depicted in **Table 3.1**.[121,122] The [5]helicene has due to the fact, that the helicene does not cover the 360° degree of the helical pitch, by far the lowest energie barrier for the racemization and shows a significant racemization already at 57 °C ($t_{1/2}$ = 62.7 min). In the [6]helicene two carbons overlap and therefore the structural deformation is hindered and the racemization needs a significantly higher temperature with 221 °C ($t_{1/2}$ = 13.4 min). In general the barrier (E_a) is higher, the longer the helicene is, but the difference between the helicenes longer than 7 are neglictible. It is importand to conclude, that carbohelicenes with six or more rings are conformational stable at room temperature.

Helicene	**E_a (kcal/mol)**	**T (K)**	**$t_{1/2}$ (min)**
[5]helicene	24.6	293	62.7 (57 °C)
[6]helicene	36.2	300	13.4 (221 °C)
[7]helicene	41.7	542	13.4 (295 °C)
[8]helicene	42.4	543	3.1 (293.2 °C)
[9]helicene	43.5	543	12.3 (293.5 °C)

Table 3.1 The stability of helicenes towards racemization.[121,122]

Computational studies for the racemization of carbohelicenes have been reported recently for [n]helicenes up to n = 24 following a conformational pathway.[123] Based on the DFT calculated mechanism study, for [n]-helicenes up to n = 7, a concerted mechanism, and for longer helicenes a multistep mechanism is involved in the racemization. The authors propose a nonplanar transition states for the racemization of [n]helicene (n > 4), which is in case of the

[5] helicene in contrast to a peviously reported mechanism via a planar transition state (**Figure 3.8**).[124]

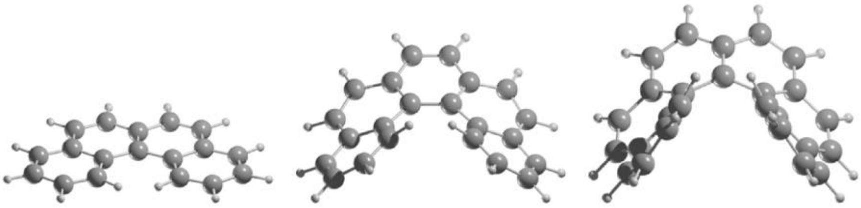

Figure 3.8 The transition states for the racemization of [4], [5], and [6]-helicenes.[123]

3.1.3 Helicene based assemblies

Marinetti *et al.* reported a ortho metallated (*R*)-1-(naphthyl)ethylamine Pd(II) complex with a [7]-helicene derivative in acetone at r.t. (**Figure 3.9**).[125] The use of the enantiopure ethylamine led to the formation of two diastereomers which could be separated via column chromatography. After separation of the diastereomers the helicene could be removed from the complex by addition of bis(diphenylphosphino)ethane yielding the enantiopure helicene derivatives without the need of a chiral HPLC system.[125]

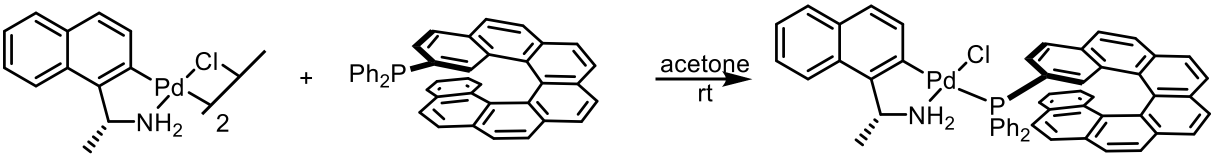

(*R*) rac (*R*,*P*) / (*R*,*M*)

Figure 3.9 A [7]-helicene derivative reported by Marinetti *et al.* to form diastereomers with a chiral Pd complex.[125]

[5]- and [6]-helicene crown ethers and their ability of chiral recognition toward racemic amine salts have been reported by Nakazaki *et al.* (**Figure 3.10**).[126] The synthesis of the helicene followed the photocyclization approach and the enantiomers were separated via chiral HPLC. To investigate the selectivity the differential transport through a bulk liquid membrane has been investigated. Therefore, the racemic guests have been solved in water and their uptake into the enantiopure host through an organic phase, which separated the aqueous host solution from the aqueous guest solution has been monitored. The results showed opposite selectivity for the [5]-helicene and [6]-helicene with a higher selectivity for the [5]-helicene with optical purities up to 77 %.

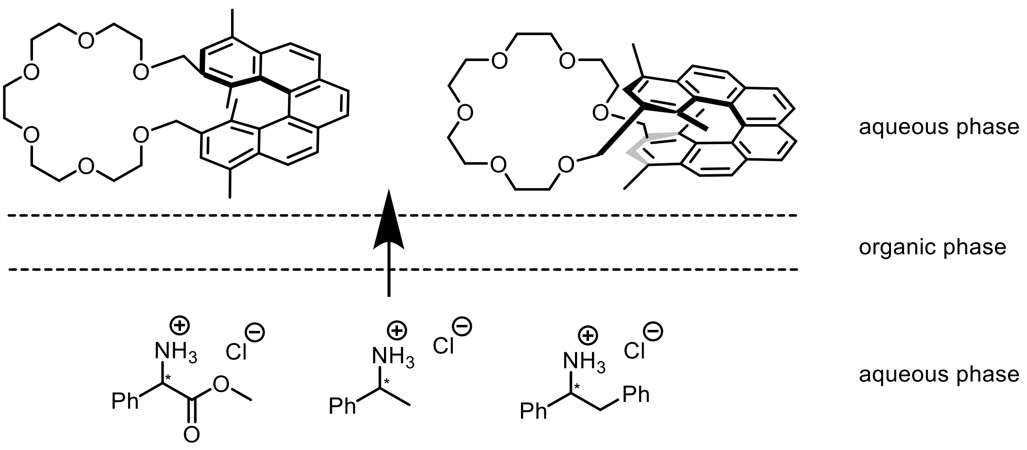

Figure 3.10 Helicene based crown ethers with the ability of chiral recognition.[126]

Autschbach, Crassous, Réau *et al*. reported a big variety of complexes containing helicene derivatives.[82,83,127] The luminescent helicene complex that was used to build a CPL emitting OLED device are discussed in chapter 2.1.3 (**Table 2.2)** .

An application of helicene containing complexes as responsive switch has been reported by Crassous *et al.* (**Figure 3.11**).[128] The Os complex can be switched between its two configurations by addition of acid and base. Under Addition of HCl, chloride coordinates to the metal center and the vinyl-Os(II) complex changes to a carbene-Os(IV)-complex. IR, CD and UV-Vis spectra proofed the reversible switching under addition of NEt_3. The stretching band of CO shows the changed properties of the complex upon the coordination of the chloride from ν_{CO} = 1895 cm^{-1} to ν_{CO} = 1932 cm^{-1}.

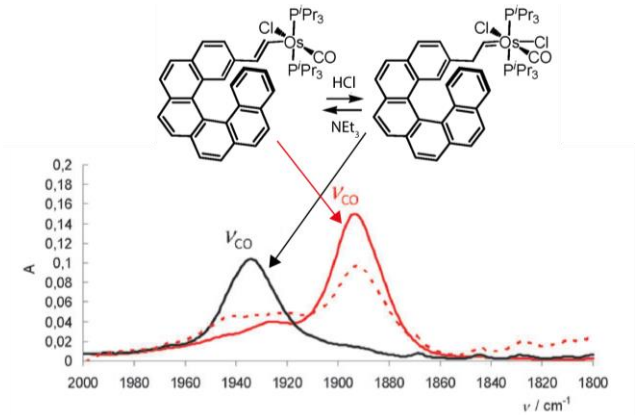

Figure 3.11 The responsive switch based on an Os complex, that can be switched by the addition of acid and base leading to a strong shift of the IR band. © Royal Society of Chemistry [128]

Recently two organic cages with helicene backbones have been published. A triple helicene cage with six [5]-helicene units was synthesized with the Yamamoto coupling reaction and could be characterized via X-ray diffraction analysis and ^1H NMR spectra by Soichiro *et al.*(**Figure 3.31**).[129] The enantiomers (*P*)-**THC-1** and (*M*)-**THC-1** could be separated via chiral HPLC and the CD spectra for both enantiomers have been recorded showing opposite bands for the enantiomers. The neutral cage has a low solubility in the most common organic solvents and is only moderately soluble in carbon disulfide. The cavity of the cage is very small and even the solvent *N*,*N*-dimethylformamide, which was used for the synthesis, is too big for the cavity provided by the cage and therefore no guest uptake could be studied.

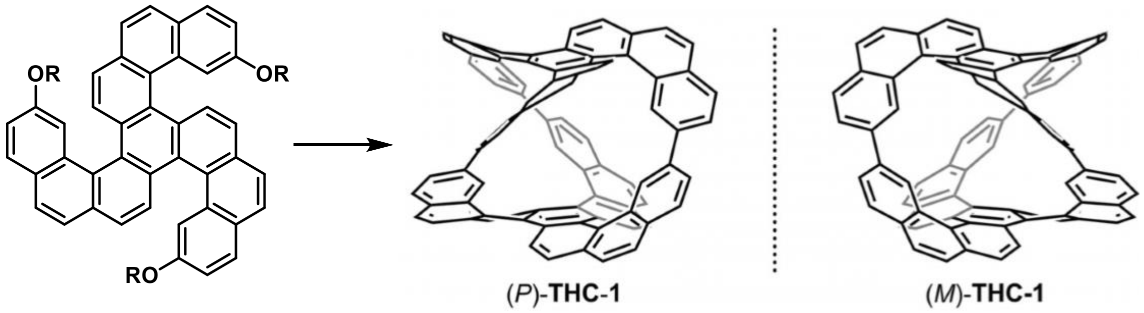

Figure 3.12 A triple helicene cage.[129]

A bigger organic cage with a triple-stranded helical structure containing three [6]helicenes was reported recently by Qiu *et al.* in 2018 (**Figure 3.13**).[130] Photocyclisation led to the 4,13-di-ethynyl[6] helicene, which was separated into the enantiomers via chiral HPLC and further functionalized to contain two aldehydes, which allowed the cage formation via imine condensation with tris(2-aminoethyl)amine in a 3:2 ratio. The cage could be characterized via X-ray structure determination, NMR and CD spectra. The cage with the (*P*)-helicenes shows strong CD bands with a maximal $\Delta\varepsilon = -708\ \mathrm{L{\cdot}mol^{-1}{\cdot}cm^{-1}}$ at 242 nm. Interestingly, the CD bands of the cage are significantly more intense than the bands of the ligand multiplied by the factor of three. The large cavity provides enough space for a variety of guests and therefore chiral adsorption experiments have been made. A racemic mixture of 1-phenylethanole dissolved in isopropanol was added to the suspension of the enantiopure cage with the (*P*)-helicene. The free guests were separated from the host-guest system and the encapsulated guest was extracted from the guest and analyzed via chiral HPLC showing an enantiomeric excess of 67 % for the (*R*)1-phenylethanol.

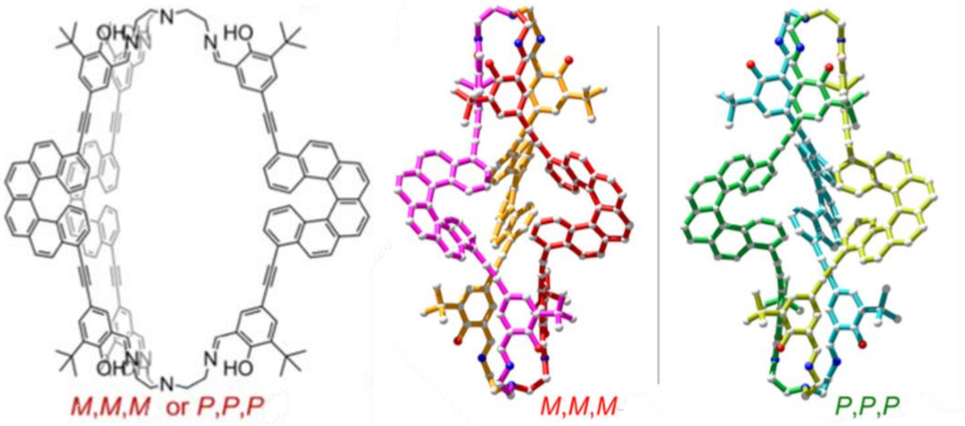

Figure 3.13 Organic cage containing three [6]helicenes.© American Chemical Society[130]

Due the mentioned interesting properties of helicenes, the idea was to develop a cage containing bispyridyl ligands with a helicene backbone, that can coordinate to a Pd(II) metal center. The design of the ligand is depicted in the next chapter.

3.2 Ligand synthesis

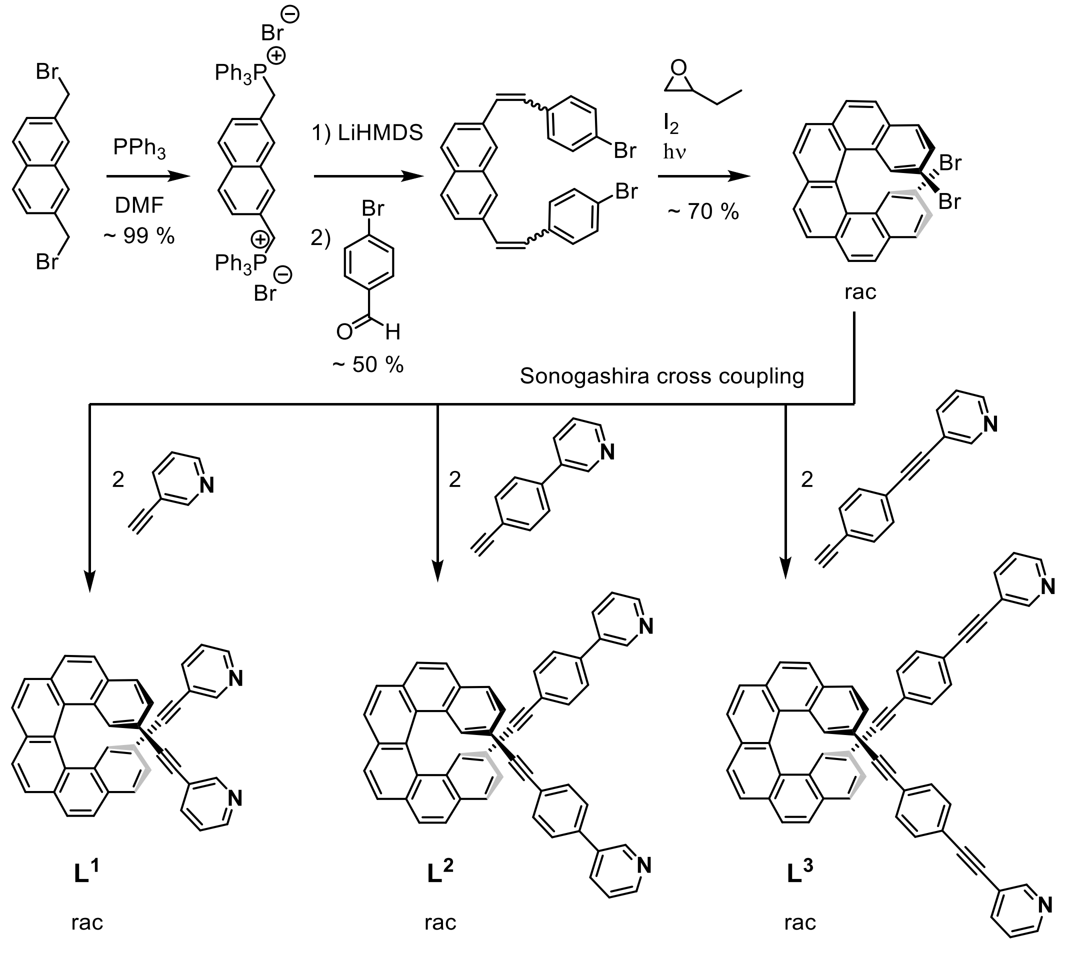

Figure 3.14 Overview over the synthesis of the 3 ligands developed for the synthesis of helicene cages.

The synthesis of the 2,15-dibromo[6]helicene was reported in literature.[126,131,132] Starting material was the commercial available 2,7-bis(bromomethyl)naphthalene which could be quantitatively transformed with triphenylphosphine in DMF into the 2,7-Bis(triphenylphosphoniomethyl)naphthalene dibromide (**Figure 3.14**). The addition of LiHMDS leads to the phosphonium ylide which reacts with parabromoacetaldehyde in a Wittig reaction under the formation of double bonds to 2,7-Bis[2-(4-bromophenyl)ethynyl]naphthalene. The Wittig reaction is not very selective and the product consists of a mixture of Z- and E-alkene isomers. Aseparation of the isomers is not necessary, as the stereo information is lost in the next synthesis step. The next step in the synthesis is the irradiation under UV-light, where the *E*-alkenes are transformed into the *Z*-alkenes, which than undergo a pericyclic reaction on both alkene positions of the molecule. The formed intermediate is oxidized by the iodine to obtain the 2,15-dibromo[6]helicene.[113] The epoxybutane is added to consume the reactive hydrogen iodide.[113,133] The ring closure is not stereoselective and both enantiomers of the helicene, the (*P*) and the (*M*) helicene are formed leading to a racemic mixture. The separation of the 2,15-dibromo[6]helicene into the enantiomers was reported and investigated, but the very low solubility made the separation impracticable. Three different ligands have been synthesized to obtain a variety of cages based on a helicene backbone, as the size of the cavity is known to be crucial for the guest uptake in host guest complexes. The alkyne for the shortest ligand, $\mathbf{L^1}$, is commercially available, where the alkynes for $\mathbf{L^2}$ and $\mathbf{L^3}$ have been synthesized with Sonogashira and Suzuki cross coupling reactions.[89] $\mathbf{L^1}$ and $\mathbf{L^2}$ could be successfully resolved into the enantiomers via chiral HPLC with Daicel CHIRALPAK IC columns using a dichloromethane/hexane/methanol/propan-2-ol (5.0%/80.0%/5.0%/10.0%) mixture as eluent for the separation of $\mathbf{L^1}$ and a dichloromethane/hexane/methanol/propan-2-ol (16.0%/69.0%/5.0%/10.0%) mixture as eluent for the separation of $\mathbf{L^2}$ (Figure 3.15). For a better solubility and higher load of the column the samples were solved in a DCM/MeOH mixture (100/1) ($\mathbf{L^1}$: c = 26 mg/1.0 mL, $V_{injection}$ = 50 µL, $\mathbf{L^2}$: c = 20 mg/1.0 mL, $V_{injection}$ = 200 µL.). No conditions for the separation of the enantiomers of $\mathbf{L^3}$ could be found.

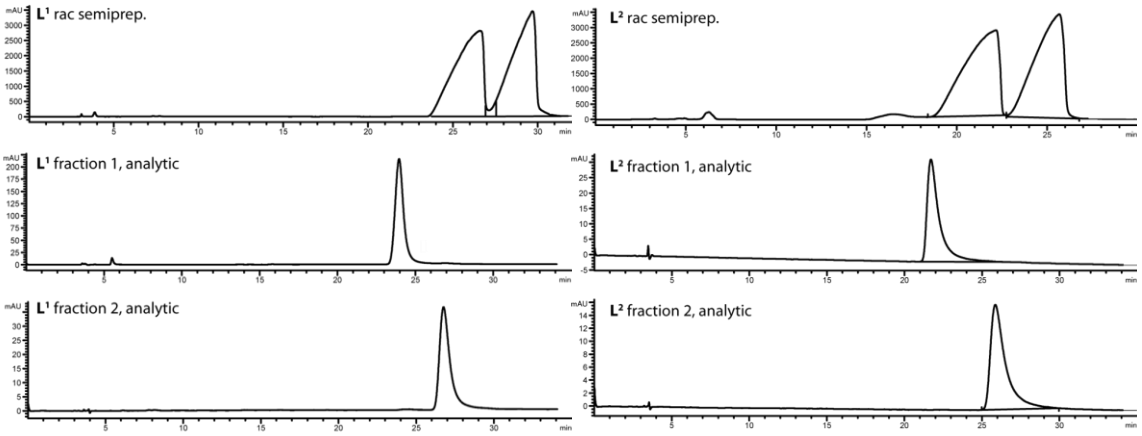

Figure 3.15. **Chromatograms of L^1 and L^2 before and after the separation of the enantiomers (Abs. 250 nm, flow rate 1 mL/min for the analytic column, flow rate 5 ml/min for the semipreparative column).**

Crystals suitable for X-ray structure determination could be grown of enantiopure $\mathbf{L^2}$ from HPLC fraction 2 in DMSO at room temperature (**Figure 3.16**). Twelve enantiopure molecules of ligands $\mathbf{L^2}$ are present in the asymmetric unit, of which nine are partially disordered, and the presence of DMSO in the crystal structure allowed the determination of the absolute structure. The absolute configuration was unambiguously determined as the (*P*) enantiomer using the method of Parsons[96] as implemented in SHELXL,[134] yielding an enantiopure distinguishing parameter of x = 0.079(8). Furthermore, the high number of molecules gave insights to the conformational flexibility of the ligand and its helicene backbone. The helical pitch can be quantified with the distances between the helicene carbons that are bond to the alkyne. The X-ray data shows an intramolecular distance of 3.86 Å, for the shortest and a 16 % bigger distance of 4.49 Å for the biggest distance between the carbons in 2,15 position.

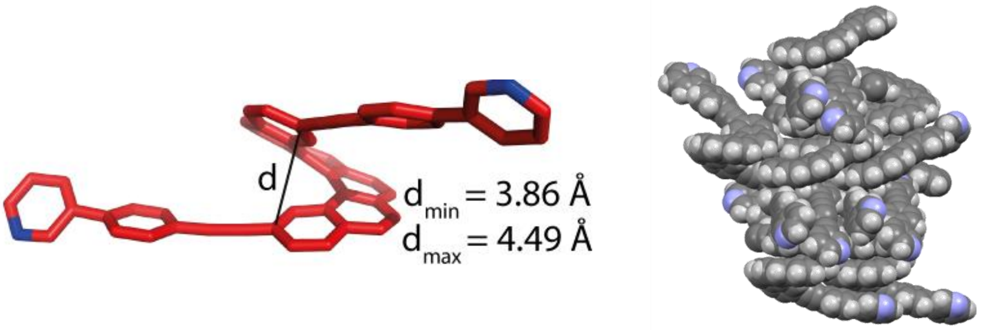

Figure 3.16 X-ray structures of L^{2P}. *left:* one ligand, carbon red, nitrogen blue; right: asymmetric unit with 12 molecules, spacefilling view, carbon grey, nitrogen blue, hydrogen light grey.

3.3 Cage formation

3.3.1 Short helicene cage C1

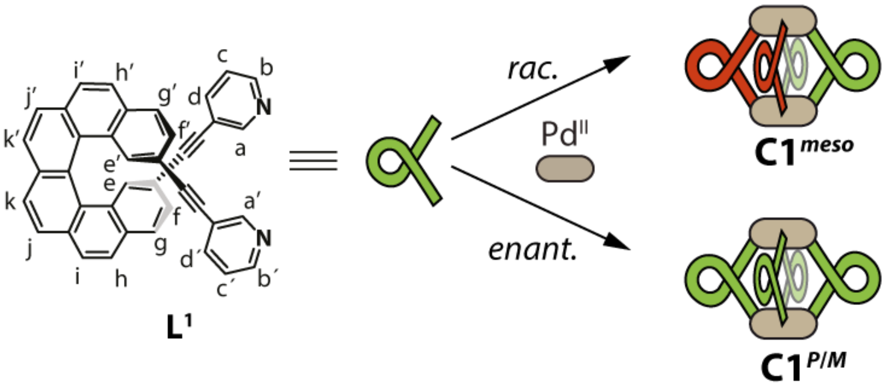

Figure 3.17 Simplified scheme of the cage formations for C1.

The formation of cages was investigated for **L^1**. 2 eq. $[Pd(CH_3CN)_4](BF_4)_2$ were added to 4 eq. of a racemic mixture of **L^1** in acetonitrile, but in the ^{1}H NMR spectrum the signals assigned to the ligand disappeared without the rising of new signals. Therefore, CD_3CN was replaced as solvent by DMSO and the addition of $[Pd(CH_3CN)_4](BF_4)_2$ led to a splitting of the ^{1}H NMR signals into a set of two and a strong downfield shift of the signals assigned to the protons H_a and H_b (**Figure 3.18**). A splitting of signals was reported before in our group for the formation of interpenetrated double cages,[135] but further analytic data revealed the nature of a self dischriminating chiral self sorting, where two (*P*)- and two (*M*)-enantiomers of the ligands are sorted around the Pd(II) metal in a *cis* manner resulting in the achiral *meso* cage (**Figure 3.17**).

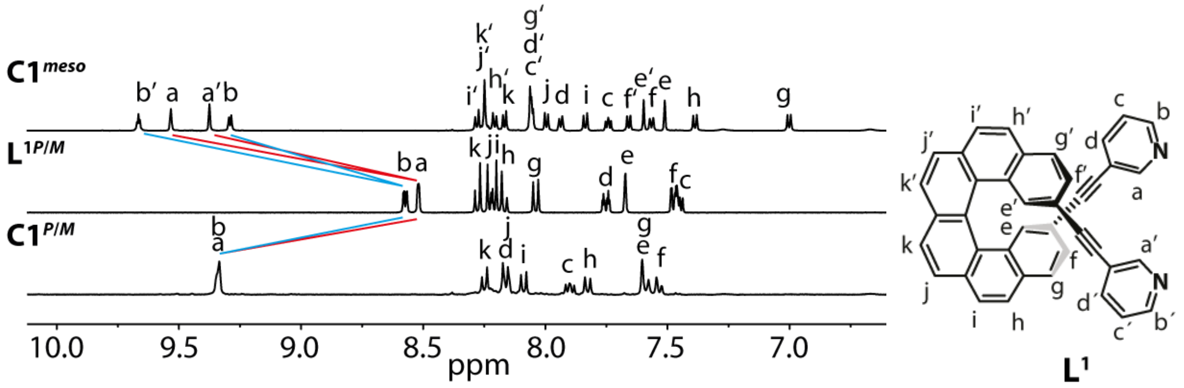

Figure 3.18 Stacked NMR spectra (DMSO-*d6*) for the cage formations with L^1.

High resolution ESI-MS spectra showed no peaks indicating an interpenetrated double cage, but showed instead the tetracationic $[Pd_2\mathbf{L^1}_4]^{4+}$, tricationic $[Pd_2\mathbf{L^1}_4+BF_4]^{3+}$ and dicationic $[Pd_2\mathbf{L^1}_4+2BF_4]^{2+}$ species which indicated the formation of a monomeric cage (**Figure 3.19**).

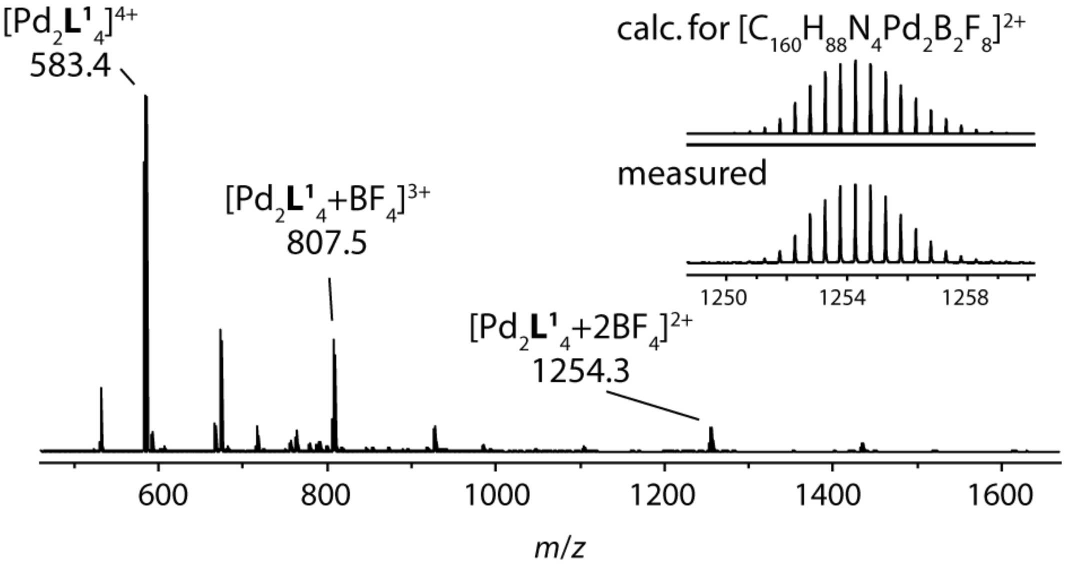

Figure 3.19 ESI mass of $C1^{meso}$.

To understand the occurrence of the splitting, 2D NMR techniques have been used and allowed the assignment of all signals. The COSY and NOESY spectra revealed that all ^{1}H NMR signals rise from one ligand, which has a different surrounding for the upper and lower half. The contact between the signals assigned to the proton H_k and $H_{k'}$ is the clear indication for the difference in the surrounding of both helicene halfs. The NOESY contacts between the signals assigned to H_b and $H_{b'}$ and between the signals assigned to H_a and $H_{a'}$ confirm the coordination to the Pd(II) metal, as the intramolecular distances in the ligands are too big and this contacts could not be found for the free ligand. These results indicate, that the upper and the lower half have to be close together.

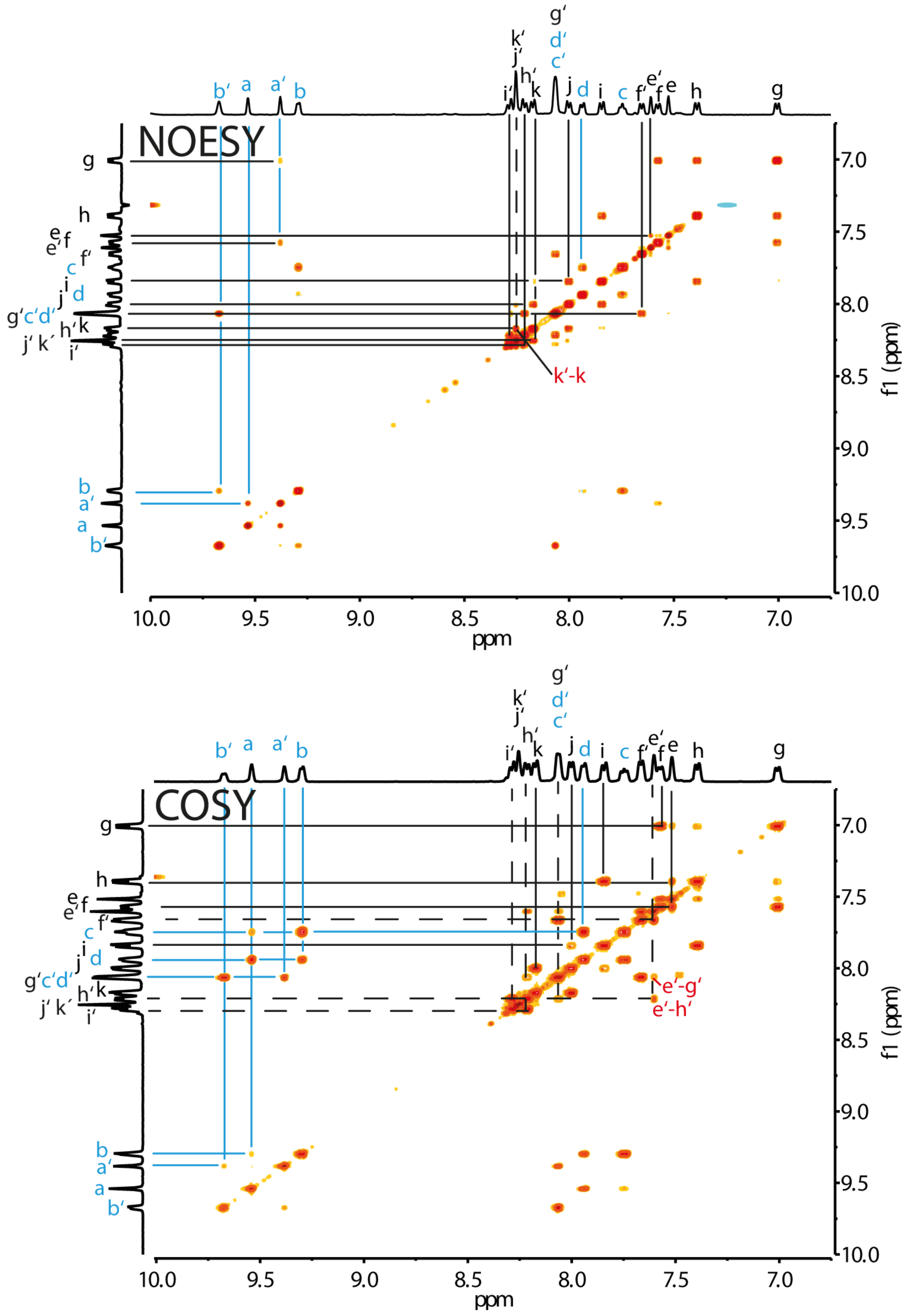

Figure 3.20 ^{1}H-^{1}H COSY and NOESY NMR spectra of C1^{meso} (600 MHz, DMSO-*d6*). The characteristic singlets of H_a and H_e as starting point allowed the assignment of all proton signals due to the COSY and NOESY contacts. The contact H_k – $H_{k'}$ in the NOESY spectra is the bridge between the split signal sets and indicates, that the upper and lower half of the helicene must have a different surrounding. In addition to this the contacts H_a–$H_{a'}$ and H_b–$H_{b'}$ show the low intermolecular distance, caused by the coordination to Pd, as the intramolecular distances are too long for this contacts.

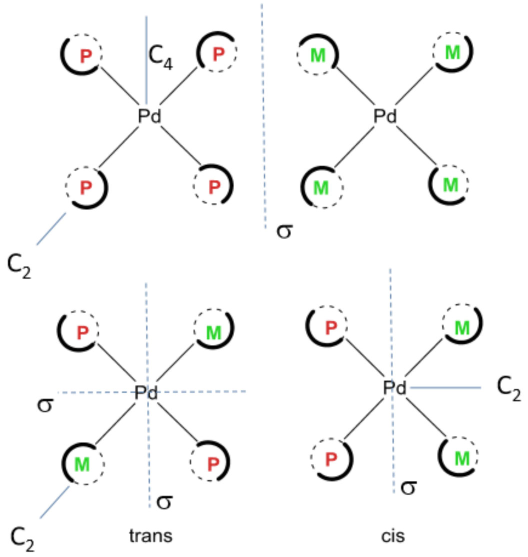

Figure 3.21 Simplified top view of the possible cage isomers to explain the splitting by symmetry operations. The *cis* coordination leading to the achiral meso cage is the only possible solution to explain the splitting into an upper and a lower half.

With the knowledge, that all signals rise from one ligand the symmetry operations have been investigated for all possible cage isomers. The simplified top view of the $Pd_2\mathbf{L^1}_4$ cage explains the splitting of the proton signals in the ^{1}H NMR for the $Pd_2\mathbf{L^1}_4$ cage via symmetry operations (**Figure 3.21**). The enantiopure cage (either 4 $\mathbf{L^{1\mathit{M}}}$ or 4 $\mathbf{L^{1\mathit{P}}}$) would not show a splitting, as the upper and lower half can be converted into each other via C_2 axes and all ligands can be converted into each other via the orthogonal C_4 axis. A *trans* coordination would not lead to splitting of the signals as the upper and lower half can be converted into each other via C_2 axes and the neighboring ligands can be converted into each other via mirror planes. The *cis* coordination explains the splitting into a set of two signals, as no symmetry operation allows to convert the upper to the lower half of the helicene. As a result, the *cis* coordination leading to the achiral meso cage is the only possible solution and shows an interesting example for the self-sorting and chiral discrimination of the ligands.

In agreement with the discussion above, the addition of $[Pd(CH_3CN)_4](BF_4)_2$ to the enantiopure ligand $\mathbf{L^1}$ did not lead to a splitting of the signals in the ^{1}H NMR, but only to a shifting upon coordination to the metal (**Figure 3.18**). The ESI-MS spectrum of the enantiopure cage $\mathbf{C1^{\mathit{P}}}$ is practically the same as the one for $\mathbf{C1^{\mathit{meso}}}$ with the tetracationic $[Pd_2\mathbf{L^1}_4]^{4+}$, tricationic $[Pd_2\mathbf{L^1}_4{+}BF_4]^{3+}$ and dicationic $[Pd_2\mathbf{L^1}_4{+}2BF_4]^{2+}$ species are present in the spectrum (**Figure 3.22**).

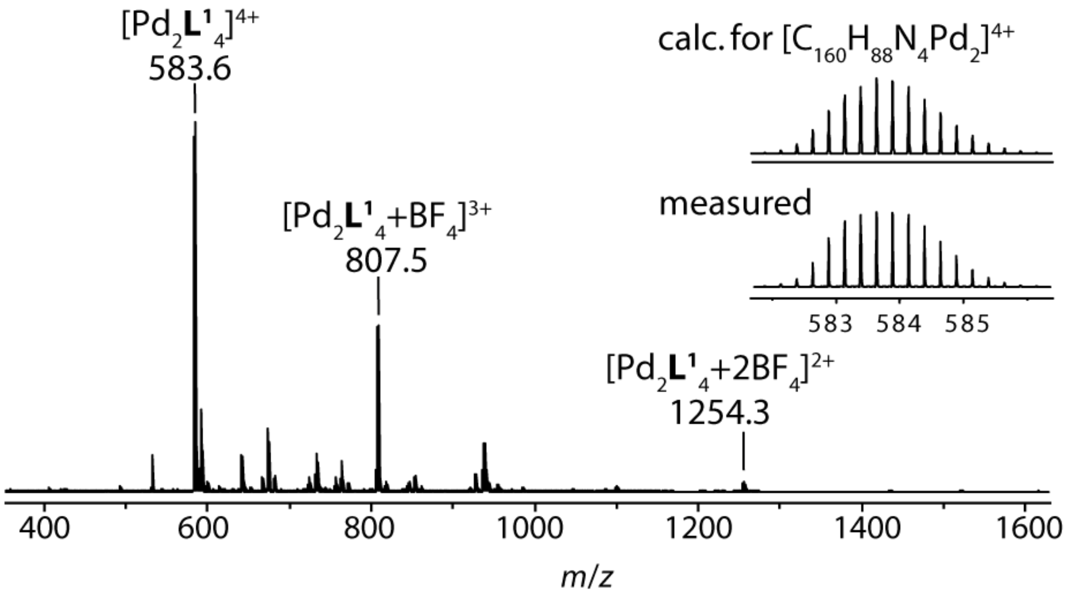

Figure 3.22 ESI mass spectrum of C1$^{P/M}$.

CD spectra have been recorded for both enantiomers of the ligands and the cages and allowed the determination of the absolute configuration by comparing with literature reported helicenes.[61] The recorded highly intense CD bands of the cage show a slight blueshift compared to the ligands. The intensity of the bands is higher for the cage compared to the ligand with maximal $\Delta\varepsilon_{371}$ of 796 cm^{-1} M^{-1} at 371 nm, but less intense per ligand than the free ligand which has a maximum $\Delta\varepsilon_{371}$ of 302 cm^{-1}M^{-1}. 100-fold dilution of the cage solutions resulted in the bands found for the free ligand, therefore the samples have been measured from undiluted ^{1}H NMR solutions (C = 0.6 mM) and very thin cuvettes with a path length of 0.1 mm, to measure the very intense bands without reaching the detector limit.

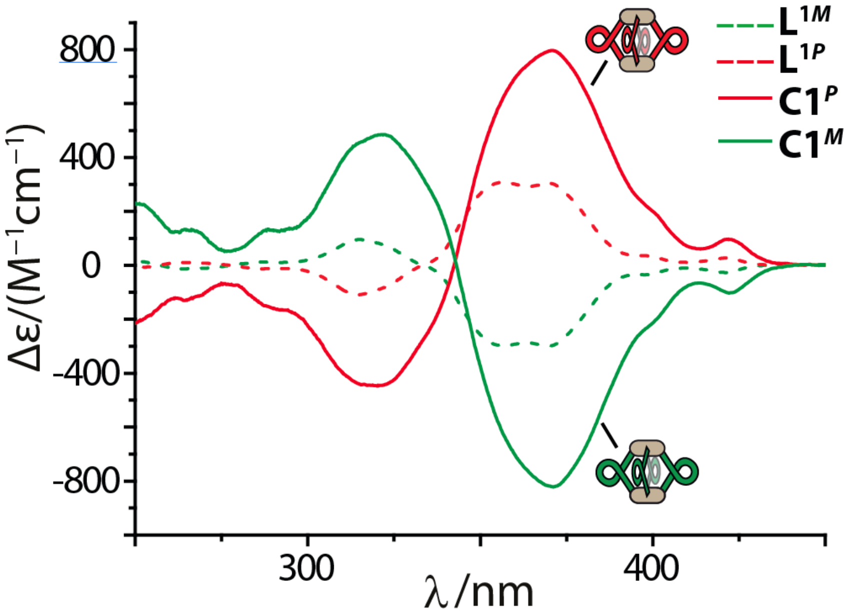

Figure 3.23 CD spectra of 1H NMR solutions of L^{1M}, L^{1P}, C1^{P}, C1^{M} in DMSO (0.6 mM). Cuvette path length 0.1 mm, wavelength: 250 nm – 500 nm, step size: 1 nm, band width: 0.5 nm.

3.3.2 Host-Guest Chemistry of C1

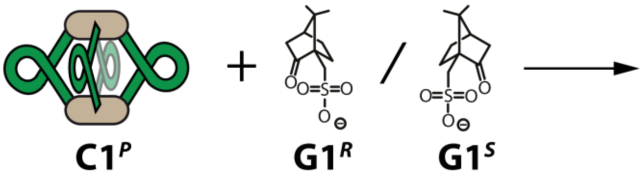

To investigate the ability of chiral discrimination of the enantiopure cages **C1**^{P} and **C1**^{M} titration experiments have been done with enantiopure camphor sulfonate anions **G1**^{R}. Representative ^{1}H NMR spectra of the titration are shown for the titration of **C1**^{P} with **G1**^{R} in (**Figure 3.24**).

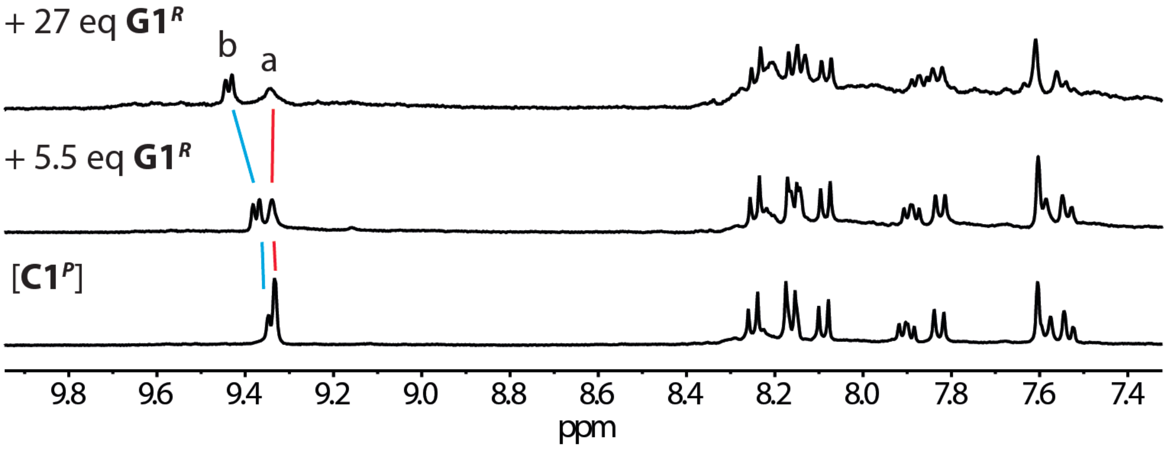

Figure 3.24 stacked ^{1}H NMR spectra (DMSO-*d6*) of the titration experiment with C1^{P}.

The signal assigned to proton H_a, which is pointing inside the cavity, does not show a significant shifting even with a large excess of the guest, which indicates, that the guest is not taken into the cavity of the host complex. In agreement with that interpretation, the only significant shifting can be observed for the signal assigned to the proton H_b, which is next to the nitrogen and therefore close to the metal, but outside of the cavity. The titration of **C1**^{P} with **G1**^{S} showed the same behavior and the $\delta\Delta$ plot, in which the starting point is the ppm signal assigned to the proton H_b before the addition of the guests, shows no difference between both guest enantiomers (**Figure 3.25**). The anionic guest is close to the cationic metal ions due to the coulomb force and causes the shift for the signal assigned to proton H_b, but as discussed before, only at the outside of the cavity without a chiral environment therefore the same behavior for both enantiomers is expected. Due to the fact, that **G1** is a small guest molecule and based on the results already too big for the cavity of **C1**, no other guests were investigated and instead modifications of the ligand have been investigated for a larger application area of the guest binding.

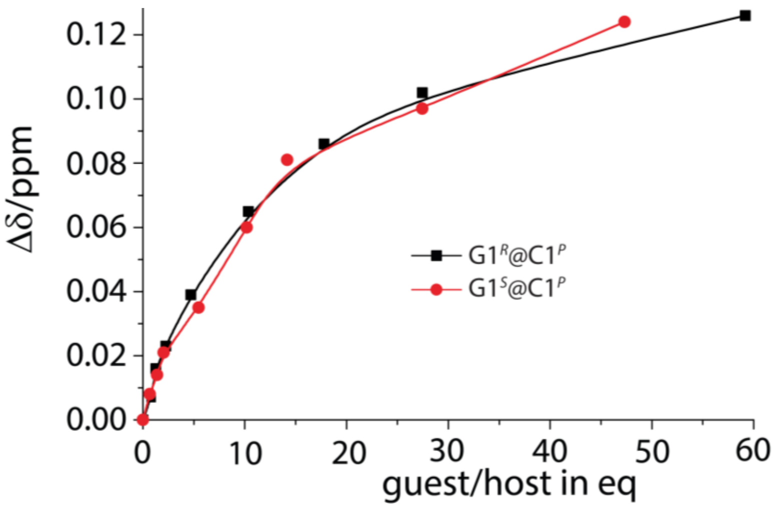

Figure 3.25 δΔ plot of the titration experiments with $C1^P$ and $G1^R/G1^S$.

3.3.3 Long helicene Cage C2

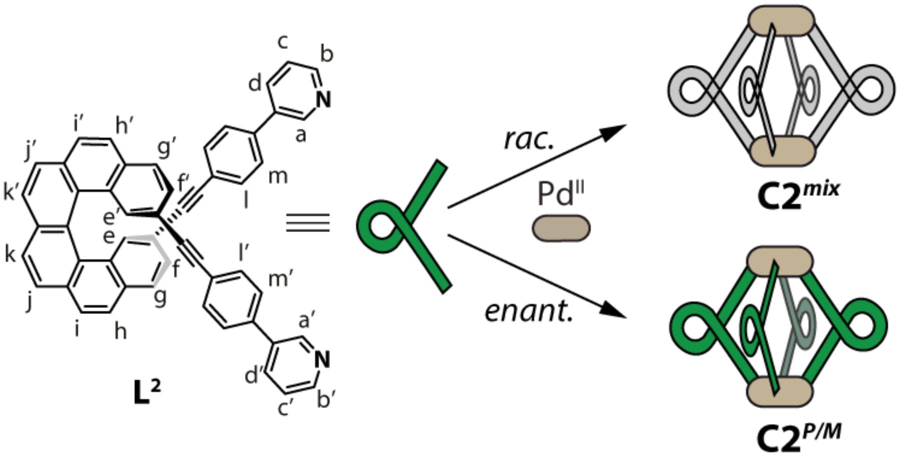

Figure 3.26 Simplified scheme of the cage formations with the ligand L^2.

As the guest uptake **C1** was not satisfactory and did not allow the chiral discrimination of camphor sulfonate ions, the ligand was modified and $\mathbf{L^2}$ consists of one additional phenyl group next to each alkyne. The modeled structures (PM6) show an increase of the Pd-Pd distance from 10.4 Å to 20.1 Å, which leads to a dramatic volume gain of the cavity of **C2** and allows the uptake of bigger guests compared to **C1** (**Figure 3.27**). The cage formation of **C2** was investigated under the same conditions as for **C1**. Interestingly the addition of $Pd(CH_3CN)_4BF_4$ to the racemic mixture of ligand $\mathbf{L^2}$ did not only result in splitting of the ^1H NMR signals into a set of two, but into an indeterminable high number (**Figure 3.28**) of signals. To understand the nature of the splitting, a high resolution ESI-MS spectra has been recorded and showed the tetracationic $[Pd_2\mathbf{L^2}_4]^{4+}$ species as the dominant species and the tricationic $[Pd_2\mathbf{L^2}_4+Cl]^{3+}$ as minor species, which indicates the formation of the $Pd_2\mathbf{L^2}_4$ cage motif (**Figure 3.29**).

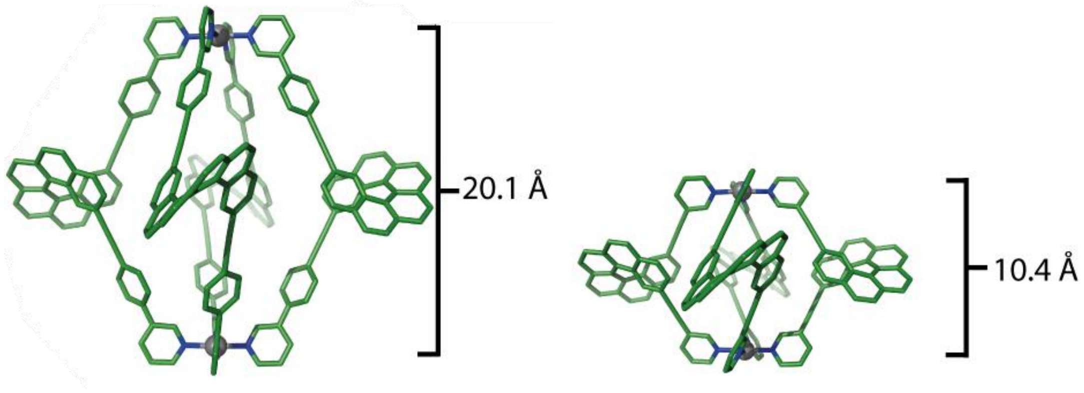

Figure 3.27 PM6 modelled structures of C1^{M} (left) and C2^{M} (right) which show the big difference in the Pd-Pd distance and cavity size.

A contamination of the MS spectrum with chloride has been reported before and chloride was not present in the ^{1}H NMR tube.[136] The splitting of the signals for **C2**$^{\mathrm{mix}}$ is high likely due to the fact, that **C2**$^{\mathrm{mix}}$ consists of a statistical mixture of all possible isomers [Pd**L**$^{2M}{}_{4}$] = [Pd**L**$^{2P}{}_{4}$] with a probability of 12.5 %, [Pd**L**$^{2M}{}_{3}$**L**^{2P}] = [Pd**L**^{2M}**L**$^{2P}{}_{3}$] with a probability of 50 %, *cis*-[Pd**L**$^{2M}{}_{2}$**L**$^{2P}{}_{2}$] with a probability of 25 % and *trans*-[Pd**L**$^{2M}{}_{2}$**L**$^{2P}{}_{2}$] with a probability of 12.5 % (Figure 5.26). Not only are this four different isomers leading to a different set of signals, but the *cis*- form is expected for a splitting into a set of two and [Pd**L**$^{2M}{}_{3}$**L**^{2P}]/ [Pd**L**^{2P}**L**$^{2M}{}_{3}$] are expected for a splitting into four sets of signals. Because of the high number of overlapping signals the assignment was not made for **C2**$^{\mathrm{mix}}$. The lack of chiral discrimination in contrast to the results for **C1**$^{\mathrm{meso}}$ can be explained with the much larger distance between the helicene backbones, which can be quantified in the shortest inter-ligand hydrogen distance found in modeled structures, which is increased from 2.4 Å for **C1** to 6.20 Å for **C2**. Further evidence for the statistical mixture of cage isomers can be found in the results for the cage formation with the enantiopure ligand:

The addition of $[\mathrm{Pd(CH_3CN)_4}](\mathrm{BF_4})_2$to the enantiopure mixtures of ligand **L**$^{\mathbf{2}}$ led to the formation of the chiral cages **C2**^{P} and **C2**^{M}. In the ^{1}H NMR spectra of the signals assigned to the protons H$_{a}$ and H$_{b}$ show the characteristic downfield shift with no signal splitting (**Figure 3.28**). All ^{1}H NMR signals of **C2**$^{P/\mathrm{M}}$ can be found in the spectra of **C2**^{mix}, but most of them are overlapped with the signals of other isomers due to the high number of signals with similar environment.

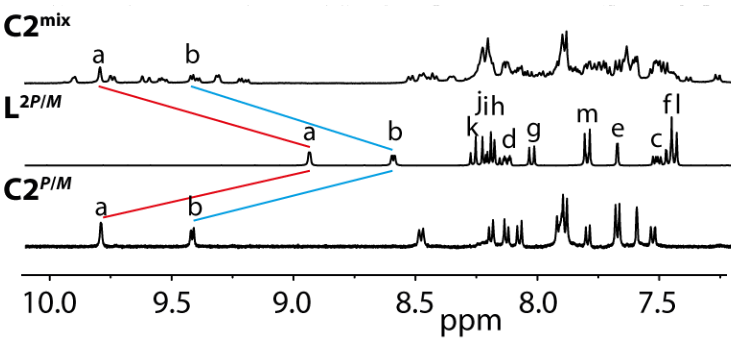

Figure 3.28 stacked ^{1}H NMR spectra (DMSO-*d6*) of C2^{mix}, L^{2} and enantiopure C2$^{P/M}$.

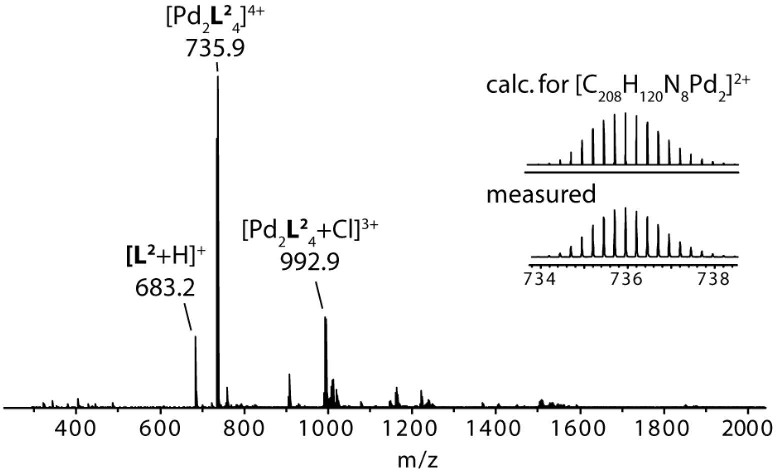

Figure 3.29 ESI-MS of the racemic mixture of L^{2} that leads to C2^{mix}.

The ESI-MS spectrum of the cage **C2**^{P} (**Figure 3.30**) is practically the same as the spectra found for **C2**^{mix} with the tetracationic [Pd_2**L**$^{2}_{4}$]$^{4+}$ as main species (**Figure 3.29**), as the isomers.

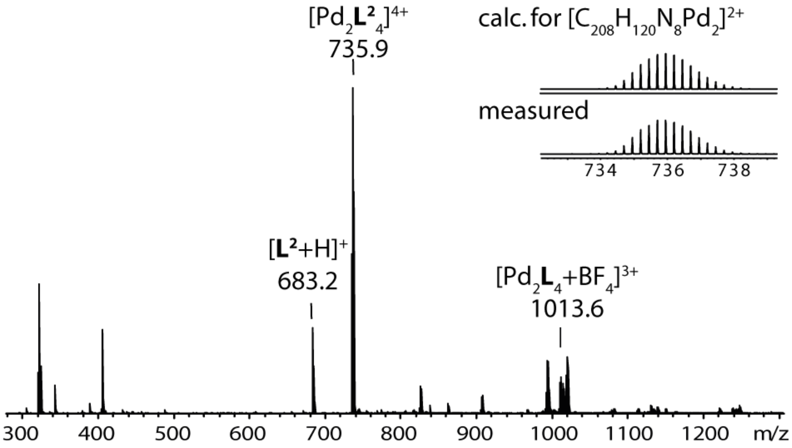

Figure 3.30 ESI-MS of C2$^{P/M}$.

3.3.4 Host Guest Chemistry of C2$^{P/M}$

The proof of the successful cage formation for **C2** allowed the procedure of chiral discrimination experiments. A solution of *S*-camphor sulfonate anion **G1**^{S} has been added in several steps to a solution of **C2**^{P} and the ratios have been determined via the integrals of the ^{1}H NMR spectra (**Figure 3.31**). In contrast to the titration experiments with **C1**^{P}, the signal assigned to the proton inside the cavity shows a significant downfield shift upon addition of the guest, which is clear evidence for the uptake into the cavity, where the signal assigned to proton H_b shows a negligible shift.

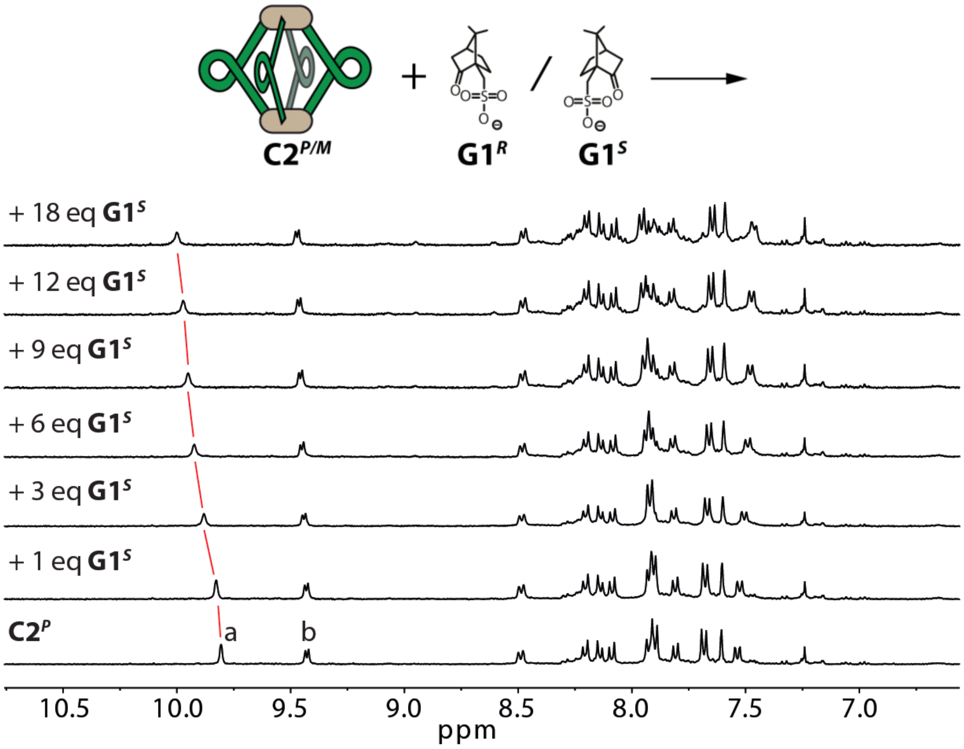

Figure 3.31 stacked ^{1}H NMR spectra (DMSO-*d6*) of the titration experiment with C2^{P}.

The titration has been repeated for all combinations and are summed up in a δΔ plot (**Figure 3.32**). The δΔ plot shows clearly, that the combination **G1**^{S}**@C2**^{P} has a different signal shifting than the combination **G1**^{R}**@C2**^{P}. The chiral discrimination is confirmed by the results of the opposite pair of enantiomers, which show the exact opposite behavior in the δΔ plot. The binding constants have been calculated with a value of 560 M^{-1} for **G1**^{S}**@C2**^{P} and **G1**^{R}**@C2**^{M}, where the oppositve pair of enantiomers has a binding constant of 1010 M^{-1} for **G1**^{R}**@C2**^{P} and **G1**^{S}**@C2**^{M}.This result is fundamental as it shows the proof of concept for chiral discrimination of guests for this new class of cages.

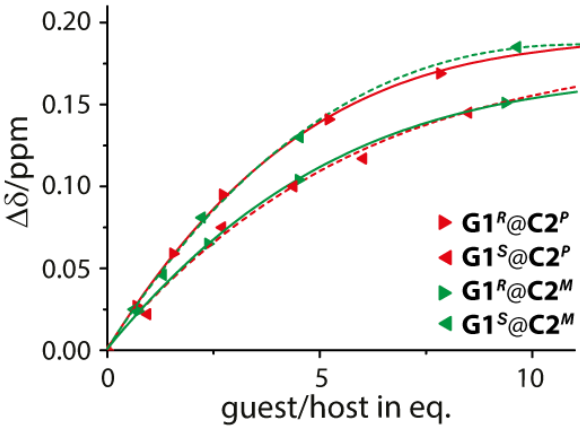

Figure 3.32 **δΔ plot for $G1^S$@$C2^P$, $G1^S$@$C2^M$, $G1^R$@$C2^P$ and $G1^R$@$C2^P$.**

CD spectra have been recorded for **C2**^{P}, **C2**^{M}, **L**^{2M} and **L**^{2P} in DMSO (**Figure 3.33 a**). **L**^{2P} shows a positive cotton effect with a maximum of 490 $M^{-1}cm^{-1}$ at 375 nm and a further strong band at 319 nm. **C2**^{P} shows a positive cotton effect with a maximum of 1050 $M^{-1}cm^{-1}$ at 374 nm and further strong band at 596 nm. The spectra of the other fractions of the HPLC show the exact opposite trend and confirm the separation of the enantiomers. The assignment of the enantiomers was based on literature reported CD spectra for helicenes and the absolute structure determinations of the X-ray structures. Similar to the results for **C1**, the CD bands of the cage **C2**$^{P/M}$ are less intense than the quadruple of the bands for the ligands itself. A reason for the weaker CD bands per ligand in the cage could be a weaker pitch in the helicene backbone upon coordination to the metal, as the pitch is related to the intensity of the bands.[120]

Additional insights into that question came with further host guest experiments, in which the strong circular dichroism of the helicenes was used for the discrimination of nonchiral guests, and investigations for an induced circular dichroism to transfer chiral information into an achiral guest.

The binding of 2,7-naphtalene disulfonate **G2** and 4,4’-biphenyl disulfonate **G3** into the cavity and their effect on the CD spectra and size of the cage has been investigated (**Figure 3.33 b**). **G2** and **G3** have been choosen for their different distance between the sulfonate groups with otherwise similar structure and a little but existent difference in the molecular weight. The small difference in weight is important for a distinguishing of the guests for a co-injection experiment in the trapped ion mobility mass spectrum and a big difference could have an influence on the results. The structural similarity between **G2** and **G3** is important to differ the influence on the cage only in size and avoid other interactions, that could occur with different guests. The binding of both guests has been verified by the shift of the signals in the ^{1}H NMR spectra, that are assigned to the proton H_a, which is pointing inside the cavity.

CD spectra have been recorded for **G2@C2**^{P} and **G3@C2**^{P} and subtracted by the CD spectra of **C2**^{P} to yield difference CD spectra (**Figure 3.33**). Keeping in mind, that the guests themself are not chiral, the differences in the spectra must have their origin in the change of the pitch of the helicene backbone or an induced chirality to the guest. Interestingly, encapsulation of the short guest **G2** leads to a strong decrease of the CD bands around 360 nm, where in contrast the long guest **G3** shows an opposite effect and causes an increase of the same CD band.

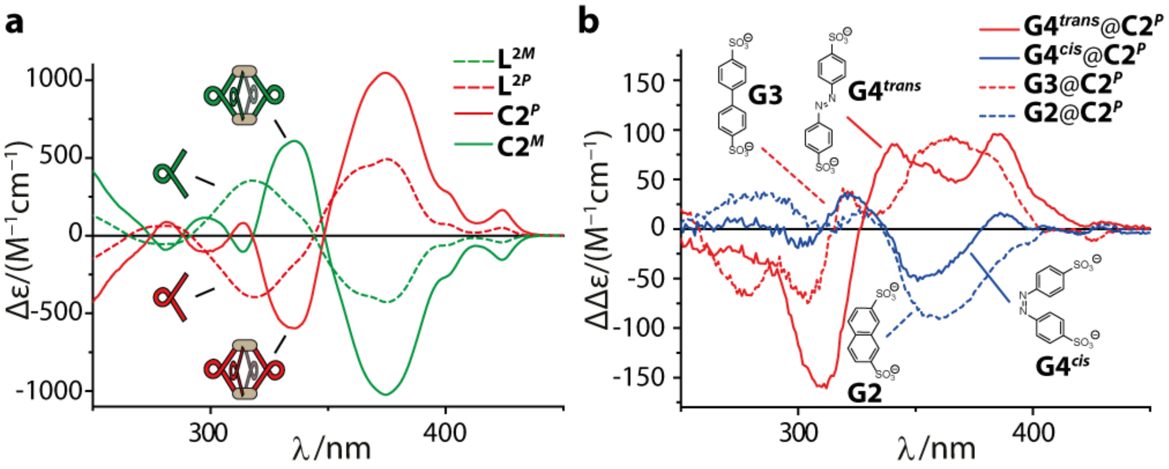

Figure 3.33 CD spectra of the L^2 and C2 enantiomers in DMSO and ΔCD spectra of C2^P after addition of guests.

To extend the scope and verify the result, CD spectra have also been recorded with a photoswitchable guest in its *cis* and in its *trans* form **G4**^{cis} and **G4**^{trans}. **G4**^{cis} and **G4**^{trans} are not chiral and show no circular dichroism (**Figure 3.33**). The switching of the guests has been controlled via ^{1}H NMR spectra before the additions to the host. The CD spectra after addition show the same size dependend trend as for **G2** and **G3**. The difference CD spectra are more complicated and could in parts show also an induced CD to guest, as **G4** shows a significant absorbance around 360 nm.

Due to the highly rigid conformation of guest **G2**, where an induced CD effect should be impossible, the influence of the helical pitch is assumed to be the only reason for the change of the CD spectra with **G2**. DFT calculations have been performed for the ligand **L**^{2P} to proof the assumption and the results are in agreement with the CD spectra, as they show an increased CD with increased pitch (**Figure 3.34**).

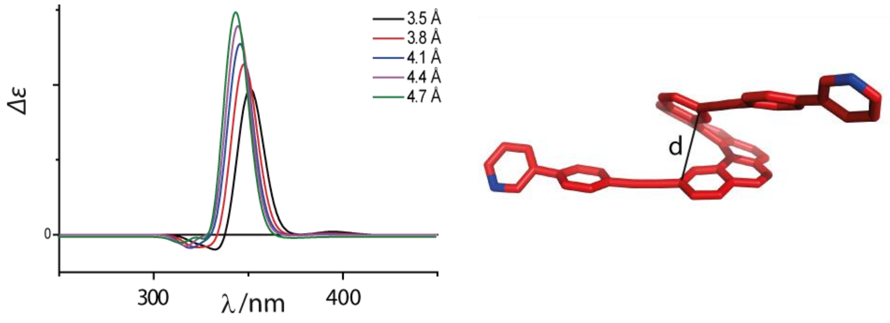

Figure 3.34. Calculated CD spectra for [6]helicene based on different C-C distances between position 2 and 15 showing the correlation of the circular dichroism with the distance d, that is correlating with the pitch.

Further evidence came from trapped ion mobility mass spectrometry[137] measurements. The measurements shows a lower mobility for **G2@C2**^{P} than for **G3@C2**^{P}, which indicates a higher collisional cross section for **G3@C2^P** and supports therefore an increased size for the cage after uptake of the longer guest (**Figure 3.35 a**). The uptake of the guests can be clearly seen with the dicationic species [**G3**@Pd$_2$**L^2**$_4$]$^{2+}$ and [**G2**@Pd$_2$**L^2**$_4$]$^{2+}$ as the dominant species (**Figure 3.35 b+c**).

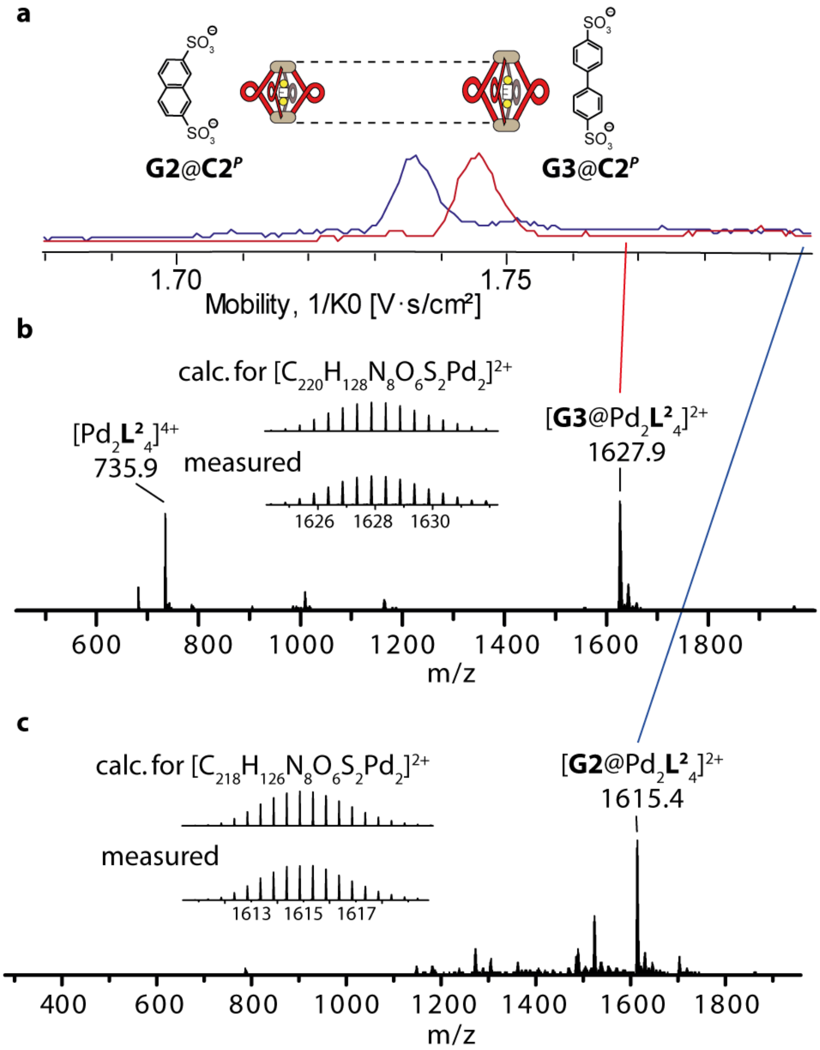

Figure 3.35 Trapped ion mobility mass spectrometry results that show the different size of cage C2 depending on the guest.

3.3.5 Formation of the chiral interpenetrated double cage DCM2

DMSO was the standard solvent for the experiments for comparable results with **C1** and the much better solubility of the ligand and the cage. Enantiopure cages could also be formed in CD_3CN with **L^1** and **L^2**. Heating of a **C2** sample in CD_3CN showed the slow rise of a new set of down and upfield shifted signals (**Figure 3.36**). Long heating of up to two weeks allowed the nearly quantitative transformation. All signals could be assigned with 2D NMR techniques and indicated the formation of an interpenetrated double cage, where two cages are linked to each other in a catenane fashion.[135]

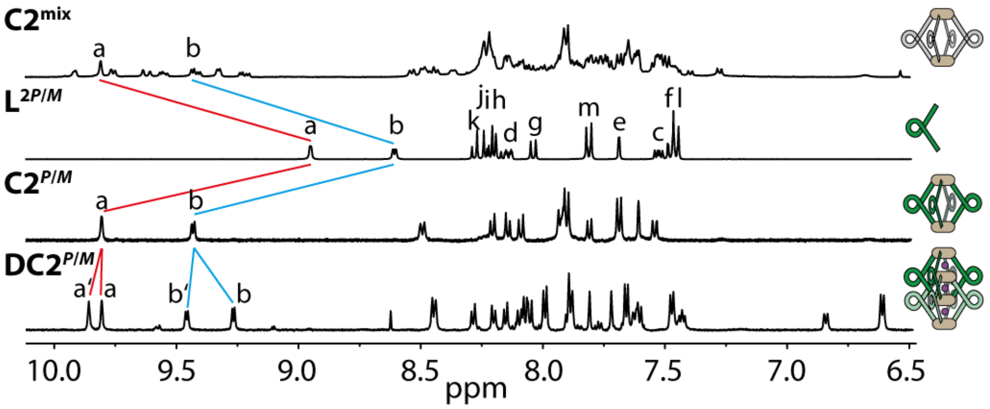

Figure 3.36 stacked ^{1}H NMR spectra of C2^{mix}, L^2, enantiopure C2$^{P/M}$ in DMSO and the double cage formed in CD_3CN.

High resolution ESI-MS showed $[Pd_4\mathbf{L}^{2P}_8{+}3BF_4]^{5+}$ as the main species (**Figure 3.37**). The uptake of three BF_4^- into the three pockets of the double cage has been reported for achiral double cages.[135]

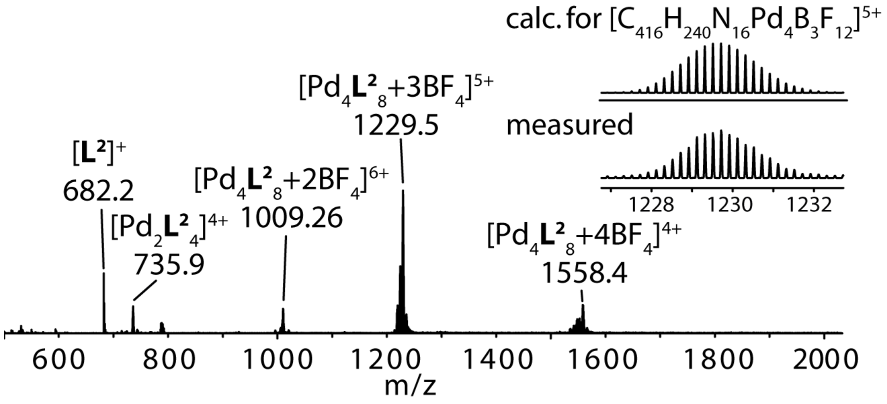

Figure 3.37 ESI-MS spectra of the double cage DC2^M.

Crystals suitable for X-ray structure determination have been grown of $[2PF_6@Pd_4\mathbf{L}^{2M}_8]$ = **DC2^M** from a monomeric cage solution at 7 °C in CD_3CN with PF_6^- as counter ion (**Figure 3.38**). Interestingly, the double cage formation could not be shown for PF_6^- in solution, even after long heating of the samples, but the X-ray structure fits perfectly to the NMR and ESI-MS results found for BF_4^- as counterion. The structure was solved in the chiral space group I222 with the point group D_2. The first fraction of the chiral HPLC separation of the ligand **L^2** was used for the cage formation and the absolute configuration of the assembly was undeniably determined with the method of Parsons,[96] as implemented in SHELXL,[134] yielding an enantiopure distinguishing parameter of $x = -0.02(2)$. Two PF_6^- ions are present in the outer cavities of the double cage. The Pd–Pd distance between the two outer Pd^{2+} ions is 27.640 Å, the Pd–Pd distance of the monomeric cage units is 18.984 Å which is close to the proposed 20.1 Å of the modeled **C2** cage.

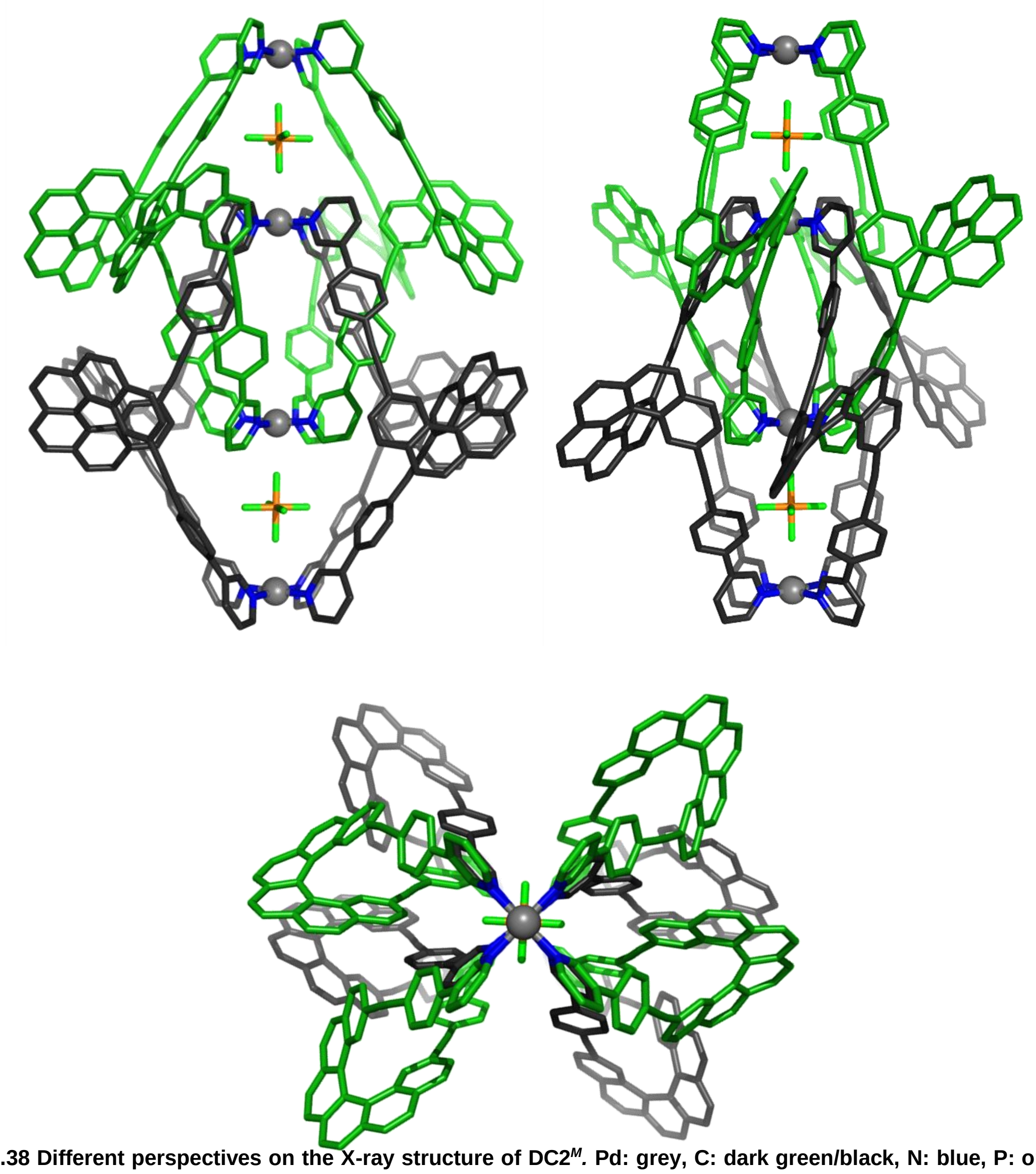

Figure 3.38 Different perspectives on the X-ray structure of DC2^{M}. Pd: grey, C: dark green/black, N: blue, P: orange, F: light green.

3.4 Conclusion

A new family of [Pd$_2$**L**$_4$] and [Pd$_4$**L**$_8$] coordination cages has been developed. The developed cages are chiral as result of the used helicene backbone. With the racemic mixture of the short version of the ligand a narcistic self-sorting was observed leading to an achiral *meso* cage. Due to the limited space in the cavity of the enantiopure cages with the short ligand, no chiral discrimination of guests could be shown. In contrast, the elongated ligand increased the cavity and the cages showed chiral discrimination of guests, which shows the potential as sensor of the chiral environment provided by the cage and could allow stereoselective catalysis in the future. The intense circular dichroism of helicenes and their size and pitch depending absorption allowed to monitor the uptake of guests with different size. A big variety of interpenetrated double cages has been reported,[138] but best to our knowledge, the helicene based double cage is the first chiral one.

4 CHIRAL STRUCTURES BASED ON NATURAL PRODUCT INSPIRED LIGANDS

4.1 Introduction

Following the “hard” approach of supramolecular assemblies (chapter 1.2),[33] chiral ligands containing pyridines for the coordination to a metal center based on two different backbones have been synthesized in cooperation with Prof. Haberhauer, Prof. Waldmann and Dr. Antonchick. Synthesis of the chiral backbones was reported before and they were modified to contain pyridine units that allow coordination to Pd(II) metal ions.[139–141]

The backbone synthesized by Prof. Haberhauer *et al.* and structural related compounds are pseudo-peptides inspired by marine metabolites that are studied for their pharmaceutical potential and their Cu(II) coordination chemistry.[142] They can be used for a variety of applications, like the chiral inductions of guest, enantiomeric recognition of primary ammonium salts or the catalyzed hydration of CO_2.[141,142] The combination of several backbones in a supramolecular assembly could give rise to new applications or enhanced properties in the host guest interaction.

The backbone synthesized by Prof. Waldmann, Dr. Antonchick *et al*. in a cascade reaction contains eight stereocenters with a 5,5,5-tricyclic scaffold.[139,143] This scaffold has been found in more than 160 natural products of which some are depicted in **Figure 4.1**.

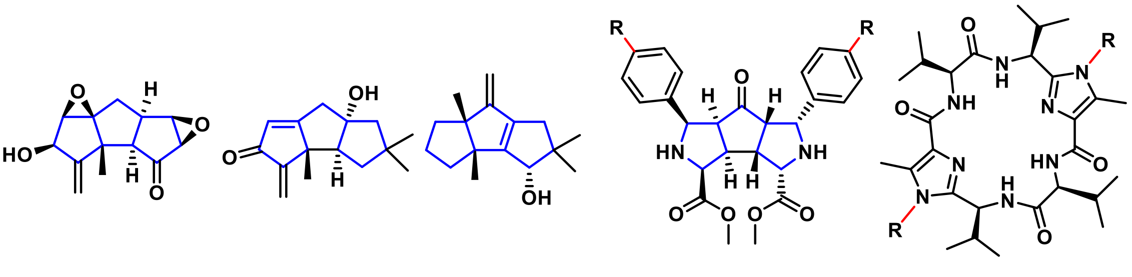

creolophin D **chondrosterin A** **cucumin H** **5,5,5-tricyclic backbone** **pseudo-peptide backbone**

Figure 4.1 Three natural compounds containing a 5,5,5-tricyclic scaffold (left) and the two nature inspired backbones used for the supramolecular assemblies in this work (right).

4.2 Assemblies with L^{H1} and L^{H2}

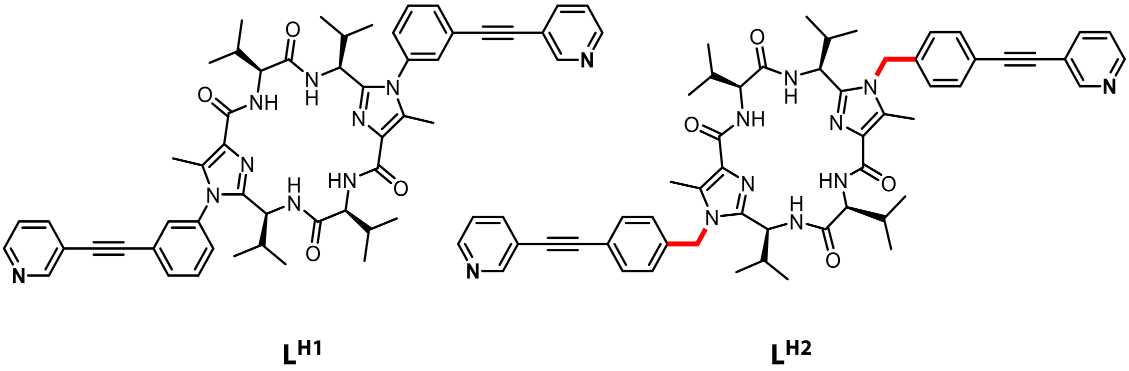

Figure 4.2 Structure of L^{H1} and L^{H2}.

Prof. Haberhauer *et al.* provided two modifications containing pyridine units which differed only in the existence of two additional CH_2 groups linked to thy cyclic core giving **L^{H2}** a higher conformational flexibility compared to **L^{H1}** (**Figure 4.2**). The ^{1}H NMR spectrum of 4 eq. **L^{H1}** in CD_3CN after the addition of 2 eq. $[Pd(CH_3CN)_4](BF_4)_2$ show vanishing of the signals (**Figure 4.3**), but a formation of precipitate was not observed. Replacement of CD_3CN with DMSO as the solvent did not lead to a significant improvement and therefore this ligand was not further investigated upon the formation of supramolecular assemblies.

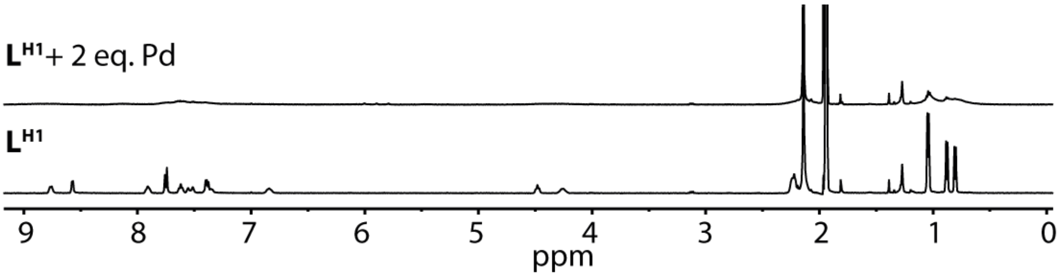

Figure 4.3 ^{1}H NMR spectra of L^{H1} in CD_3CN before and after the addition of 2 eq. $Pd(CH_3CN)_4(BF_4)_2$.

In contrast for the results with **L^{H1}**, under the same conditions, the addition of 2 eq. Pd(II) to 4 eq. **L^{H2}** in CD_3CN led to shifting of the proton signals in the ^{1}H NMR spectrum without vanishing signals (**Figure 4.4 d**). The signals observed in the ESI-MS spectrum of the assembly $[Pd_2\mathbf{L^{H2}}_4]$ are in excellent agreement with the calculated mass for the ion $[BF_4@Pd_2\mathbf{L^{H2}}_4]^{3+}$, which was found as the main species. Switching to DMSO as solvent showed as well a shifting of the signals. Based on the results the formation of a cage was assumed, but the reproduction of the NMR spectrum was not possible in CD_3CN and resulted in a spectrum with multiple splitting of the signals (**Figure 4.4 e**). Also heating of samples and different counter ions like PF_6^- and SbF_6^- did not allow the reproduction of the first experiments in CD_3CN (**Figure 4.4 e-i**). Even the ligand NMR spectrum differed in CD_3CN (**Figure 4.4 a,b,c**), but the reason is still unclear and needs further investigations. The long time period between the measurements, a contamination and different batches of the ligand could be a reason.

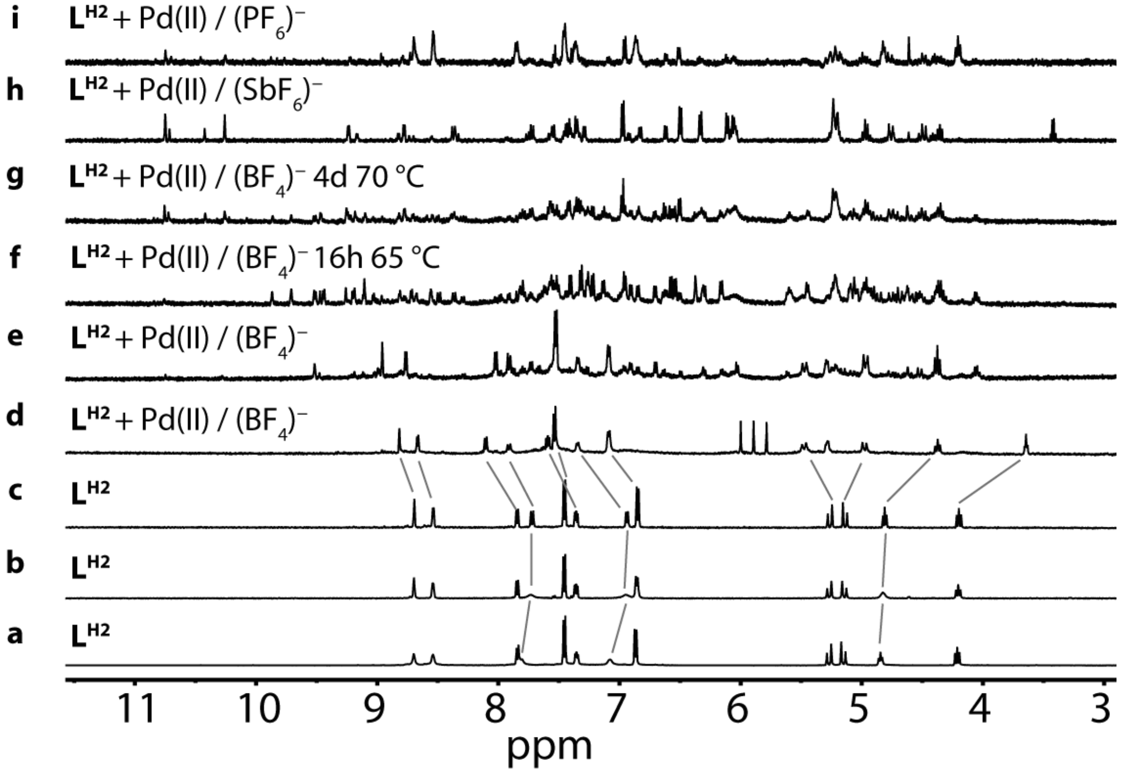

Figure 4.4 ^1H NMR spectra in CD_3CN: a-c: L^{H2} which spectra differed for unknown reasons; d: the first attempt showed only a shifting of the signals; e-g: attempts to reproduce the spectrum of d resulted in very different spectra every time; i-h: change to different counterions led also to multiple splitted signals with a strong shift.

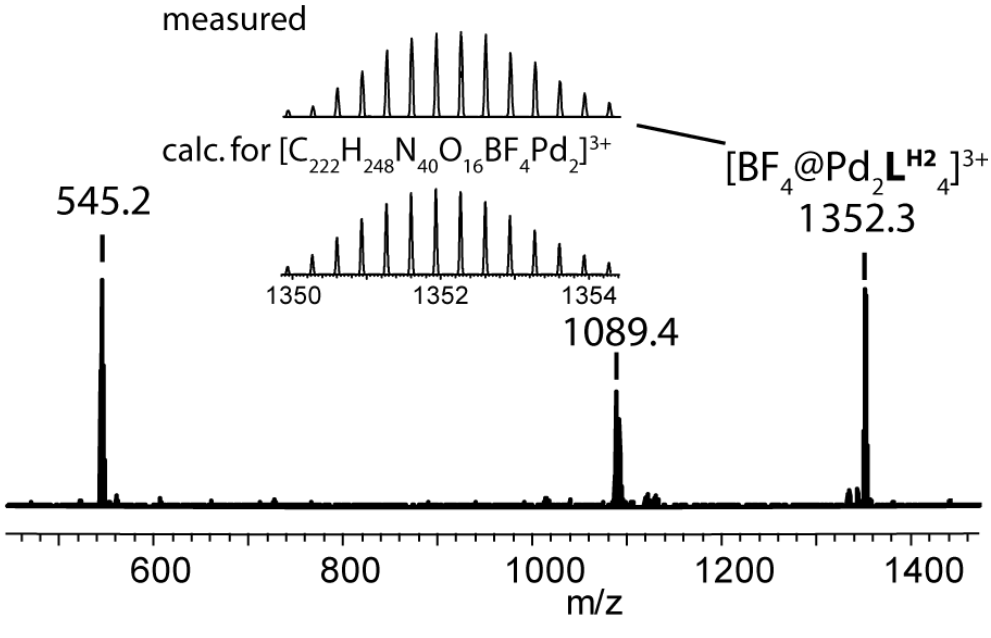

Figure 4.5 ESI-MS of $[Pd_2L^{H2}_4](BF_4)_4$ showing $[BF_4@Pd_2L^{H2}_4]^{3+}$ as the main species.

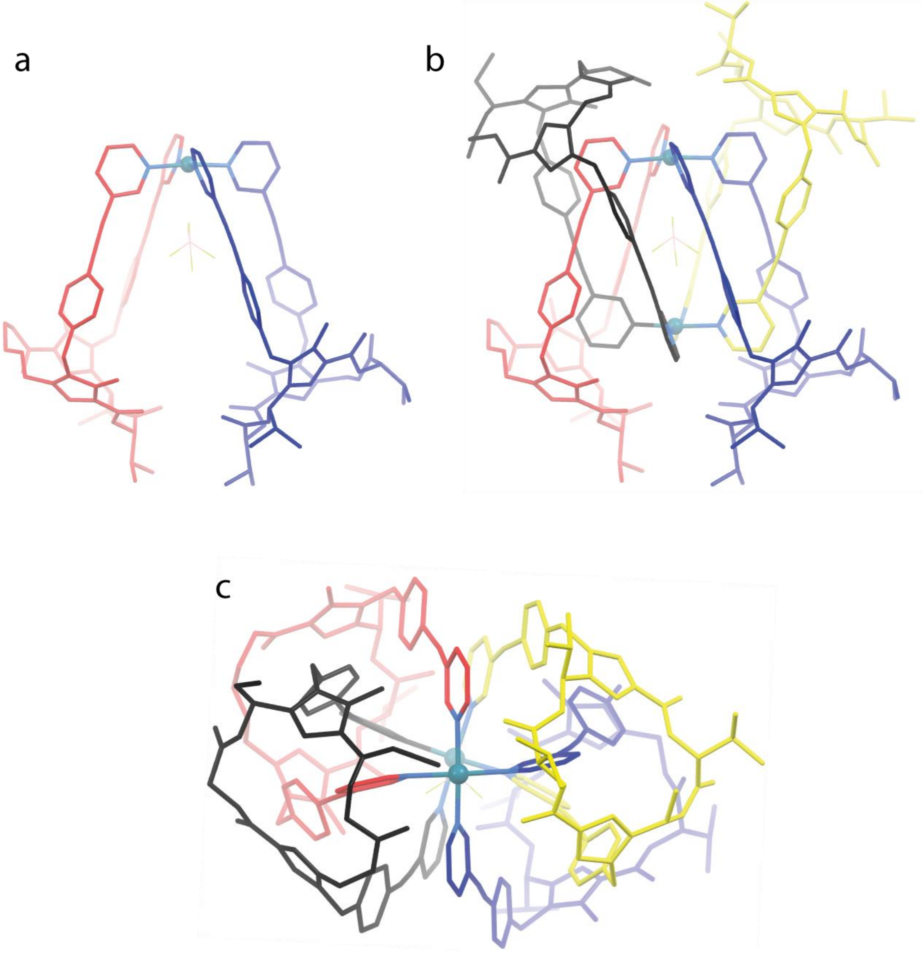

Figure 4.6 Preliminary X-ray structure of $[BF_4@Pd_2L^{H2}_4]^{3+}$, that consists of two $[PdL^{H2}_2]$ units (a) that are interlocked into each other (b and c). Each ligand in separate color for better clearance of the structural motive.

Crystals suitable for a preliminary X-ray structure determination could be grown by slow diffusion of Et_2O into a mixture of $\mathbf{L}^{\mathbf{H2}}$ with 0.5 eq. $Pd(CH_3CN)_4(BF_4)_2$ in acetonitrile containing the structure of a catenane with two $[Pd_2\mathbf{L}^{\mathbf{H2}}_2]^{3+}$ (**Figure 4.6 b,c**). One BF_4^- ion is present in the cavity between the two Pd(II) metal ions. The Pd-Pd distance is around 8.1 Å and the assembly crystallized in the space group $P2_1$ and the point group C_2. One of each pyridine groups of each ligands is centered under the ring of another ligand, where-as the second pyridine group is positioned between two rings of two ligands. The symmetry reduction should lead to splitting in the ^{1}H NMR spectrum, therefore the ^{1}H spectrum that showed only a shifting of the ligand signals after addition of Pd(II) is not corresponding to the X-ray structure. With the actual data it is not possible to assign a ^{1}H spectrum to the found X-ray structure and more experiments need to be done. The ESI-MS spectrum is in agreement with the X-ray structure (**Figure 4.5**) but further experiments need to be done, as isomers like a $[Pd_2\mathbf{L}^{\mathbf{H2}}_4]^{4+}$ cage structure would lead to the same ESI-MS spectrum. The results, especially the X-ray structure determination, highlight the potential of the ligand for the formation of very interesting supramolecular assemblies and should be of further investigation.

4.3 5,5,5-Tricyclic backbone for assemblies

4.3.1 L^{W1}

In principle, the backbone provided by Waldmann *et al*. could be modified via cross coupling reactions to a variety of ligands. Due to the small amount of the backbone, only two modifications have been synthesized. $\mathbf{L}^{W1}$ was synthesized via a Sonogashira cross coupling reaction with the meta substituted 3-ethynylpyridine. The addition of 0.5 eq. $Pd(CH_3CN)_4(BF_4)_2$ in CD_3CN led to the formation of a *trans* or *cis* coordinated complex $Pd\mathbf{L}^{W1}{}_2$(**Figure 4.7**).

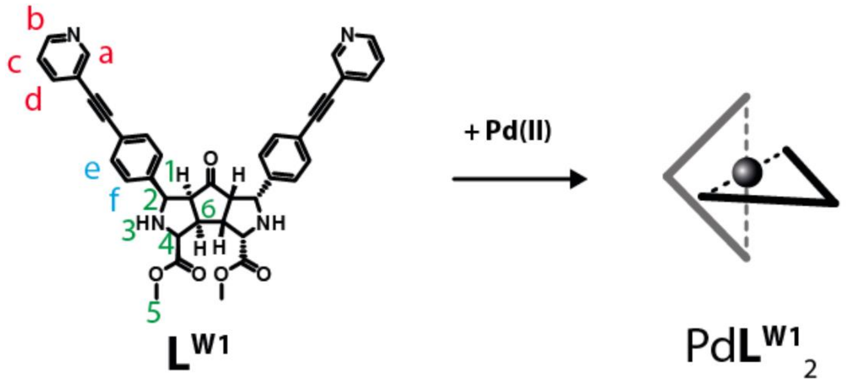

Figure 4.7 Structure of L^{W1} and the formed complex $PdL^{W1}{}_2$.

In the ^{1}H NMR spectrum most signals are downfield shifted upon coordination to the metal and all signals could be assigned using 2D NMR techniques (**Figure 4.8**). No splitting of the signals was observed. The signals observed in the ESI-MS spectra are in perfect agreement with the calculated signals for the formation of a $[Pd_1\mathbf{L}^{W1}{}_2]^{2+}$ complex. Only a minor signal indicates the formation of cage $[Pd_2\mathbf{L}^{W1}{}_4]^{3+}$. The flexibility of the ligand allows two possible coordination motifs, comparable to the results found for $[Pt\mathbf{L}^{CN}{}_2]$ (chapters 2.4.2 and 2.4.4).

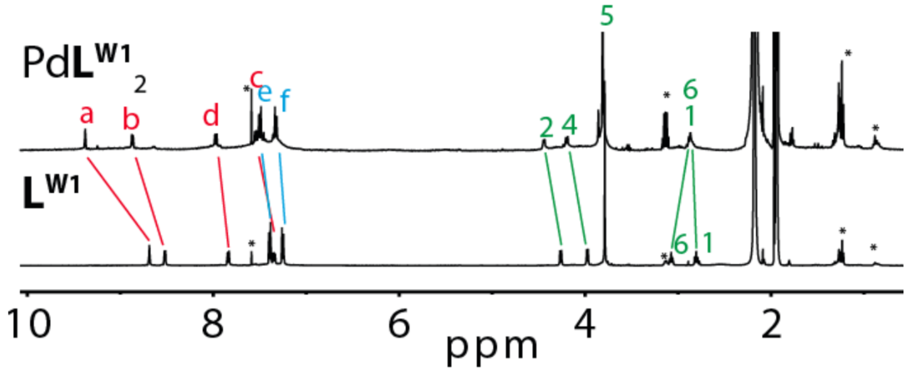

Figure 4.8 ^{1}H NMR spectra (CD_3CN) of the ligand and after addition of 0.5 eq. Pd(II) leading to the formation of a PdL_2 species.

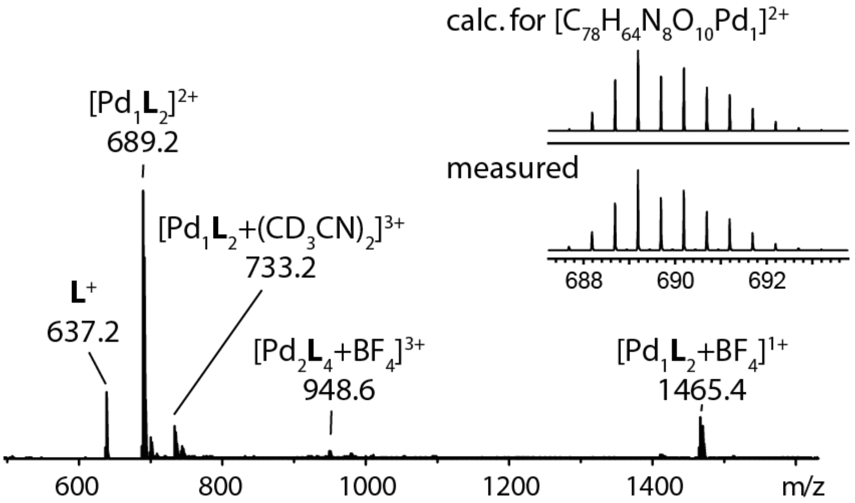

Figure 4.9 ESI-MS spectrum of $[PdL^{W1}_2]^{2+}$ as the main species (left).

The modeled structures (PM6) for the *cis*- and the *trans*- coordinated structures are depicted (**Figure 4.10**), but with the actual data none of the isomers can be excluded and further experiments should be performed for an undoubted determination of the structure.

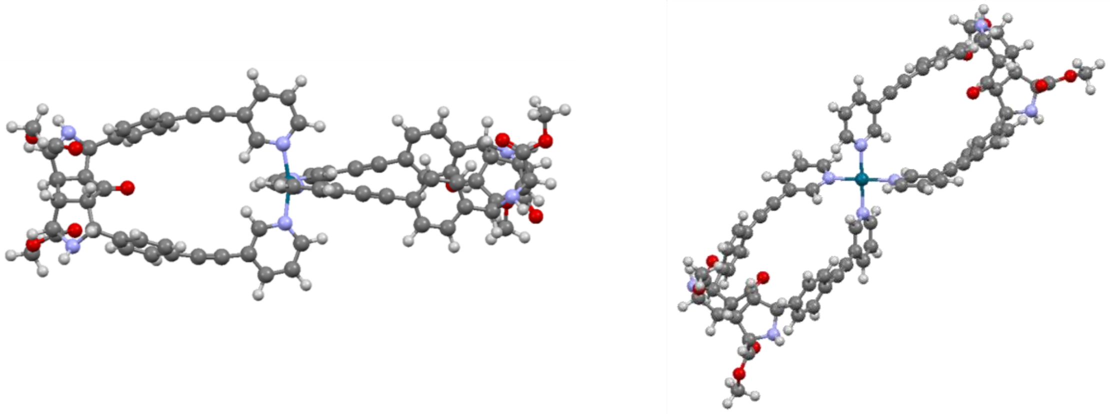

Figure 4.10 PM6 models of the two possible isomers for $[PdL^{W1}_2]^{2+}$. Left: the *trans* coordinated complex right: the *cis* coordinated complex.

As the modelled structures showed, a prolonging of the ligand would only prolong the ligand but most likely not lead to another coordination motif. Consequently, a *para* substituted pyridine was synthesized and investigated for the formation of supramolecular assemblies, as the formation of a PdL_2 complex should be impossible.

4.3.2 L^{W2}

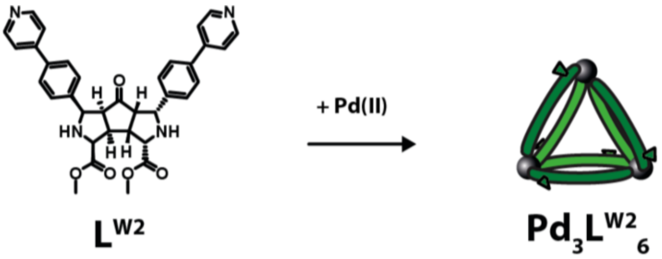

Figure 4.11 Structure of the ligand L^{W2} and the presumable structure of the assembly [Pd$_3$L^{W2}$_6$].

^{1}H NMR spectra have been recorded in CD_3CN and DMSO before and after the addition of 2 eq. $Pd(CH_3CN)_4(BF_4)_2$ to 4 eq. **L**^{W2} and caused a splitting of the signals into a set of two in both solvents (**Figure 4.12**).

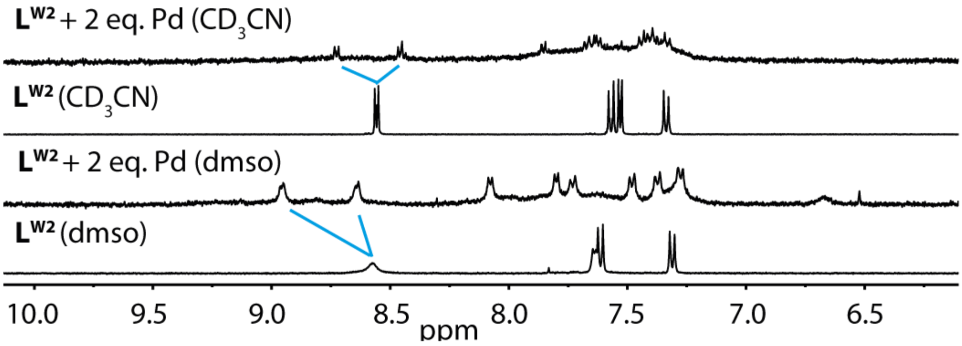

Figure 4.12 The ^{1}H spectra of the ligand in CD_3CN and DMSO before and after the addition of 2 eq Pd(II) in DMSO and CD_3CN, that results in a splitting of the signals due to the formation of the Pd_3L_6 assembly.

The signals observed in the ESI-MS spectrum reveal [Pd$_3$**L**^{W2}$_6$] as the main species[144] with different numbers of BF_4^- anions as counter ions in form of [Pd$_3$**L**^{W2}$_6$]$^{6+}$, [BF$_4$@Pd$_3$**L**^{W2}$_6$]$^{5+}$, [2BF$_4$Pd$_3$**L**^{W2}$_6$]$^{4+}$ and [3BF$_4$@Pd$_3$**L**^{W2}$_6$]$^{3+}$ (**Figure 4.13**). Only one weak signal could be assigned to $[BF_4@Pd_2L_4]^{3+}$ which is probably the result of a fragmentation of the [Pd$_3$**L**^{W2}$_6$] assembly.

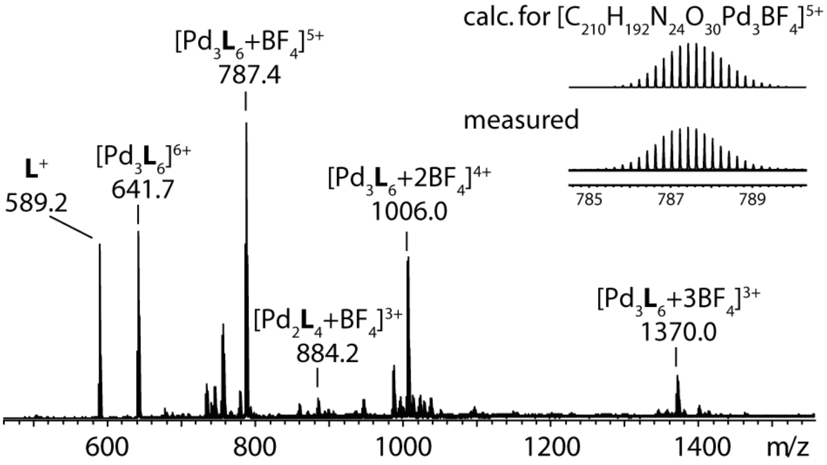

Figure 4.13 ESI-MS spectrum showing the formation of $[Pd_3L_6]^{6+}$ and its related assemblies with BF_4 anions as the main species.

The splitting in the ^{1}H NMR spectrum can be explained via symmetry operations. Therefore, the PM6 modeled structures are depicted from different perspectives in **Figure 4.14**. With C_3 and C_2 symmetry axes all ligands can be turned into each other, but no symmetry operation allows the transformation from the inside half of the ligands to the outside half due to the chirality of the ligand.

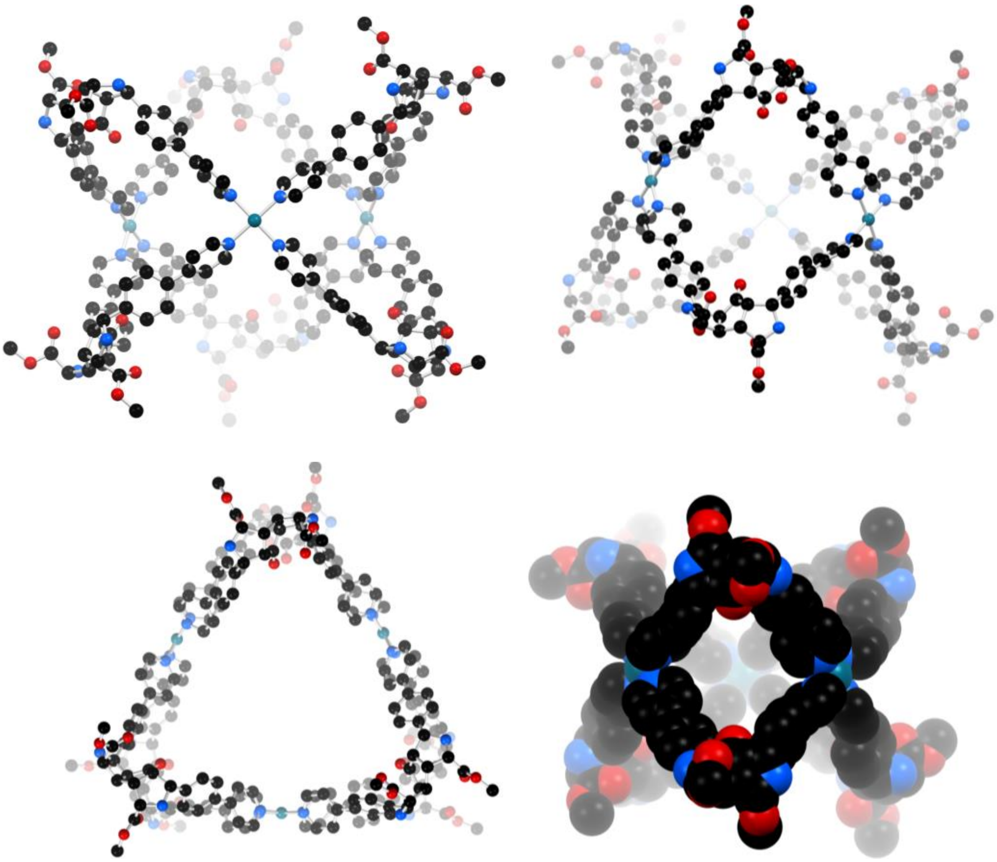

Figure 4.14 PM6 modelled structure of [$Pd_3L^{W2}_6$]$^{6+}$ from different perspectives and as space filling model.

4.4 Conclusion

Two new chiral backbones based on nature inspired compounds have been developed and their ability to form a variety of supramolecular assemblies could be shown. Further studies should lead to a complete characterization and could show the chiral discrimination of guests due to the cavities provided by the enantiopure assemblies, as shown for the helicene based cages in chapter 3.3.4. The high flexibility and the high number of functional groups of the ligand **L^{H2}** probably led to the formation of several assemblies, but further research could find conditions for a selective formation or switching between the different assemblies. The functional groups of the backbone have been reported for catalyzed reactions and therefore the catalytic potential in the defined cavities of the supramolecular assemblies should be investigated.

5 EXPERIMENTAL SECTION

All experiments were, if needed, performed under nitrogen atmosphere using standard Schlenk techniques. Commercially available reagents were used as received without further purification. Diethyl ether and tetrahydrofurane were, if needed, freshly distilled under argon from sodium. Recycling gel permeation chromatography was performed on a JAI LC-9210 II NEXT GPC system equipped with Jaigel 1H and 2H columns in series using chloroform as the eluent.

Chiral high performance liquid chromatography was performed on an Agilent Technologies 1260 infinity HPLC system equipped with Daicel CHIRALPAK IC columns (250 x 4,6 mm and 250 x 10 mm) using a dichloromethane/hexane/propan-2-ol (40.0%/59.5%/0.5%) mixture as eluent for the separation of ***trans*-2** and a dichloromethane/methanol (99.5%/0.5%) mixture as eluent for the separation of **1**, a dichloromethane/hexane/methanol/propan-2-ol (5.0%/80.0%/5.0%/10.0%) mixture as eluent for the separation of **L^1** and a dichloromethane/hexane/methanol/propan-2-ol (16.0%/69.0%/5.0%/10.0%) mixture as eluent for the separation of **L^2**.

NMR measurements were conducted on Avance 300 III, Avance 400 III HD, Avance 500 III HD, Avance 600 III HD instruments from Bruker. Mass spectrometric measurements were performed on a maXis ESI-TOF MS and an ESI-timsTOF machine from Bruker, a LTQ Orbitrap from Thermo-Fisher and on an AccuTOF from JEOL (EI, FD).

Dichloromethane (DCM) of spectroscopic-grade (Kanto Chemical Co., Inc.) was used for absorption or emission measurements of ***trans*-2**, respectively, without further purification. All of the measurements at room temperature were conducted at 25 ± 2°C unless otherwise stated. The absorption spectra of the ***trans*-2** complexes were measured by using a JASCO V-560 spectrophotometer. All of the samples were dissolved in DCM. The absorption spectral band shapes of the studied complexes were independent of the concentration in the concentration range studied. The corrected emission spectra of the complexes at room temperature and 77 K were measured by using a JACSO F6500 fluorescence spectrometer (excitation wavelengths = 350 and 400 nm). The absolute emission quantum yields (Φem) of the complexes were measured by a Hamamatsu C9920-02 system equipped with an integrating sphere and a PMA-12 multichannel photodetector (excitation wavelength = 400 nm). Emission decay profiles were measured by using a Hamamatsu C11200 streak camera as a photodetector by exciting at 355 nm using a nanosecond Q-switched Nd:YAG laser (Continum® MiniliteTM, fwhm ≈ 10–12 ns, repetition rate = 10 Hz). For emission spectroscopy, the absorbance of a sample solution was set <0.05 at the excitation wavelength, and sample solutions were deaerated by purging an Ar-gas stream over 30 min.

Circular dichroism spectra were recorded in HPLC grade DCM and DMSO-d_6 with an Applied Photophysics Chirascan qCD Spectrometer. The spectra were background corrected and smoothed with a window size of 3.

CPL measurements in DCM solutions have been recorded with a home built apparatus,[101,103] excitation wavelength 370 nm, 90° geometry, incident beam polarized parallel to the direction of emission collection, 8 scans.

The irradiation for the helicene synthesis was performed with a 500 W Hg Arc lamp from LOT-Quantum Design.

5.1 Chiral-at-Metal Phosphorescent Square-Planar Pt(II)- Complexes from an Achiral Organometallic Ligand

5.1.1 Synthesis and characterization

5.1.1.1 [(2-Bromophenyl)ethynyl]trimethylsilane

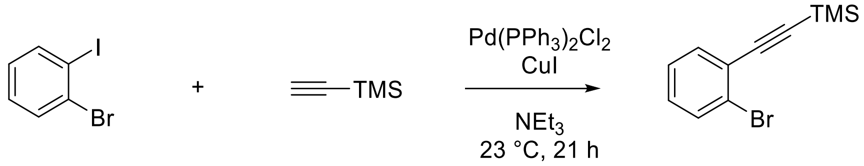

A suspension of 2-bromoiodobenzene (3.10 g, 10.6 mol, 1.0 eq.), trimethylsilylacetylene (1.15 g, 11.7 mmol, 1.10 eq.), $Pd(PPh_3)_2Cl_2$ (112 mg, 0.159 mmol, 1.5 mol%) and CuI (85 mg, 0.446 mmol, 4.2 mol%) was stirred under nitrogen atmosphere in NEt_3 (40 mL) for 21 h at 23 °C. The solvent was removed under vacuum and the reaction mixture was subjected to column chromatography (hexane) yielding the target product as yellow oil (2.67 g, 10.5 mmol, 96 %).

^{1}H NMR (300 MHz, $CDCl_3$): δ (ppm) = 7.57 (dd, J = 8.0, 1.3 Hz, 1H, 6-H), 7.49 (dd, J = 7.6, 1.8 Hz, 1H, 3-H), 7.24 (td, J = 7.6, 1.3 Hz, 1H, Ar-H), 7.15 (td, J = 7.7, 1.8 Hz, 1H, Ar-H), 0.28 (s, 9H, $-CH_3$).

^{13}C NMR (75 MHz, $CDCl_3$): δ (ppm) = 133.8, 132.5, 129.7, 127.0, 125.9, 125.4, 103.2, 99.8, 0.0.

MS (EI): *m/z* (found) = 252.0 $[M+H]^+$

m/z (calc.) = 252.0 $[M+H]^+$

5.1.1.2 2-((2-((Trimethylsilyl)ethynyl)phenyl)ethynyl)pyridine

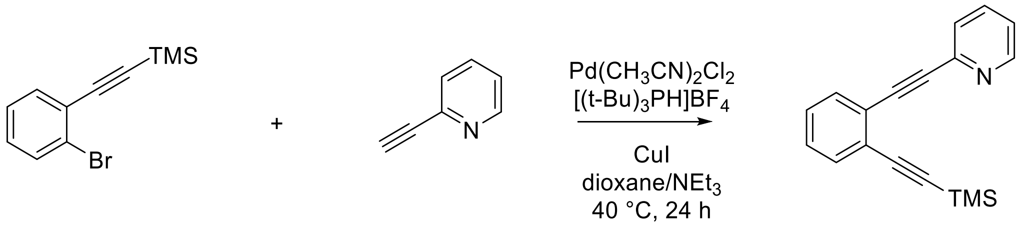

A suspension of [(2-bromophenyl)ethynyl]trimethylsilane (2.38 g, 9.40 mol, 1.0 eq.), 2-ethynylpyridine (1.19 g, 11.5 mmol, 1.2 eq.), $Pd(CH_3CN)_2Cl_2$ (115 mg, 0.443 mmol, 4.7 mol%), $[(t\text{-Bu})_3PH]BF_4$ (168 mg, 0.579 mmol, 6.2 mol%), CuI (22.8 mg, 0.120 mmol, 1.3 mol%) in dioxane (30 mL) and NEt_3 (12 mL) was stirred for 24 h at 40 °C under a nitrogen atmosphere.

The solvent was removed and the crude product was purified by column chromatography (SiO_2, ethyl acetate/hexane: 1:4). The desired product was obtained as a brown oil (2.20 g, 7.99 mmol, 85 %).

^{1}H NMR (300 MHz, $CDCl_3$): δ (ppm) = 8.63 (ddd, *J* = 5.0, 1.7, 0.9 Hz, 1H), 7.68 (td, *J* = 7.7, 1.8 Hz, 1H), 7.62 – 7.48 (m, 3H), 7.36 – 7.25 (m, 2H), 7.30 – 7.19 (m, 1H), 0.26 (s, 9H, $-CH_3$).

^{13}C NMR (75 MHz, $CDCl_3$): δ (ppm) = 150.2, 143.7, 136.1, 132.4, 128.7, 128.4, 127.5, 126.2, 125.2, 122.9, 103.4, 99.1, 92.5, 88.1, 0.13.

HRMS (ESI(+)): *m/z* (found) = 276.1203 $[M+H]^+$

m/z (calc.) = 276.1203 $[M+H]^+$

5.1.1.3 2-((2-Ethynylphenyl)ethynyl)pyridine

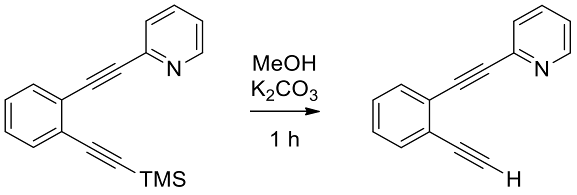

A mixture of 2-((2-((trimethylsilyl)ethynyl)phenyl)ethynyl)pyridine (2.20 g, 7.99 mmol, 1.0 eq.) and potassium carbonate (2.20 g, 15.9 mmol, 2.0 eq.) was stirred for 1 h in methanol (9 mL) at room temperature. The solvent was removed under reduced pressure, chloroform (15 mL) was added and the organic phase was washed with HCl solution (1 M, 10 mL) and a saturated NaCl sol. (10 mL) and dried over Na_2SO_4. The solvent was removed under reduced pressure and the desired product could be obtained as a dark oil that showed satisfactory analytical data despite its color and was used successfully in the subsequent step (1.37 g, 6.74 mmol, 84 %).

^{1}H NMR (300 MHz, $CDCl_3$): δ (ppm) = 8.63 (d, J = 5.0 Hz, 1H), 7.69 (td, J = 7.7, 1.8 Hz, 1H), 7.67 – 7.49 (m, 3H), 7.39 – 7.28 (m, 2H), 7.31 – 7.20 (m, 1H), 3.39 (s, 1H).

^{13}C NMR (75 MHz, $CDCl_3$): δ (ppm) = 150.1, 143.4, 136.4, 132.8, 132.5, 128.8, 128.7, 127.8, 125.4, 125.2, 123.1, 92.4, 87.9, 82.1, 81.7.

HRMS (EI(+)): *m/z* (found) = 203.0732 $[M]^+$

m/z (calc.) = 203.0735 $[M]^+$

5.1.1.4 2-((2-((2-Bromophenyl)ethynyl)phenyl)ethynyl)pyridine L^{CN}-Br

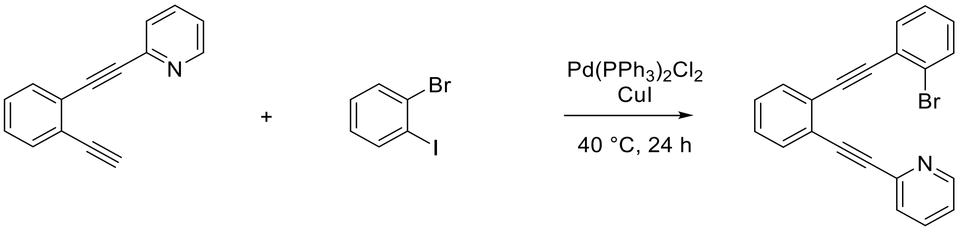

A suspension of 2-((2-ethynylphenyl)ethynyl)pyridine (1.37 g, 6.74 mmol, 1.0 eq.), 2-bromoiodobenzene (2.29 g, 8.09 mmol, 1.2 eq.), $PdCl_2$ (59.8 mg, 0.337 mmol, 5.0 mol%), PPh_3 (195 mg, 0.741 mmol, 0.11 eq.) and CuI (64.2 mg, 0.337 mmol, 5.0 mol%) in degased NEt_3 (20 mL) and dioxane (10 mL) was stirred under nitrogen atmosphere for 24 h at 40 °C. The solvent was removed under reduced pressure and the crude product was purified by column chromatography (SiO_2, ethyl acetate/hexane: 1:4). The desired product could be obtained as brown solid. Recrystallization from hot acetonitrile yielded the clean ligand **L^{CN}**-Br as a colorless solid (1.19 g, 3.32 mmol, 49 %).

^{1}H NMR (300 MHz, $CDCl_3$): δ (ppm) = 8.64 (s, 1H), 7.70 – 7.61 (m, 4H), 7.61 – 7.52 (m, 2H), 7.40 – 7.33 (m, 2H), 7.31 – 7.22 (m, 2H), 7.22 – 7.11 (m, 1H).

^{13}C NMR (75 MHz, $CDCl_3$): δ (ppm) = 150.1, 143.6, 136.1, 133.8, 132.6, 132.5, 132.3, 129.7, 128.8, 128.5, 127.6, 127.1, 125.9, 125.6, 125.5, 124.9, 122.9, 92.7, 92.5, 92.3, 88.0.

HRMS (ESI(+)): *m/z* (found) = 358.0222 $[M+H]^+$

m/z (calc.) = 358.0226 $[M+H]^+$

5.1.1.5 [PtL^{CN}Cl(SEt$_2$)] (1) and [PtL^{CN}$_2$] (2)

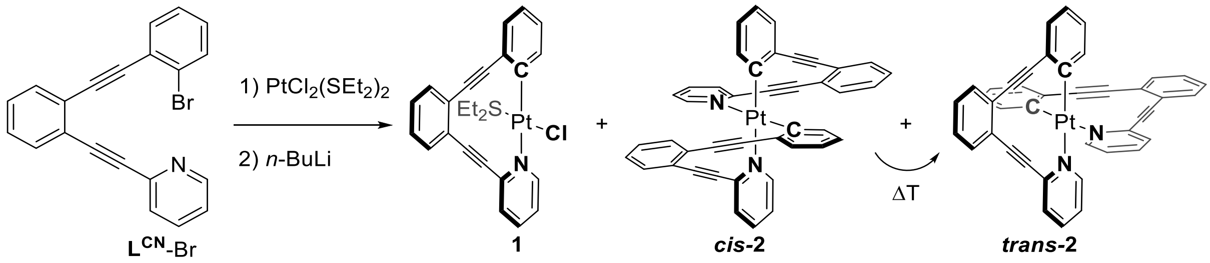

The reaction conditions have been variied to optimize the yield of ***trans*-2** in respect of order of the addition, temperature and solvent ratios. With the procedure as described below, but in pure THF the formation of **1** was prefered over the formation of ***trans*-2** and the formation of ***cis*-2** could not be observed. The use of a THF/ether mixture increased the formation of ***trans*-2**, but ***trans*-2** was very difficult to isolate from the now formed ***cis*-2** complex.

Synthesis of **1** and ***trans*-2**: **L^{CN}**-Br (306 mg, 0.854 mmol, 2.1 eq.) and PtCl$_2$(SEt$_2$)$_2$ (182 mg, 0.406 mmol, 1.0 eq.) were dissolved in dry THF (4 mL) and dry Et$_2$O (16 mL). A solution of *n*-BuLi (2.5 M, 0.342 mL, 0.854 mmol, 2.1 eq.) in hexane was added dropwise at –78 °C and the red solution warmed up to 23 °C overnight. The solvent was removed under reduced pressure and the products **1** and **2** were isolated via column chromatography (SiO$_2$, dichloromethane/hexane 50:50 → dichloromethane → methanol/dichloromethane 3:100). Further purification of **1** was carried out via GPC yielding a yellow solid (15.3 mg, 0.0255 mmol, 6 %). **2** was further purified by washing with DCM (10 mL) yielding a yellow solid (47.5 mg, 0.0632 mmol, 16 %). 29.3 mg of a column fraction with a ***cis*-2/*trans*-2** mixture, that contained mainly ***cis*-2**, was transformed to ***trans*-2** in 100 mL chloroform at 50 °C over night, resulting in a total yield for ***trans*-2** (76.8 mg, 0.0632 mmol, 25 %).

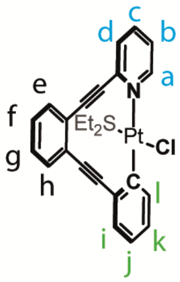

[PtL^{CN}Cl(SEt$_2$)] **1**:

^{1}H NMR (600 MHz, CDCl$_3$): *δ* (ppm) = 8.79 (d, *J* = 5.5 Hz, 1H), 7.83 – 7.75 (m, 1H), 7.74 (d, *J* = 7.3 Hz, 1H), 7.67 (d, *J* = 7.6 Hz, 1H), 7.64 (d, *J* = 7.8 Hz, 1H), 7.47 (d, *J* = 7.7 Hz, 1H), 7.42 (t, *J* = 7.5 Hz, 1H), 7.42 – 7.35 (m, 2H), 7.32 (t, *J* = 7.6 Hz, 1H), 7.03 (t, *J* = 7.0

Hz, 1H), 6.93 (t, *J* = 7.5 Hz, 1H), 2.72 – 2.53 (m, 2H), 2.38 – 2.18 (m, 2H), 1.46 – 1.35 (m, 3H), 1.22 – 1.13 (m, 3H).

^{13}C NMR (151 MHz, $CDCl_3$): *δ* (ppm) = 151.8, 144.6, 137.4, 137.1, 137.1, 132.9, 131.9, 131.6, 129.8, 129.6, 129.5, 128.6, 128.0, 126.9, 124.5, 123.6, 123.0, 100.8, 96.8, 90.2, 87.4, 30.5, 28.9, 12.8, 12.7.

MS (ESI(+)): *m/z* (found) = 473.1 [M −SEt_2−Cl)]$^+$

m/z (calc.) = 473.1 [M −SEt_2−Cl)]$^+$

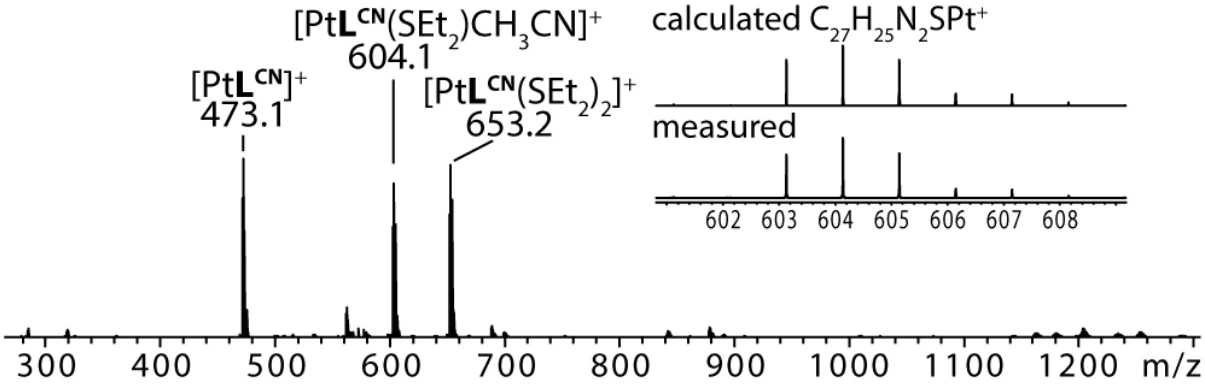

Figure 5.1. ESI-MS of 1.

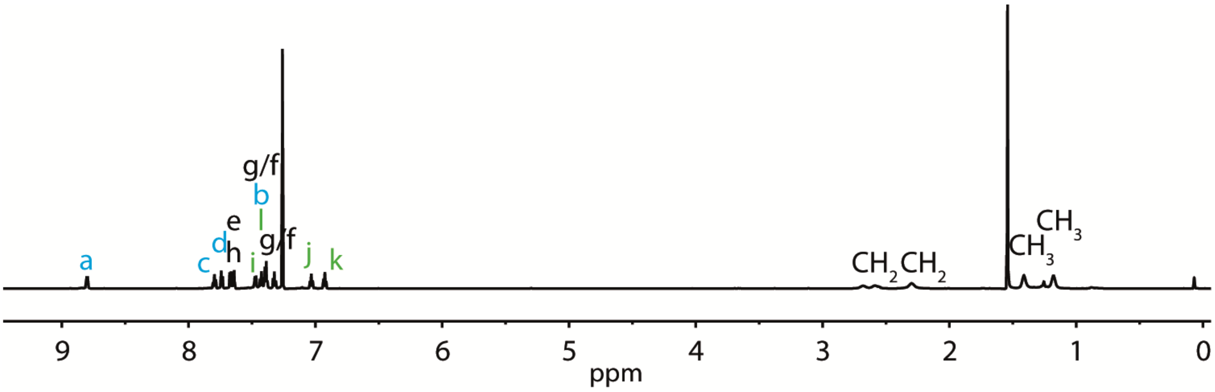

Figure 5.2. ^{1}H NMR of 1 (600 MHz, $CDCl_3$).

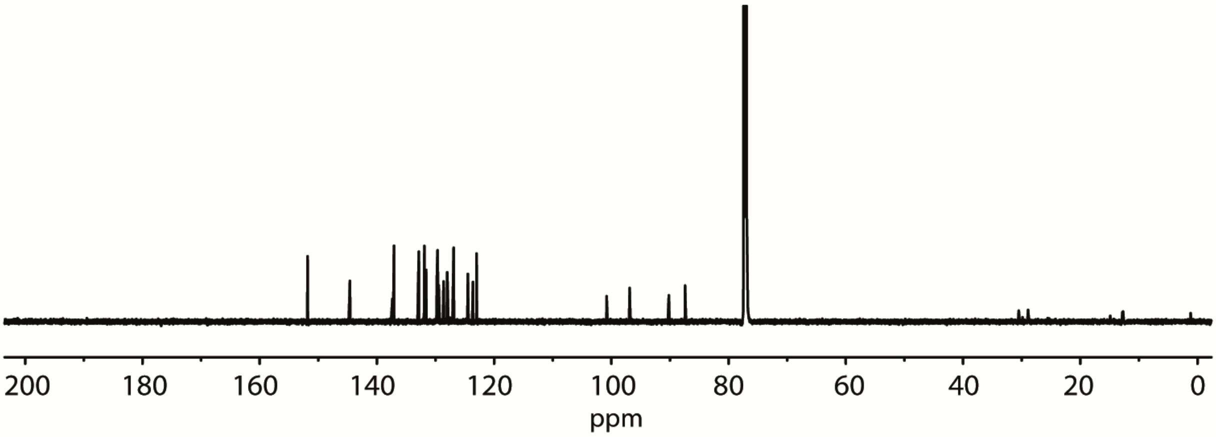

Figure 5.3. ^{13}C NMR of 1 (151 MHz, $CDCl_3$).

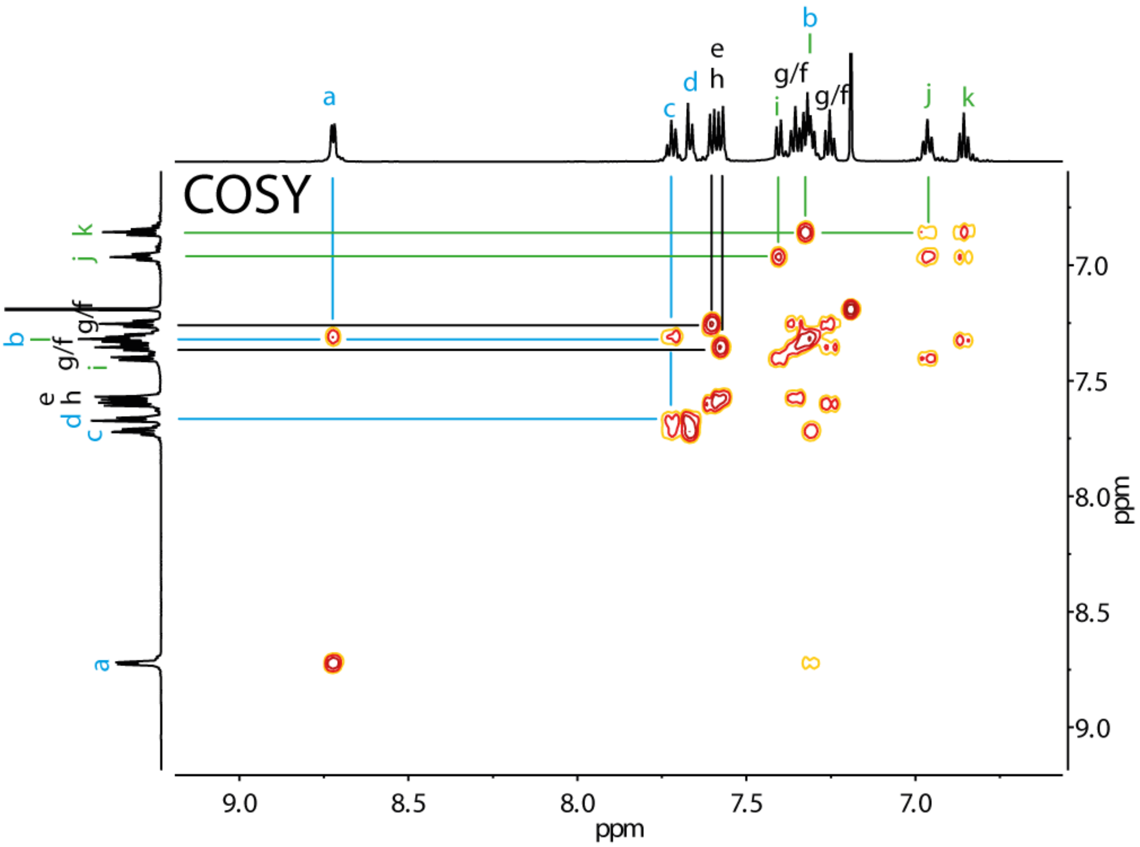

Figure 5.4. ^{1}H-^{1}H COSY NMR spectrum of 1 (600 MHz, $CDCl_3$).

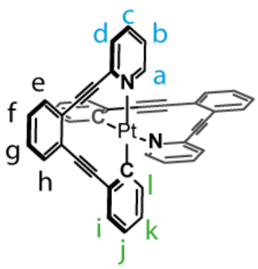

[Pt**L**^{CN}$_2$] ***trans*-2**:

^{1}**H NMR** (600 MHz, CD_2Cl_2): δ (ppm) = 9.39 (dt, J = 5.6, 1.4 Hz, 1H), 7.85 (dd, J = 7.7, 1.4 Hz, 1H), 7.82 (td, J = 7.7, 0.7 Hz, 2H), 7.60 – 7.49 (m, 3H), 7.45 (td, J = 7.7, 1.3 Hz, 1H) 7.24 (dd, J = 7.3, 1.8 Hz, 1H), 7.09 (td, J = 6.1, 2.8 Hz, 1H), 6.68 (td, J = 7.3, 1.6 Hz, 1H), 6.64 (td, J = 7.3, 1.6 Hz, 1H).

^{13}**C NMR** (151 MHz, CD_2Cl_2): δ (ppm) = 153.3, 149.7, 143.8, 139.2, 135.8, 132.8, 131.7, 130.5, 129.5, 129.3, 129.1, 128.6, 126.8, 126.6, 124.1, 123.8, 121.0, 102.4, 94.3, 90.7, 84.2.

MS (FD(+)): *m/z* (found) = 751.1 $[M]^+$

m/z (calc.) = 751.2 $[M]^+$

EA: calc. for $C_{42}H_{24}N_2Pt \cdot H_2O$: C: 65.5, H: 3.4, N: 3.6

found: C: 65.6, H: 3.6, N: 3.8

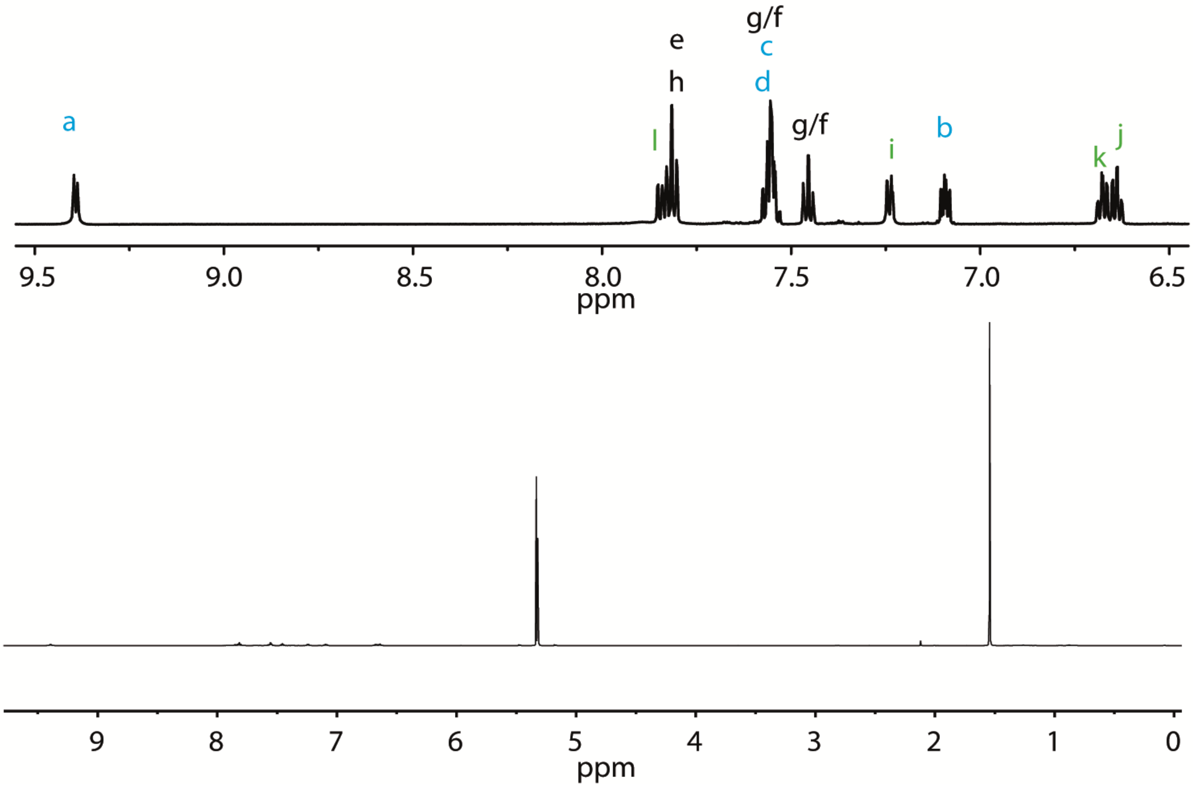

Figure 5.5. ^{1}H NMR spectrum of *trans*-**2** (600 MHz, CD_2Cl_2). The full spectrum reveals that the signals assigned to $CDHCl_2$ and H_2O are relatively high due to the bad solubility of **2**.

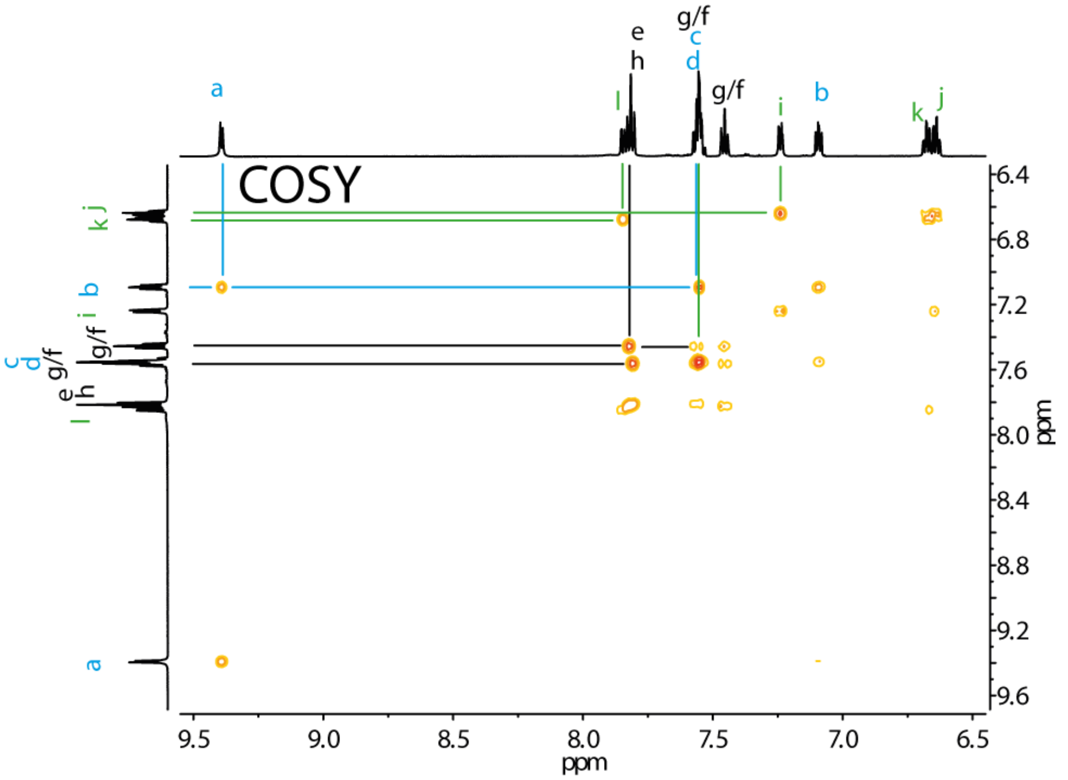

Figure 5.6 ^{1}H-^{1}H COSY NMR spectrum of *trans*-**2** (600 MHz, CD_2Cl_2).

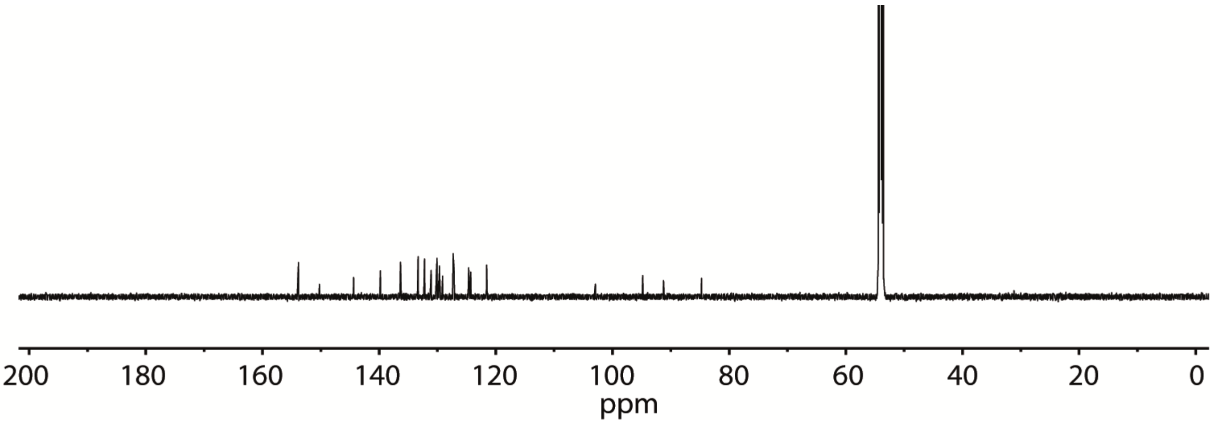

Figure 5.7. ^{13}C NMR spectrum of *trans*-2 (151 MHz, CD_2Cl_2).

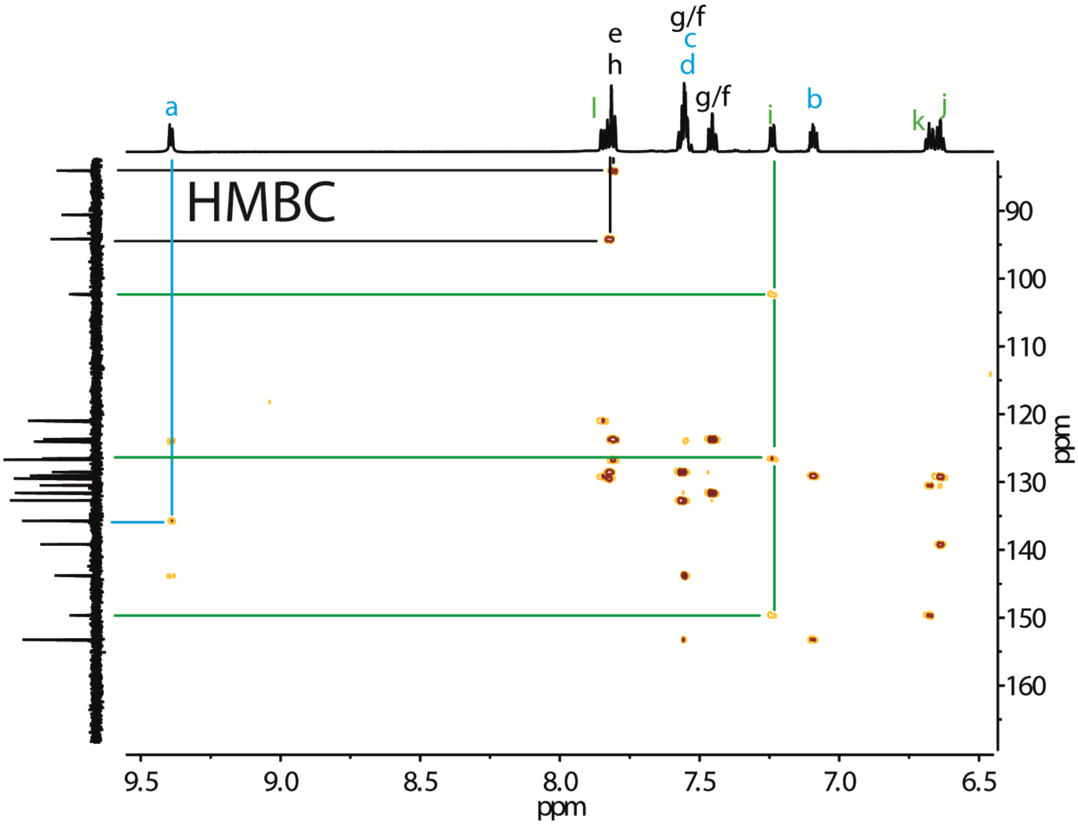

Figure 5.8. HMBC NMR spectrum of *trans*-2 (600 MHz, CD_2Cl_2).

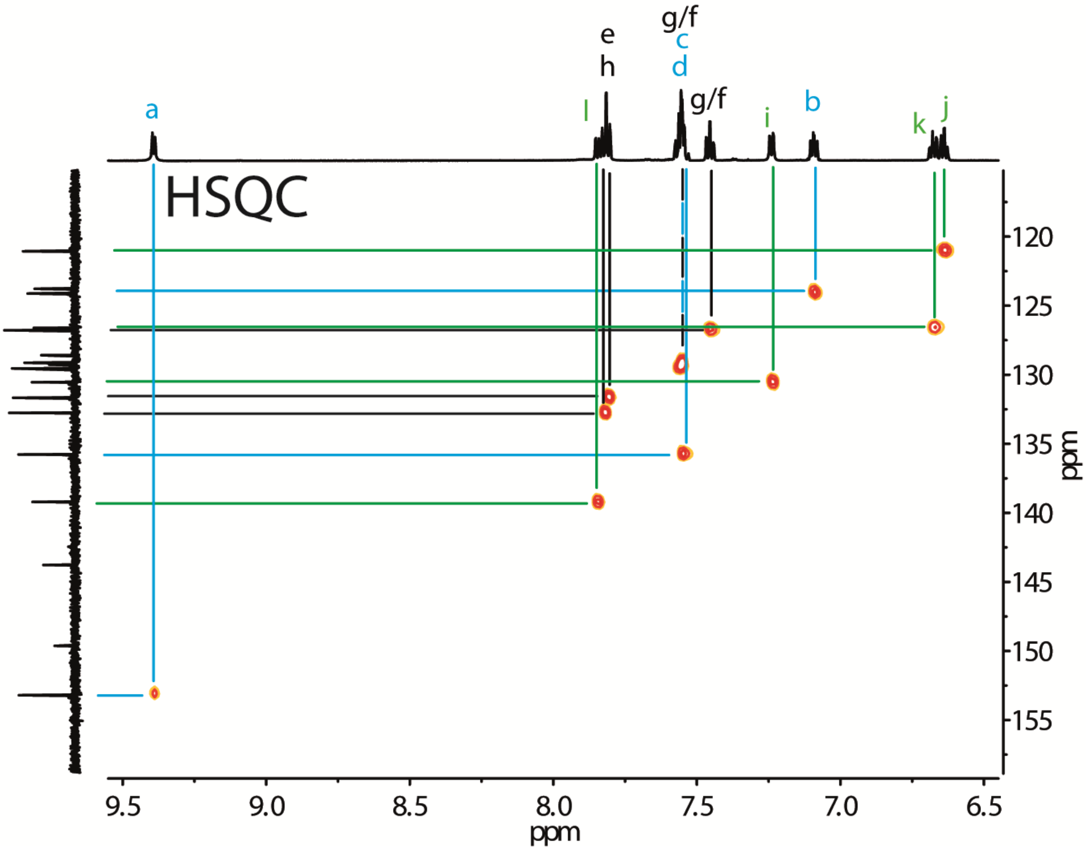

Figure 5.9. HSQC NMR spectrum of *trans*-2 (600 MHz, CD_2Cl_2).

[PtL$^{CN}{}_2$)] ***cis*-2**:

^{1}H NMR (600 MHz, CD_2Cl_2): δ (ppm) = 9.09 (d, J = 5.6 Hz, 1H), 7.85 (dd, J = 7.7, 1.4 Hz, 1H), 7.70 (d, J = 7.7 Hz, 1H), 7.62 – 7.56 (m, 2H), 7.53 (td, J = 7.7, 1.3 Hz, 1H), 7.40 (td, J = 7.6, 1.3 Hz, 1H), 7.29 (d, J = 7.8 Hz, 1H), 7.13 (ddd, J = 7.6, 5.6, 1.4 Hz, 1H), 7.04 (dd, J = 7.5, 1.5 Hz, 1H), 6.83 (td, J = 7.5, 1.5 Hz, 1H), 6.63 (td, J = 7.4, 1.4 Hz, 1H).

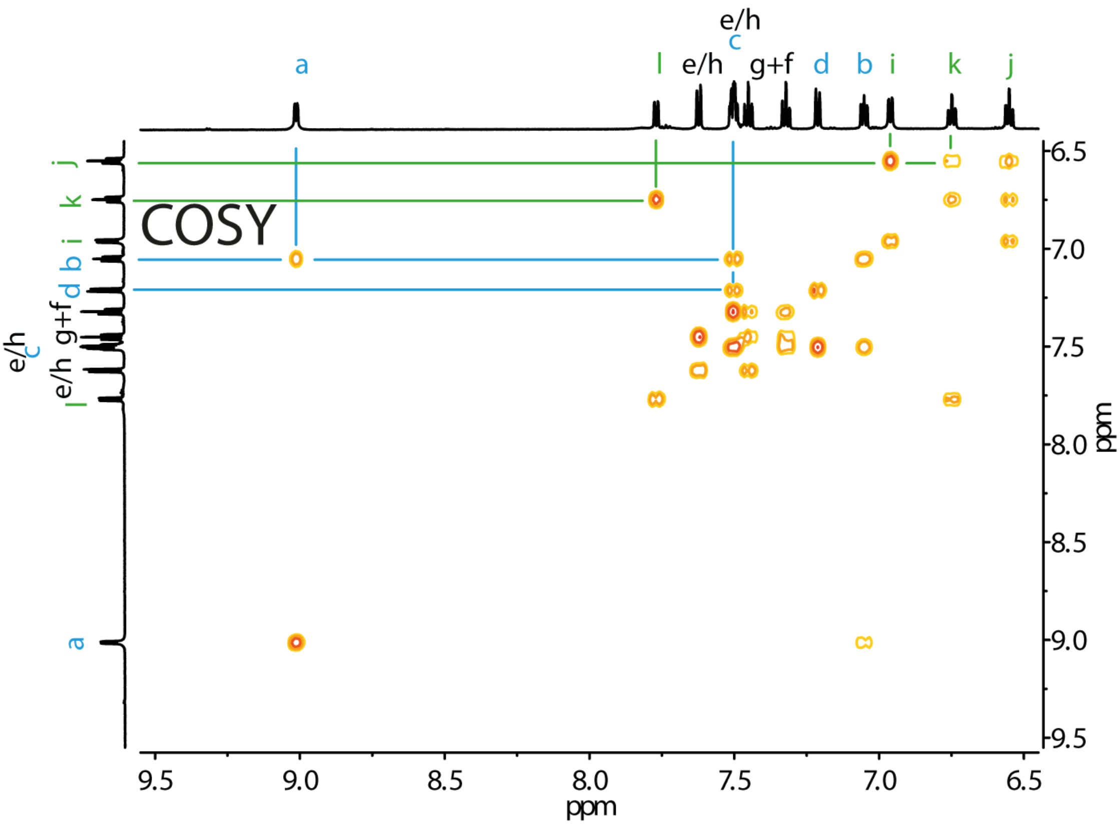

Figure 5.10. COSY NMR spectrum of *cis*-2 (600 MHz, CD_2Cl_2).

5.1.2 Single-crystal X-ray Crystallography

The crystals of **1** and racemic ***trans*-2** were mounted on top of glass fiber using inert perfluorinated polyether oil and placed in the 100(2) K cold gas stream of an Oxford Cryostream low-temperature device on a Bruker D8 three circle diffractometer. The data of **1** was collected using an Incoatec microsource (Ag *Kα* = 0.56086 Å) and data for racemic ***trans*-2** was measured with a Bruker TXS rotating anode (Mo *Kα* = 0.71073 Å), both machines utilize Montel beam shaping optics. Data integration for all three structures was done with *SAINT* 8.30C. Data scaling and absorption correction were performed with *SADABS* 2016/2. The space group was determined using *XPREP*. The structure was solved by direct methods using *SHELXT*.[145] Full-matrix least squares refinement was done with *SHELXL*-2016/5 within the *SHELXLe*-GUI.[134,146] The hydrogen atoms were refined isotropically on calculated positions using a riding model with their U_{iso} values constrained to 1.5 U_{eq} of their respective pivot atoms for terminal sp^3 carbon atoms and 1.2 times for all other carbon atoms. All non-hydrogen atoms were refined with anisotropic displacement parameters.

5.1.2.1 X-ray data of 1

Table 5.1. Crystal data and structure refinement for 1.

Identification code	PtLClSEt2	
CCDC no.	1507376	
Empirical formula	$C_{26} H_{23} Cl_4 N Pt S$	
Formula weight	718.40	
Temperature	100(2) K	
Wavelength	0.56086 Å	
Crystal system	Monoclinic	
Space group	$P2_1/n$	
Unit cell dimensions	a = 7.566(2) Å	α= 90°.
	b = 20.775(3) Å	β= 92.01(2)°.
	c = 17.105(2) Å	γ = 90°.
Volume	2686.7(9) $Å^3$	
Z	4	
Density (calculated)	1.776 Mg/m^3	
Absorption coefficient	3.089 mm^{-1}	
F(000)	1392	
Crystal size	0.419 x 0.176 x 0.150 mm^3	
Theta range for data collection	1.217 to 27.927°.	
Index ranges	-12<=h<=12, -34<=k<=34, -28<=l<=28	
Reflections collected	147537	
Independent reflections	13101 [R(int) = 0.0434]	
Completeness to theta = 19.665°	100.0 %	
Absorption correction	Semi-empirical from equivalents	
Max. and min. transmission	0.6469 and 0.4303	
Refinement method	Full-matrix least-squares on F^2	
Data / restraints / parameters	13101 / 927 / 424	
Goodness-of-fit on F^2	1.186	
Final R indices [I>2sigma(I)]	R1 = 0.0253, wR2 = 0.0474	
R indices (all data)	R1 = 0.0300, wR2 = 0.0487	
Largest diff. peak and hole	1.480 and -2.735 e.$Å^{-3}$	

5.1.2.2 X-ray data of racemic *cis*-2

Table 5.2. Crystal data and structure refinement for racemic *cis*-2:

Identification code	***cis*-2**	
CCDC no.	1543318	
Empirical formula	$C_{43} H_{26} Cl_2 N_2 Pt$	
Formula weight	836.65	
Temperature	100(2) K	
Wavelength	0.71073 Å	
Crystal system	Triclinic	
Space group	$P\bar{1}$	
Unit cell dimensions	a = 9.4057(12) Å	α= 81.006(4)°.
	b = 11.9467(16) Å	β= 88.203(4)°.
	c = 15.1002(19) Å	γ = 79.304(4)°.
Volume	1646.8(4) $Å^3$	
Z	2	
Density (calculated)	1.687 Mg/m^3	
Absorption coefficient	4.458 mm^{-1}	
F(000)	820	
Crystal size	0.378 x 0.321 x 0.084 mm^3	
Theta range for data collection	2.554 to 26.370°.	
Index ranges	-11<=h<=11, -14<=k<=14, -15<=l<=18	
Reflections collected	28776	
Independent reflections	6701 [R(int) = 0.0394]	
Completeness to theta = 25.242°	99.5 %	
Absorption correction	Semi-empirical from equivalents	
Max. and min. transmission	0.7465 and 0.5954	
Refinement method	Full-matrix least-squares on F^2	
Data / restraints / parameters	6701 / 24 / 442	
Goodness-of-fit on F^2	1.047	
Final R indices [I>2sigma(I)]	R1 = 0.0274, wR2 = 0.0667	
R indices (all data)	R1 = 0.0300, wR2 = 0.0684	
Largest diff. peak and hole	2.432 and -2.497 e.$Å^{-3}$	

5.1.2.3 X-ray data of racemic *trans*-2

Crystals of racemic ***trans*-2** suitable for X-ray structure determination were obtained by slow evaporation from a DCM/Hexane solution. Both enantiomers are present in the crystal structure. The distance between the ligand planes is ~3.5 Å.

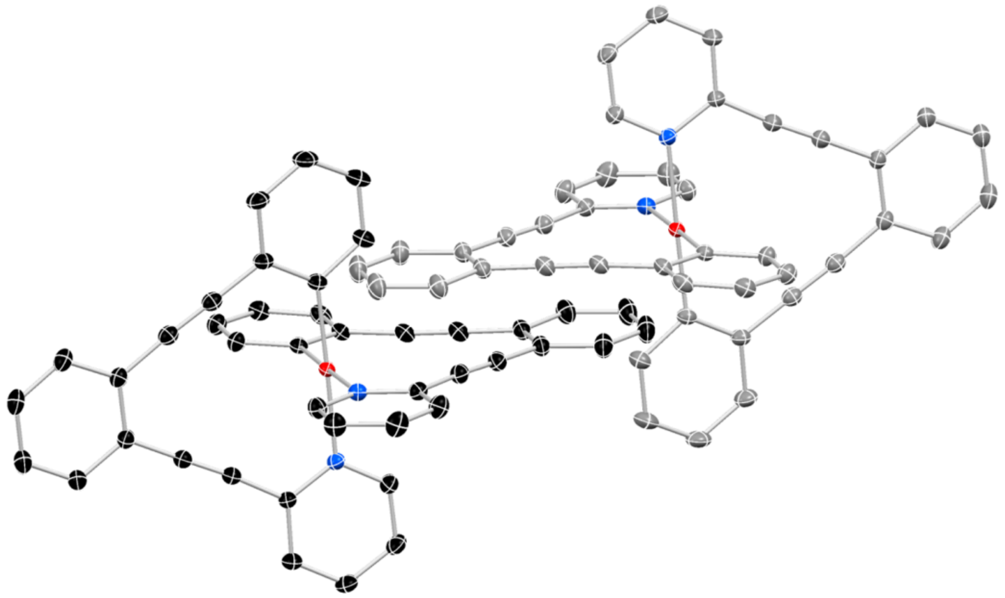

Figure 5.11. **ORTEP drawing of racemic $[PtL^{CN}_2]$** *trans*-2. **C: black/grey, N: blue, Pt: red. H atoms.**

Table 5.3. **Crystal data and structure refinement for racemic** *trans*-2:

Identification code	***trans*-2**	
CCDC no.	1507375	
Empirical formula	$C_{42} H_{24} N_2 Pt$	
Formula weight	751.72	
Temperature	100(2) K	
Wavelength	0.71073 Å	
Crystal system	Monoclinic	
Space group	$P2_1/c$	
Unit cell dimensions	a = 17.492(3) Å	α= 90°.
	b = 9.249(2) Å	β= 97.13(2)°.
	c = 18.881(2) Å	γ = 90°.
Volume	3031.0(9) Å^3	
Z	4	
Density (calculated)	1.647 Mg/m^3	
Absorption coefficient	4.663 mm^{-1}	
F(000)	1472	
Crystal size	0.122 x 0.115 x 0.104 mm^3	
Theta range for data collection	1.173 to 36.352°.	
Index ranges	-29<=h<=29, -15<=k<=15, -31<=l<=31	
Reflections collected	114524	
Independent reflections	14542 [R(int) = 0.0240]	

Completeness to theta = 25.242°	100.0 %
Absorption correction	Semi-empirical from equivalents
Max. and min. transmission	0.7549 and 0.6612
Refinement method	Full-matrix least-squares on F^2
Data / restraints / parameters	14542 / 0 / 406
Goodness-of-fit on F^2	1.054
Final R indices [I>2sigma(I)]	R1 = 0.0176, wR2 = 0.0430
R indices (all data)	R1 = 0.0204, wR2 = 0.0441
Largest diff. peak and hole	1.953 and -0.723 e.Å^{-3}

5.1.2.4 X-ray data of enantiopure ***trans*-2(*S*$_a$)**

Crystals of enantiopure ***trans*-2** (*S*$_a$ enantiomer) suitable for X-ray structure determination were obtained by slow evaporation from a DCM/Hexane solution. The crystal of enantiopure ***trans*-2** (S$_a$) was mounted on a molecular dimensions micro mount using NVH oil and placed in the 100(2) K cold gas stream of an Oxford Cryostream low-temperature device on a Bruker D8 four circle diffractometer. The data was collected using an Incoatec microsource 2.0 (Mo *Kα* = 0.71073 Å) utilize Montel beam shaping optics. With the purpose of determining the absolute configuration of the HPLC peak 1 an extensive data collection was performed in which most Friedel pairs were measured in the same frame. A resolution up to 0.67 Å reached (100% complete up to 0.75 Å) with an overall multiplicity of 13. Nevertheless, the absolute structure determination remained challenging, as the chirality of the molecule and corresponding anomalous differences from resonant scattering originate only from the difference of one nitrogen atom compared to one carbon atom, both sitting next to the platinum atom. The structure was solved in space group $P2_1$ with two identical enantiomers in the asymmetric unit. In the CHECKCIF routine an additional (pseudo) symmetry element c and corresponding space group change to $P2_1/c$ is suggested. This is however not suggested when the ADSYMM EXACT calculation in PLATON is performed. We therefore conclude that the space group $P2_1$ is correct. The enantiopure distinguishing parameters calculated with methods of Flack [x = 0.164(8)], Hooft [y = 0.138(7)] and Parsons [z = 0.166(8)] confirm that the absolute structure has been correctly assigned.[96,97] 8848 Bivoet differences from the dataset have been analyzed using Basian statistics in the PLATON program,[147] yielding a probability [P(2) and P(3)] of 1.00 that the absolute structure assignment is correct. Although the absolute value of x/y/z exceeds the usually applied tolerance criteria for a “strong indication” of enantiopurity (x ≤ 0.10) the obtained results indicate, that HPLC fraction 1 is the *S*$_a$ enantiomer. Hence, the CD and X-ray results for assigning the absolute configuration are in accordance with each other. We conclude that the absolute structure of

HPLC peak 1 of compound **2** has been successfully identified as S_a enantiomer using Mo Kα radiation.

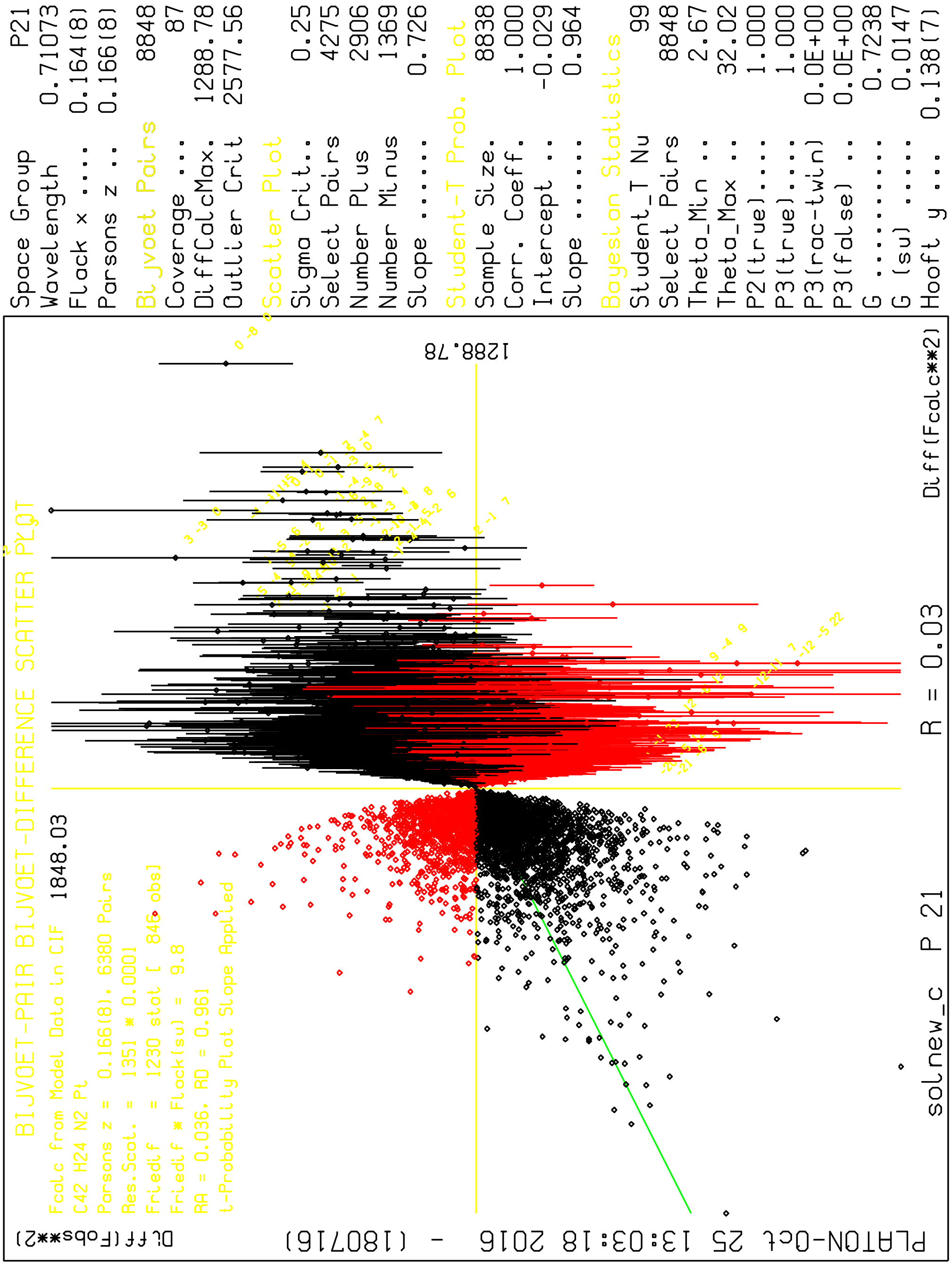

```
Space Group          P21
WaveLength       0.71073
Flack x .....   0.164(8)
Parsons z ..    0.166(8)
Bijvoet Pairs       8848
Coverage ....         87
DiffCalcMax.     1288.78
Outlier Crit     2577.56
Scatter Plot
Sigma Crit..        0.25
Select Pairs        4275
Number Plus         2906
Number Minus        1369
Slope ......       0.726
Student-T Prob. Plot
Sample Size.        8838
Corr. Coeff.       1.000
Intercept ..      -0.029
Slope ......       0.964
Bayesian Statistics
Student_T Nu          99
Select Pairs        8848
Theta_Min ..        2.67
Theta_Max ..       32.02
P2(true)....       1.000
P3(true)....       1.000
P3(rac-twin)     0.0E+00
P3(false) ..     0.0E+00
G ..........      0.7238
G (su) .....      0.0147
Hooft y ....    0.138(7)
```

BIJVOET-PAIR BIJVOET-DIFFERENCE SCATTER PLOT
Fcalc from Model Data in CIF 1848.03
C42 H24 N2 Pt
Parsons z = 0.166(8), 6380 Pairs
Res.Scal. = 1351 * 0.0001
FriedIf = 1230 stat [846 obs]
FriedIf * Flack(su) = 9.8
RA = 0.036, RD = 0.961
t-Probability Plot Slope Applied
1288.78
Diff(Fcalc**2)
R = 0.03
solnew_c P 21
Diff(Fobs**2)
PLATON-Oct 25 13:03:18 2016 - (180716)

Figure 5.12 Bivoet analysis output of enantiopure 2 (S_a) from the PLATON program.[147]

Table 5.4. Crystal data and structure refinement for enantiopure *trans*-2(*S*$_a$).

Identification code	enantiopure ***trans*-2**(*S*$_a$)	
CCDC no.	1511719	
Empirical formula	C42 H24 N2 Pt	
Formula weight	751.72	
Temperature	100(2) K	
Wavelength	0.71073 Å	
Crystal system	Monoclinic	
Space group	$P2_1$	
Unit cell dimensions	a = 17.5938(12) Å	α= 90°.
	b = 9.2189(6) Å	β= 96.984(3)°.
	c = 18.8427(14) Å	γ = 90°.
Volume	3033.5(4) Å^3	
Z	4	
Density (calculated)	1.646 Mg/m^3	
Absorption coefficient	4.660 mm^{-1}	
F(000)	1472	
Crystal size	0.192 x 0.059 x 0.050 mm^3	
Theta range for data collection	2.451 to 32.251°.	
Index ranges	-25<=h<=25, -13<=k<=13, -27<=l<=27	
Reflections collected	152787	
Independent reflections	19280 [R(int) = 0.0565]	
Completeness to theta = 25.242°	99.8 %	
Absorption correction	Semi-empirical from equivalents	
Max. and min. transmission	0.7464 and 0.6273	
Refinement method	Full-matrix least-squares on F^2	
Data / restraints / parameters	19280 / 649 / 811	
Goodness-of-fit on F^2	1.035	
Final R indices [I>2sigma(I)]	R1 = 0.0307, wR2 = 0.0445	
R indices (all data)	R1 = 0.0564, wR2 = 0.0487	
Absolute structure parameter	0.142(9)	
Largest diff. peak and hole	0.769 and -0.936 e.Å^{-3}	

5.2 Helicene based Cages

5.2.1 Synthesis of the compounds L^1 and L^2

5.2.1.1 2,7-Bis(triphenylphosphoniomethyl)naphthalene Dibromide

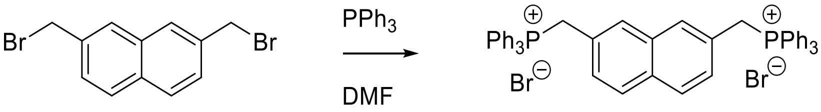

Commercial available 2,7-bis(bromomethyl)naphthalene (2.06 g, 6.56 mmol, 1.0 eq.) and PPh_3 (4.11 g, 15.7 mmol, 2.4 eq.) were dissolved in DMF (20 mL) and stirred at r.t. for 24 h. A white solid precipitated, toluene (30 ml) was added and the mixture was stirred for additional 30 min. The product was filtered off, washed with toluene (50 mL) and dried in vacuo yielding the clean product (5.49 g, 6.55 mol, 99 %).[108,131]

^{1}H NMR (300 MHz, DMSO-d6) δ = 5.35 (d, *J* = 15.8 Hz, 4H), 7.08 (d, *J* = 8.3 Hz, 2H), 7.17 – 7.27 (m, 2H), 7.79 – 7.61 (m, 26H), 7.86 – 7.97 (m, 6H).

^{13}C NMR (75 MHz, DMSO-d6) δ = 28.18 (d, *J* = 47.0 Hz), 117.70 (d, *J* = 85.6 Hz), 126.59 (d, *J* = 9.1 Hz), 128.29, 128.73, 129.80 (d, *J* = 8.9 Hz), 130.10 (d, *J* = 12.6 Hz), 131.35, 132.02, 134.00 (d, *J* = 10.1 Hz), 135.14.

^{31}P NMR (121 MHz, DMSO-d6) δ = 23.09.

HRMS (ESI): *m/z* (found) = 677.2489 $[M–2Br–H]^+$

m/z (calc.) = 677.2522 $[M–2Br–H]^+$.

5.2.1.2 2,7-Bis[2-(4-bromophenyl)ethynyl]naphthalene

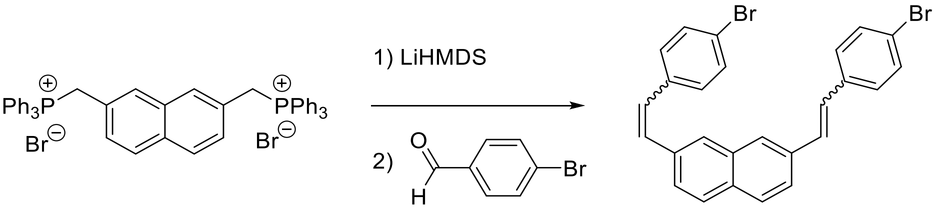

To a suspension of 2,7-bis(triphenylphosphoniomethyl)naphthalene dibromide (2.00 g, 2.39 mmol, 1.0 eq.) in dry THF (30 mL) LiHMDS in THF/ethylbenzene (1.06 M, 5.2 ml, 5.5 mmol, 2.3 eq) was added at −78 °C over 2 min.. The mixture was warmed up to r.t. over 30 min and the solution turned red. A solution of fresh sublimated *p*-bromobenzaldehyde (1.10 g, 6.43 mmol, 2.7 eq.) in dry THF (1.3 mL) was added and the color changed from red to yellow/brown. The mixture was stirred for 24 h at r.t.. The precipitate was filtered off and washed with cold methanol (30 mL) yielding the mixture of the isomers (758 mg, 1.55 mmol, 65 %).[132]

^{1}H NMR (500 MHz, Chloroform-d) δ = 6.60 (d, *J* = 11.9 Hz, 2H), 6.77 (d, *J* = 12.4 Hz, 2H), 7.15 (d, *J* = 8.0 Hz, 4H), 7.26 – 7.32 (m, 2H), 7.35 (d, *J* = 8.0 Hz, 4H), 7.56 – 7.66 (m, 4H).

^{13}C NMR (126 MHz, Chloroform-d) δ = 121.26, 127.07, 127.59, 128.15, 128.18, 129.52, 130.74, 130.94, 131.54, 131.56, 131.98, 134.89, 136.19.

HRMS (ESI(+)): *m/z* (found) = 489.9748

m/z (calc.) = 489.9757.

5.2.1.3 2,15-Dibromo[6]helicene

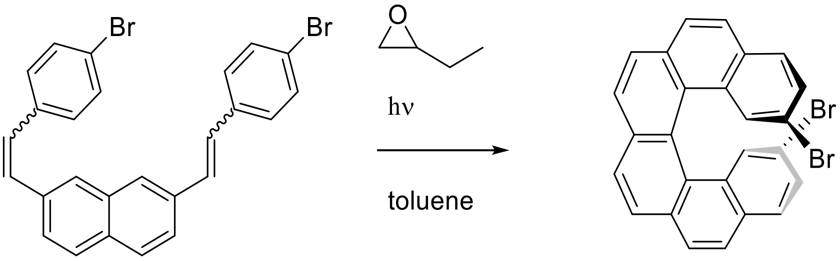

The reaction has been carried out several times, the optimised conditions are presented:

A suspension of 2,7-Bis[2-(4-bromophenyl)ethynyl]naphthalene (80.0 mg, 0.16 mmol, 1.0 eq.), I_2 (85.9 mg, 0.34 mmol, 2.1 eq.) in dry toluene (80.0 mg) was degassed with the freeze pump-thaw-method. Epoxybutane (4 ml) expands upon freezing and therefore was added to the degassed mixture. The mixture was irradiated for 6 h with a 500 W Hg lamp, until the color faded from red to slightly yellow. The solvent of the organic phase was removed in vacuum with an attached liquid nitrogen cooling trap and the residue washed with a minimum amount of $CHCl_3$ (2 x 0.4 ml) yielding the clean product (57.4 mg, 0.12 mmol, 74 %).[126,132]

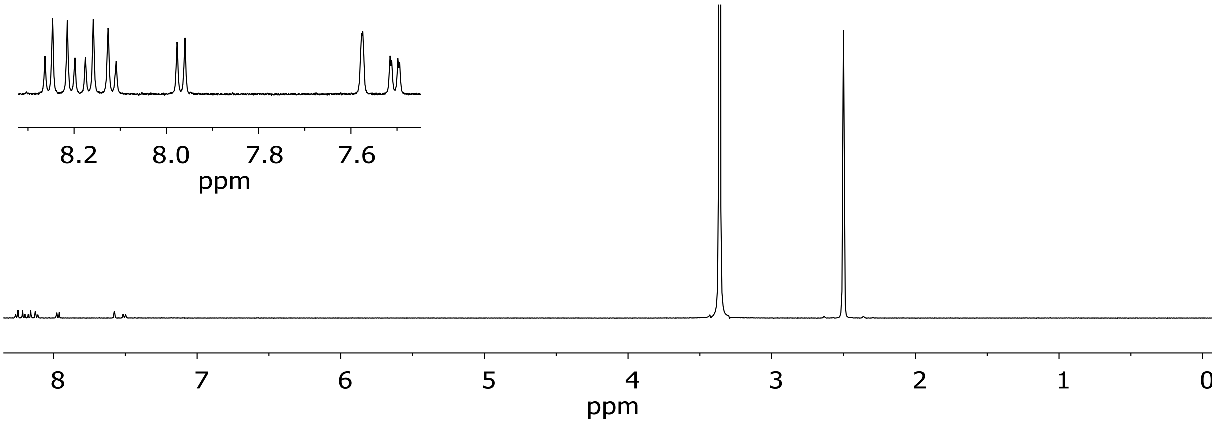

Figure 5.13. **^{1}H NMR spectra in DMSO.**

^{1}H NMR (500 MHz, DMSO-d6): δ = 7.50 (dd, J = 8.5, 2.0 Hz, 2H), 7.58 (d, J = 1.9 Hz, 2H), 7.97 (d, J = 8.5 Hz, 2H), 8.12 (d, J = 8.6 Hz, 2H), 8.17 (d, J = 8.6 Hz, 2H), 8.21 (d, J = 8.2 Hz, 2H), 8.25 (d, J = 8.2 Hz, 2H).

^{1}H NMR (300 MHz, CS_2/CD_2Cl_2 (6/1)): 7.33 – 7.43 (m, 2H), 7.67 (dd, J = 2.1 Hz, 0.8, 2H), 7.74 (d, J = 8.5 Hz, 2H), 7.87 – 8.10 (m, 8H).

^{13}C NMR (75 MHz, CS_2/CD_2Cl_2 (6/1)): δ = 120.36, 124.41, 127.01, 127.42, 128.25, 128.37, 128.40, 129.66, 129.92, 130.56, 131.11, 131.38, 132.58, 133.90.

MS (EI(+)): *m/z* (found) = 485.9

m/z (calc.) = 485.9.

5.2.1.4 3-(4-bromophenyl)pyridine

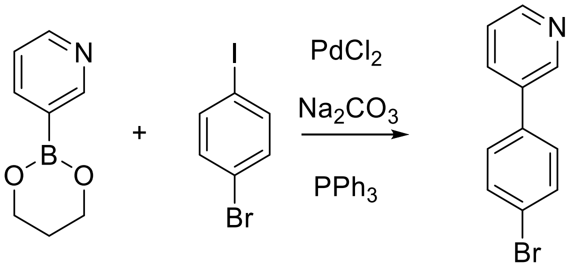

A mixture of 3-pyridineboronic acid 1,3-propanediol ester (370 mg, 2.27 mmol, 1.0 eq.), 1-bromo-4-iodobenzene (936 mg, 3.31 mmol, 1.5 eq.), $PdCl_2$ (20.6 mg, 0.117 mmol, 0.05 eq.), Na_2CO_3 (98.0 mg, 0.924 mmol, 0.4 eq.), PPh_3 (63.6 mg, 0.242 mmol,), toluene (6 ml), ethanol (6 ml) and water (3 ml) were stirred for 24 h at 70 °C. Toluene (30 ml) was added at r.t. and the organic phase was separated from the aqueous phase. The aqueous phase was extracted with ethyl acetate (10 ml). The solvent of the combined organic phases was removed and hydrochloric acid (2M, 12 mL) was added. The aqueous phase was washed with ethyl acetate (10 ml). The aqueous phase was neutralised with sodium hydroxide solution and extracted with ethyl acetate (30 ml). The organic phase was separated and the solvent removed under reduced pressure yielding the target product (447 mg, 1.91 mmol, 84 %).

^{1}H NMR (300 MHz, $CDCl_3$) δ = 7.37 (ddd, J = 7.9, 4.8, 0.9 Hz, 1H), 7.41 – 7.47 (m, 2H), 7.54 – 7.65 (m, 2H), 7.83 (ddd, J = 7.9, 2.4, 1.6 Hz, 1H), 8.62 (dd, J = 4.8, 1.6 Hz, 1H), 8.82 (d, J = 1.8 Hz, 1H).

^{13}C NMR (75 MHz, $CDCl_3$) δ = 122.75, 123.89, 128.79, 132.36, 134.61, 135.79, 136.62, 147.69, 148.44.

MS (EI(+)): *m/z* (found) = 232.9834 *m/z* (calc.) = 232.9840.

5.2.1.5 3-(4-((trimethylsilyl)ethynyl)phenyl)pyridine

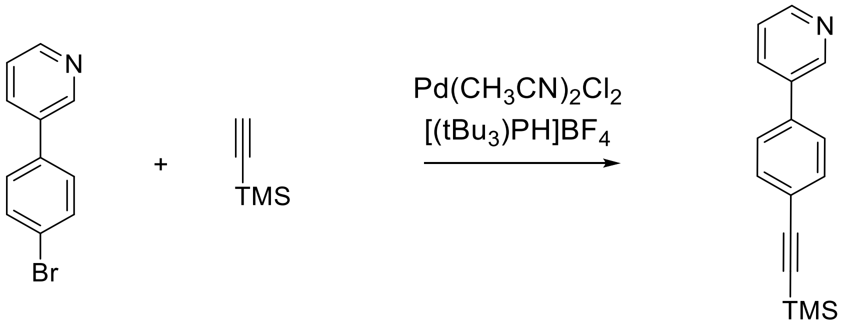

A suspension of 3-(4-bromophenyl)pyridine (393 mg, 1.68 mmol, 1.0 eq.), ethynyltrimethylsilane (220 mg, 2.24 mmol, 1.4 eq.), $Pd(CH_3CN)_2Cl_2$ (58 mg, 0.224 mmol, 6 mol%), $[(t\text{-}Bu)_3PH]BF_4$ (85 mg, 0.293 mmol, 8 mol%), CuI (10 mg, 0.0525 mmol, 3 mol%) in dioxane (10 mL) and NEt_3 (1 mL) was stirred for 24 h at 23 °C under a nitrogen atmosphere.

The solvent was removed and the crude product was purified by column chromatography (SiO_2, ethyl acetate/hexane: 1:2). The desired product was obtained as brown solid (319 mg, 1.27 mmol, 76 %).

^{1}H NMR (300 MHz, $CDCl_3$): δ = 0.27 (s, 9H), 7.38 (s, 1H), 7.47 – 7.61 (m, 4H), 7.86 (d, *J* = 7.9 Hz, 1H), 8.64 (s, 1H), 8.87 (s, 1H).

^{13}C NMR (75 MHz, $CDCl_3$) δ = 0.07, 95.74, 104.61, 123.15, 126.99, 132.75, 134.15, 137.92, 147.78, 148.30.

MS (EI(+)): *m/z* (found) = 236.1[M–CH_3)]$^+$

m/z (calc.) = 236.1[M–CH_3]$^+$.

5.2.1.6 L^1

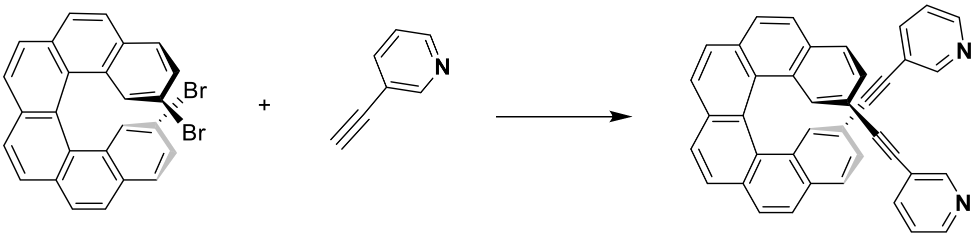

L^1

A suspension of 2,15-Dibromo[6]helicene (100 mg, 0.206 mmol, 1.0 eq.), 3-ethynylpyridine (74.2 mg, 0.720 mmol, 3.5 eq.), $Pd(PPh_3)_4$ (11.9 mg, 0.0103 mmol, 5.0 mol%) and CuI (1.96 mg, 0.0103 mmol, 5.0 mol%) in degased NEt_3 (1 mL) and DMF (15 mL) was stirred under nitrogen atmosphere for 24 h at 85 °C. The solvent was removed under reduced pressure and the crude product was purified by column chromatography (SiO_2, methanol/dichloromethane: 1/100 → 1/10). Recrystallization from hot acetonitrile yielded the clean ligand **L^1** (56.3 mg, 0.106 mmol, 52 %).

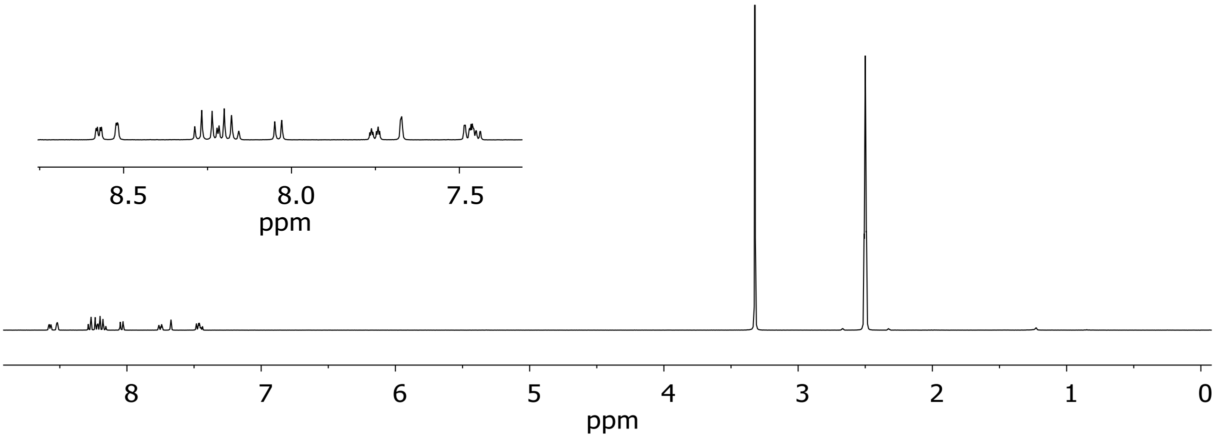

Figure 5.14. ^{1}H NMR spectra of L^1 in DMSO.

^{1}H NMR (300 MHz, DMSO-d6) δ = 7.40 – 7.51 (m, 4H), 7.67 (d, *J* = 1.6 Hz, 2H), 7.75 (dt, *J* = 7.9, 1.9 Hz, 2H), 8.04 (d, *J* = 8.3 Hz, 2H), 8.13 – 8.34 (m, 8H), 8.52 (s, 2H), 8.58 (d, *J* = 3.7 Hz, 2H).

^{1}H NMR (300 MHz, $CDCl_3$) δ = 7.20 – 7.26 (m, 2H), 7.37 (dd, *J* = 8.3, 1.5 Hz, 2H), 7.52 – 7.65 (m, 2H), 7.74 – 7.89 (m, 4H), 7.90 – 8.07 (m, 8Hr), 8.54 (d, *J* = 13.5 Hz, 4H).

^{1}H NMR (400 MHz, CD_3CN) δ = 7.35 (ddd, *J* = 7.9, 4.9, 0.9 Hz, 2H), 7.39 (dd, *J* = 8.2, 1.6 Hz, 2H), 7.67 (ddd, *J* = 7.9, 2.2, 1.7 Hz, 2H), 7.69 – 7.73 (m, 2H), 7.93 (d, *J* = 8.2 Hz, 2H), 8.02 – 8.07 (m, 2H), 8.09 – 8.14 (m, 4H), 8.17 (d, *J* = 8.3 Hz, 2H), 8.51 (dd, *J* = 2.4, 0.9 Hz, 2H), 8.53 (dd, *J* = 5.0, 1.7 Hz, 2H).

^{13}C NMR (75 MHz, $CDCl_3$): δ = 85.33, 93.15, 118.76, 123.14, 124.01, 127.22, 127.50, 127.55, 127.66, 127.77, 127.81, 128.03, 129.21, 131.95, 132.01, 132.25, 133.50, 138.19, 148.35, 152.27.

HRMS (ESI(+)): *m/z* (found) = 531.1869

m/z (calc.) = 531.1856.

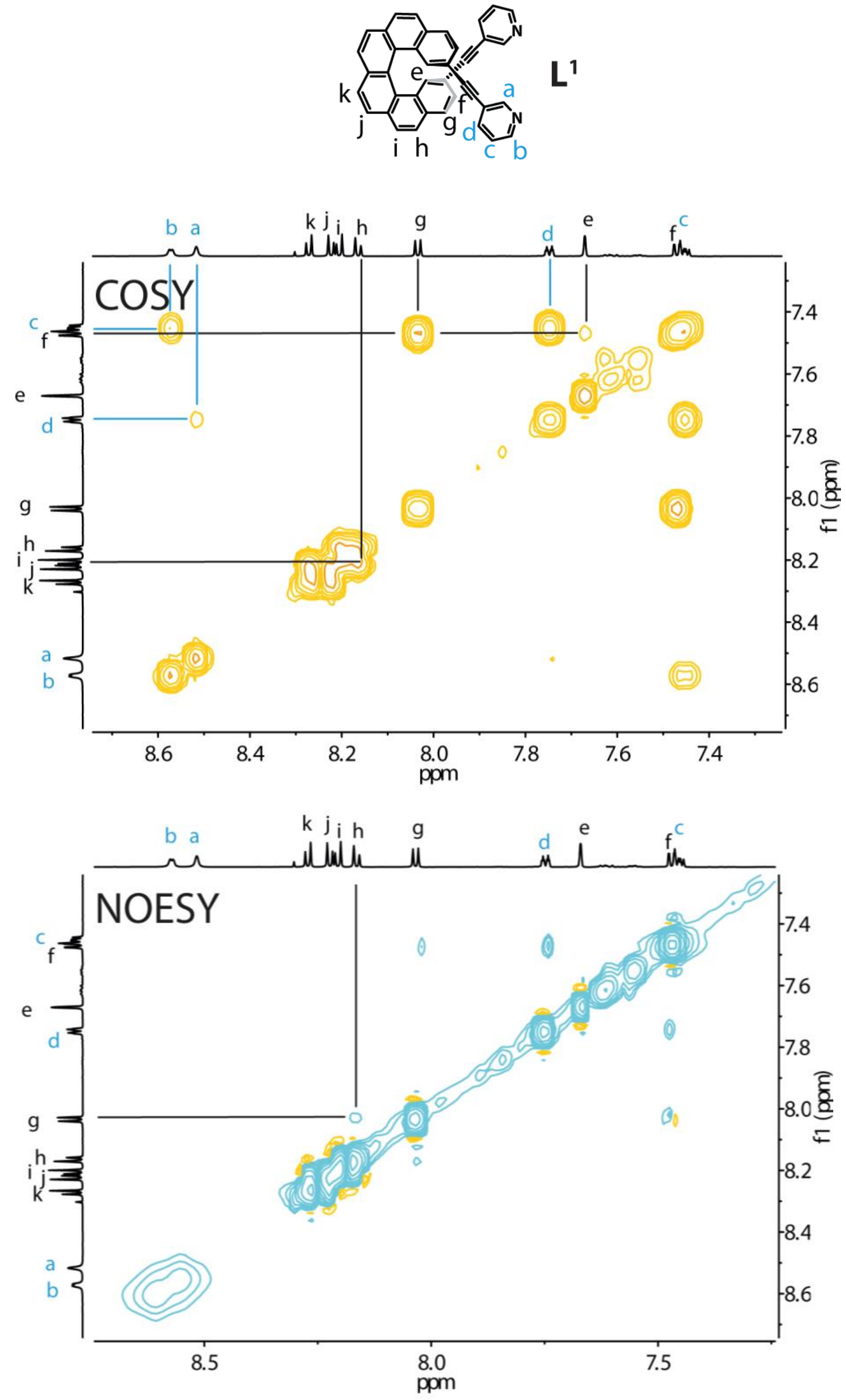

Figure 5.15 ^{1}H-^{1}H COSY and NOESY NMR spectra of L^1 (600 MHz, DMSO-d6). The characteristic signals assigned to H$_a$ and H$_e$ as starting point allowed the assignment of all proton signals due to the COSY and NOESY contacts.

5.2.1.7 L^2

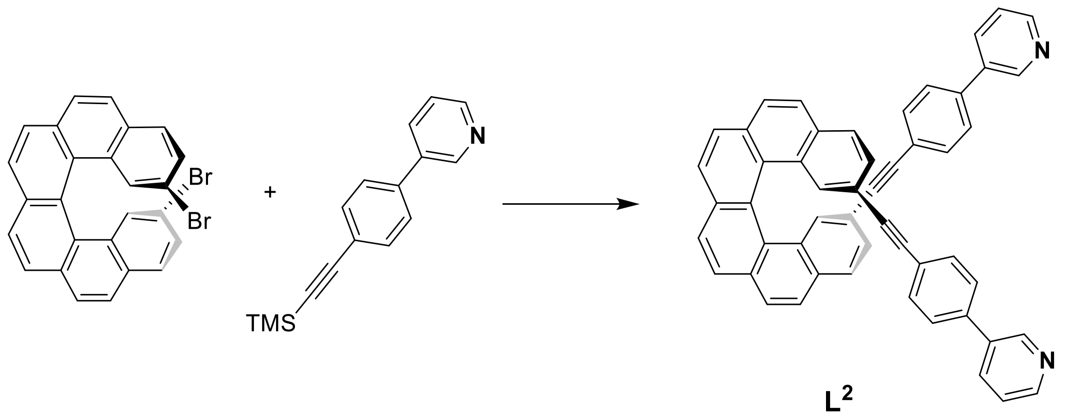

A suspension of 2,15-Dibromo[6]helicene (100 mg, 0.206 mmol, 1.0 eq.), 3-(4-((trimethylsilyl)ethynyl)phenyl)pyridine (155 mg, 0.617 mmol, 3.0 eq.), Pd(PPh$_3$)$_4$ (11.9 mg, 0.0103 mmol, 5.0 mol%), CuI (1.96 mg, 0.0103 mmol, 5.0 mol%) and tetrabutylammonium fluoride solution in THF (1.0 M, 0.72 mL, 0.72 mmol, 3.5 eq.) in degased NEt$_3$ (1 mL) and DMF (15 mL) was stirred under nitrogen atmosphere for 21 h at 85 °C. The solvent was removed under reduced pressure and the crude product was purified by column chromatography (SiO$_2$, methanol/dichloromethane: 1/100 → 1/10). Recrystallization from hot acetonitrile yielded the clean ligand **L^2** (100 mg, 0.147 mmol, 71 %).

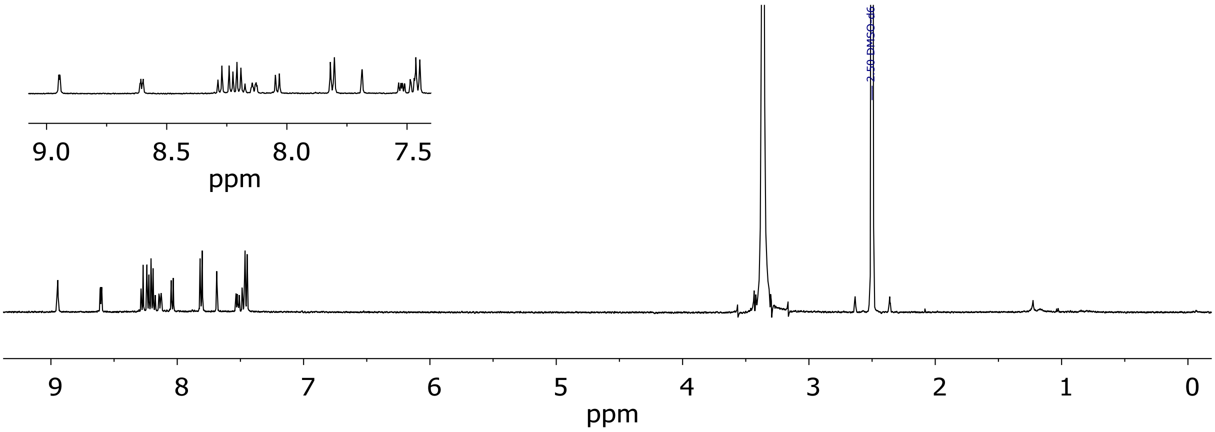

Figure 5.16 ^{1}H NMR spectra in DMSO.

^{1}H NMR (500 MHz, DMSO-d_6): δ = 7.46 (d, J = 8.3 Hz, 4H), 7.48 (dd, J = 8.3 Hz, 1.6, 2H), 7.49 – 7.56 (m, 2H), 7.69 (d, J = 1.5 Hz, 2H), 7.81 (d, J = 8.4 Hz, 4H), 8.04 (d, J = 8.2 Hz, 2H), 8.14 (dt, J = 8.0 Hz, 1.9, 2H), 8.17 – 8.21 (m, 4H), 8.23 (d, J = 8.0 Hz, 2H), 8.28 (d, J = 8.2 Hz, 2H), 8.60 (dd, J = 4.8 Hz, 1.6, 2H), 8.95 (d, J = 2.4 Hz, 2H).

^{13}C NMR (151 MHz, CD_3CN): δ = 89.23, 91.22, 120.09, 123.53, 124.43, 124.70, 127.66, 128.19, 128.48, 128.61, 128.65, 128.70, 129.11, 130.03, 132.29, 132.81, 132.87, 132.93, 134.49, 135.09, 136.28, 138.68, 148.91, 149.86.

HRMS (ESI(+)): *m/z* (found) = 683.2472 $[M+H]^+$

m/z (calc.) = 683.2482 $[M+H]^+$.

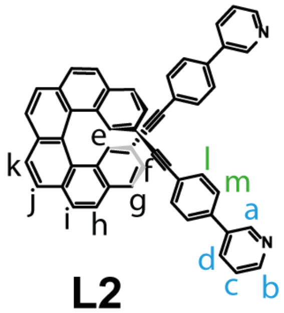

L2

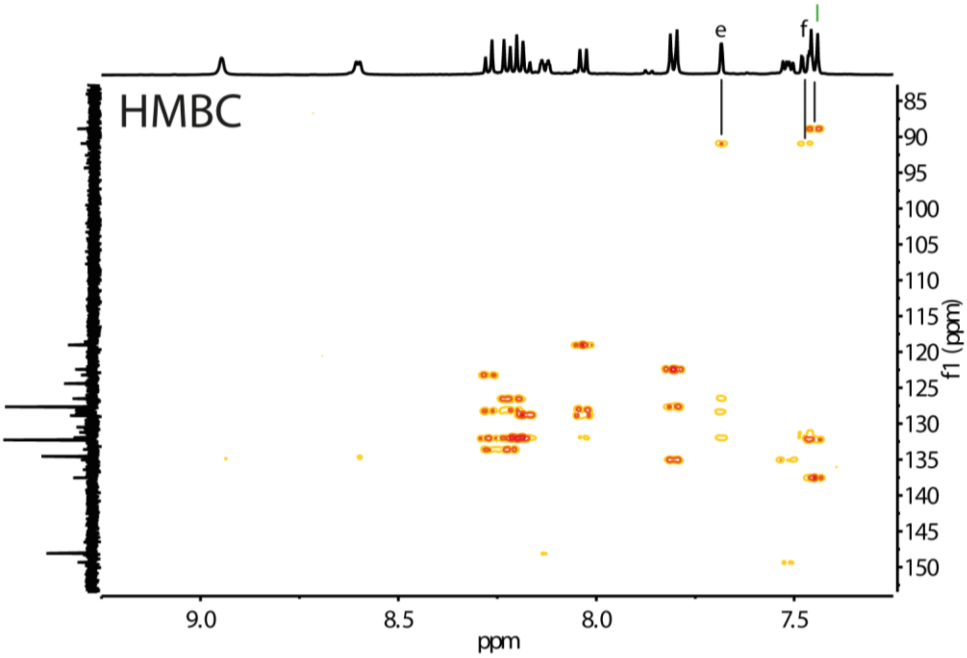

Figure 5.17The ^{1}H-^{13}C HMBC spectra(600 MHz, DMSO-d6) allows the assignment of H_e, H_f and H_l due to the contact with the alkyne carbon atoms.

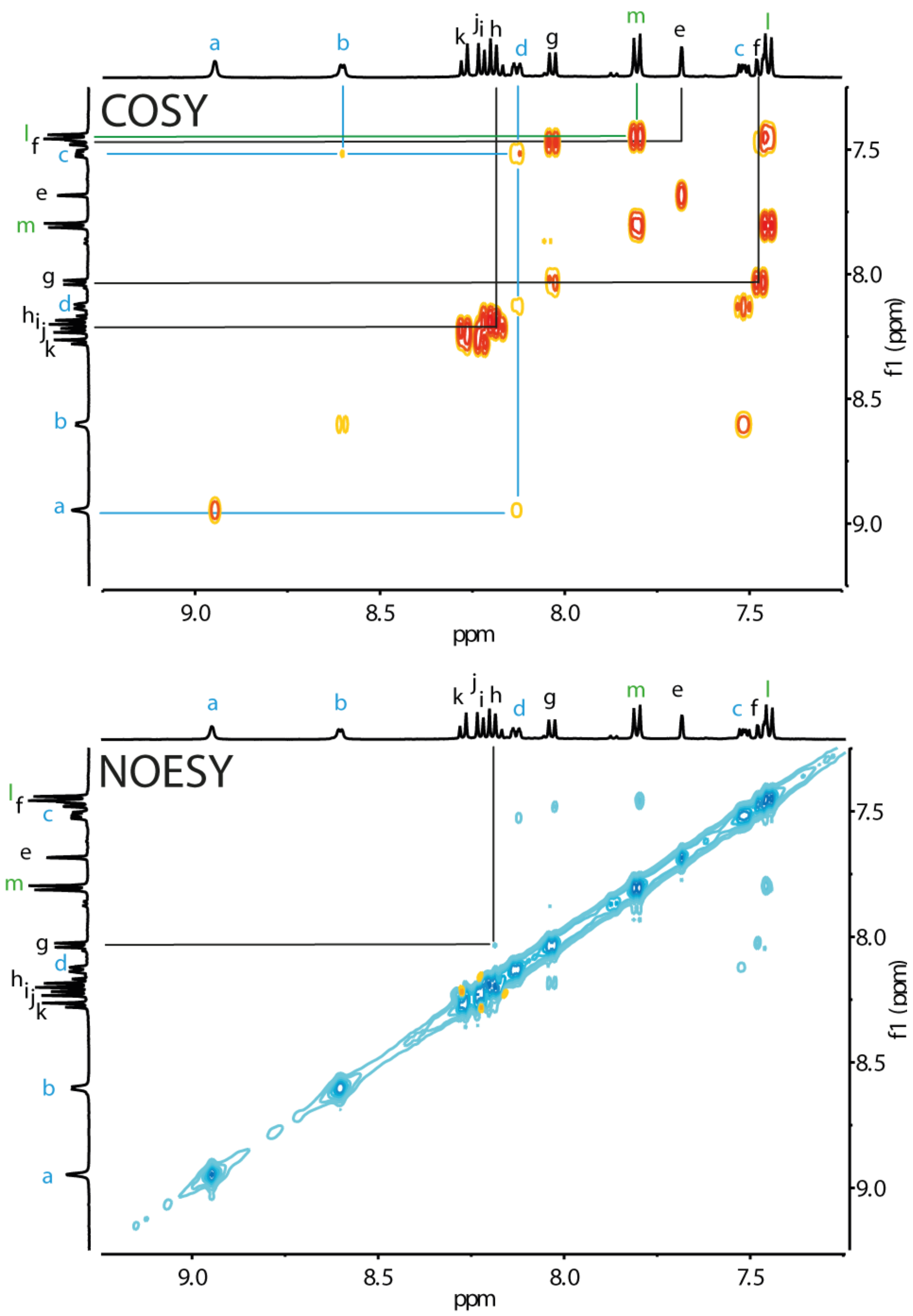

Figure 5.18 ^{1}H-^{1}H COSY and NOESY NMR spectra of L^2 (600 MHz, DMSO-d6). The characteristic singlets of H$_a$ and H$_e$ as starting point allowed the assignment of all proton signals due to the COSY and NOESY contacts.

5.2.2 Cage synthesis

The cage compounds **C1**^{meso}, **C1**$^{P/M}$, **C2**^{mix} and **C2**$^{P/M}$ were prepared in quantitative yields by mixing of the ligands (1.38 µmol, 1.8 eq.) in 550 µL DMSO with 50 µL of a 15 mM DMSO solution of $Pd(CH_3N)_4(BF_4)_2$ (0.72 µmol, 1.0 eq.) at r.t..

C1^{meso} was prepared with the racemic mixture of **L**^{1}. **C1**^{M} was prepared with the first HPLC fraction of **L**^{1}. **C1**^{P} was prepared with the second HPLC fraction of **L**^{1}. **C2**^{P} was prepared with the second HPLC fraction of **L**^{2}. **C2**^{M} was prepared with the first HPLC fraction of **L**^{2}.

The cage compound **DC2**^{M} was prepared by mixing of the first HPLC fraction of **L**^{2} (1.38 mol, 1.8 eq.) in 550 µL CD_3CN with 50 µL of a 15 mM CD_3CN solution of $Pd(CH_3N)_4(BF_4)_2$ (0.72 mol, 1.0 eq.) at 75 °C for 2 weeks and filtering. The cage compound **DC2**^{P} were prepared by mixing of the second HPLC fraction of **L**^{2} (1.38 mol, 1.8 eq.) in 550 µL CD_3CN with 50 µL of a 15 mM CD_3CN solution of $Pd(CH_3N)_4(BF_4)_2$ (0.72 mol, 1.0 eq.) at 75 °C for 2 weeks and filtering. For crystallization attempts, the cage compound **C2**^{M} was also prepared by mixing of the ligands (1.38 µmol, 1.8 eq.) in 550 µL CD_3CN with 50 µL of a 15 mM CD_3CN solution of $Pd(CH_3N)_4(PF_6)_2$ (0.72 µmol, 1.0 eq.) at r.t..

5.2.2.1 C1^{meso}

^{1}H NMR (400 MHz, DMSO-d6) δ = 7.00 (d, J = 8.3 Hz, 4H), 7.39 (d, J = 8.6 Hz, 4H), 7.51 (d, J = 1.4 Hz, 4H), 7.57 (d, J = 8.2 Hz, 4H), 7.60 (d, J = 1.4 Hz, 4H), 7.66 (dd, J = 8.1, 1.5 Hz, 4H), 7.72 – 7.77 (m, 4H), 7.84 (d, J = 8.7 Hz, 4H), 7.94 (d, J = 8.0 Hz, 4H), 7.99 (d, J = 8.1 Hz, 4H), 8.04 – 8.08 (m, 12H), 8.17 (d, J = 8.2 Hz, 4H), 8.19 – 8.33 (m, 16H), 9.29 (d, J = 5.7 Hz, 4H), 9.38 (s, 4H), 9.53 (d, J = 1.9 Hz, 4H), 9.67 (t, J = 3.7 Hz, 4H).

5.2.2.2 C1$^{P/M}$

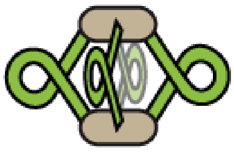

^{1}H NMR (500 MHz, DMSO-d6): δ = 7.53 (d, J = 8.2 Hz, 4H), 7.58 (s, 8H), 7.79 (d, J = 8.8 Hz, 4H), 7.87 (t, J = 6.9 Hz, 4H), 8.06 (d, J = 8.7 Hz, 4H), 8.14 (d, J = 8.2 Hz, 8H), 8.23 (d, J = 8.3 Hz, 4H), 9.34 (d, J = 5.8 Hz, 4H), 9.37 (s, 4H).

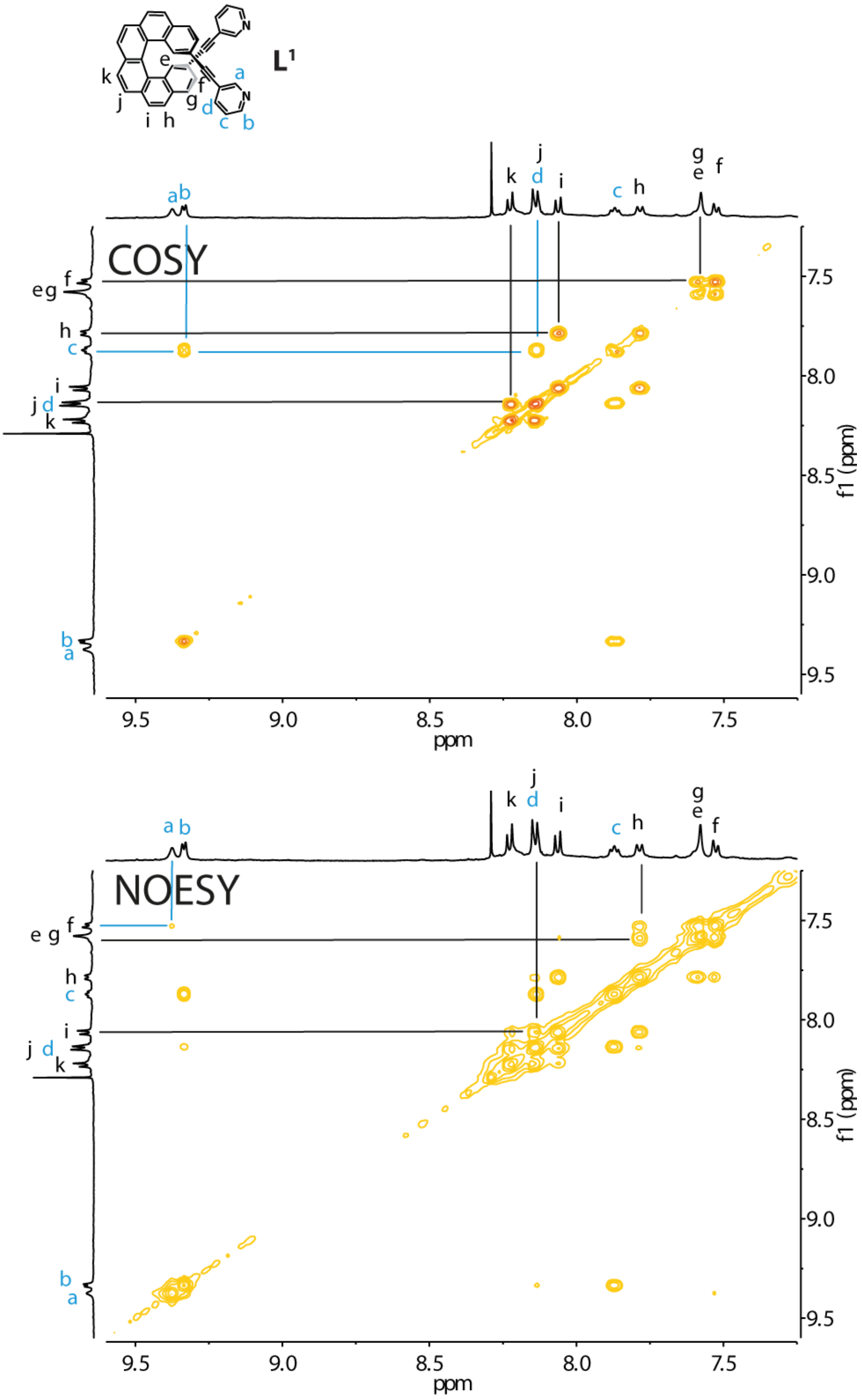

Figure 5.19 ^{1}H-^{1}H COSY and NOESY NMR spectra of C1$^{P/M}$ (500 MHz, DMSO-d6) with $CHCl_3$ for better separation of H_a and H_b.

5.2.2.3 C2$^{P/M}$ enantiopure DMSO

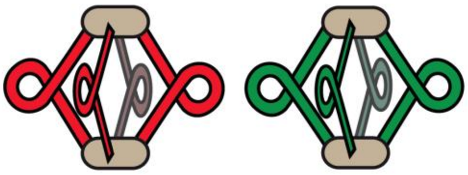

^{1}H NMR (500 MHz, DMSO-d6): *δ* = 7.54 (dd, *J* = 7.9, 1.6 Hz, 8H), 7.60 (s, 8H), 7.69 (d, *J* = 8.2 Hz, 16H), 7.81 (d, *J* = 8.2 Hz, 8H), 7.88 – 7.95 (m, 32H), 8.09 (d, *J* = 8.8 Hz, 8H), 8.14 (d, *J* = 8.2 Hz, 8H), 8.20 (d, *J* = 8.4 Hz, 8H), 8.49 (d, J = 8.1 Hz, 8H), 9.43 (d, *J* = 6.0 Hz, 8H), 9.82 (s, 8H).

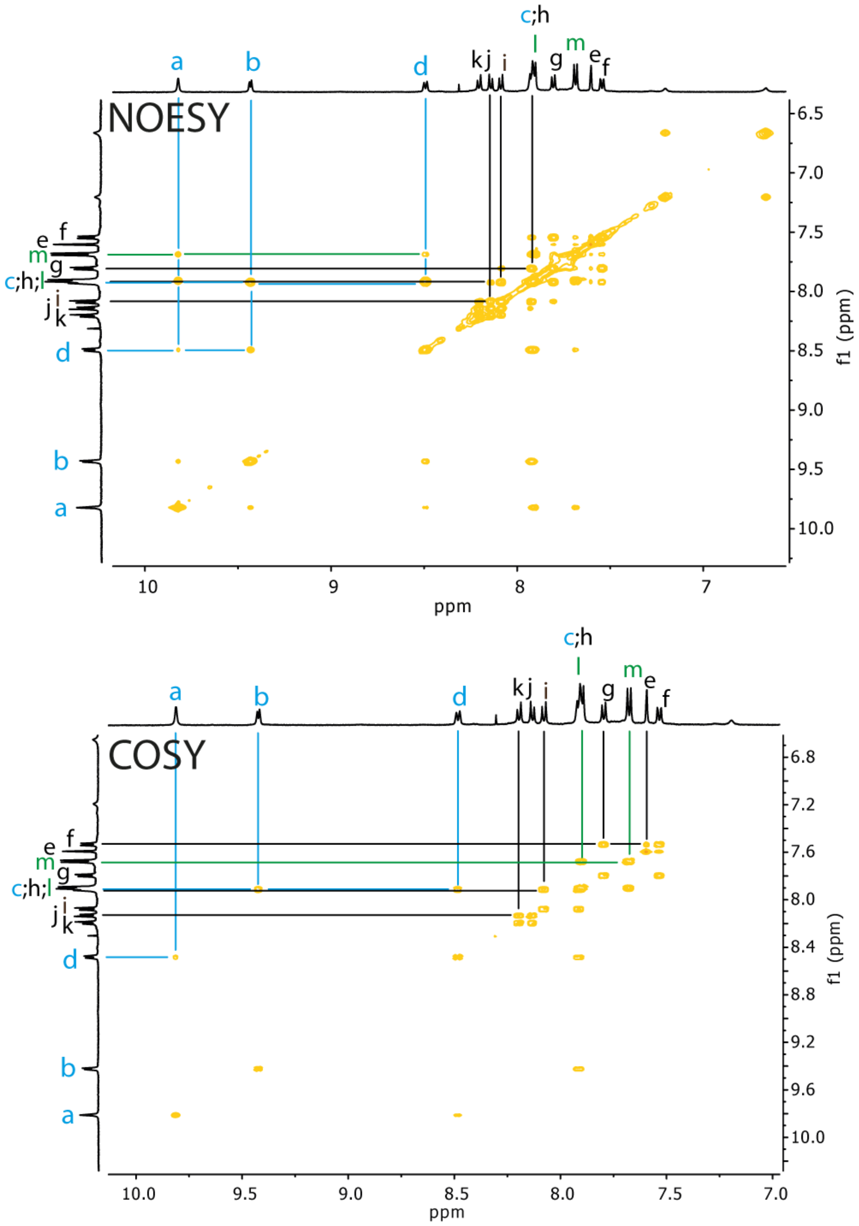

Figure 5.20^{1}H-^{1}H COSY and NOESY NMR spectra of C2$^{P/M}$ (500 MHz, DMSO-d6).

5.2.2.4 C2$^{P/M}$ enantiopure CD$_3$CN (PF$_6$)

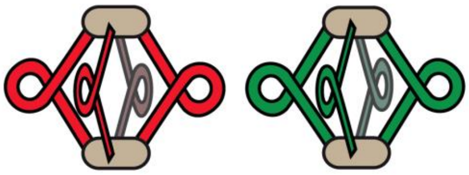

^{1}**H NMR** (500 MHz, CD$_3$CN): δ = 1H NMR (600 MHz, CD$_3$CN) δ = 7.45 (dd, J = 8.0 Hz, 1.6, 8H), 7.63 (d, J = 8.1 Hz, 16H), 7.68 (s, 8H), 7.73 (dd, J = 7.9, 5.9 Hz, 8H), 7.76 (d, J = 8.1 Hz, 16H), 7.78 (d, J = 8.0 Hz, 8H), 7.85 (d, J = 8.7 Hz, 8H), 8.01 (d, J = 8.7 Hz, 8H), 8.06 (d, J = 8.1 Hz, 8H), 8.12 (d, J = 8.2 Hz, 8H), 8.27 (d, J = 8.2 Hz, 8H), 9.09 (d, J = 5.2 Hz, 8H), 9.56 (s, 8H).

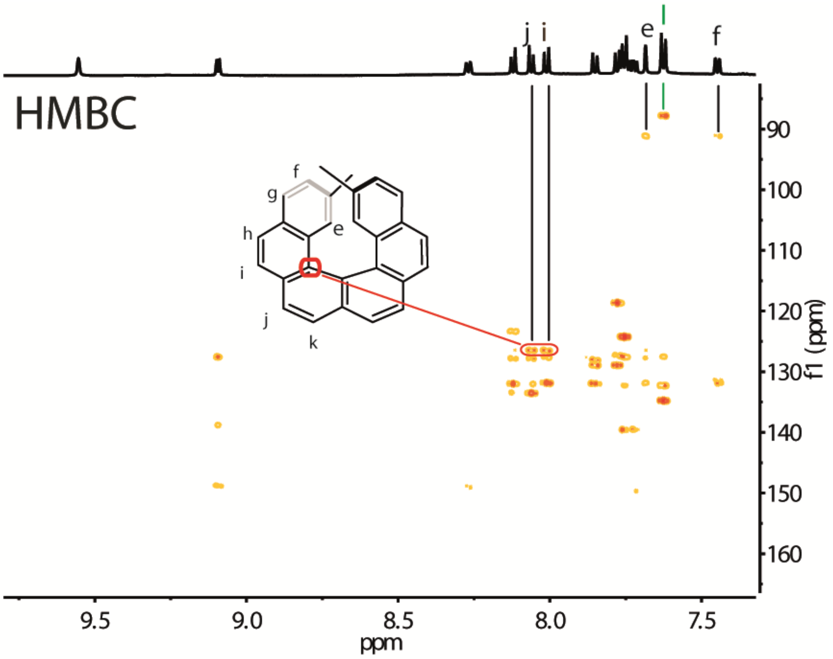

Figure 5.21. **The ^{1}H-^{13}C HMBC NMR spectra of C2$^{P/M}$ (500 MHz, CD$_3$CN) allows the assignment of H$_e$, H$_f$ and H$_l$ due to the contacts with the alkyne carbon atoms and supports the assignment for H$_i$ and H$_j$ based on COSY and NOESY spectra.**

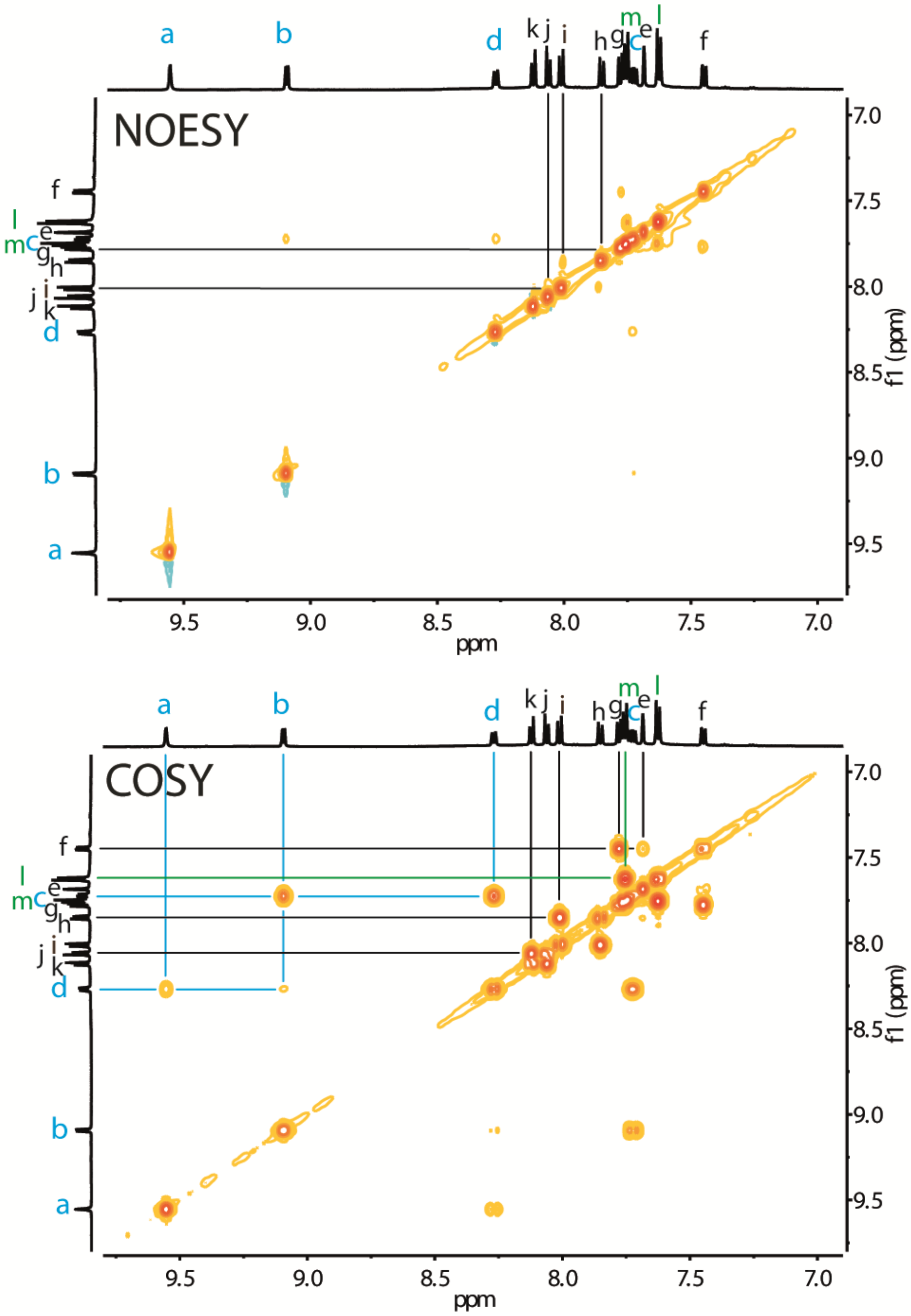

Figure 5.22. ^{1}H-^{1}H COSY and NOESY NMR spectra of C2$^{P/M}$ (500 MHz, CD$_3$CN). All signals could be assigned.

5.2.2.5 DC2$^{M/P}$ enantiopure CD$_3$CN interpenetrated cage

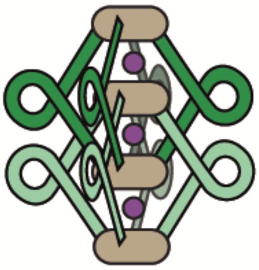

^{1}H NMR (600 MHz, CD$_3$CN): δ = 6.02 (d, J = 7.7 Hz, 8H), 6.62 (d, J = 7.4 Hz, 16H), 6.85 (d, J = 7.8 Hz, 8H), 7.41 – 7.46 (m, 8H), 7.48 (d, J = 7.5 Hz, 16H), 7.61 (t, J = 8.1 Hz, 16H), 7.66 (d, J = 7.7 Hz, 16H), 7.72 (s, 8H), 7.81 (s, 8H), 7.89 (d, J = 8.2 Hz, 24H), 7.99 (d, J = 7.9Hz, 16H), 8.03 – 8.13 (m, 24H), 8.16 (d, J = 8.2 Hz, 8H), 8.21 (d, J = 8.0 Hz, 8H), 8.29 (d, J = 8.2 Hz, 8H), 8.45 (d, J = 7.6 Hz, 16H), 9.26 (d, J = 6.0 Hz, 8H), 9.46 (d, J = 5.9 Hz, 8H), 9.81 (s, 8H), 9.86 (s, 8H).

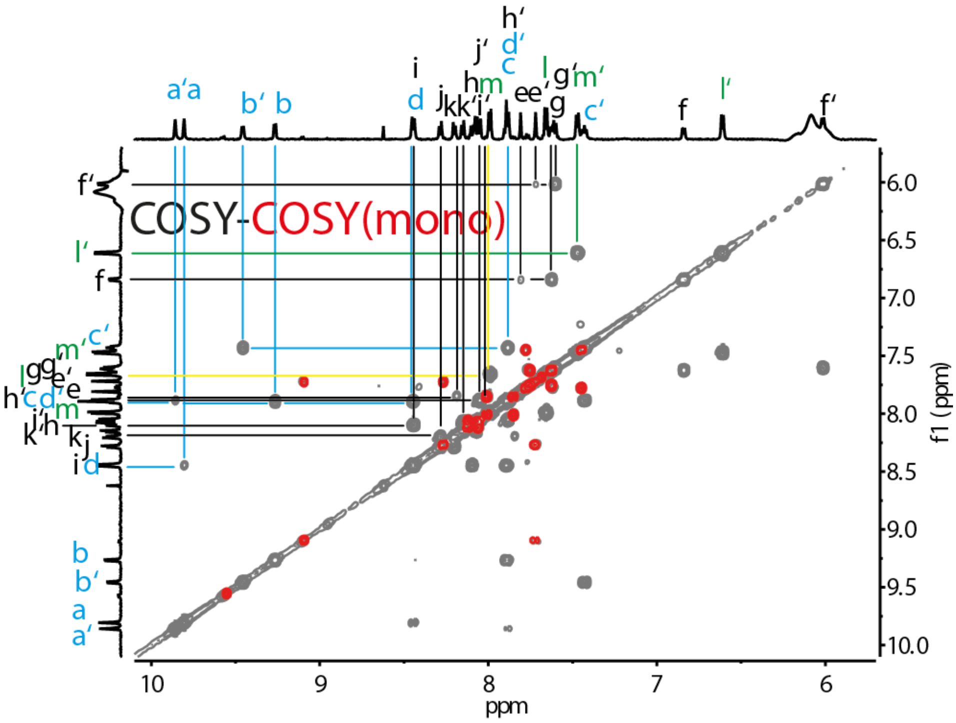

Figure 5.23. COSY of DC2$^{P/M}$ (black) (600 MHz, CD_3CN) and C2$^{P/M}$ (red) (500 MHz, CD_3CN) to allow clear assignment of the proton contacts of DC2$^{P/M}$, as a few percent of monomeric cage remained in the sample of the double cage.

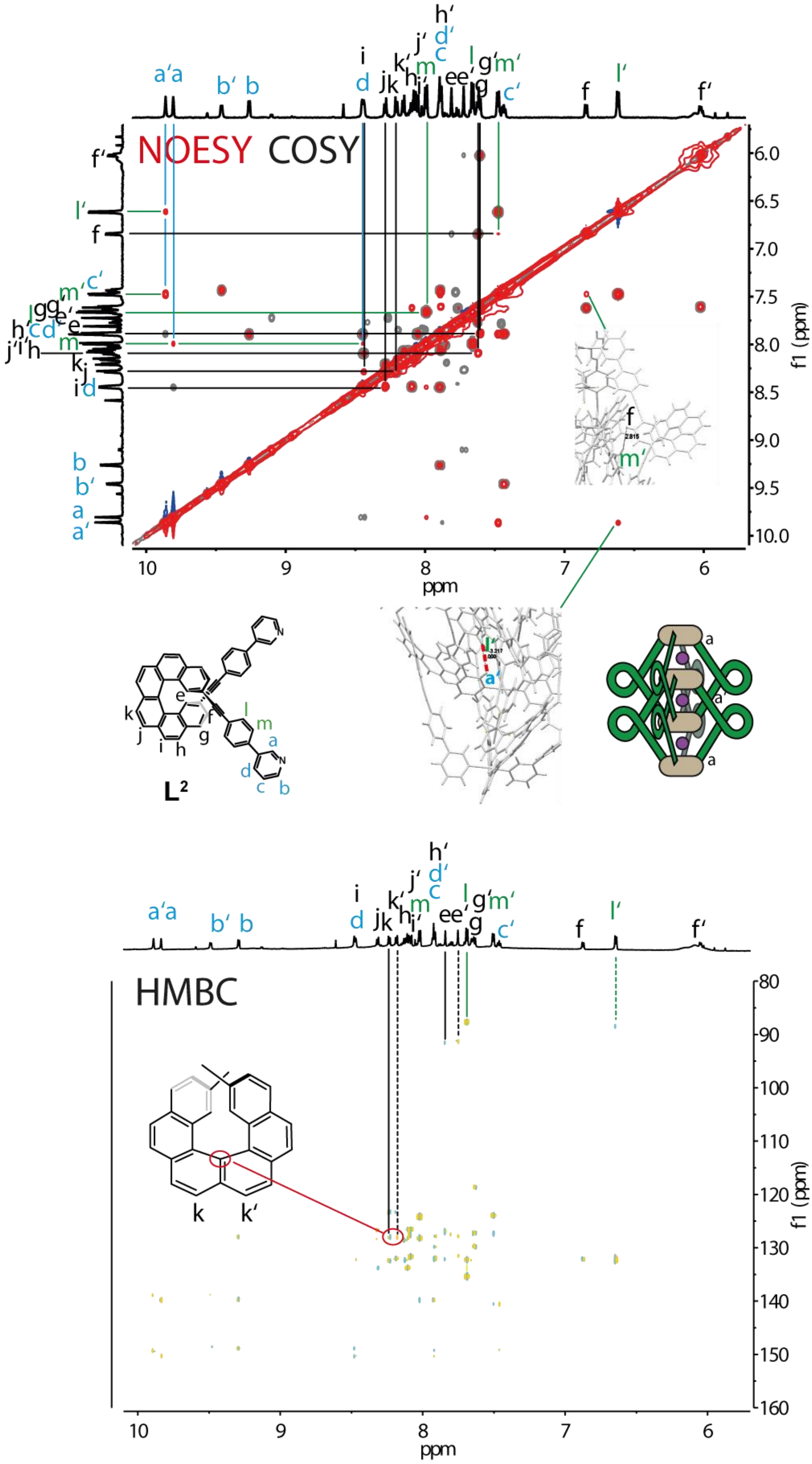

Figure 5.24. **Combined ^{1}H-^{1}H COSY and NOESY NMR spectra of DC2$^{P/M}$ (600 MHz, CD$_3$CN) and the ^{1}H-^{13}C HMBC spectrum. All contacts could be assigned and are in agreement with the crystal structure of DC2^M.**

5.2.3 DOSY of C1^{meso}, C1$^{P/M}$ and C2$^{P/M}$

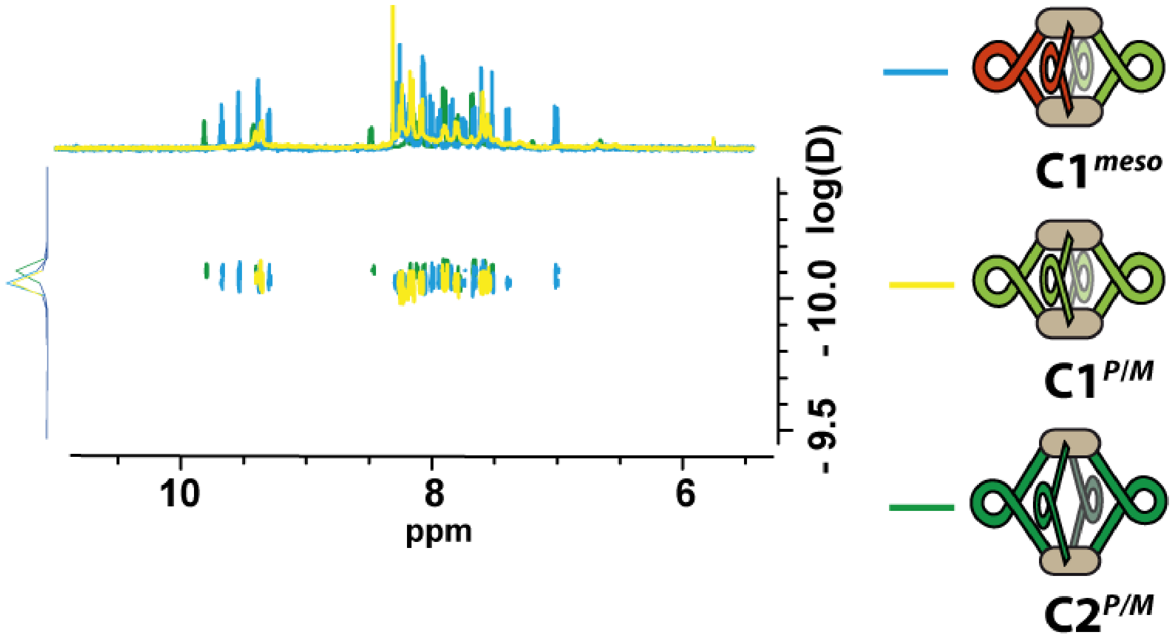

Figure 5.25. **Superimposed ^{1}H DOSY spectra of C1^{meso}, C1$^{P/M}$ and C2$^{P/M}$.**

The hydrodynamic radii were calculated using the Stokes-Einstein equation:

$$r = \frac{k \cdot T}{6 \cdot \pi \cdot \eta \cdot D}$$

With r = radius, k = Boltzmann const., T = Temp., η = dynamic viscosity of DMSO and D = Diffusion values estimated by the DOSY experiment.

C1^{meso} d = 25.7 Å

C1$^{P/M}$ d = 25.4 Å

C2$^{P/M}$ d = 28.1 Å

The results differ only slightly, even so **C2** has a Pd-Pd distance that is around twice as big, as the one for the **C1** cage, but the distance between the helicene backbones opposite to each other is only slightly affected.

5.2.4 Titration Experiments

The camphor sulfonate, 4,4’biphenyl bis-sulfonate, 2,7naphtalene bis-sulfonate and 4,4′-azobenzene bis-sulfonate guests were prepared as reported in literature.[136,148] The host/guest ratio was controlled via ^{1}H NMR for every titration step.

5.2.5 Pascal's triangle for the cage formation with a racemic ligand mixture

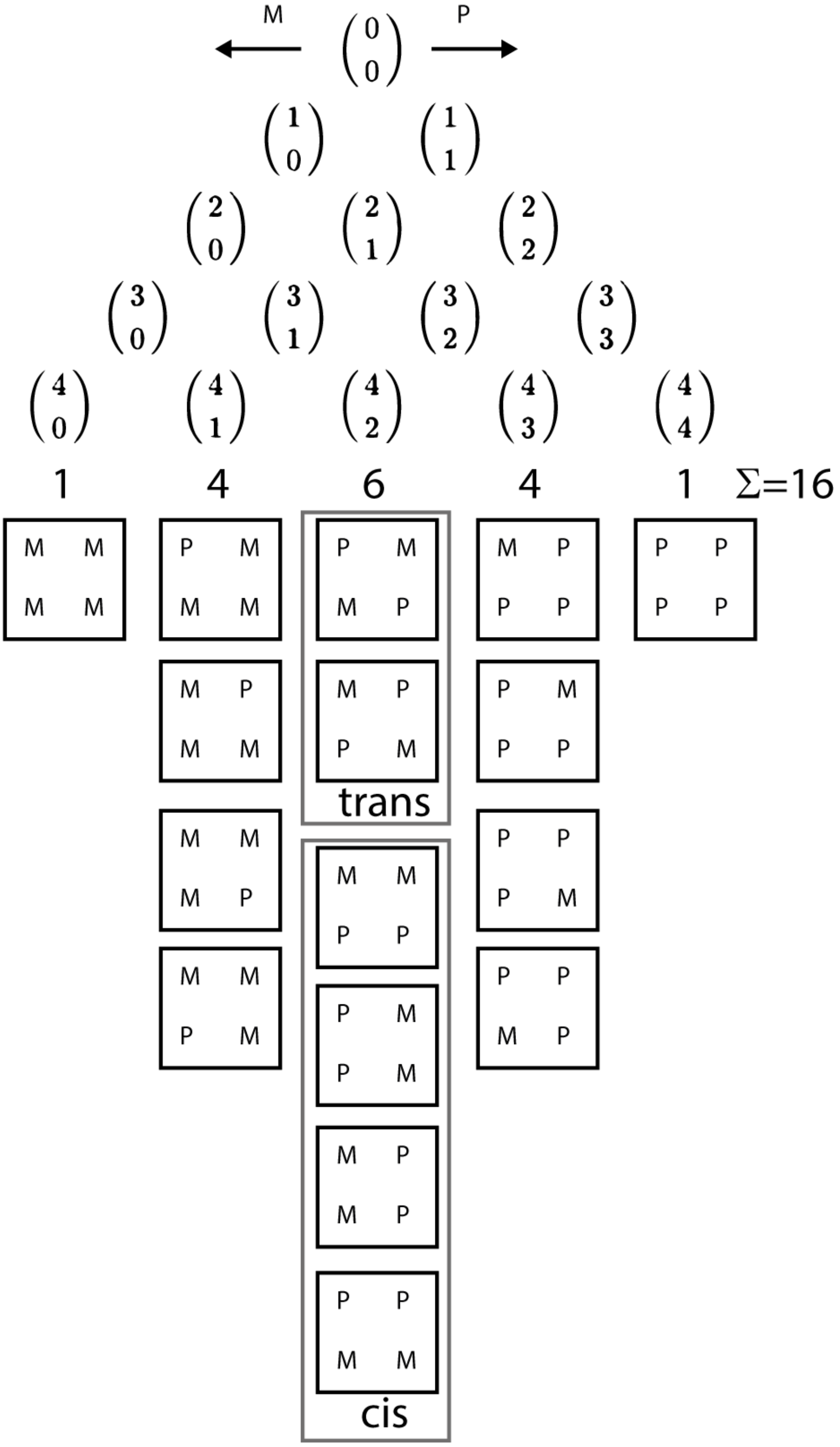
M
P
1
4
6
4
1
Σ=16
M M M M
P M M M
M P M M
M M M P
M M P M
P M M P
M P P M
trans
M M P P
P M P M
M P M P
P P M M
cis
M P P P
P M P P
P P P M
P P M P
P P P P

Figure 5.26 Pascal's triangle for the cage formation with a racemic ligand mixture. The probability is the number of combinations for one set, divided by the total number of combinations.

5.2.6 Single-crystal X-ray Crystallography

5.2.6.1 X-ray data of L^{2P}

Single crystals of $\mathbf{L}^{2P}$ were obtained by slow evaporation of a DMSO solution. A single crystal was mounted in NVH oil on a nylon loop. X-ray diffraction data were collected at 100(2) K on a Bruker D8 venture equipped with an Incoatec microfocus source (Iµs 2.0) using Mokα radiation and an Oxford Cryostream 800 at 100(2) K. Data integration and reduction were undertaken with SAINT and XPREP. Multi-scan empirical absorption correction was applied to the data using SADABS. The structure was solved by direct methods using SHELXD[149] and refined with SHELXL[134] using 22 CPU cores for full-matrix least-squares routines on F^2 and ShelXle[146] as a graphical user interface. Hydrogen atoms were included as invariants at geometrically estimated positions. There are twelve independent helicene molecules in the asymmetric unit. Nine of which are partially disordered due to their conformational flexibility. All four DMSO solvent molecules are disordered. Techniques commonly applied for macromolecular structures were employed to generate a molecular model and increase robustness of the refinement. Stereochemical restraints for helicene ligands (TSP), and disordered DMSO solvent molecules of the structure were generated by the GRADE program using the GRADE Web Server (http://grade.globalphasing.org) and applied in the refinement. A GRADE dictionary for SHELXL contains target values and standard deviations for 1.2-distances (DFIX) and 1.3-distances (DANG), as well as restraints for planar groups (FLAT). The refinement of ADP's for non-hydrogen atoms was enabled by using the rigid bond restraint (RIGU)[150] in the SHELXL program. SIMU restraints were additionally employed The TABS keyword behind the ACTA instruction was employed to generate the CIF. Similar distance restraints (SADI) were used additionally for 1.2 and 1.3 distances of DMSO solvent molecules to ensure similarity of bonds and angles in between the 8 disordered DMSO components. The absolute configuration was unambiguously determined using the method of Parsons[96] as implemented in SHELXL, yielding an enantiopure distinguishing parameter of x = 0.079(8).

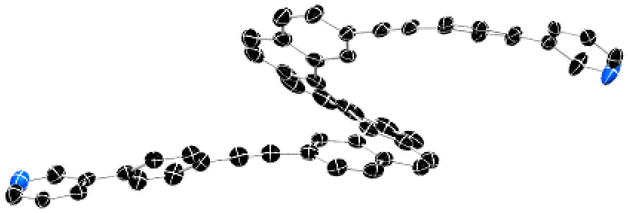

Figure 5.27 ORTEP drawing of one of the twelve ligands L^{2P}, which are present in the asymmetric unit.

Table S1. Crystal data and structure refinement for **L**^{2P} (CCDC 1558206).

Identification code	tspl2	
Empirical formula	C632 H384 N24 O4 S4	
Formula weight	8505.85	
Temperature	100(2) K	
Wavelength	1.54178 Å	
Crystal system	Monoclinic	
Space group	$P2_1$	
Unit cell dimensions	a = 18.2938(7) Å	α= 90°.
	b = 39.7389(15) Å	β= 91.609(2)°.
	c = 30.4852(11) Å	γ = 90°.
Volume	22153.3(14) Å^3	
Z	2	
Density (calculated)	1.275 Mg/m^3	
Absorption coefficient	0.743 mm^{-1}	
F(000)	8880	
Crystal size	0.248 x 0.120 x 0.064 mm^3	
Theta range for data collection	2.224 to 79.341°.	
Index ranges	-23<=h<=22, -50<=k<=49, -24<=l<=36	
Reflections collected	410955	
Independent reflections	91631 [R(int) = 0.0712]	
Completeness to theta = 67.679°	99.6 %	
Absorption correction	Semi-empirical from equivalents	
Max. and min. transmission	0.7542 and 0.6931	
Refinement method	Full-matrix least-squares on F^2	
Data / restraints / parameters	91631 / 16769 / 6907	
Goodness-of-fit on F^2	1.032	
Final R indices [I>2sigma(I)]	R1 = 0.0738, wR2 = 0.1878	
R indices (all data)	R1 = 0.1282, wR2 = 0.2254	
Absolute structure parameter	0.079(8)	
Extinction coefficient	n/a	
Largest diff. peak and hole	0.748 and -0.482 e.Å^{-3}	

5.2.6.2 X-ray data of DC2^{M}

Single crystals of [2PF$_6$@Pd$_4$**L**$^{\mathbf{2}M}{}_8$] (**DC2^{M}**) suitable for X-ray structure analysis were obtained by slow diffusion of ether into an acetonitrile solution of the mono cage. The very thin, needle shaped crystals are extremely volatile due to loss of solvent. Single crystals were mounted in on a nylon loop using NVH oil and immediately flash cooled and stored in liquid nitrogen to prevent subsequent solvent loss. Due to their tiny dimensions of 0.1 x 0.001 x 0.001 mm^3 crystals required synchrotron radiation in order to achieve a resolution sufficient for structure solution using direct methods. Hence, X-ray data were collected at 80(2) K at the DESY beamline P11 using a radiation wavelength of 0.6889 Å.[151] A single 360° φ scan was collected in steps of 0.2° and 0.2 seconds exposure time per frame at a detector distance of 156 mm and 100% transmission filter. Data integration and reduction were undertaken using XDS.[152] Due to disorder in the solvent region a higher resolution could not be achieved, with such small crystal dimensions (0.1 x 0.001 x 0.001 mm). The data was cut at 0.97 A, as the signal to noise ration has dropped below $I/\sigma(I) < 2.0$. The structure was solved by intrinsic phasing/direct methods using SHELXT[145] and refined with SHELXL using 22 CPU cores for full-matrix least-squares routines on F^2 and ShelXle as a graphical user interface. Hydrogen atoms were included as invariants at geometrically estimated positions.

Techniques commonly applied for macromolecular structures were employed to generate a molecular model and increase robustness of the refinement. Stereochemical restraints for the TSP ligands and ETO [(Et)$_2$O] solvent of the structure were generated by the GRADE program using the GRADE Web Server (http://grade.globalphasing.org) and applied in the refinement. A GRADE dictionary for SHELXL contains target values and standard deviations for 1.2-distances (DFIX) and 1.3-distances (DANG), as well as restraints for planar groups (FLAT). The ETO solvent is disordered over a special position (2 fold axis) and the GRADE restraint dictionary was manually adapted to match the symmetry equivalent atoms. All non-hydrogen atoms, but the atoms of (Et)$_2$O solvent were refined anisotropically. The refinement of ADP's for non-hydrogen atoms was enabled by using the new rigid bond restraint (RIGU) in the SHELXL program. SIMU restraints were additionally employed. The contribution of the electron density associated with disordered counterions and solvent molecules, which could not be modelled with discrete atomic positions were handled using the SQUEEZE[147] routine in PLATON[153]. Solvent masks (.fab files) generated by PLATON were included in the SHELXL refinement via the ABIN instruction leaving the original structure factors untouched.

The absolute configuration was unambiguously determined using the method of Parsons[96] as implemented in SHELXL[134], yielding an enantiopure distinguishing parameter of $x = -0.02(2)$.

Table S2. Crystal data and structure refinement for **DC2**^{M} (CCDC 1581540).

Identification code	sl660c_sq	
Empirical formula	C420 H250 F30 N16 O P5 Pd4	
Formula weight	6686.80	
Temperature	80(2) K	
Wavelength	0.6888 Å	
Crystal system	Orthorhombic	
Space group	I222	
Unit cell dimensions	a = 18.482(4) Å	α= 90°.
	b = 29.545(6) Å	β= 90°.
	c = 36.264(7) Å	γ = 90°.
Volume	19802(7) Å^3	
Z	2	
Density (calculated)	1.121 Mg/m^3	
Absorption coefficient	0.242 mm^{-1}	
F(000)	6838	
Crystal size	0.1 x 0.001 x 0.001 mm^3	
Theta range for data collection	0.862 to 20.796°.	
Index ranges	-19<=h<=19, -30<=k<=30, -37<=l<=37	
Reflections collected	75625	
Independent reflections	11362 [R(int) = 0.0833]	
Completeness to theta = 20.796°	100.0 %	
Absorption correction	None	
Refinement method	Full-matrix least-squares on F^2	
Data / restraints / parameters	11362 / 2381 / 1109	
Goodness-of-fit on F^2	0.993	
Final R indices [I>2sigma(I)]	R1 = 0.0795, wR2 = 0.2151	
R indices (all data)	R1 = 0.1105, wR2 = 0.2430	
Absolute structure parameter	-0.02(2)	
Extinction coefficient	n/a	
Largest diff. peak and hole	1.324 and -0.452 e.Å^{-3}	

5.2.7 Conformational flexibility of the helicene backbone

The presence of twelve independent ligands in the **L**^{2P} structure and two ligands in the **DC2**^{M} structure, allows us to better understand the flexibility of the helicene backbone. The distance between the two terminal carbon atoms (C15 and C39) bound to the adjacent imine groups was chosen as representative value for this purpose. It was calculated with standard uncertainty using SHELXL and varies in between: 3.8285 ± 0.0063 Å (residue 6) and 4.4653 ± 0.0071 Å (residue 10) of **L**^{2P}.

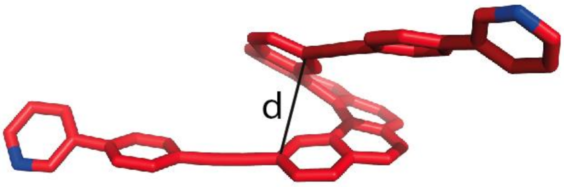

Table 5.5. **d from the crystal structure of DC2**^{M}**.**

d	residue	between
4.0251	(0.0195)	C15_2 - C39_2
4.3275	(0.0211)	C15_3 - C39_3

Table 5.6. **d from the crystal structure of L**^{2P}**:**

d	residue	between
4.3073	(0.0077)	C15_1 - C39_1
4.2875	(0.0071)	C15_2 - C39_2
3.8622	(0.0062)	C15_3 - C39_3
3.8427	(0.0069)	C15_4 - C39_4
4.3608	(0.0068)	C15_5 - C39_5
3.8285	(0.0063)	C15_6 - C39_6
3.8870	(0.0059)	C15_7 - C39_7
4.4886	(0.0066)	C15_8 - C39_8
4.4506	(0.0067)	C15_9 - C39_9
4.4653	(0.0071)	C15_10 - C39_10
4.4224	(0.0073)	C15_11 - C39_11
4.4368	(0.0066)	C15_12 - C39_12

5.3 Nature inspired backbones for supramolecular assemblies

5.3.1 L^{H2} in DMSO

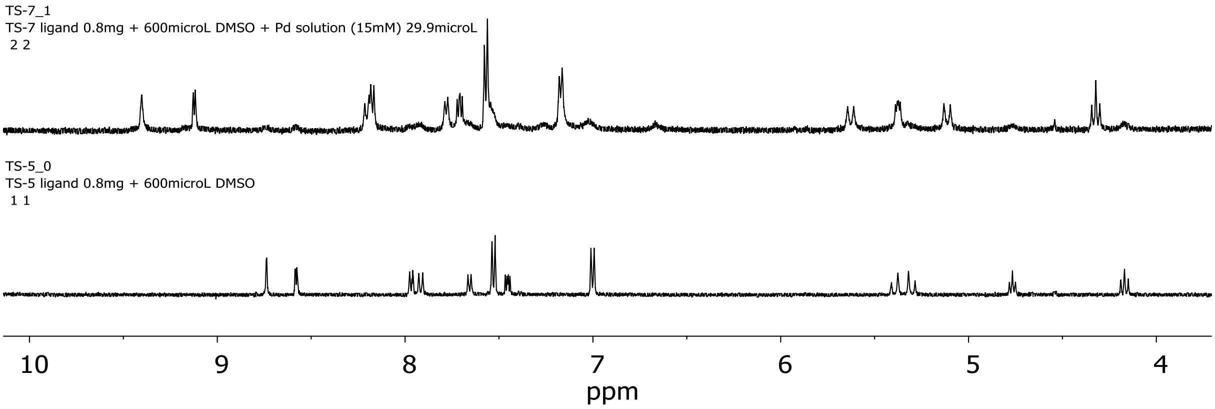

Figure 5.28 ^{1}H NMR spectra (500 MHz) of L^{H2} before and after the addition of Pd(CH_3CN)$_4$(BF_4)$_4$.

6 LIST OF FIGURES

Figure 1.1 a: Silver fulminate discovered by Wöhler and silver cyanate discovered by Liebig led to the concept of constituion; b: the first stereoisomers discovered by Pasteur.[9] 2

Figure 1.2 a: The enantiomers of the first reported chiral octahedral complex by Werner $[Co(en)_2(NH_3)X]X_2$ (X = Cl, Br)]; b: the enantiomers of the metal complex $[Ru(bpy)_3]^{2+}$. 3

Figure 1.3 The intelligent design of the ligands was used to prove the square planar coordination sphere of Pt(II). Only in case of the square planar coordination sphere the complex is chiral and can show optical activity after separation of the isomers.[15] 3

Figure 1.4 The first crown ether, that was accidently synthesized by Pedersen.[17] 4

Figure 1.5 Structures of 12-Crown-4, 15-Crown-5, 18-Crown-6 and 21-Crown-7, their inner diameter and selectivity towards Li^+, Na^+, K^+, Cs^+. 5

Figure 1.6 Four different hosts with the same number of binding sites but different binding constants due to the level of preorganization of the host. 5

Figure 1.7: a: [2]catenane reported by Sauvage, the Cu(I) is used as template before the ring closure leading to high yields for the formation; b: simplified schematic overview of reported catenanes, a rotaxane and the chiral trefoil knot.[22] 6

Figure 1.8 The combination of photoisomerization and thermal isomerization leads to a clockwise monodirectional rotation of the first reported molecular motor.[30] 7

Figure 1.9 The four combinations of stereoisomers in the case of two chiral centers and their relationship to each other as enantiomers and diastereomers.[1] 7

Figure 1.10 The “soft” approach: All parts are achiral but the assembly is chiral as result of the spatial arrangement or a twisting of the ligands.[33] 8

Figure 1.11 The “hard” approach: One component of the assembly is chiral leading to chirality of the whole assembly, that can be a ligand attached to the metal center, that does not link to another metal center or a ligand that connects two (or more) metal centers.[33] 9

Figure 1.12 left: Tetrahedral cluster with Ga^{III} ions in the corners; right: proposed catalytic cycle of 3-aza Cope rearrangement inside the assembly. © American Chemical Society, Wiley-VCH Verlag GmbH & Co[39,40] 10

Figure 1.13 The trigonal antiprism based on calixarene ligands is able to switch between the enantiomers (L' = PPh_3). Copyright © American Chemical Society[44] 10

Figure 1.14 a: Coordination modes of LT1 and LT2; b: Enantiomers of the edge directed tetrahedron T1 based on LT1 and enantiomers of the face directed tetrahedron T2 based on LT2. © Royal Society of Chemistry[45] 11

Figure 1.15 A tetranuclear assembly forming a molecular square with the use of a *cis*-blocked metal center. © American Chemical Society[46] 12

Figure 1.16 top: a: The achiral cage; b-d: the chiral auxiliary ligands leading to the chiral cage ; bottom: [2 + 2] Photoaddition reaction of N- cyclohexylmaleimide with fluoranthene(-derivative, R = H/Me) inside the cage. © American Chemical Society [50] 12

Figure 1.17 RI-BLYP/SVP (TZVP for copper) optimized structures of the three possible diastereomeric doublestranded helicates (a, b, c), but the (*M*)-enantiomers of the ligands selectively induce the (Δ,Δ)-helicate (a). © American Chemical Society[51] 13

Figure 1.18 The chiral ligands and their resulting supramolecular structures $[2BF_4^-+4CH_3CN@Pd_4L_8]^{6+}$ (X-ray structure)[53], $[Pd_6L_{12}]^{12+}$(DFT-optimized structure) and $[Pd_{12}L_{24}]^{24+}$ (DFT-optimized structure) upon addition of Pd(II). Petrol: Pd, red: O, blue: N, gray C. © Wiley-VCH Verlag GmbH & Co[52,53] 14

Figure 1.19 Chiral tetragonal and hexagonal prisms. © American Chemical Society[54] 15

Figure 1.20 Two (*P*)-helicene-capped helicands closely assembled around four Cu(I) metal centers upon addition of the Cu^+ cations. ©The Royal Society of Chemistry[56] 15

Figure 2.1 a: principle of anti-glare filtes, b: effect of anti-glare filter on "normal" OLED, c: effect of anti-glare filter on CPL OLED.[62] 18

Figure 2.2 CPL used as a chiral probe. The coordination of the protein leads to an induced CPL (dark blue: no CPL before coordination; orange: CPL because of the coordinated protein). © The Royal Society of Chemistry [58] 19

Figure 2.3 a: irradiation with polarized light with the writing laser, b: writing laser is turned off, c: irradiation with circularly polarized light to erase the information saved in the polymer. 20

Figure 2.4 The modified Jabłoński diagram. 21

Figure 2.5 Structures of the first cyclometalated Pt(II) complexes reported by Zelewsky (a + b) and a recently further developed complex (c) with very high luminescence quantum efficiency. 22

Figure 2.6 Structures of the chiral thienylpyridine based ligands for Pt(II) complexes and the ORTEP plot of the X-ray structure for the Pt(II) complex formed with c. © 1996 American Chemical Society 23

Figure 2.7 Structures of chiral Pt(II)complexes synthesized with achiral ligands and the X-ray structure showing the helical chirality of one formed complex. © 1997 American Chemical Society[76,78,79] 23

Figure 2.8 Structures of cyclometalated helicene based Pt(II) complexes. 24

Figure 2.9 left: Structure of the Ligand L^{NN} right: ORTEP drawing of the cation $[PdL^{NN}_2]^{2+}$. © 2002 American Chemical Society[85] 25

Figure 2.10 Synthesis of the trans chelating ligand enantiomer (*S*) and the X-ray structure of (*R*) enantiomers coordinated to Pd(II). © Wiley-VCH Verlag GmbH & Co[86] 25

Figure 2.11 The target structure: the trans cyclometalated Pt(II) complex. 26

Figure 2.12 Retrosynthetic analysis for ligand L^{CN}-Br 27

Figure 2.13 synthesis of 1. 28

Figure 2.14 ^{1}H NMR of 1 (600 MHz, $CDCl_3$). 28

Figure 2.15 ESI-MS of 1. 29

Figure 2.16: X-Ray structure of compound 1, solvent omitted for clarity. 29

Figure 2.17 Chromatograms of 1 (dichloromethane/methanol (99.5%/0.5%) mixture as eluent, Abs. 300 nm). Both enantiomers could be isolated as base-line separated peaks (c = 5 mg/mL, inject. V = 400µL). They are named “fraction 1” (eluted first) and “fraction 2” (eluted second). 30

Figure 2.18 a) CD spectra of 1 fraction 1 and 1 fraction 2 in dichloromethane; b) CD spectra after 60 min heating at 40, 60 and 70 °C that show the racemization of 1 fraction 1 in acetonitrile. 31

Figure 2.19 Chromatograms of enantiopure 1 (dichloromethane/methanol (99.5%/0.5%) (Abs. 300 nm) and after racemization for 2 h at 60 °C and the linear plot of ln(ee) for a series of injections vs time period at 60 °C indicating the first order kinetics. 31

Figure 2.20 Reaction scheme with the two formed stereoisomers of *trans*-2. 32

Figure 2.21 ^{1}H NMR of *trans*-2, 1 and the ligand before the lithiation L^{CN}. 32

Figure 2.22 FD(+) MS of *trans*-2. 33

Figure 2.23 ORTEP drawings (50 % probability) of *trans*-2. C black; N blue; Pt red, H omitted for clarity. 33

Figure 2.24 Chromatograms of *trans*-2 (Abs. 300 nm, flow rate 5 mL/min); dichloromethane/hexane/propan-2-ol(40.0%/59.5%/0.5%) mixture as eluent for the separation of *trans*-2. Both enantiomers were solved in DCM and could be isolated as base-line separated peaks (c = 1 mg/mL, inject. V = 90µL). They are named “fraction 1” (eluted first) and “fraction 2” (eluted second) in the discussion of the CD and CPL data and the absolute configuration. 34

Figure 2.25 left: assignment of the axial chirality; right: ORTEP drawing of the asymmetric unit with two molecules of *trans*-2(S_a); C: black, N: blue; Pt: red; H: grey. 35

Figure 2.26 ^{1}H NMR of *trans*-2 (CD_2Cl_2), 1 ($CDCl_3$), L^{CN} ($CDCl_3$), crude reaction mixtures after addition of *t*-BuLi. 36

Figure 2.27 ^{1}H NMR spectra of: a) *trans*-2 (CD_2Cl_2), b) 1 ($CDCl_3$), c) L^{CN} ($CDCl_3$), d-g) crude reaction mixtures after heating, that showed no significant signal indicating a coordination of the ligand L^{CN} without lithiation. 36

Figure 2.28 ^{1}H NMR spectra of: a) *trans*-2 (CD_2Cl_2), b) 1 ($CDCl_3$), c) L^{CN} ($CDCl_3$), d+e) crude reaction mixtures which show, that the replacement of THF by Et_2O did not result in significant formation of complex 1 or *trans*-2. 37

Figure 2.29 The *cis* chelating stereoisomers formed as kinetic product. 37

Figure 2.30: ^{1}H NMR of *cis*-2 (CD_2Cl_2), *trans*-2 (CD_2Cl_2), 1 ($CDCl_3$) and L^{CN} ($CDCl_3$). 38

Figure 2.31. NOESY NMR spectrum of *cis*-2 (600 MHz, CD_2Cl_2) 38

Figure 2.32: X-ray structure of *cis*-2 from three different angles. 39

Figure 2.33 ^{1}H NMR spectra of the transformation of *cis*-2 to *trans*-2 within 9 h (500 MHz, $CDCl_3$, 40 °C) 40

Figure 2.34 Combined UV-vis and emission spectra (excitation wavelength = 350 nm). 40

Figure 2.35 Emission lifetime measurement under argon atmosphere of *trans*-2 (left), normalized emission spectra for solution and solid state samples at 77 and 293 K (right). 41

Figure 2.36: CD (left) and CPL spectra (right) of the enantiomers of *trans*-2. 42

Figure 3.1 (*P*)-[6]-helicene and (*M*)-[6]-helicene. 43

Figure 3.2 Statistics of the literature published from 1969 to 2017, found via Scifinder for the keyword “helicene”, retrieved on May 29th, 2018. 43

Figure 3.3 the first reported (hetero-)helicenes. 44

Figure 3.4 Last step of the synthesis (left) and X-ray structure (right) of [16]helicene, R = triisopropylsilyl. 44

Figure 3.5 photocyclodehydrogenation of stilbene into phenanthrene. 45

Figure 3.6 The selectivity caused by the electron distribution can lead to the selective synthesis of helicenes, if the starting material is well planned.[109,114] 45

Figure 3.7 Experimental CD spectra for the (*P*) enantiomers of [5]-,[6]-,[7]-,[8]- and [9]-helicenes. © American Chemical Society [120] 47

Figure 3.8 The transition states for the racemization of [4], [5], and [6]-helicenes.[123] 48

Figure 3.9 A [7]-helicene derivative reported by Marinetti *et al.* to form diastereomers with a chiral Pd complex.[125] 48

Figure 3.10 Helicene based crown ethers with the ability of chiral recognition.[126] 49

Figure 3.11 The responsive switch based on an Os complex, that can be switched by the addition of acid and base leading to a strong shift of the IR band. © Royal Society of Chemistry [128] 49

Figure 3.12 A triple helicene cage.[129] 50

Figure 3.13 Organic cage containing three [6]helicenes.© American Chemical Society[130] 50

Figure 3.14 Overview over the synthesis of the 3 ligands developed for the synthesis of helicene cages.......... 51

Figure 3.15. Chromatograms of L^1 and L^2 before and after the separation of the enantiomers (Abs. 250 nm, flow rate 1 mL/min for the analytic column, flow rate 5 ml/min for the semipreparative column).......... 52

Figure 3.16 X-ray structures of L^{2P}. *left:* one ligand, carbon red, nitrogen blue; right: asymmetric unit with 12 molecules, spacefilling view, carbon grey, nitrogen blue, hydrogen light grey. 53

Figure 3.17 Simplified scheme of the cage formations for C1.......... 53

Figure 3.18 Stacked NMR spectra (DMSO-*d6*) for the cage formations with L^1... 54

Figure 3.19 ESI mass of $C1^{meso}$.......... 54

Figure 3.20 ^{1}H-^{1}H COSY and NOESY NMR spectra of $C1^{meso}$ (600 MHz, DMSO-*d6*). The characteristic singlets of H_a and H_e as starting point allowed the assignment of all proton signals due to the COSY and NOESY contacts. The contact H_k – $H_{k'}$ in the NOESY spectra is the bridge between the split signal sets and indicates, that the upper and lower half of the helicene must have a different surrounding. In addition to this the contacts H_a−$H_{a'}$ and H_b−$H_{b'}$ show the low intermolecular distance, caused by the coordination to Pd, as the intramolecular distances are too long for this contacts. 55

Figure 3.21 Simplified top view of the possible cage isomers to explain the splitting by symmetry operations. The *cis* coordination leading to the achiral meso cage is the only possible solution to explain the splitting into an upper and a lower half. 56

Figure 3.22 ESI mass spectrum of C1$^{P/M}$. 57

Figure 3.23 CD spectra of 1H NMR solutions of L^{1M}, L^{1P}, C1^{P}, C1^{M} in DMSO (0.6 mM). Cuvette path length 0.1 mm, wavelength: 250 nm – 500 nm, step size: 1 nm, band width: 0.5 nm. 57

Figure 3.24 stacked ^{1}H NMR spectra (DMSO-*d6*) of the titration experiment with C1^{P}. 58

Figure 3.25 δΔ plot of the titration experiments with C1^{P} and G1^{R}/G1^{S}. 59

Figure 3.26 Simplified scheme of the cage formations with the ligand L^{2}. 59

Figure 3.27 PM6 modelled structures of C1^{M} (left) and C2^{M} (right) which show the big difference in the Pd-Pd distance and cavity size. 60

Figure 3.28 stacked ^{1}H NMR spectra (DMSO-*d6*) of C2^{mix}, L^{2} and enantiopure C2$^{P/M}$. 61

Figure 3.29 ESI-MS of the racemic mixture of L^{2} that leads to C2^{mix}. 61

Figure 3.30 ESI-MS of C2$^{P/M}$. 61

Figure 3.31 stacked ^{1}H NMR spectra (DMSO-*d6*) of the titration experiment with C2^{P}. 62

Figure 3.32 δΔ plot for G1^{S}@C2^{P}, G1^{S}@C2^{M}, G1^{R}@C2^{P} and G1^{R}@C2^{P} 63

Figure 3.33 CD spectra of the L^{2} and C2 enantiomers in DMSO and ΔCD spectra of C2^{P} after addition of guests. 64

Figure 3.34. Calculated CD spectra for [6]helicene based on different C-C distances between position 2 and 15 showing the correlation of the circular dichroism with the distance d, that is correlating with the pitch. 64

Figure 3.35 Trapped ion mobility mass spectrometry results that show the different size of cage C2 depending on the guest. 65

Figure 3.36 stacked ^{1}H NMR spectra of C2^{mix}, L^{2}, enantiopure C2$^{P/M}$ in DMSO and the double cage formed in CD$_3$CN. 66

Figure 3.37 ESI-MS spectra of the double cage DC2^{M}. 66

Figure 3.38 Different perspectives on the X-ray structure of DC2^{M}. Pd: grey, C: dark green/black, N: blue, P: orange, F: light green. 67

Figure 4.1 Three natural compounds containing a 5,5,5-tricyclic scaffold (left) and the two nature inspired backbones used for the supramolecular assemblies in this work (right). 68

Figure 4.2 Structure of L^{H1} and L^{H2}. 69

Figure 4.3 ^{1}H NMR spectra of L^{H1} in CD_3CN before and after the addition of 2 eq. $Pd(CH_3CN)_4(BF_4)_2$. 69

Figure 4.4 ^{1}H NMR spectra in CD_3CN: a-c: L^{H2} which spectra differed for unknown reasons; d: the first attempt showed only a shifting of the signals; e-g: attempts to reproduce the spectrum of d resulted in very different spectra every time; i-h: change to different counterions led also to multiple splitted signals with a strong shift. 70

Figure 4.5 ESI-MS of $[Pd_2L^{H2}_4](BF_4)_4$ showing $[BF_4@Pd_2L^{H2}_4]^{3+}$ as the main species. 70

Figure 4.6 Preliminary X-ray structure of $[BF_4@Pd_2L^{H2}_4]^{3+}$, that consists of two $[PdL^{H2}_2]$ units (a) that are interlocked into each other (b and c). Each ligand in separate color for better clearance of the structural motive. 71

Figure 4.7 Structure of L^{W1} and the formed complex PdL^{W1}_2. 72

Figure 4.8 ^{1}H NMR spectra (CD_3CN) of the ligand and after addition of 0.5 eq. Pd(II) leading to the formation of a PdL_2 species. 72

Figure 4.9 ESI-MS spectrum of $[PdL^{W1}_2]^{2+}$ as the main species (left). 73

Figure 4.10 PM6 models of the two possible isomers for $[PdL^{W1}_2]^{2+}$. Left: the *trans* coordinated complex right: the *cis* coordinated complex. 73

Figure 4.11 Structure of the ligand L^{W2} and the presumable structure of the assembly $[Pd_3L^{W2}_6]$. 74

Figure 4.12 The ^{1}H spectra of the ligand in CD_3CN and DMSO before and after the addition of 2 eq Pd(II) in DMSO and CD_3CN, that results in a splitting of the signals due to the formation of the Pd_3L_6 assembly. 74

Figure 4.13 ESI-MS spectrum showing the formation of $[Pd_3L_6]^{6+}$ and its related assemblies with BF_4 anions as the main species........ 74

Figure 4.14 PM6 modelled structure of $[Pd_3L^{W2}_6]^{6+}$ from different perspectives and as space filling model........ 75

Figure 5.1. ESI-MS of 1. 82

Figure 5.2. ^{1}H NMR of 1 (600 MHz, $CDCl_3$). 82

Figure 5.3. ^{13}C NMR of 1 (151 MHz, $CDCl_3$). 82

Figure 5.4. ^{1}H-^{1}H COSY NMR spectrum of 1 (600 MHz, $CDCl_3$)........ 83

Figure 5.5. ^{1}H NMR spectrum of *trans*-2 (600 MHz, CD_2Cl_2). The full spectrum reveals that the signals assigned to $CDHCl_2$ and H_2O are relatively high due to the bad solubility of 2. 84

Figure 5.6 ^{1}H-^{1}H COSY NMR spectrum of *trans*-2 (600 MHz, CD_2Cl_2). 84

Figure 5.7. ^{13}C NMR spectrum of *trans*-2 (151 MHz, CD_2Cl_2). 85

Figure 5.8. HMBC NMR spectrum of *trans*-2 (600 MHz, CD_2Cl_2)........ 85

Figure 5.9. HSQC NMR spectrum of *trans*-2 (600 MHz, CD_2Cl_2). 86

Figure 5.10. COSY NMR spectrum of *cis*-2 (600 MHz, CD_2Cl_2). 87

Figure 5.11. **ORTEP drawing of racemic [Pt**L^{CN}$_2$**]** *trans*-2. **C: black/grey, N: blue, Pt: red. H atoms. 90**

Figure 5.12 Bivoet analysis output of enantiopure 2 (*S*$_a$) from the PLATON program.[147] 92

Figure 5.13. **^{1}H NMR spectra in DMSO. 95**

Figure 5.14. ^{1}H NMR spectra of L^1 in DMSO. 98

Figure 5.15 ^{1}H-^{1}H COSY and NOESY NMR spectra of L^1 **(600 MHz, DMSO-d6). The characteristic signals assigned to H_a and H_e as starting point allowed the assignment of all proton signals due to the COSY and NOESY contacts. 99**

Figure 5.16 ^{1}H NMR spectra in DMSO. 100

Figure 5.17The ^{1}H-^{13}C HMBC spectra(600 MHz, DMSO-d6) allows the assignment of H_e, H_f and H_l due to the contact with the alkyne carbon atoms. 101

Figure 5.18 ^{1}H-^{1}H COSY and NOESY NMR spectra of L^2 (600 MHz, DMSO-d6). The characteristic singlets of H_a and H_e as starting point allowed the assignment of all proton signals due to the COSY and NOESY contacts. 102

Figure 5.19 ^{1}H-^{1}H COSY and NOESY NMR spectra of $C1^{P/M}$ (500 MHz, DMSO-d6) with $CHCl_3$ for better separation of H_a and H_b. 104

Figure 5.20^{1}H-^{1}H COSY and NOESY NMR spectra of $C2^{P/M}$ (500 MHz, DMSO-d6). 105

Figure 5.21. **The ^{1}H-^{13}C HMBC NMR spectra of $C2^{P/M}$ (500 MHz, CD_3CN) allows the assignment of H_e, H_f and H_l due to the contacts with the alkyne carbon atoms and supports the assignment for H_i and H_j based on COSY and NOESY spectra. 106**

Figure 5.22. **^{1}H-^{1}H COSY and NOESY NMR spectra of $C2^{P/M}$ (500 MHz, CD_3CN). All signals could be assigned. 107**

Figure 5.23. **COSY of $DC2^{P/M}$ (black) (600 MHz, CD_3CN) and $C2^{P/M}$ (red) (500 MHz, CD_3CN) to allow clear assignment of the proton contacts of $DC2^{P/M}$, as a few percent of monomeric cage remained in the sample of the double cage. 108**

Figure 5.24. **Combined ^{1}H-^{1}H COSY and NOESY NMR spectra of $DC2^{P/M}$ (600 MHz, CD_3CN) and the ^{1}H-^{13}C HMBC spectrum. All contacts could be assigned and are in agreement with the crystal structure of $DC2^{M}$. 109**

Figure 5.25. **Superimposed ^{1}H DOSY spectra of $C1^{meso}$, $C1^{P/M}$ and $C2^{P/M}$. 110**

Figure 5.26 Pascal's triangle for the cage formation with a racemic ligand mixture. The probability is the number of combinations for one set, divided by the total number of combinations. 111

Figure 5.27 ORTEP drawing of one of the twelve ligands L^{2P}, which are present in the asymmetric unit. 112
Figure 5.28 ^{1}H NMR spectra (500 MHz) of L^{H2} before and after the addition of $Pd(CH_3CN)_4(BF_4)_4$. 117

7 REFERENCES

[1] G. A. Hembury, V. V. Borovkov, Y. Inoue, *Chem. Rev.* **2008**, *108*, 1.

[2] J. W. Steed, J. L. Atwood, *Supramol. Chem.*, Wiley, Chichester, UK, **2009**.

[3] Ryoji Noyori, *Angew. Chem. Int. Ed.* **2002**, 2008.

[4] a) J. M. McBride, J. C. Tully, *Nat.* **2008**, *452*, 161; b) U. Meierhenrich, A. Brack, G. Horneck, C. P. McKay, H. Stan-Lotter (Eds.) *Advances in Astrobiology and Biogeophysics*, Springer, Berlin, Heidelberg, **2008**.

[5] a) M. D. Levin, D. M. Kaphan, C. M. Hong, R. G. Bergman, K. N. Raymond, F. D. Toste, *J. Am. Chem. Soc.* **2016**, *138*, 9682; b) W. B. Motherwell, M. J. Bingham, Y. Six, *Tetrahedron* **2001**, *57*, 4663.

[6] I. Newton (Ed.) *Isaac Newton letter to Robert Hooke*, **1675**.

[7] Alain Berthod, *Anal. Chem.* **2006**, 2093.

[8] S. Esteban, *J. Chem. Educ.* **2008**, *85*, 1201.

[9] F. Kurzer, *J. Chem. Educ.* **2000**, *77*, 851.

[10] G. P. Moss, *Pure and Appl. Chem.* **1996**, *68*, 2193.

[11] H. Werner, *Angew. Chem.* **2013**, *125*, 6262.

[12] a) A. Werner, *Ber. Dtsch. Chem. Ges.* **1911**, *44*, 1887; b) E. C. Constable, *Chemical Society reviews* **2013**, *42*, 1637.

[13] V. Balzani, S. Campagna (Eds.) *Topics in Current Chemistry*, Springer Berlin Heidelberg, Berlin, Heidelberg, **2007**.

[14] M. C. Biagini, M. Ferrari, M. Lanfranchi, L. Marchiò, M. A. Pellinghelli, *J. Chem. Soc., Dalton Trans.* **1999**, 1575.

[15] W. H. Mills, T. H. H. Quibell, *J. Chem. Soc.* **1935**, 839.

[16] F. Biedermann, H.-J. Schneider, *Chem. Rev.* **2016**, *116*, 5216.

[17] K. Ariga, T. Kunitake, *Supramolecular chemistry - fundamentals and applications*. *Advanced textbook*, Springer, Berlin, Heidelberg, **2006**.

[18] C. J. Pedersen, *J. Am. Chem. Soc.* **1967**, *89*, 7017.

[19] T. Frängsmyr, B. G. Malmström (Eds.) *Nobel lectures*, *including presentation speeches and laureates' biographies ; chemistry ; 6*, Elsevier, Amsterdam, **1992**.

[20] D. J. Cram, *Angew. Chem. Int. Ed. Engl.* **1986**, *25*, 1039.

[21] R. van Noorden, D. Castelvecchi, *Nat.* **2016**, *538*, 152.

[22] C. O. Dietrich-Buchecker, J.-P. Sauvage, A. de Cian, J. Fischer, *J. Chem. Soc., Chem. Commun.* **1994**, 2231.

[23] a) E. Wasserman, *J. Am. Chem. Soc.* **1960**, *82*, 4433; b) D. B. Amabilino, J. F. Stoddart, *Chem. Rev.* **1995**, *95*, 2725.

[24] D. B. Amabilino, P. R. Ashton, A. S. Reder, N. Spencer, J. F. Stoddart, *Angew. Chem. Int. Ed. Engl.* **1994**, *33*, 1286.

[25] G. Schill, H. Zollenkopf, *Justus Liebigs Ann. Chem.* **1969**, *721*, 53.

[26] C. O. Dietrich-Buchecker, J.-P. Sauvage, *Angew. Chem. Int. Ed. Engl.* **1989**, *28*, 189.

[27] a) R. S. Forgan, J.-P. Sauvage, J. F. Stoddart, *Chem. rev.* **2011**, *111*, 5434; b) F. M. Raymo, J. F. Stoddart, *Chem. Rev.* **1999**, *99*, 1643; c) G. Gil-Ramírez, D. A. Leigh, A. J. Stephens, *Angew. Chem. Int. Ed.* **2015**, *54*, 6110.

[28] M. Peplow, *Nat.* **2015**, *525*, 18.

[29] C. Cheng, P. R. McGonigal, S. T. Schneebeli, H. Li, N. A. Vermeulen, C. Ke, J. F. Stoddart, *Nat. Nanotech.* **2015**, *10*, 547.

[30] N. Koumura, R. W. J. Zijlstra, R. A. van Delden, N. Harada, B. L. Feringa, *Nat.* **1999**, *401*, 152 EP -.

[31] J.-M. Lehn, *Angew. Chem. Int. Ed.* **1988**, *27*, 89.

[32] J.-M. Lehn, *Angew. Chem. Int. Ed.* **2013**, *52*, 2836.

[33] L.-J. Chen, H.-B. Yang, M. Shionoya, *Chem. Soc. Rev.* **2017**, *46*, 2555.

[34] a) D. L. Caulder, K. N. Raymond, *J. Chem. Soc., Dalton Trans.* **1999**, 1185; b) A. M. Castilla, W. J. Ramsay, J. R. Nitschke, *Chem. Lett.* **2014**, *43*, 256.

[35] A. J. Terpin, M. Ziegler, D. W. Johnson, K. N. Raymond, *Angew. Chem.* **2001**, *113*, 161.

[36] A. V. Davis, D. Fiedler, M. Ziegler, A. Terpin, K. N. Raymond, *J. Am. Chem. Soc.* **2007**, *129*, 15354.

[37] M. Ziegler, A. V. Davis, D. W. Johnson, K. N. Raymond, *Angew. Chem. Int. Ed.* **2003**, *42*, 665.

[38] a) D. H. Leung, D. Fiedler, R. G. Bergman, K. N. Raymond, *Angew. Chem. Int. Ed.* **2004**, *43*, 963; b) D. H. Leung, R. G. Bergman, K. N. Raymond, *J. Am. Chem. Soc.***2006**, *128*, 9781.

[39] D. Fiedler, D. H. Leung, R. G. Bergman, K. N. Raymond, *Acc. Chem. Res.* **2005**, *38*, 349.

[40] D. Fiedler, R. G. Bergman, K. N. Raymond, *Angew. Chem. Int. Ed.* **2004**, *43*, 6748.

[41] C. J. Hastings, M. D. Pluth, R. G. Bergman, K. N. Raymond, *J. Am. Chem. Soc.***2010**, *132*, 6938.

[42] M. D. Pluth, R. G. Bergman, K. N. Raymond, *Angew. Chem. Int. Ed.* **2007**, *46*, 8587.

[43] a) Z. J. Wang, C. J. Brown, R. G. Bergman, K. N. Raymond, F. D. Toste, *J. Am. Chem. Soc.***2011**, *133*, 7358; b) D. H. Leung, R. G. Bergman, K. N. Raymond, *J. Am. Chem. Soc.* **2007**, *129*, 2746.

[44] A. Ikeda, H. Udzu, Z. Zhong, S. Shinkai, S. Sakamoto, K. Yamaguchi, *J. Am. Chem. Soc.* **2001**, *123*, 3872.

[45] P. Howlader, P. S. Mukherjee, *Chem. Sci.* **2016**, *7*, 5893.

[46] B. Olenyuk, J. A. Whiteford, P. J. Stang, *J. Am. Chem. Soc.* **1996**, *118*, 8221.

[47] M. Yoshizawa, M. Tamura, M. Fujita, *J. Am. Chem. Soc.***2004**, *126*, 6846.

[48] Y. Nishioka, T. Yamaguchi, M. Yoshizawa, M. Fujita, *J. Am. Chem. Soc.***2007**, *129*, 7000.

[49] M. Yoshizawa, J. K. Klosterman, M. Fujita, *Angew. Chem. Int. Ed.* **2009**, *48*, 3418.

[50] Y. Nishioka, T. Yamaguchi, M. Kawano, M. Fujita, *J. Am. Chem. Soc.***2008**, *130*, 8160.

[51] J. Bunzen, T. Bruhn, G. Bringmann, A. Lützen, *J. Am. Chem. Soc.***2009**, *131*, 3621.

[52] C. Gütz, R. Hovorka, C. Klein, Q.-Q. Jiang, C. Bannwarth, M. Engeser, C. Schmuck, W. Assenmacher, W. Mader, F. Topić et al *Angew. Chem. Int. Ed.* **2014**, *53*, 1693.

[53] C. Klein, C. Gütz, M. Bogner, F. Topić, K. Rissanen, A. Lützen, *Angew. Chem. Int. Ed.* **2014**, *53*, 3739.

[54] Y. Ye, T. R. Cook, S.-P. Wang, J. Wu, S. Li, P. J. Stang, *J. Am. Chem. Soc.***2015**, *137*, 11896.

[55] V. Vreshch, M. El Sayed Moussa, B. Nohra, M. Srebro, N. Vanthuyne, C. Roussel, J. Autschbach, J. Crassous, C. Lescop, R. Réau, *Angew. Chem. Int. Ed.* **2013**, *52*, 1968.

[56] N. Saleh, C. Shen, J. Crassous, *Chem. Sci.* **2014**, *5*, 3680.

[57] T. R. Schulte, J. J. Holstein, L. Krause, R. Michel, D. Stalke, E. Sakuda, K. Umakoshi, G. Longhi, S. Abbate, G. H. Clever, *J. Am. Chem. Soc.***2017**, *139*, 6863.

[58] R. Carr, N. H. Evans, D. Parker, *Chem. Soc. Rev.* **2012**, *41*, 7673.

[59] C. Wang, H. Fei, Y. Qiu, Y. Yang, Z. Wei, Y. Tian, Y. Chen, Y. Zhao, *Appl. Phys. Lett.* **1999**, *74*, 19.

[60] J. R. Brandt, X. Wang, Y. Yang, A. J. Campbell, M. J. Fuchter, *J. Am. Chem. Soc.***2016**, *138*, 9743.

[61] C.-F. Chen, Y. Shen, *Helicene Chemistry*, Springer Berlin Heidelberg, Berlin, Heidelberg, **2017**.

[62] R. Singh, K. N. Narayanan Unni, A. Solanki, Deepak, *Optical Materials* **2012**, *34*, 716.

[63] R. Carr, L. Di Bari, S. Lo Piano, D. Parker, R. D. Peacock, J. M. Sanderson, *Dalton Trans.* **2012**, *41*, 13154.

[64] V. W. W. Yam (Ed.) *Green Energy and Technology*, Springer Berlin Heidelberg, Berlin, Heidelberg, **2010**.

[65] B. Minaev, G. Baryshnikov, H. Agren, *PCCP* **2014**, *16*, 1719.

[66] J. Colegrove in *Handbook of Visual Display Technology* (Eds.: J. Chen, W. Cranton, M. Fihn), Springer International Publishing, Cham, **2016**, pp. 3369–3377.

[67] K. Blankenbach in *Handbook of Visual Display Technology* (Eds.: J. Chen, W. Cranton, M. Fihn), Springer Berlin Heidelberg, Berlin, Heidelberg, **2014**, pp. 1–17.

[68] M. Muccini, S. Toffanin, *Organic light-emitting transistors*. *Towards the next generation display technology*, John Wiley & Sons, Hoboken, New Jersey, **2016**.

[69] M. A. Baldo, D. F. O'Brien, Y. You, A. Shoustikov, S. Sibley, M. E. Thompson, S. R. Forrest, *Nat.* **1998**, *395*, 151.

[70] C.-C. Kwok, S. C. F. Kui, S.-W. Lai, C.-M. Che in *Green Energy and Technology* (Ed.: V. W. W. Yam), Springer Berlin Heidelberg, Berlin, Heidelberg, **2010**, pp. 79–104.

[71] a) R. Ballardini, G. Varani, M. T. Indelli, F. Scandola, *Inorg. Chem.* **1986**, *25*, 3858; b) F. Barigelletti, D. Sandrini, M. Maestri, V. Balzani, A. von Zelewsky, L. Chassot, P. Jolliet, U. Maeder, *Inorg. Chem.* **1988**, *27*, 3644.

[72] D. Sandrini, M. Maestri, V. Balzani, L. Chassot, A. von Zelewsky, *J. Am. Chem. Soc.* **1987**, *109*, 7720.

[73] G. Zhou, W.-Y. Wong, X. Yang, *Chemistry, an Asian journal* **2011**, *6*, 1706.

[74] a) C.-L. Ho, H. Li, W.-Y. Wong, *Journal of Organometallic Chemistry* **2014**, *751*, 261; b) H. Fukagawa, T. Shimizu, H. Hanashima, Y. Osada, M. Suzuki, H. Fujikake, *Adv. Mat.* **2012**, *24*, 5099.

[75] M. Gianini, A. Forster, P. Haag, A. von Zelewsky, H. Stoeckli-Evans, *Inorg. Chem.* **1996**, *35*, 4889.

[76] M. Gianini, A. von Zelewsky, H. Stoeckli-Evans, *Inorg. Chem.* **1997**, *36*, 6094.

[77] U. Knof, A. von Zelewsky, *Angew. Chem. Int. Ed.* **1999**, *38*, 302.

[78] A. von Zelewsky, *Coord. Chem. Rev.* **1999**, *190-192*, 811.

[79] C. Deuschel-Cornioley, H. Stoeckli-Evans, A. von Zelewsky, *J. Chem. Soc., Chem. Commun.* **1990**, *26*, 121.

[80] W. H. Pirkle, D. L. Sikkenga, M. S. Pavlin, *J. Org. Chem.* **1977**, *42*, 384.

[81] L. Norel, M. Rudolph, N. Vanthuyne, J. A. G. Williams, C. Lescop, C. Roussel, J. Autschbach, J. Crassous, R. Réau, *Angew. Chem. Int. Ed.* **2010**, *49*, 99.

[82] E. Anger, M. Rudolph, L. Norel, S. Zrig, C. Shen, N. Vanthuyne, L. Toupet, J. A. G. Williams, C. Roussel, J. Autschbach et al., *Chemistry* **2011**, *17*, 14178.

[83] D. Mendola, N. Saleh, N. Vanthuyne, C. Roussel, L. Toupet, F. Castiglione, T. Caronna, A. Mele, J. Crassous, *Angew. Chem.* **2014**, *126*, 5896.

[84] E. Bosch, C. L. Barnes, *Inorg. Chem.* **2001**, *40*, 3097.

[85] Y.-Z. Hu, C. Chamchoumis, J. S. Grebowicz, R. P. Thummel, *Inorg. Chem.* **2002**, *41*, 2296.

[86] G. Meyer-Eppler, F. Topić, G. Schnakenburg, K. Rissanen, A. Lützen, *Eur. J. Inorg. Chem.* **2014**, *2014*, 2495.

[87] R. Chinchilla, C. Najera, *Chem. Rev.* **2007**, *107*, 874.

[88] Z. Li, N. Kishi, K. Yoza, M. Akita, M. Yoshizawa, *Chemistry* **2012**, *18*, 8358.

[89] T. Hundertmark, A. F. Littke, S. L. Buchwald, G. C. Fu, *Org. Lett.* **2000**, *2*, 1729.

[90] B. H. Kaae, K. Harpsøe, T. Kvist, J. M. Mathiesen, C. Mølck, D. Gloriam, H. N. Jimenez, M. A. Uberti, S. M. Nielsen, B. Nielsen et al., *ChemMedChem* **2012**, *7*, 440.

[91] L. Chassot, A. von Zelewsky, *Inorg. Chem.* **1987**, *26*, 2814.

[92] L. Chassot, E. Mueller, A. von Zelewsky, *Inorg. Chem.* **1984**, *23*, 4249.

[93] E. V. Anslyn, D. A. Dougherty, *Modern physical organic chemistry*, University Science Books, Mill Valley, California, **2006**.

[94] L. Varennikov, E. Yedemsky (Eds.) *Materials science and technologies*, Nova Publishers, Hauppauge New York, **2013**.

[95] a) D. Kim, J.-L. Brédas, *J. Am. Chem. Soc.***2009**, *131*, 11371; b) A. Aliprandi, D. Genovese, M. Mauro, L. de Cola, *Chem. Lett.* **2015**, *44*, 1152; c) M. Micksch, M. Tenne, T. Strassner, *Organometallics* **2014**, *33*, 3464.

[96] S. Parsons, H. D. Flack, T. Wagner, *Acta crystallographica Section B, Structural science, crystal engineering and materials* **2013**, *69*, 249.

[97] R. W. W. Hooft, L. H. Straver, A. L. Spek, *Journal of applied crystallography* **2010**, *43*, 665.

[98] H. D. Flack, *Acta Crystallogr A Found Crystallogr* **1983**, *39*, 876.

[99] R. Luisi, V. Capriati, S. Florio, B. Musio, *Org. Lett.* **2007**, *9*, 1263.

[100] C. J. Woltermann, J. A. Schwindeman, *ChemInform* **2004**, *35*, 5.

[101] E. Castiglioni, S. Abbate, F. Lebon, G. Longhi, *Methods Appl. Fluores.* **2014**, *2*, 24006.

[102] a) E. Castiglioni, S. Abbate, G. Longhi, *Applied spectroscopy* **2010**, *64*, 1416; b) C. Citti, U. M. Battisti, G. Ciccarella, V. Maiorano, G. Gigli, S. Abbate, G. Mazzeo, E. Castiglioni, G. Longhi, G. Cannazza, *Journal of chromatography. A* **2016**, *1467*, 335; c) G. Mazzeo, M. Fusè, G. Longhi, I. Rimoldi, E. Cesarotti, A. Crispini, S. Abbate, *Dalton Trans.* **2016**, *45*, 992.

[103] G. Longhi, E. Castiglioni, J. Koshoubu, G. Mazzeo, S. Abbate, *Chirality* **2016**, *28*, 696.

[104] R. S. Cahn, C. Ingold, V. Prelog, *Angew. Chem. Int. Ed. Engl.* **1966**, *5*, 385.

[105] M. Gingras, *Chem. Soc. Rev.* **2013**, *42*, 968.

[106] J. Meisenheimer, K. Witte, *Ber. Dtsch. Chem. Ges.* **1903**, *36*, 4153.

[107] R. Weitzenböck, H. Lieb, *Monatshefte für Chemie* **1912**, *33*, 549.

[108] K. Mori, T. Murase, M. Fujita, *Angew. Chem. Int. Ed.* **2015**, *54*, 6847.

[109] W. H. Laarhoven, W. J. C. Prinsen in *Topics in Current Chemistry* (Eds.: F. L. Boschke, M. J. S. Dewar, J. D. Dunitz, K. Hafner, E. Heilbronner, S. Ito, J.-M. Lehn, K. Niedenzu, K. N. Raymond, C. W. Rees et al.), Springer Berlin Heidelberg, Berlin, Heidelberg, **1984**, pp. 63–130.

[110] W. Carruthers, *J. Chem. Soc., C* **1967**, 1525.

[111] M. Scholz, M. Mühlstädt, F. Dietz, *Tetrahedron Letters* **1967**, *8*, 665.

[112] M. Flammang-Barbieux, J. Nasielski, R. H. Martin, *Tetrahedron Letters* **1967**, *8*, 743.

[113] L. Liu, B. Yang, T. J. Katz, M. K. Poindexter, *J. Org. Chem.* **1991**, *56*, 3769.

[114] T. Wismonski-Knittel, E. Fischer, *J. Chem. Soc., Perkin Trans. 2* **1979**, 449.

[115] Q. Lefebvre, M. Jentsch, M. Rueping, *Beilstein journal of organic chemistry* **2013**, *9*, 1883.

[116] R. H. Martin, M. Flammang-Barbieux, J. P. Cosyn, M. Gelbcke, *Tetrahedron Letters* **1968**, *9*, 3507.

[117] R. H. Martin, M. J. Marchant, *Tetrahedron* **1974**, *30*, 343.

[118] P. W. Atkins, J. de Paula, *Atkins' physical chemistry*, Oxford Univ. Press, Oxford, **2006**.

[119] M. S. Newman, D. Lednicer, *J. Am. Chem. Soc.* **1956**, *78*, 4765.

[120] Y. Nakai, T. Mori, Y. Inoue, *The journal of physical chemistry. A* **2012**, *116*, 7372.

[121] C. Goedicke, H. Stegemeyer, *Tetrahedron Lett.* **1970**, *11*, 937.

[122] R. H. Martin, M. J. Marchant, *Tetrahedron* **1974**, *30*, 347.

[123] J. Barroso, J. L. Cabellos, S. Pan, F. Murillo, X. Zarate, M. A. Fernandez-Herrera, G. Merino, *Chem. Comm.* **2018**, *54*, 188.

[124] H. J. Lindner, *Tetrahedron* **1975**, *31*, 281.

[125] R. El Abed, F. Aloui, J.-P. Genêt, B. Ben Hassine, A. Marinetti, *Journal of Organometallic Chemistry* **2007**, *692*, 1156.

[126] M. Nakazaki, K. Yamamoto, T. Ikeda, T. Kitsuki, Y. Okamoto, *J. Chem. Soc., Chem. Commun.* **1983**, 787.

[127] a) E. Anger, M. Rudolph, C. Shen, N. Vanthuyne, L. Toupet, C. Roussel, J. Autschbach, J. Crassous, R. Réau, *J. Am. Chem. Soc.***2011**, *133*, 3800; b) C. Shen, E. Anger, M. Srebro, N. Vanthuyne, K. K. Deol, T. D. Jefferson, G. Muller, J. A. Gareth Williams, L. Toupet, C. Roussel et al., *Chemical science* **2014**, *5*, 1915; c) C. Shen, E. Anger, M. Srebro, N. Vanthuyne, L. Toupet, C. Roussel, J. Autschbach, R. Réau, J. Crassous, *Chemistry* **2013**, *19*, 16722; d) A. I. Aranda Perez, T. Biet, S.

Graule, T. Agou, C. Lescop, N. R. Branda, J. Crassous, R. Réau, *Chemistry* **2011**, *17*, 1337.

[128] E. Anger, M. Srebro, N. Vanthuyne, C. Roussel, L. Toupet, J. Autschbach, R. Réau, J. Crassous, *Chem. Comm.* **2014**, *50*, 2854.

[129] T. Matsushima, S. Kikkawa, I. Azumaya, S. Watanabe, *ChemistryOpen* **2018**, *7*, 278.

[130] A. U. Malik, F. Gan, C. Shen, N. Yu, R. Wang, J. Crassous, M. Shu, H. Qiu, *J. Am. Chem. Soc.* **2018**, *140*, 2769.

[131] A. Terfort, H. Görls, H. Brunner, *Synthesis* **1997**, *1997*, 79.

[132] J. M. Fox, D. Lin, Y. Itagaki, T. Fujita, *J. Org. Chem.* **1998**, *63*, 2031.

[133] N. Hoffmann, *Journal of Photochemistry and Photobiology C: Photochemistry Reviews* **2014**, *19*, 1.

[134] G. M. Sheldrick, *Acta crystallographica. Section C, Structural chemistry* **2015**, *71*, 3.

[135] S. Freye, J. Hey, A. Torras-Galán, D. Stalke, R. Herbst-Irmer, M. John, G. H. Clever, *Angew. Chem. Int. Ed.* **2012**, *51*, 2191.

[136] D. M. Engelhard, S. Freye, K. Grohe, M. John, G. H. Clever, *Angew. Chem. Int. Ed.* **2012**, *51*, 4747.

[137] J.-F. Greisch, J. Chmela, M. E. Harding, D. Wunderlich, B. Schäfer, M. Ruben, W. Klopper, D. Schooss, M. M. Kappes, *PCCP* **2017**, *19*, 6105.

[138] G. H. Clever, P. Punt, *Accounts of chemical research* **2017**, *50*, 2233.

[139] M. Potowski, C. Merten, A. P. Antonchick, H. Waldmann, *Chemistry* **2015**, *21*, 4913.

[140] M. Schnopp, S. Ernst, G. Haberhauer, *Eur. J. Org. Chem.* **2009**, *2009*, 213.

[141] G. Haberhauer, *Angew. Chem. Int. Ed.* **2007**, *46*, 4397.

[142] P. Comba, N. Dovalil, L. R. Gahan, G. R. Hanson, M. Westphal, *Dalton Trans.* **2014**, *43*, 1935.

[143] L. F. Tietze, U. Beifuss, *Angew. Chem. Int. Ed. Engl.* **1993**, *32*, 131.

[144] a) D. K. Chand, K. Biradha, M. Kawano, S. Sakamoto, K. Yamaguchi, M. Fujita, *Chem.Asian J.* **2006**, *1*, 82; b) O. Jurček, P. Bonakdarzadeh, E. Kalenius, J. M. Linnanto, M. Groessl, R. Knochenmuss, J. A. Ihalainen, K. Rissanen, *Angew. Chem. Int. Ed.* **2015**, *54*, 15462; c) K. Suzuki, M. Kawano, M. Fujita, *Angew. Chem. Int. Ed.* **2007**, *46*, 2819; d) D. Samanta, A. Chowdhury, P. S. Mukherjee, *Inorganic chemistry* **2016**, *55*, 1562; e) S. Ganta, D. K. Chand, *Dalton Trans.* **2015**, *44*, 15181.

[145] G. M. Sheldrick, *Acta crystallographica. Section A, Foundations and advances* **2015**, *71*, 3.

[146] C. B. Hübschle, G. M. Sheldrick, B. Dittrich, *J. Appl. Crystallogr.* **2011**, *44*, 1281.

[147] A. L. Spek, *Acta crystallographica. Section C, Structural chemistry* **2015**, *71*, 9.

[148] a) G. H. Clever, S. Tashiro, M. Shionoya, *J. Am. Chem. Soc.* **2010**, *132*, 9973; b) S. Löffler, J. Lübben, A. Wuttke, R. A. Mata, M. John, B. Dittrich, G. H. Clever, *Chem. Sci.* **2016**, *7*, 4676.

[149] G. M. Sheldrick, *Acta crystallographica. Section D, Biological crystallography* **2010**, *66*, 479.

[150] A. Thorn, B. Dittrich, G. M. Sheldrick, *Acta Crystallogr.* **2012**, *68*, 448.

[151] A. Burkhardt, T. Pakendorf, B. Reime, J. Meyer, P. Fischer, N. Stübe, S. Panneerselvam, O. Lorbeer, K. Stachnik, M. Warmer et al., *Eur. Phys. J. Plus* **2016**, *131*, 25.

[152] W. Kabsch, *Acta crystallographica. Section D, Biological crystallography* **2010**, *66*, 125.

[153] A. L. Spek, *Acta crystallographica. Section D, Biological crystallography* **2009**, *65*, 148.